ACOUSTICS IN NANOTECHNOLOGY: MANIPULATION, DEVICE APPLICATION AND MODELING

A Dissertation
Presented to
The Academic Faculty

by

Brent Alan Buchine

In Partial Fulfillment
of the Requirements for the Degree
Doctor of Philosophy in the
School of Materials Science and Engineering

Georgia Institute of Technology
August 2007

ACOUSTICS IN NANOTECHNOLOGY: MANIPULATION, DEVICE APPLICATION AND MODELING

Approved by:

Dr. Zhong L. Wang, Advisor
School of Materials Science and Engineering
Georgia Institute of Technology

Dr. Meilin Liu
School of Materials Science and Engineering
Georgia Institute of Technology

Dr. F. Levent Degertekin
Woodruff School of Mechanical Engineering
Georgia Institute of Technology

Dr. Rina Tannenbaum
Materials Science and Engineering
Georgia Institute of Technology

Dr. Robert L. Snyder
School of Materials Science and Engineering
Georgia Institute of Technology

Date Approved: August 29, 2007

Dedicated to my wife and child

ACKNOWLEDGEMENTS

I would like to start by thanking my advisor and committee members who each played an integral role in my maturation as a scientist. To Dr. Zhong Lin Wang for your guidance and support over the last five years; your enthusiasm for science is contagious. To Dr. F. Levent Degertekin for lessons learned along side you in the lab and in your office. I would like to thank Dr. Meilin Liu for the inspiration to pursue research in the area of functional ceramics. To Dr. Rina Tannenbaum, for the care you show for students. It was classes taught by you that helped develop my thirst for knowledge. To Dr. Robert L. Snyder, your passion for science is always evident in every conversation. Thank you for the open door.

To those around me as colleagues and collaborators, I would like to thank William Hughes for being a mentor. You are as much one of my greatest teacher as you are one of my greatest friends. Reza Abdolvand, your intellect is unsurpassed. Our midnight discussions will always be a valued part of my memory. Thank you to Guclu Onaran, Rasim Guidiken, Arnab Choudry and Carter Dietz for your dependable assistance. To Ryan Westafer, Chris Corso and Tony Dickherber, thank you for sharing your knowledge in the area of acoustics. Our political discussions were always a welcome break from work. To Christopher Ma, Puxian Gao, Xudong Wang, your leadership by example has helped guide me over the last five years. To Jenny Ruth Morber and Benjamin Weintraub, thank you both for your critical feedback with regards to my research. I've enjoyed our time together as friends as much as our time together as colleagues. To Todd Walters, thank you for the laughs. Sharing an office with you has

been a joy. To Susan Bowman, having you in the department is like having a second mother. Thank you for the support you provide me and the students of MSE.

To those that are dear to me through family and friendship. I would like to thank Norbert Zaragoza for his emotional support. To Dad and Ellen, thank you for the enthusiasm and pride you've shown for my work. I would like to thank my Brothers, Jesse, Isaac and Roni Buchine. Even though our time together is limited, you are forever on my mind and your e-mails always make me smile. To my Grandparents Albert and Dorothy Cohen, your unwavering support for all my endeavors has helped guide me throughout my life. This dissertation belongs to you as much as it does me. To my mother, the man I am today is a consequence of your upbringing. The bond you and I share is unbreakable.

To my wife Heather, your warm heart and sweet spirit comes across in the care you provide. You are my strength. You are my motivation. I could have not asked for a more loving and caring partner to go through the world with. And finally, to my child, the greatest joy in my life was the day your mother and I found out you were entering the world. Each new day is better than the previous because it bring me one day closer to meeting you for the first time.

TABLE OF CONTENTS

LIST OF TABLES

LIST OF FIGURES

LIST OF ABBREVIATIONS

0D	Zero Dimensional
1D	One Dimensional
2D	Two Dimensional
3D	Three Dimensional
AC	Alternating Current
AFM	Atomic Force Microscopy
ALD	Atomic Layer Deposition
BAR	Bulk Acoustic Resonator
BAW	Bulk Acoustic Wave
BOE	Buffered Oxide Etchent
BVD	Butterworth Van-Dyke Model
CMOS	Complimentary Metal Oxide Semiconductor
CVD	Chemical Vapor Deposition
DC	Direct Current
DI	Deionized Water
DUT	Device Under Test
FBAR	Thin Film Bulk Acoustic Resonator
FIB	Focused Ion Beam Microscope
GSG	Ground-Signal-Ground
HMTA	Hexamethylenetetramine
HRTEM	High Resolution Transmission electron Microscopy
ICP	Inductively Coupled Plasma
IPA	Isopropyl Alcohol

ISTS	Impulsive Stimulated Thermal Scattering
KLM	Krimholt-Leedom-Matthaei Model
LFE	Lateral Field Excitation
LMIS	Liquid Metal Ion Source
MBE	Molecular Beam Epitaxy
MEMS	Micro-Electro-Mechanical Systems
MOCVD	Metal Organic Chemical Vapor Deposition
MWCNT	Multi-Walled Carbon Nanotube
NEMS	Nano-Electro-Mechanical Systems
PECVD	Plasma Enhanced Chemical Vapor Deposition
PLD	Pulsed Laser Deposition
PMMA	Polymethylmethacrylate
PSD	Polar Surface Dominated
PVD	Physical Vapor Deposition
RPM	Revolutions Per Minute
SAW	Surface Acoustic Wave
SEM	Scanning Electron Microscope
SMR	Solidly Mounted Resonator
SOI	Silicon on Insulator
STM	Scanning Tunneling Microscope
SWCNT	Single-Walled Carbon Nanotube
TE	Thickness Excitation
TEM	Transmission Electron Microscope
TMAH	Tetremethylammoniumhydroxide
UV	Ultra Violet

LIST OF SYMBOLS

:	Matrix Multiplication
∇	Gradient Operator
$\nabla \cdot$	Divergence Operator
$\nabla \times$	Curl Operator
∇^2	Laplacian Operator
A	Area [m^2]
a_o	Lattice Constant [Å]
a	Acceleration [m/s^2]
B	Magnetic Field [T]
C	Capacitance [C/V]
C_p	Parasitic Capacitance [C/V]
C_o	Clamped Capacitance [C/V]
C_m	Motional Capacitance [C/V]
c	Elastic Stiffness Coefficient [N/m^2]
c_o	Lattice Constant [Å]
D	Electric displacement [C/m^2]
d	Dipole Spacing [m]
d	Piezoelectric Coefficient (strain-charge form) [C/N]
E	Electric Field [V/m]
e	Piezoelectric Coefficient (stress-charge form) [C/m^2]
ε	Permittivity [F/m]
ε_0	Permittivity of Free Space [F/m]

ε_r	Relative Permittivity [F/m]
F	Force [N]
f_r	Resonant Frequency (or series resonance) [Hz]
f_a	Antiresonant Frequency (or parallel resonance) [Hz]
Δf	Change in Resonant Frequency [Hz]
f_{ro}	Unloaded Resonance [Hz]
G_q	Shear Modulus [N/m^2]
Γ_{ij}	Christoffel Matrix
Γ	Reflection Coefficient [dimensionless]
H	Magnetic Field Strength [A/m]
I	Current [A]
J	Free Current Density [A/m^2]
j	$\sqrt{-1}$
K^2	Piezoelectric Coupling Constant [dimensionless]
k_t^2	Electromechanical Coupling Coefficient [dimensionless]
$\hat{L},$	Plane Wave Propagation Direction/Directions
l_x, l_y, l_z	Projections of $\hat{L},$ on three Cartesian axes
L	Inductance [H]
L_m	Motional Inductance [H]
m	mass [kg]
Δm_q	mass [kg]
N	Number of Dipoles per Unit Volume [m^{-3}]
P	Power [W]
P_{loss}	Power Dissipated [W]

P	Polarization Vector [C/m^2]
p	Dipole Moment [Cm]
Q	Quality Factor [dimensionless]
π	3.14159265
q_1, q_2	Point Charge [C]
q_o	Test Charge [C]
R	Resistance [Ohms]
R_m	Motional Resistance [Ohms]
ρ, ρ_q	Density [kg/m^3]
ρ_e	Electric Charge Density [C/m^3]
S	Strain [m/m]
s	Elastic Compliance Coefficient [m^2/N]
T	Stress [N/m^2]
T	Time [s]
u	Particle Displacement [m]
V	Potential [V]
$V_{incident}$	Incident Potential [V]
$V_{reflected}$	Reflected Potential [V]
$V_{transmitted}$	Transmitted Potential [V]
v	Particle Velocity[m/s]
v_a	Phase Velocity [m/s]
W_m	Average Magnetic Energy Stored [Nm]
W_e	Average Electricl Energy Stored [Nm]
ω	Angular Frequency [Hz]
ω_o	Angular Resonant Frequency [Hz]

ω_R	Angular Series ResonantFrequency [Hz]
ω_A	Angular Parallel Resonant Frequency [Hz]
χ	Susceptibility [dimensionless]
Z	Impedance [Ohms]
Z_o	Characteristic Impedance [Ohms]
Z_L	Load Impedance [Ohms]
z	Distance [m]
Φ	Electric Flux [Nm^2/C]
θ	Phase Angle [Degrees]
μ_o	Magnetic Permeability [H/m]

SUMMARY

Advancing the field of nanotechnology to incorporate the unique properties observed at the nanoscale into functional devices has become a major scientific thrust of the 21st century. New fabrication tools and assembly techniques are required to design and manufacture devices based on one-dimensional nanostructures. Three techniques for manipulating nanomaterials post-synthesis have been developed. Two of them involve direct contact manipulation through the utilization of a physical probe. The third uses optically generated surface acoustic waves to reproducibly control and assemble one-dimensional nanostructures into desired locations. The nature of the third technique is non-contact and limits contamination and defects from being introduced into a device by manipulation.

While the effective manipulation of individual nanostructures into device components is important for building functional nanosystems, commercialization is limited by this one-device-at-a-time process. A new approach to nanostructure synthesis was also developed to site-specifically nucleate and grow nanowires between two electrodes. Integrating synthesis directly with prefabricated device architectures leads to the possible mass production of NEMS, MEMS and CMOS systems based upon one-dimensional nanomaterials.

The above processes have been pursued to utilize piezoelectric ZnO nanobelts for applications in high frequency electronic filtering as well as biological and chemical sensing. The high quality, single crystal, faceted nature of these materials make them ideal candidates for studying their properties through the designs of a bulk acoustic resonator. The first ever piezoelectric bulk acoustic resonator based on bottom-up synthesized belts will be demonstrated. Initial results are promising and new designs are implemented to scale the device to sub-micron dimensions.

Multiple models will be developed to assist with design and testing. Some of models presented will help verify experimental results while others will demonstrate some of the problems plaguing further investigations.

CHAPTER 1

INTRODUCTION

The first chapter of this thesis is intended to provide the framework upon which the following dissertation may be viewed in its entirety. Background information, scientific principles and fundamental equations will be presented in order to arm the reader with the necessary tools to comprehend the impact of this body of work on the scientific community. An introduction to nanotechnology and one-dimensional nanostructure synthesis will be provided along with a fundamental description of piezoelectricity and acoustic wave propagation in elastic media. Lastly, a brief outline of the thesis body will be given to chronicle the remainder of the document.

1.1 Nanotechnology

Richard Feynman gave a talk on December 29th 1959 to the American Physical Society at the California Institute of Technology (Caltech) entitled, "There's Plenty of Room at the Bottom: An Invitation to Enter a New Field of Physics." He proposed a new area of solid-state physics where little research had been done, but had the potential to teach scientists a great deal about "strange phenomena in complex situations." His speech began by addressing the problem of "manipulating and controlling things at a small scale." Feynman talked about storing information, entire encyclopedias, by writing data on the head of a pin. He addressed limitations in electron microscopy and the necessity to "see" with atomic resolution (in order to read the head of the pin, of course). Feynman theorized that the properties of matter made up of only a few atoms would no longer obey the classical rules of physics, opening up a new realm of properties and applications for materials. He anticipated problems with lubrication in motors at the nanoscale due to the increased viscosity in fluids and also foresaw problems with electrical resistance in building small scale electronic circuits. Feynman introduced a paradigm shift in the way scientists view science. He envisioned what is now termed the

"bottom-up" approach to manufacturing by building molecules, one atom at a time, to atomic perfection; His vision was Nanotechnology.

Towards the end of the talk, Feynman asked, 'How do we make such a tiny mechanism?" His response was merely, "I leave that to you." Little was it known, that on that day, a vision for the new millennium of science and research was born[1].

Thirteen years later, in 1972, Cowley first demonstrated the ability to see atoms using transmission electron microscopy (TEM)[2], but it wasn't until the 1980's that scientists truly began to innovate in the area of nanotechnology. It was the invention of the scanning tunneling microscope (STM) by Binning and Rohrer at IBM labs in Zurich, Switzerland, in 1981, that enabled scientists to explore at the atomic scale. In STM, a sharp probe tip, with a radius on the order of one or two atoms, is scanned over the surface of a material at a distance of approximately 1nm. A voltage is then applied between the surface and the probe tip. At a certain potential, electrons begin to tunnel between the tip and the sample resulting in a weak electrical current. A feedback loop is used to maintain a constant tunneling current by adjusting the height of the tip relative to the surface as it rasters back-and-forth. By monitoring the change in height during a scan, a map of the surface topography can be reconstructed with a high enough resolution to distinguish individual atoms. The advantage of this technique is not only in its ability to resolve atoms, but in its ability to touch them [3].

In 1989, Eigler demonstrated the STM's ability to manipulate individual xenon atoms on a single crystal nickel surface with atomic precision. Eigler operated under the principle that the tip of the STM always exerts a finite force on an adsorbed atom which contained both electrostatic and Van Der Waals contributions. He was able to tune the magnitude of the applied force by adjusting the height of the tip and amplitude of the applied potential. Taken with the fact that it required less force to pull an atom across the surface rather than completely detach it, made it possible to drag atoms into desired

locations while leaving them bound. Figure 1 shows the experiment Eigler performed to construct an "array" of xenon atoms on a single crystal (110) nickel surface[4].

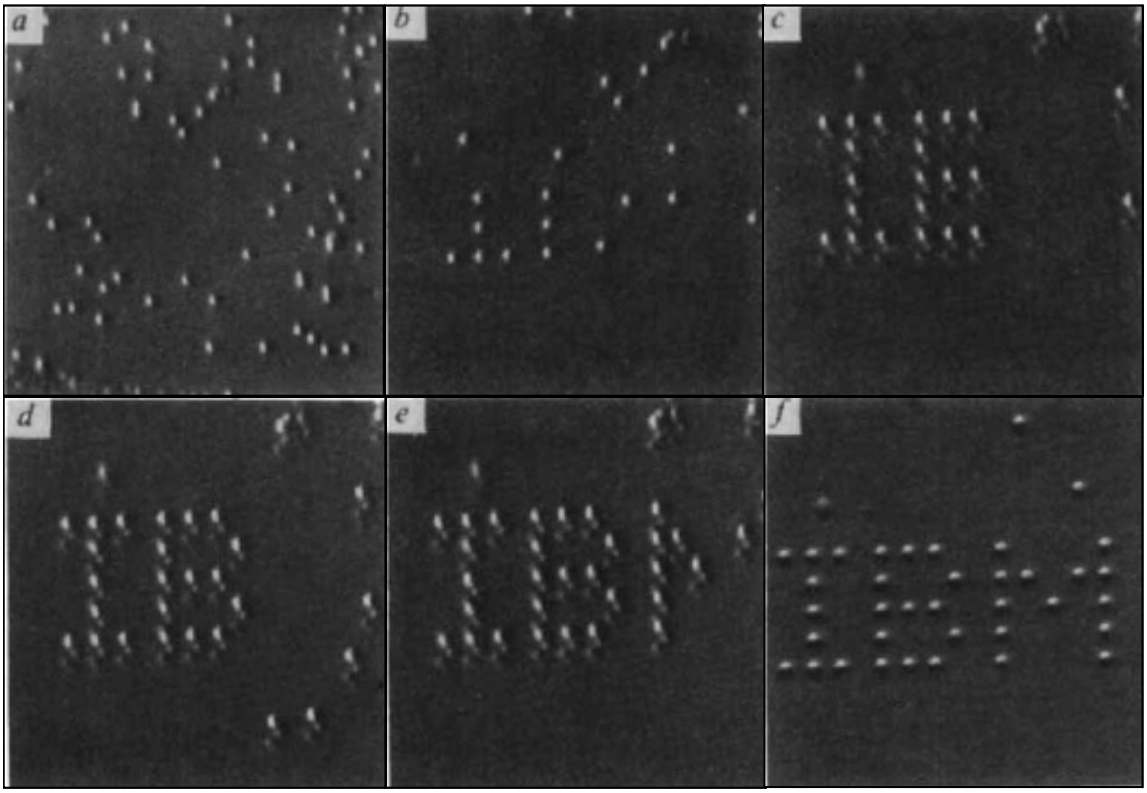

Figure 1.1 A sequence of STM images taken during Eigler's experiment to construct a patterned array of xenon atoms on a (110) nickel surface in order to spell out IBM[4].

Beyond this initial experiment, Eigler was also able to design and build one of the first nanoscale devices. By reversibly moving a single xenon atom back-and-forth between two stationary conducting leads (a conductive surface and the STM probe), he demonstrated a new class of small electronic devices—an atomic switch[5]. While this work is interesting from a scientific standpoint, the problem of scalability limits any

practical application of this one-device-at-a-time process. The ability to build multiple nanodevices simultaneously is one of the critical hurdles still being addressed in the scientific community today. It is also a major thrust of the work presented in this thesis.

While Eigler and his colleagues were manipulating atoms one at a time, designing molecules to atomic precision, and building nanodevices, other less brute force techniques were being developed in order to synthesize nanomaterials on a larger scale. Techniques such as arc-discharge[6], laser ablation[7] and chemical vapor deposition[8] all helped lead to the first discovery and mainstreaming of the carbon nanotube.

A single walled carbon nanotube (SWCNT) consists of individual sheets of graphite, commonly known as graphene, rolled up into a seamless tubular cylinder. The direction in which the nanotube rolls dictates its chirality as well as some of its material properties. The top left corner of Figure 1.2 shows a schematic of a graphite sheet demonstrating the different rolling directions. A pair of indices (n,m), called the chiral vector, are used to indicate the potential unit vectors in the two-dimensional honeycomb lattice. If m=0 then the nanotube is referred to as *zig-zag*. If n=m the nanotube is termed *armchair*. If the nanotube exhibits some other combination of values in between the two vectors then it is simply called *chiral*. Typically, carbon nanotubes are composed of more than just a single sheet of grapheme; rather they consist of multiple graphite cylinders sheathed one-by-one coaxially[9]. These are called multi-walled carbon nanotubes (MWCNT) as shown below in Figure 1.2 as well.

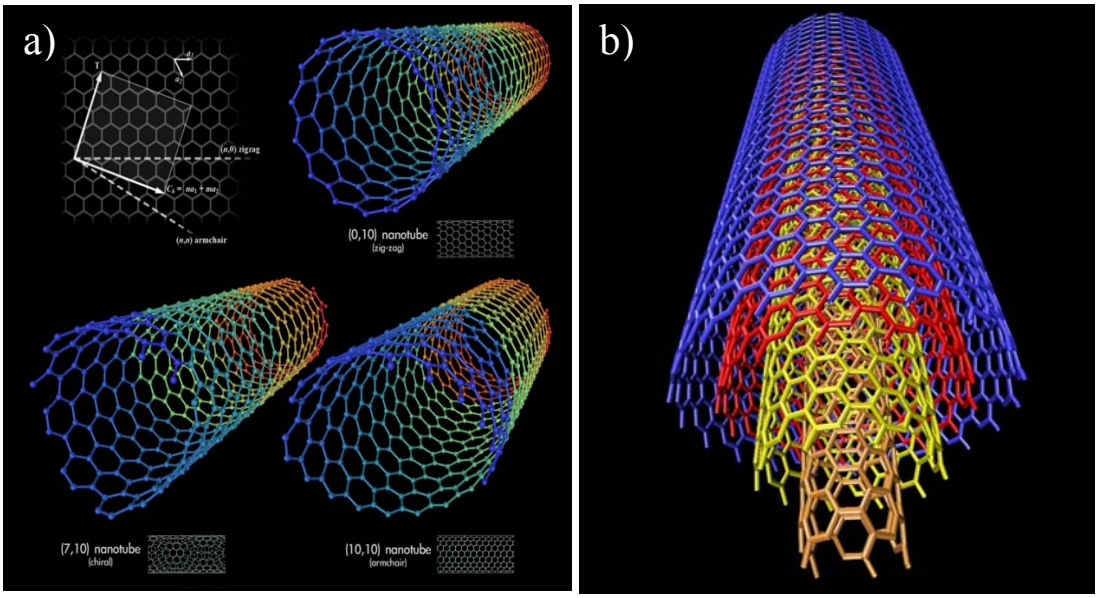

Figure 1.2 (a) Model of single-walled carbon nanotube. (b) Model of multi-walled carbon nanotube. [10, 11]

The intrigue behind the carbon nanotube stems from one of Feynman's initial hypotheses: "Materials at the nanoscale exhibit properties different from their bulk constituents." Carbon nanotubes exhibit a wide variety of interesting and useful properties and are being pursued for multiple applications. For example, armchair nanotubes behave as ballistic conductors where their current densities exceed that of copper and silver by more than 1000 times[12]; their tensile strength is more than 50 times that of carbon steel[13]. MWCNTs can also act as low friction bearings whereby each carbon sheath is able to freely rotate around each other, addressing Feynman's problem of lubrication in nanoscale motors[14].

The first discovery of MWCNTs is credited to Iijima who reported the observation in 1991[15]. Iijima subsequently published a paper in 1993 reporting the existence of single-walled carbon nanotubes. However, there is some question as to who really first observed the SWCNT due to another submission by Bethune within the same time span [16, 17]. Credit ultimately went to Iijima since his paper was received a month

earlier. Realistically, the existence of carbon nanotubes was known many years prior, in the 1970s, due to a controversial image published by Oberlin in 1976[18]. The image depicts a 5nm carbon wire that resembles a carbon nanotube. The authors did not claim it as such and to this day still raises question as to whether or not this is a SWCNT or MWCNT. Even with the discovery in 1976, existence of nanosized carbon filaments can be traced back even further to a paper published in the Journal of Physical Chemistry of Russia in 1952[19], and in some cases to as early as 1889 in a patent filed by Edison to use such filaments in light-bulb applications.

So, with all of this rediscovery of carbon nanotubes, why wasn't it until 1991 that the scientific community finally accepted the phenomenon? One possible answer is that the mechanism of carbon nanotube growth was being investigated in order to prevent it from forming in the coal and steel industry. Since its existence was highly undesirable, there were no real advantageous applications associated with the structure in order to pursue it further. It wasn't until the 1990s that an interest in nanotechnology motivated scientists to study the carbon nanotube in an attempt to control its properties and increase its prevalence[20].

The term nanotechnology was officially coined in 1986 and defined as, "A technology based on the manipulation of individual atoms and molecules to build structures to complex, atomic specifications[21]." The National Nanotechnology Initiative broadened the definition in the '90s to, "The understanding and control of matter at dimensions of roughly 1 to 100 nanometers, where unique phenomena enable novel applications[22]." Since then, we have morphed these definitions into what we now term *nanoscience* and *nanotechnology*. Nanoscience describes the physical, chemical, and biological properties of materials at the nanoscale that are either enhanced or differ from the properties of bulk matter. Nanotechnology is a process by which to manufacture materials and machines to atomic precision using a bottom-up approach.

1.2 One-Dimensional Nanostructures and Synthesis

In the previous section, a brief description of carbon nanotubes along with a few of the synthesis techniques used to grow them was introduced. Here, a clear definition of one-dimensional nanostructures will be presented along with other nanostructure morphologies in order to help differentiate between common nanomaterial nomenclatures. This section will be used to introduce one-dimensional metal oxide nanowires and nanobelts with a focus on the synthesis techniques used to grow them. A detailed explanation of the synthesis methodologies used within the body of this dissertation will be given.

1.2.1 Nanostructure Classifications

A nanostructure is defined as a material system or object where at least one of the dimensions lies below 100nm. Oxide nanostructures can be classified into three different categories: zero-dimensional (0D); one-dimensional (1D); two-dimensional (2D). 0D nanostructures are materials in which all three dimensions are at the nanoscale. A good example of these materials are buckminster fullerenes[23] and quantum dots[24]. 1D nanostructures are materials that have two physical dimensions in the nanometer range while the third dimension can be large, such as in the carbon nanotube described above. 2D nanostructures, or thin films, only have one dimension in the nanometer range and are used readily in the processing of complimentary metal-oxide semiconductor (CMOS) transistors[25] and micro-electro-mechanical systems (MEMs)[26]. Since the focus of this work is on one-dimensional metal oxide nanostructures, all others from this point forward will cease to be discussed.

1D nanostructures have stimulated a great deal of interest due to their importance in fundamental scientific research and potential technological applications in nano-electronic, nano-optoelectronic and nano-electro-mechanical systems [27-44]. Many unique properties have already been demonstrated for this class of materials, such as

superior mechanical toughness [45], increased luminescent efficiency [46], enhanced thermoelectric figure of merit [47] and lower lasing threshold [48]. While most of the work to date has focused on semiconductor systems such as Si[49], Ge[50], GaN[51], GaAs[52], InAs[53], it is only recently that 1D oxide nanostructures have emerged as promising nanoscale building blocks due to their diverse functionality, surface cleanliness and chemical/thermal stability[54].

Within the class of 1D nanostructures exists a sub-category of morphologies reported in literature. This includes nanotubes[7], nanorods[55], nanowires[56] and most recently, nanobelts[57]. Each can be seen in Figure 1.3.

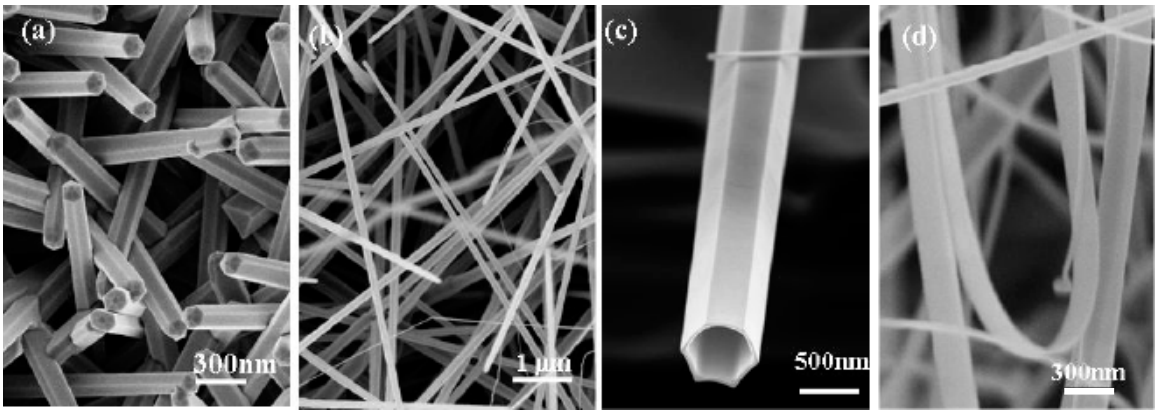

Figure 1.3 SEM micrographs of four one-dimensional nanostructure types (a) nanorods (b) nanowires (c) nanotubes (d) nanobelts[58].

Nanorods and nanowires are similar in that they have an outer diameter with a solid center. In some cases this diameter has a cylindrical cross-section, while others can have facets with symmetry about the long axis. The terms *rod* and *wire* are merely used to differentiate between large aspect ratios (nanowires) and small aspect ratios (nanorods) within this classification. The figure above depicts ZnO nanorods (Figure 1.3a) and nanowires (Figure 1.3b). Nanotubes, like the carbon nanotube described above and the ZnO nanotube depicted in Figure 1.3c, have a similar cross-section to nanowires. However, nanotubes are defined by an inner diameter in addition to its outer diameter

resulting in a hollow center. The fourth structure, the nanobelt, differs from the other three 1D nanostructures in that they have a faceted belt or beam-like morphology with a rectangular cross-section. This structure is especially interesting since it enables the study of dimensionally-confined transport phenomena in functional oxides in all three dimensions[44, 54]. Nanobelts will be highlighted in the following section since they are the structure of interest with regards to applications pursued in later chapters.

1.2.2 Nanobelts

Since their inception in 2001 by Pan *et. al.*, nanobelts have attracted a significant amount of interest due to their unique morphology and structure-dependent physical, chemical, and electrical characteristics. As-synthesized, nanobelts are pure, structurally uniform, single-crystals with well defined crystallographic planes and most are free from defects or dislocations [57]. Nanobelts are commonly classified by their composition, growth direction, and faceted surfaces. Nanobelt sizes typically range from 30-300nm in width, width-to-thickness ratios of 5-10, and lengths of up to a few millimeters. As a consequence of their large aspect ratio, nanobelts are extremely flexible when compared to the bulk ceramics counterparts from which they are composed. In addition, nanobelt size and geometry can be controlled by simply varying the pressure, temperature and length of time in which a synthesis experiment is conducted—a detailed description of the synthesis process will be given shortly. Figure 1.4 depicts a series of TEM images with the respective electron diffraction patterns showing the length (a), flexibility (b, c), thickness (d, e), and single-crystal nature (f) of ZnO nanobelts [57]. An SEM image of the spaghetti-like deposit can be seen in Figure 1.5a along with high resolution TEM images in Figure 1.5e showing the low defect nature of the structure.

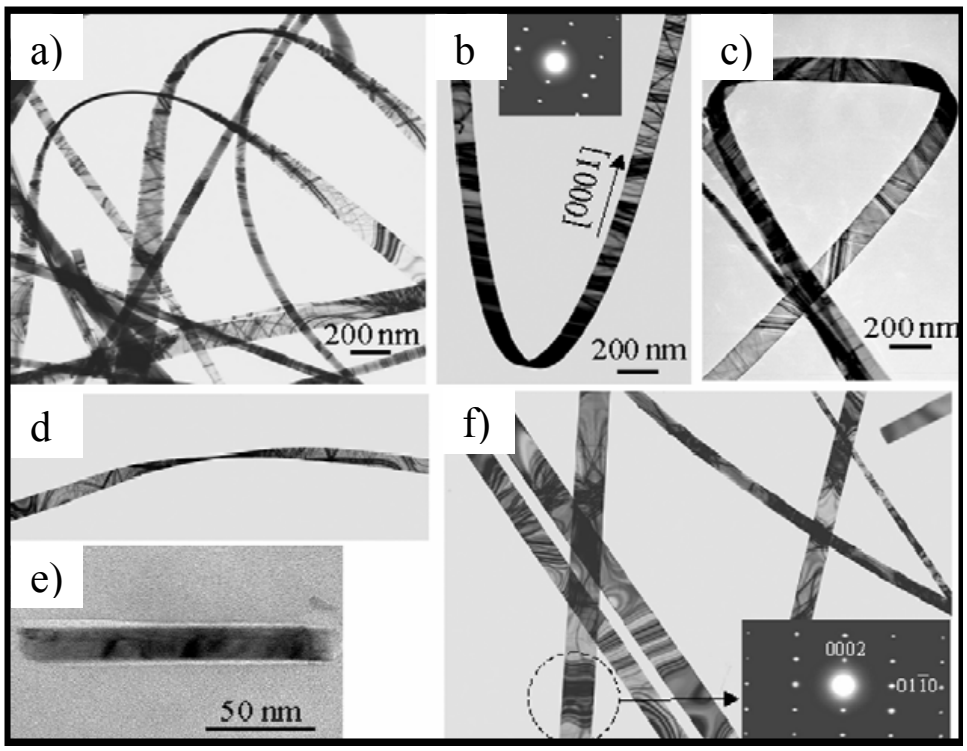

Figure 1.4 Transmission electron microscopy images with respective electron diffraction patterns for ZnO showing the length (a), flexibility (b, c), thickness (d, e), and single crystallinity (f) of nanobelts[57].

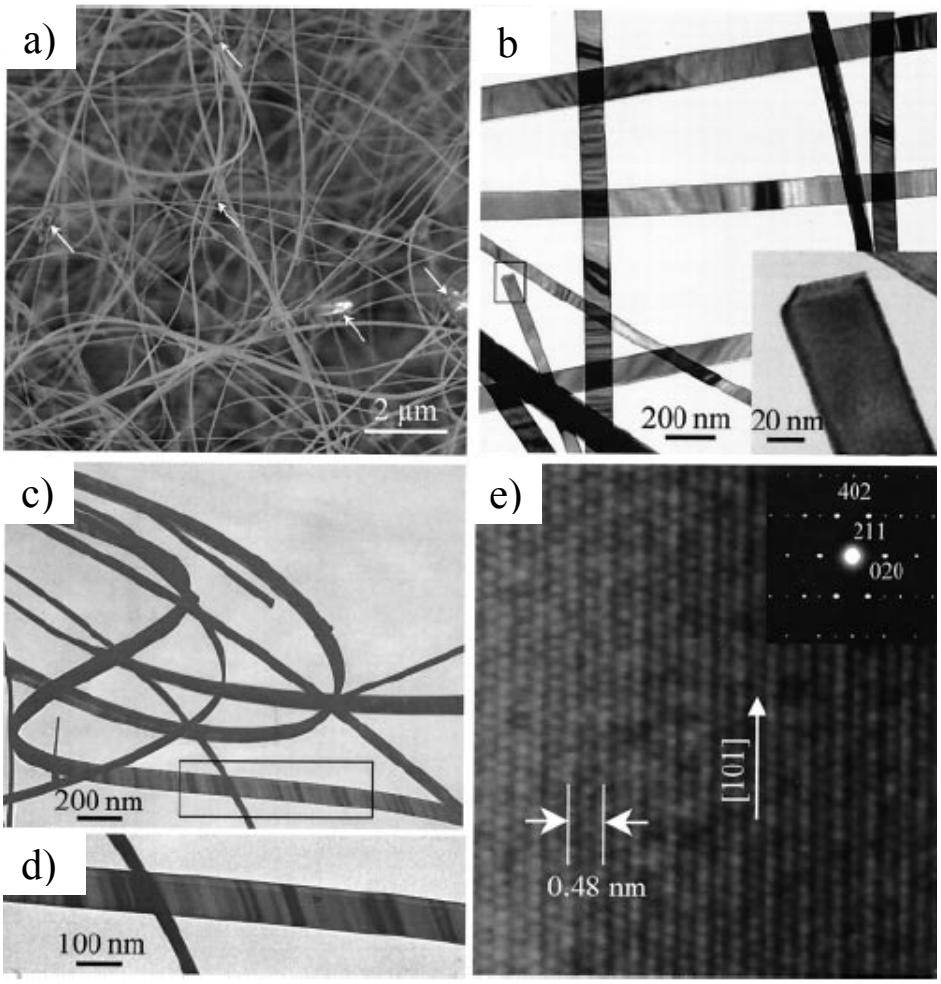

Figure 1.5 (a) SEM image of as-synthesized ZnO nanobelts (b) (c) (d)Transmission electron microscopy images (e) HRTEM image of a defect free nanobelt. From the diffraction patterns it can be seen that the nanobelts are single crystals[57].

As previously mentioned, nanobelts are commonly classified according to their growth direction and faceted surfaces. Although bulk ZnO naturally occurs in both wurtzite (hexagonal) and zinc blende (cubic) crystal structures, ZnO nanobelts are always hexagonal and are defined by the three lowest energy surfaces within the crystal: $\{0001\}, \{01\bar{1}0\}, \{2\bar{1}\bar{1}0\}$. Figure 1.6 schematically shows four possible nanobelt configurations and their crystallographic orientations with respect to one another. It is important to note that each of these configurations has been observed and can be

achieved by controlling the relative growth parameters inside the synthesis vessel. Zinc oxide nanobelts with the 1st configuration grow along the $[0001]$ direction. They are commonly observed because the $[0001]$ direction is the fastest growth direction within the wurtzite crystal. However, the lowest energy configuration for this growth direction is the nanowire depicted in Figure 1.3b, and the most common ZnO nanobelt is found with the 2nd configuration growing along the $[01\bar{1}0]$ direction. In this orientation, planar defects such as stacking faults are occasionally observed. Finally, the 3rd and 4th configurations grow along the $[01\bar{1}0]$ and $[2\bar{1}\bar{1}0]$ directions, respectively, and are defined as polar-surface-dominated (PSD) nanobelts because their primary surfaces (largest surfaces) correspond to the polar $\pm(0001)$ surfaces of Figure 6. These configurations are extremely rare and lead to many of the unique spring- and ring-like morphologies documented in literature[59, 60].

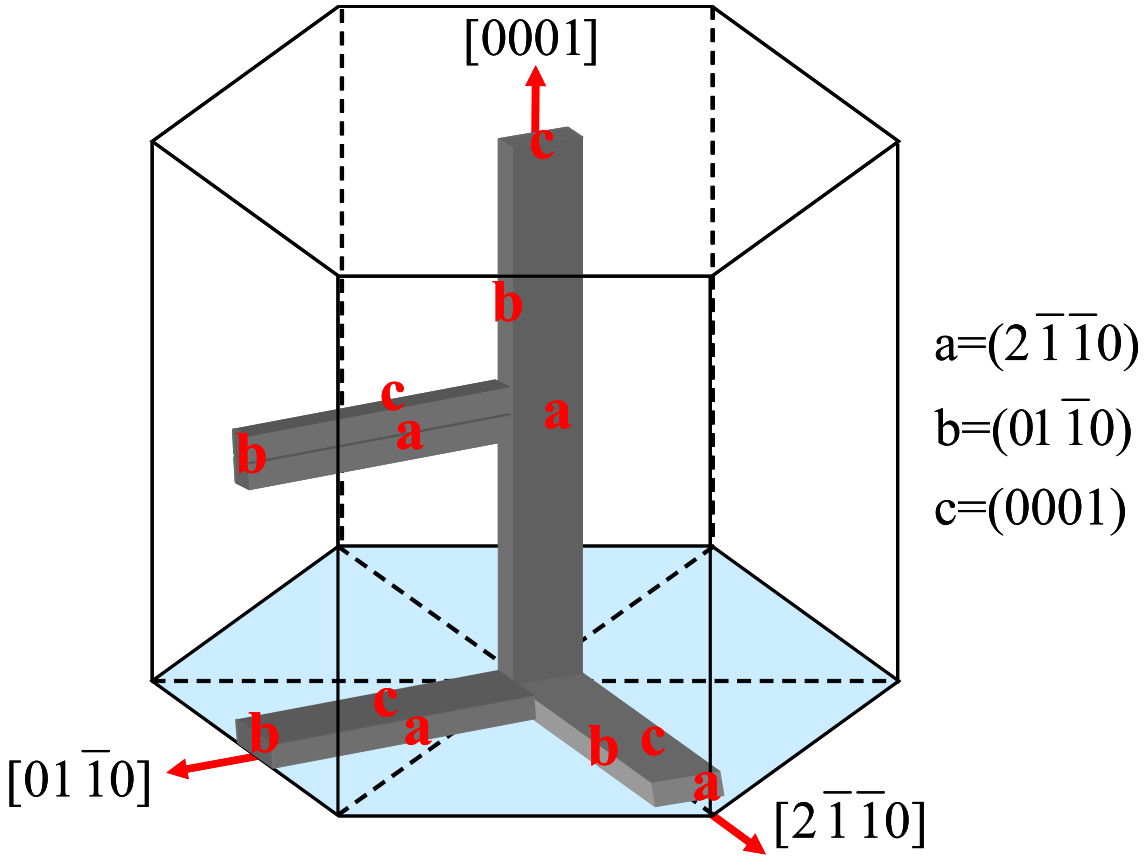

Figure 1.6 Schematic showing four types of ZnO belts and their crystallographic orientations with respect to one another, where a, b, c are the three defining surfaces of each belt. Configurations 3 and 4 are polar-surface-dominated belts.

Although initial research in nanobelt synthesis has focused on semiconducting oxides such as: ZnO, CdO, In_2O_3, Ga_2O_3, and SnO_2 [57], more recent investigations have produced a variety of compound semiconductors such as ZnS [59], GaP [60], AlN [61], Al_2O_3 [62], GaN [63] and CdSe[61]. Table 1.1 summarizes common nanobelt materials along with their growth direction and characteristic surfaces[9, 62]. It can be seen that this belt-like morphology is common to a variety of materials and crystal classes.

Table 1.1 List of materials synthesized as nanobelts

Material	Crystal Structure	Growth Direction	Top Surface	Side Surfaces
ZnO	Wurtzite	$[0001]$, $[01\bar{1}0]$ or $[2\bar{1}\bar{1}0]$	$\{2\bar{1}\bar{1}0\}$ or $\{0001\}$	$\{01\bar{1}0\}$, $\{0001\}$ or $\{2\bar{1}\bar{1}0\}$
Ga_2O_3	Monoclinic	$[001]$ or $[010]$	$\{100\}$ or $\{100\}$	$\{010\}$ or $\{10\bar{1}\}$
t-$Sn0_2$	Rutile	$[101]$	$\{10\bar{1}\}$	$\{010\}$
o-SnO_2	Orthorhombic	$[010]$	$\{100\}$	$\{001\}$
In_2O_3	C-rare earth	$[001]$	$\{100\}$	$\{010\}$
CdO	NaCl	$[001]$	$\{100\}$	$\{010\}$
PbO_2	Rutile	$[010]$	$\{201\}$	$\{10\bar{1}\}$
MoO_3	Orthorhombic	$[001]$	$\{010\}$	$\{100\}$
MgO	Face center cubic	$[100]$	$\{001\}$	$\{010\}$
CuO	Monoclinic	$[10\bar{1}]$	$\{110\}$	$\{001\}$
Al_2O_3	Hexagonal	$[0001]$	$\{01\bar{1}0\}$	$\{11\bar{2}0\}$
ZnS	Wurtzite	$[01\bar{1}0]$	$\{11\bar{2}0\}$	$\{0001\}$
CdSe	Wurtzite	$[01\bar{1}0]$	$\{11\bar{2}0\}$	$\{0001\}$
GaN	Wurtzite	$[10\bar{1}0]$	$\{01\bar{1}0\}$	$\{0001\}$
GaP	Zinc blende	$[111]$	$\{100\}$	$\{0\bar{1}1\}$
AlN	Wurtzite	$[0001]$	$\{11\bar{2}0\}$	$\{01\bar{1}0\}$

From the above listed nanobelt materials, ZnO is the most extensively studied and will be considered in detail from hereafter[62].

1.2.3 Synthesis

During the last decade, one-dimensional nanostructures have been extensively investigated with an emphasis on synthesis and characterization. Several approaches have been well established, which include chemical vapor deposition (CVD)[63, 64], physical vapor deposition (PVD)[28, 54, 57, 59], pulsed laser deposition (PLD)[42, 56, 65], molecular beam epitaxy (MBE)[66-68], atomic layer deposition (ALD)[69, 70], metal-organic chemical vapor deposition (MOCVD)[71-73], and wet chemical processes (hydrothermal synthesis)[74-76]. Since only PVD and hydrothermal synthesis were used in this body of work, a detailed description of both is given below.

1.2.3.1 Physical Vapor Deposition (PVD)

The nanobelts utilized for this dissertation were grown using a physical vapor deposition process (PVD) by way of thermal evaporation. The technique is based on the sublimation of a heated powder source material at the center of a single zone tube furnace under vacuum. Water-cooled end caps are placed on the outside ends of the furnace system to create a temperature gradient that decreases moving away from the center. The resulting vapor phase flows downstream into cooler regions via a carrier gas where it condenses on a deposition substrate. A schematic of the entire system can be seen in Figure 1.7. The geometry of the nanomaterial deposit is controlled by varying the conditions inside the furnace during synthesis (temperature, ramp-rate, pressure, carrier gas, vapor concentration and experimental duration). This direct deposition implies that no chemical reactions are permitted to occur either in the vapor, or between the vapor and the deposition substrate.

The furnace system used for this technique is made up of two main components: the furnace and the vacuum system. A Thermolyne 79300 single-zone split-tube furnace was used to carry out the experiments. Exposed heating element coils embedded into a ceramic fiber insulation enabled the heating of the furnace to a maximum of 1500 °C.

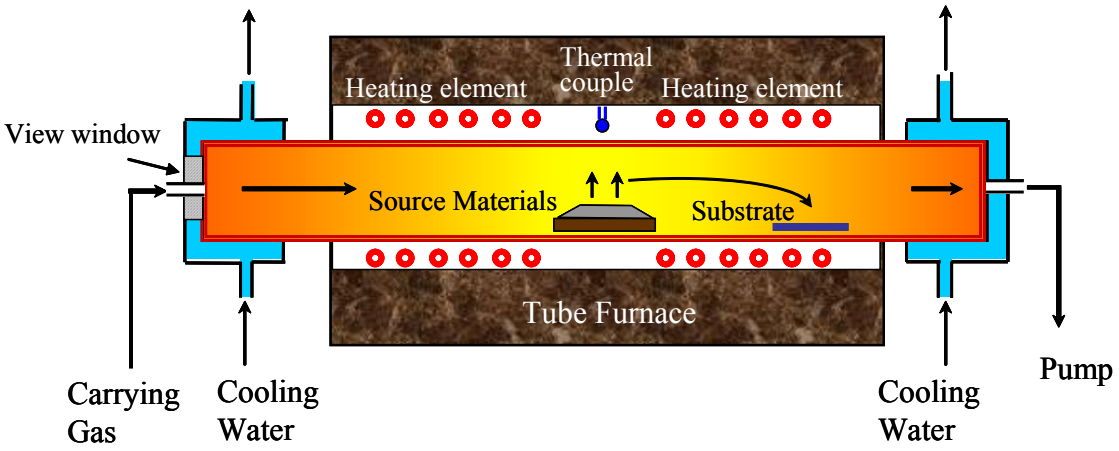

Figure 1.7 Single zone tube furnace used to synthesize nanobelts.

An alumina tube measuring 30” in length, with a 1.75” outer diameter and 1.50” inner diameter, was placed inside the furnace. The alumina tube was routinely cleaned with ethanol prior to each run. Since the furnace only measures 24” in length, the alumina tube protrudes outside the furnace body six inches on either side. Three-inch diameter tube collars where placed on either end in order to support the tube inside the furnace. Once the tube was in position, the source material and collection substrates were loaded inside. A designated amount of source material was weighed on a Denver Instrument XE-3100D mass balance. The source was then transferred to an alumina boat and inserted 15” into the center of the tube. Deposition substrates were cut out of square alumina wafers using a tile saw and were positioned 13cm away from the end of the tube, downstream from the source. Once the substrates and source material were in position, the synthesis chamber was sealed. Two water-cooled end caps were designed to fit on each end of the alumina tube. One was connected to the pressure system and the other to the mass flow controller. Rubber O-rings coated with high temperature vacuum grease were used to seal the end caps to the alumina tube and connect the vacuum system and the furnace together.

A BOC Edwards RV8 hydrocarbon rotary vacuum pump was used to remove residual gases inside the furnace system prior to starting an experiment. The mechanical pump was connected to the synthesis chamber through a series of aluminum t-bars and cross-bars. The pump was then turned on in order to begin the evacuation process. Monitoring the pressure inside the alumina tube was achieved through the use of two analog gauges, one being a BOC Edwards analog Pirani vacuum gauge series 500, which monitors lower pressures ranging from 10^{+2}- 10^{-3} mbar. This gauge was only used during the initial evacuation of the furnace.

Once the mechanical pump was turned on, the closed diaphragm isolation valve was slowly opened so that the purging rate of the chamber was ~100 mbar/s. This relatively slow evacuation rate was employed to ensure that the powder source material was not disturbed during evacuation. The ultimate pressure achieved with the rotary pump was ~$2x10^{-3}$ mbar which required ~2hrs of pumping, after which the synthesis process could begin by heating the furnace to its set-temperature.

The furnace was ramped to temperature using a C1 programmable controller with one stored program of eight segments. Each segment consisted of three sub-segments: a ramp rate (ranging from 1 °C/min to 60 °C/min), a temperature set point (ranging from 100°C to 1500°C), and a dwell time (ranging from 0.1 min to 999.9 min). A BOC Edwards analog dial vacuum gauge series CG16K was used to monitor the system pressure and control it within an acceptable range. The dial gauge measures pressures from 20 to 1000 mbar in increments of 20mbar. A Cole-Palmer multi-turn needle valve was also used during synthesis to make fine adjustments in order to maintain the pressure constant.

Unless otherwise stated, all synthesis experiments were run in the following manner: The furnace would continuously heat at a rate of 20 ºC/min until it reached a set-point of 800^{o}C; the furnace was held for 30 minutes in order to allow the system to equilibrate; an inert Argon (Ar) gas was allowed to flow through an Aalborg mass flow

controller which regulated the gas to 50 standard cubic centimeters (sccm); the gas would enter the chamber via 3/8" plastic tubing connected from the flow controller to the water-cooled end cap; once the system was equilibrated to ~ 300mbar ±20mbar, the furnace would begin to ramp again at 20 ºC/min to the final set-point of 1450 ^{o}C for ZnO nanobelt synthesis; the temperature and pressure was held for the duration of the experiment which ranged from 0.5 hours to 24 hours.

Once the experiment reached the designated experimental duration, the furnace controller was shut off, allowing the furnace to cool to room temperature. In some cases a cooling fan might be used in order to quench the system as quickly as possible. This was critical for temperatures that were much higher than the minimum sublimation temperature of the source material. If the system was permitted to cool slowly, then deposition could occur for several minutes after the furnace was turned off. In addition, as the system cooled the temperature gradient changed which could possibly affect the morphology of the as-deposited material. The pressure was maintained throughout the duration to ensure that this parameter would not influence the morphology during the cool down phase. Once the cooling process was complete, the flow of the carrier gas into the system was stopped. The diaphragm valve was then fully opened so that any potentially harmful vapor still left in the chamber would be purged from the system[61].

1.2.3.2 Hydrothermal Synthesis

Recently, wet chemical methods for growing 1D nanostructures have become an attractive alternative to PVD because of their ability to synthesize nanomaterials at much lower temperatures (50-95^{o}C). Utilization of polymers as a growth substrate for flexible electronic devices has been one of the key drivers for reducing the synthesis temperature. In 1990, Verges et al. reported the first ZnO micro-rods grown in an aqueous solution at temperatures below 80 ^{o}C[74]. About 10 years later, others successfully decreased the

size of the wires to sub-micron dimensions and reported well aligned ZnO arrays [75, 76].

The process for growing ZnO nanowires hydrothermally involves a 50 mL aqueous solution made up of Fluka brand $Zn(NO_3)_2 \bullet 6H_20$, (zinc nitrate hexahydrate with a MW of 297.47 g/mol) and $C_6H_{12}N_4$, (hexamethylenetetramine, HMTA, with a MW of 140.22 g/mol). The solution was mixed inside a Pyrex bottle and capped to prevent the solvent from evaporating during synthesis. Synthesis employed the use of a Yamato DKN400 box furnace with $\pm 1^oC$ control over the internal temperature up to 210^oC. Here, the synthesis vessel was not introduced into the box furnace until it reached its equilibrium temperature; therefore, the ramp rate was not crucial. In addition, no system for controlling the pressure was implemented and was assumed to be 1 atm. Like PVD, experiment durations can range anywhere from 0.5 hours up to 24 hours depending on the desired length and radius of the nanowire growth. The aqueous solution was heated to temperatures between 50 - 95 ^oC resulting in ZnO nanowires due to the following chemical reactions[77]:

$$C_6H_{12}N_4 + 6H_2O \leftrightarrow 6CH_2O + 4NH_3 \quad (1.1)$$

$$NH_3 + H_2O \leftrightarrow NH_4^+ + OH^- \quad (1.2)$$

$$2OH^- + Zn^{2+} \rightarrow ZnO_{(s)} + H_2O \quad (1.3)$$

Hydroxide ions are formed through the decomposition of HMTA which reacts with Zn^{2+} to precipitate ZnO. Au films and ZnO seed layers are sometimes utilized to initiate nucleation and growth.

1.3 Piezoelectricity

In the late 1870's the Curie bothers were conducting investigations and categorizing materials such as tourmaline, quartz, topaz, cane sugar and rochelle salt that displayed surface charge when they were mechanically stressed. As a result, they published the first scientific work describing the phenomena in 1880[78]. The observation was considered a dramatic discovery and the term *piezoelectricity* was coined to describe the effect. The word "piezo," which means "to press," came from the ancient Greeks who were actually credited for observing a "mysterious attractive power" when materials were rubbed. They called this property *elektron* (amber).

The necessary condition for a material to exhibit piezoelectricity is quantified by its crystal symmetry. Piezoelectric materials have non-centrosymmetric crystals; thereby, when the crystal is deformed, the lack of symmetry results in a dipole that is established across the bulk of the material. Piezoelectricity was defined by Cady as, "an electric polarization produced by mechanical strain in crystals belonging to certain classes, the polarization being proportional to the strain and changing sign with it."[79] The direct piezoelectric effect described here can be written as:

$$P_i = d_{ij}\, T_j \tag{1.4}$$

Where P_i is the polarization vector, d_{ij} is the piezoelectric coefficient and T_j is a stress tensor. In addition to the direct effect, the converse effect is:

$$S_j = d_{ij}\, E_i \tag{1.5}$$

where an applied electric field (Ei) across a non-centrosymmetric crystal results in a mechanical strain (Sj). The direct/converse piezoelectric effects state that piezoelectric materials are electro-mechanical transducers with the ability to convert mechanical energy into electrical energy and conversely convert electrical energy into mechanical energy. While the direct effect was discovered by the Curie brothers, the converse effect was first predicted thermodynamically by Lippmann in 1881[80]. However, the Curie

brothers were the first to experimentally verify the converse effect following Lippmann's work.

This was not fully exploited until World War I when Paul Langevin developed the first serious application of piezoelectric materials for ultrasonic submarine detection. The transducer he built was made of a thin quartz crystal glued between two steel plates. The device was used to transmit a high frequency "chirp" signal into the water and measure the depth by timing the return echo. It was the invention of sonar that first initiated an intense research interest in the area of piezoelectrics resulting in many of the modern applications such as microphones, accelerometers, ultrasonic transducers, etc.[81]

1.3.1 Elastic Constitutive Equations

To fully understand the origin of the piezoelectric effect, it is necessary to introduce the constitutive equations that describe it. Hooke's law describes the stress/strain relationship between the application of an external force on a solid body that results in internal stresses and distortions. The linear relationship can be described in three dimensions by

$$T_{ij} = c_{ijkl} S_{kl} \tag{1.6}$$

$$S_{ij} = s_{ijkl} T_{kl} \tag{1.7}$$

where T is stress (N/m^2), S is strain (m/m), c is the elastic stiffness coefficient or Young's modulus (N/m^2), and s is the elastic compliance coefficient (m^2/N)—the inverse of c. Within these equations, the indices i and j correspond to stress terms while k and l correspond to strain terms; where i, j, k, l represent x, y, z.

Written in expanded notation, (1.6) and (1.7) respectively contain nine equations with nine terms. Although not fully independent, the stiffness (c) and compliance (s) coefficients can be organized into 9x9 matrices with 81 elements in each. (1.8) is the expanded matrix format of (1.6).

$$\begin{bmatrix} T_{xx} \\ T_{xy} \\ T_{xz} \\ T_{yx} \\ T_{yy} \\ T_{yz} \\ T_{zx} \\ T_{zy} \\ T_{zz} \end{bmatrix} = \begin{bmatrix} c_{xxxx} & c_{xxxy} & c_{xxxz} & c_{xxyx} & c_{xxyy} & c_{xxyz} & c_{xxzx} & c_{xxzy} & c_{xxzz} \\ c_{xyxx} & c_{xyxy} & c_{xyxz} & c_{xyyx} & c_{xyyy} & c_{xyyz} & c_{xyzx} & c_{xyzy} & c_{xyzz} \\ c_{xzxx} & c_{xzxy} & c_{xzxz} & c_{xzyx} & c_{xzyy} & c_{xzyz} & c_{xzzx} & c_{xzzy} & c_{xzzz} \\ c_{yxxx} & c_{yxxy} & c_{yxxz} & c_{yxyx} & c_{yxyy} & c_{yxyz} & c_{yxzx} & c_{yxzy} & c_{yxzz} \\ c_{yyxx} & c_{yyxy} & c_{yyxz} & c_{yyyx} & c_{yyyy} & c_{yyyz} & c_{yyzx} & c_{yyzy} & c_{yyzz} \\ c_{yzxx} & c_{yzxy} & c_{yzxz} & c_{yzyx} & c_{yzyy} & c_{yzyz} & c_{yzzx} & c_{yzzy} & c_{yzzz} \\ c_{zxxx} & c_{zxxy} & c_{zxxz} & c_{zxyx} & c_{zxyy} & c_{zxyz} & c_{zxzx} & c_{zxzy} & c_{zxzz} \\ c_{zyxx} & c_{zyxy} & c_{zyxz} & c_{zyyx} & c_{zyyy} & c_{zyyz} & c_{zyzx} & c_{zyzy} & c_{zyzz} \\ c_{zzxx} & c_{zzxy} & c_{zzxz} & c_{zzyx} & c_{zzyy} & c_{zzyz} & c_{zzzx} & c_{zzzy} & c_{zzzz} \end{bmatrix} \bullet \begin{bmatrix} S_{xx} \\ S_{xy} \\ S_{xz} \\ S_{yx} \\ S_{yy} \\ S_{yz} \\ S_{zx} \\ S_{zy} \\ S_{zz} \end{bmatrix} \tag{1.8}$$

The number of elements can be reduced by applying symmetrical stress and strain conditions. For example, symmetry of T causes $c_{ijkl} = c_{ijkl}$ for $j \neq i$ and reduces the number of variables from 81 to 54. In addition, symmetry of S causes $c_{ijkl} = c_{ijkl}$ for $l \neq k$ and reduces the number of variables from 54 to 36. Such operations significantly reduce the complexity of the equation and are shown below in (1.9).

$$\begin{bmatrix} T_{xx} \\ T_{yy} \\ T_{zz} \\ T_{yz} \\ T_{zx} \\ T_{xy} \end{bmatrix} = \begin{bmatrix} c_{xxxx} & c_{xxyy} & c_{xxzz} & c_{xxyz} & c_{xxzx} & c_{xxxy} \\ c_{yyxx} & c_{yyyy} & c_{yyzz} & c_{yyyz} & c_{yyzx} & c_{yyxy} \\ c_{zzxx} & c_{zzyy} & c_{zzzz} & c_{zzyz} & c_{zzzx} & c_{zzxy} \\ c_{yzxx} & c_{yzyy} & c_{yzzz} & c_{yzyz} & c_{yzzx} & c_{yzxy} \\ c_{zxxx} & c_{zxyy} & c_{zxzz} & c_{zxyz} & c_{zxzx} & c_{zxxy} \\ c_{xyxx} & c_{xyyy} & c_{xyzz} & c_{xyyz} & c_{xyzx} & c_{xyxy} \end{bmatrix} \bullet \begin{bmatrix} S_{xx} \\ S_{yy} \\ S_{zz} \\ S_{yz} \\ S_{zx} \\ S_{xy} \end{bmatrix} \tag{1.9}$$

Adopting the abbreviated notation $c_{ijkl} \Rightarrow c_{IJ}$, where I and J represent 1 through 6, Hooke's Law is written in reduced matrix format by following the procedure outlined in Table 1.2. Within this matrix the upper left, upper right, lower left and lower right quadrants represent coupling between longitudinal stresses and strains, longitudinal stresses and shear strains, shear stresses and longitudinal strains, and shear stresses and

strains respectively. Equation (1.10) represents the ability of a material to strain (*stress*) in the direction of applied stress (*strain*), as well as, in directions perpendicular to the stress (*strain*). Stated otherwise, an x-directed stress will couple to y- and z-directed strains with varying magnitude. It should be noted that an equivalent matrix is also available for (1.7). In this simplified notation, indices 1,2,3 represent the Cartesian directions *x*,*y*,*z*, while 4,5,6 represent shear directions *yz*, *zx*, *xy*.

Table 1.2 Matrix notation

ij* or *kl	**Cartesian**	***I* or *J***
11	xx	1
22	yy	2
33	zz	3
23 or 32	yz or zy	4
31 or 13	zx or xz	5
12 or 21	xy or yx	6

$$\begin{bmatrix} T_1 \\ T_2 \\ T_3 \\ T_4 \\ T_5 \\ T_6 \end{bmatrix} = \left[\begin{array}{ccc|ccc} c_{11} & c_{12} & c_{13} & c_{14} & c_{15} & c_{16} \\ c_{21} & c_{22} & c_{23} & c_{24} & c_{25} & c_{26} \\ c_{31} & c_{32} & c_{33} & c_{34} & c_{35} & c_{36} \\ \hline c_{41} & c_{42} & c_{43} & c_{44} & c_{45} & c_{46} \\ c_{51} & c_{52} & c_{53} & c_{54} & c_{55} & c_{56} \\ c_{61} & c_{62} & c_{63} & c_{64} & c_{65} & c_{66} \end{array}\right] \bullet \begin{bmatrix} S_1 \\ S_2 \\ S_3 \\ S_4 \\ S_5 \\ S_6 \end{bmatrix} \tag{1.10}$$

For accuracy and consistency among the nomenclature, the abbreviated components outlined above in Table 1.2 do not always correspond to the respective tensor components. For example, a multiplicative factor of 2 is required for shear strains because of their inherent definition[82]. Subsequent relationships are found for the elastic compliance coefficient (*s*) as well. Table 1.3 summarizes the relationship between the abbreviated indices and their respective tensor components.

Table 1.3 Abbreviated indices compared to their respective tensors

Stress	$T_{ij} = T_J$	$i = j$ and/or $i \neq j$
Elastic Stiffness	$c_{ijkl} = c_{IJ}$	$i = j$ and/or $i \neq j$
Strain	$S_{ij} = S_J$ $2S_{ij} = S_J$	$i = j$ $i \neq j$
Elastic Compliance	$s_{ijkl} = s_{IJ}$ $2s_{ijkl} = s_{IJ}$ $4s_{ijkl} = s_{IJ}$	$i = j$ and $k = l$ $i \neq j$ or $k \neq l$ $i \neq j$ and $k \neq l$

Adopting the abbreviated notation, the linear constitutive equations for elasticity are:

$$T_I = c_{IJ} S_J \tag{1.11}$$

$$S_I = s_{IJ} T_J \tag{1.12}$$

where I and J represent 1 through 6. In the section to follow an equivalent constitutive equation will be developed for electrostatics.

1.3.2 Charge Consideration

In addition to the elastic equations, it is also necessary to consider the force of attraction and repulsion between two point charges, calculate the electric field from a point charge and calculate the electric field from a dipole. As defined by Coulomb's Law, the electrostatic force of attraction or repulsion between two point charges (q_1 and q_2) are separated by a distance r is given by:

$$F = \frac{1}{4\pi\varepsilon_o} \frac{|q_1||q_2|}{r^2} \tag{1.13}$$

where ε_o is the permittivity of free space (F/m). Each point charge exerts a force equal in magnitude and opposite in direction to its neighboring charge, and thus forms an action-reaction pair. As a sign convention, a positive test charge q_0 replaces q_2 in Coulomb's

Law when calculating the electric field caused by a point charge. When incorporated into the definition of an electric field, the magnitude of the electric field vector at a point charge is given by:

$$E = \frac{F}{q_0} = \frac{1}{4\pi\varepsilon_o}\frac{|q_1|}{r^2} \tag{1.14}$$

The direction of the electric field coincides with the direction of force: towards the point source if q_1 is negative; away from the point source if q_1 is positive. In order to develop the concept of the piezoelectric effect, we must extend the above listed formulation to an electric dipole, thereby accounting for the interaction between anions and cations.

An electric dipole is defined as a pair of point charges with equal magnitude and opposite signs that are separated by a fixed distance. As shown below in Figure 1.8, an electric dipole produces an electric field at a distance z from the midpoint of the dipole along its axis. Within this schematic, it is assumed that the distance between the electric dipole d is significantly smaller than the distance z.

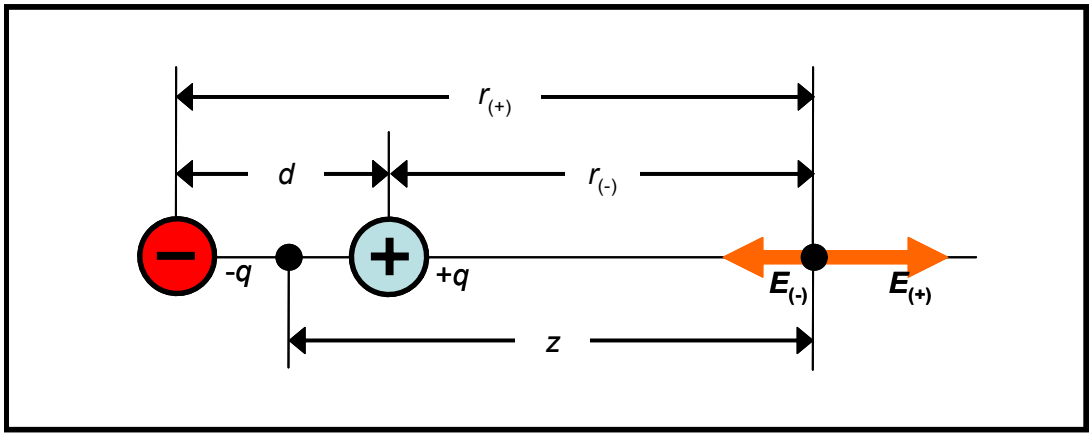

Figure 1.8 Electric field vectors $\boldsymbol{E}_{(-)}$ and $\boldsymbol{E}_{(+)}$ caused by the two charges at $r_{(-)}$ and $r_{(+)}$[62].

Applying the superposition principle for electric fields, the magnitude of the electric field E at a distance z is calculated by;

$$\begin{aligned} E &= E_{(+)} - E_{(-)} \\ E &= \frac{1}{4\pi\varepsilon_o}\frac{|q|}{r_{(+)}^2} - \frac{1}{4\pi\varepsilon_o}\frac{|q|}{r_{(-)}^2} \\ E &= \frac{1}{4\pi\varepsilon_o}\frac{|q|}{(z-0.5d)^2} - \frac{1}{4\pi\varepsilon_o}\frac{|q|}{(z+0.5d)^2} \\ E &= \frac{q}{4\pi\varepsilon_o z^2}\left[\left(1-\frac{d}{2z}\right)^{-2} - \left(1+\frac{d}{2z}\right)^{-2}\right] \end{aligned} \tag{1.15}$$

where $E_{(+)}$ and $E_{(-)}$ are the electric field vectors at distances $r_{(+)}$ and $r_{(-)}$, respectively. Expanding the above equation via the binomial theorem provides simplification; $d/2z$ is much smaller than one and therefore only the first two terms of the expansion need to be considered when calculating the electric field intensity [83]. Equation (1.16) shows that the electric-field intensity of a dipole is proportional to the dipole moment ($p=qd$). Consequently, any change in the dipole moment (qd) will cause a corresponding change in the electric field. This concept is the origin of the piezoelectric effect[84].

$$\begin{aligned} E &= \frac{q}{4\pi\varepsilon_o z^2}\left[\left(1+\frac{2d}{2z(1!)}+\ldots\right) - \left(1-\frac{2d}{2z(1!)}+\ldots\right)\right] \\ E &= \frac{q}{4\pi\varepsilon_o z^2}\left[\left(1+\frac{d}{z}+\ldots\right) - \left(1-\frac{d}{z}+\ldots\right)\right] \\ E &= \frac{q}{4\pi\varepsilon_o z^2}\left[\frac{2d}{z}\right] = \frac{1}{2\pi\varepsilon_o}\frac{qd}{z^3} = \frac{1}{2\pi\varepsilon_o}\frac{p}{z^3} \end{aligned} \tag{1.16}$$

Prior to external stimuli, the model depicted in Figure 1.9 is neutral since its centers-of-charge coincide. However, upon mechanical deformation the centers-of-charge separates, thereby producing a dipole moment ($p=qd$). The accumulation of dipole moments within a piezoelectric crystal causes the polarization (P) of surface charges. Such polarization generates an electric field (as described above in Figure 1.8) and is commonly used to transform mechanical energy into electrical energy.

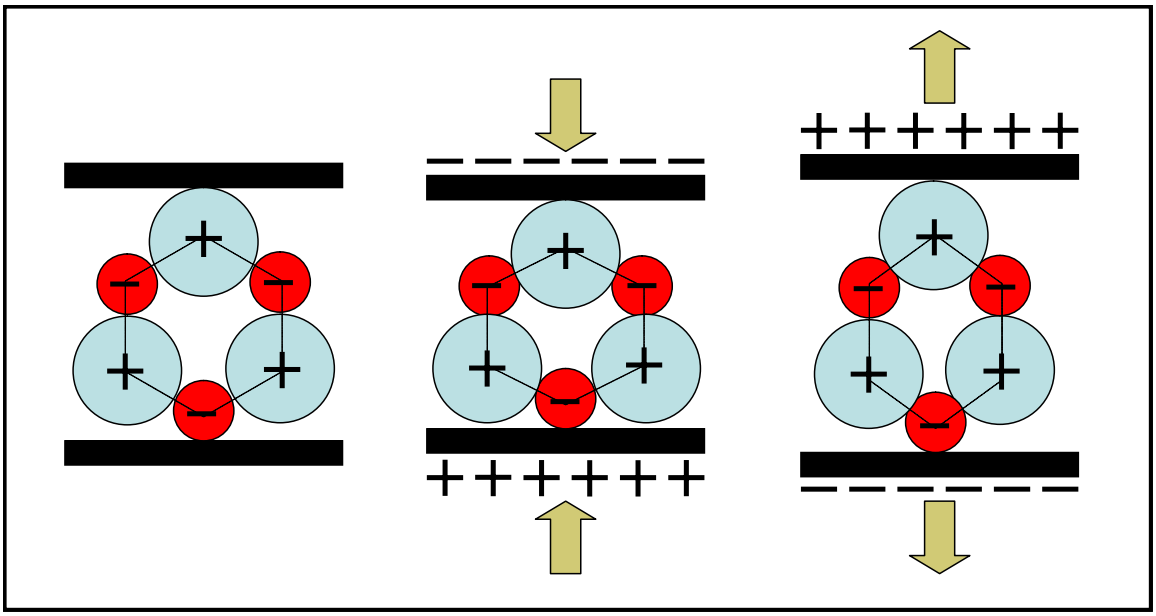

Figure 1.9 Electric polarization produced by mechanical deformation. The polarization is proportional to the strain and changing sign with it[85].

Although the models are intuitive, they are far too simple to provide a comprehensive understanding and appreciation for the complexity of piezoelectricity in real-world applications. In the sections to follow, linear piezoelectric constitutive equations will be defined in three-dimensions using tensor notation.

1.3.3 Dielectric Constitutive Equations

In order to properly characterize piezoelectricity, both coupled and uncoupled polarization must be considered. When a potential difference is applied across a dielectric material, molecular dipoles accumulate throughout the volume of the crystal and cause uncoupled polarization. Uncoupled polarization is given by $P = Np$; where P is the polarization vector (C/m^2), N is the number of dipoles per unit volume (m^{-3}) and p is the dipole moment (Cm). The polarization is, in general, proportional to the electric field and given by:

$$P_i = \varepsilon_o x_{ik} E_k \qquad i = 1,2,3 \tag{1.17}$$

where ε_o is the permittivity of free space (F/m), x is the electric susceptibility (dimensionless), and *E* is the electric field (V/m). As defined, the electric susceptibility expresses how readily a material will polarize when subjected to an electric field.

The significance of (1.17) is that polarization is not necessarily in the same direction as the induced electric field, and therefore may couple to other directions. "This may occur, for example, if the charges are constrained at certain symmetry directions (which constrains the direction of *P*) while the external field is skewed to these directions."[82] For convenience, uncoupled polarization is often replaced with electrical displacement to limit the electrical variables in the dielectric constitutive equation to *E* and *D* via;

$$\begin{aligned} D_i &= \varepsilon_o E_j + P_i \\ D_i &= \varepsilon_o E_j (1 + x_{ij}) \\ D_i &= \varepsilon_{ij} E_j \quad \text{for} \quad i = 1,2,3 \end{aligned} \tag{1.18}$$

where *D* is the electrical displacement (C/m^2) and $\varepsilon_{ij} = \varepsilon_o \left(1 + x_{ij}\right)$.

1.3.4 Resulting Piezoelectric Constitutive Equations

Although all materials will polarize under the influence of an external electric field, only piezoelectric materials will supplement the total polarization via charge separation. As described above, the Curie brothers are unequivocally recognized for experimentally determining the coupling relationships between stress and polarization (*direct effect*), as well as strain and electric field (*converse effect*). More precisely, the direct and converse piezoelectric effects are expressed again using the abbreviated nomenclature listed above:

$$\textit{Direct}: \qquad P_i = d_{iJ} T_J \qquad i = 1 \text{ to } 3 \quad J = 1 \text{ to } 6 \tag{1.19}$$

$$\textit{Converse}: \qquad S_J = d'_{Ji} E_i \qquad J = 1 \text{ to } 6 \quad i = 1 \text{ to } 3 \tag{1.20}$$

where *d* is the piezoelectric coupling coefficient (C/N) for the strain-charge form. Within these equations, the indices *i* and *J* respectively represent polarization and mechanical stress/strain components. More specifically, for the direct effect, the first subscript, *i,* of the piezoelectric coupling coefficient, *d*, refer to the direction of the electric field, while the second subscript, *J,* refers to the direction of the longitudinal or shear stress. Among the six components of the stress tensor, *J*=1,2,3 represents longitudinal stresses while J=4,5,6 represents shear stresses. For example, d_{33} possesses an electric field parallel to the z-axis and a piezoelectric-induced tensile strain in the same direction. It should be noted that the abbreviated notation has reduced the piezoelectric strain matrix from 27 terms to 18 independent terms by once again applying the symmetry condition $T_{ij} = T_{ji}$.

The fundamental linear constitutive equations for piezoelectricity are shown below in abbreviated notation (1.21) to (1.24), where all specified variables are summarized in Table 1.4. In addition, the superscripts among each equation denote the constant conditions from which variables must be measured. For example, the superscripts *E* and *T* within (1.21) state that the compliance and permittivity must be measured under conditions of constant electric field and stress, respectively. Although the piezoelectric equations listed below can be derived by combining and manipulating (1.11), (1.12), (1.19) and (1.20), they can also be derived by the thermodynamic principles outlined by Cady, Ikeda, and the IEEE standard on Piezoelectricity[79, 86, 87].

$$1.21 \begin{cases} \textit{Strain-Charge Form} \\ S_I = s_{IJ}^E T_J + d_{kJ} E_k \\ D_i = d_{iJ} T_J + \varepsilon_{ik}^T E_k \end{cases} \qquad 1.22 \begin{cases} \textit{Stress-Charge Form} \\ T_I = c_{IJ}^E S_J - e_{kJ} E_k \\ D_i = e_{iJ} S_J + \varepsilon_{ik}^S E_k \end{cases}$$

$$1.23 \begin{cases} \textit{Strain-Voltage Form} \\ S_I = s_{IJ}^D T_J + g_{kJ} D_k \\ E_i = -g_{iJ} T_J + \beta_{ik}^T D_k \end{cases} \qquad 1.24 \begin{cases} \textit{Stress-Voltage Form} \\ T_I = c_{IJ}^D S_J - h_{kJ} D_k \\ E_i = -h_{iJ} S_J + \beta_{ik}^S D_k \end{cases}$$

Table 1.4 Matrix variables used in the piezoelectric constitutive equations

Symbol	Meaning	Object Type	Size	Units
T	stress components	vector	6x1	N/m^2
S	strain components	vector	6x1	m/m
E	electric field components	vector	3x1	N/C
D	electric charge density displacement components	vector	3x1	C/m^2
s	compliance components	matrix	6x6	m^2/N
c	stiffness components	matrix	6x6	N/m^2
ε	electric permittivity	matrix	3x3	F/m
d	piezoelectric coupling coefficient for strain-charge form	matrix	3x6	C/N
e	piezoelectric coupling coefficient for stress-charge from	matrix	3x6	C/m^2
g	piezoelectric coupling coefficient for strain-voltage form	matrix	3x6	m^2/C
h	piezoelectric coupling coefficient for stress-voltage form	matrix	3x6	N/C

Of the 32 classes of crystals, 21 of them are non-centrosymmetric, of which 20 exhibit the direct piezoelectric phenomena. Of these 20 crystal structures, emphasis of this thesis will focus on the wurtzite structure of ZnO[62, 86].

1.4 Zinc Oxide (ZnO)

Zinc oxide (ZnO) is a piezoelectric, transparent, semiconducting oxide. It is commonly used as a catalyst[88], sensor[85], piezoelectric transducer[89], surface acoustic wave propagator[90] and photonic material [91]. With a direct bandgap of 3.37 eV and a large excitation binding energy (60 meV), ZnO exhibits near-UV emission, transparent conductivity, and resistance to high temperature electronic degradation. In addition, ZnO is the hardest of the II-VI semiconductors (therefore more resistant to wear), as well as one of the semiconductors with the most dominant piezoelectric properties.

Structurally, ZnO has a non-centrosymmetric wurtzite crystal structure with polar surfaces as shown in Figure 1.10.

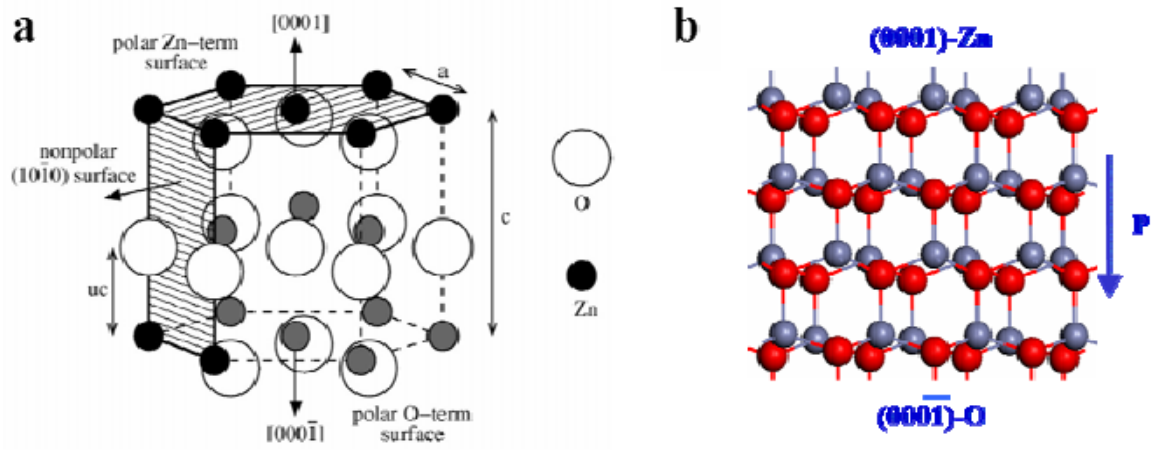

Figure 1.10 Crystal structure of ZnO (a) 3-D representation (b) 2-D representation.

It is categorized as a hexagonal Bravias lattice (a_o = 3.25Å and c_o = 5.20Å) with 6mm point group symmetry; where '6mm' is the Herman-Mauguin crystallographic nomenclature used to describe the 6 mirror planes within the basal planes of the crystal. As a consequence of ZnO's hexagonal symmetry, the stiffness, piezoelectric and dielectric matrices are reduced to the following:

$$c = \begin{bmatrix} c_{11} & c_{12} & c_{13} & 0 & 0 & 0 \\ c_{12} & c_{11} & c_{13} & 0 & 0 & 0 \\ c_{13} & c_{13} & c_{33} & 0 & 0 & 0 \\ 0 & 0 & 0 & c_{44} & 0 & 0 \\ 0 & 0 & 0 & 0 & c_{44} & 0 \\ 0 & 0 & 0 & 0 & 0 & c_{66} \end{bmatrix} \tag{1.25}$$

where $c_{66} = 1/2(c_{11} - c_{12})$

$$e = \begin{bmatrix} 0 & 0 & 0 & e_{14} & e_{15} & 0 \\ 0 & 0 & 0 & e_{24} & e_{25} & 0 \\ e_{31} & e_{32} & e_{33} & 0 & 0 & 0 \end{bmatrix} \tag{1.26}$$

where $e_{15} = e_{24}$, $e_{31} = e_{32}$, and $e_{14} = e_{25} = 0$ (three independent components)

$$\varepsilon = \begin{bmatrix} \varepsilon_{11} & 0 & 0 \\ 0 & \varepsilon_{11} & 0 \\ 0 & 0 & \varepsilon_{33} \end{bmatrix} \tag{1.27}$$

The values of each independent parameter are provided below in Table 1.5.

Table 1.5 Physical properties of ZnO

Parameter	Value	Units
Density	5.7	10^3 kg/m^3
ε_{11}	8.6	dimensionless
ε_{33}	10.0	
e_{33}	1.32	
e_{31}	-0.57	C/m^2
e_{15}	-0.48	
c_{11}	210	
c_{12}	121	
c_{13}	105	10^9 N/m^2
c_{33}	211	
c_{44}	43	

It is important to reiterate that ZnO nanobelts grow in three primary directions: the $<0001>$, $<01\bar{1}0>$ and $<2\bar{1}\bar{1}0>$ families. Since the direct and converse piezoelectric effects are dependent on the direction in which the stimulus is applied, the maximum piezoelectric effect will be experienced in the polar direction, though all of the nanobelts, regardless of orientation, can be utilized in piezoelectric applications[62]. This will provide a unique opportunity to explore the "piezoelectric confinement" effects at the nanoscale in ZnO nanobelts.

1.5 Acoustic Waves in Elastic Media

Acoustics is defined as the study of time-varying deformation in material media concerned with the macroscopic phenomena as if matter were a continuum—does not deal with atomic levels. Most people only associate acoustics with sound; however, in principle, it describes any mechanical vibration or elastic wave that is not an electromagnetic wave. In this section, the groundwork is laid for the study of crystal acoustics by developing fundamental mechanical equations. The properties of acoustic wave propagation in solids, as well as their electrical excitation and detection in piezoelectric materials, will be explored.

An elastic medium (or material) can be modeled as a distributed mass-spring element where the displacement of a single element or "particle" results in the propagation of strain throughout the structure. Particles are not molecules in the physical or chemical sense; they do not have defined physical or chemical properties. A particle is an imaginary infinitesimally small volume of the medium that exists in the mind's eye so that this movement can be visualized and described quantitatively. In this case, it is best to think of a particle as a grouping of atoms that move in unison.

Waves that propagate in a solid depend both on the material properties of the solid as well as the boundary conditions. A particle at a free surface is different from one interior to the bulk, in that it is constrained by adjacent particles from only one side. For this reason, surface disturbances can behave somewhat differently from those in the interior of a solid. The following four figures pictorially represent some of the different acoustic waves commonly observed in elastic media. The first two are bulk waves and the last two are surface waves. In each case the wave propagation is from left to right and the particle displacement distinguishes each of the wave types[92].

In a longitudinal wave, as shown in Figure 1.11, the particle displacement is parallel to the direction of wave propagation. Imagine the red wall in the figure oscillating back and forth to send a compression wave down the tube of the solid. The

particles do not move down the tube with the wave; they simply oscillate back and forth about their individual equilibrium positions. Notice the periodicity in the particles that create high-density regions about which the particles oscillate.

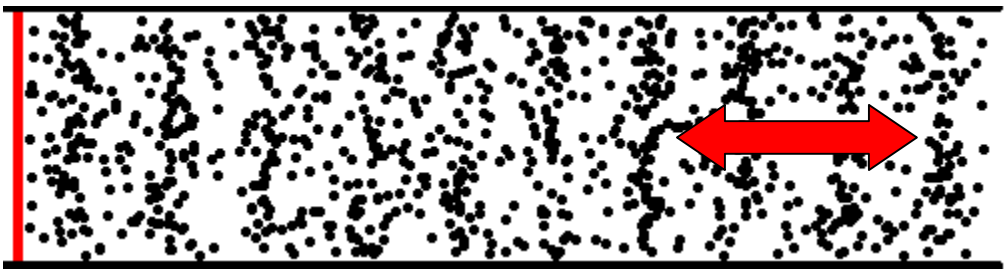

Figure 1.11 Longitudinal wave propagating from left to right, parallel to the particle displacement. Red arrow denotes particle displacement.

In a transverse wave (shear wave), as shown in Figure 1.12, the particle displacement is perpendicular to the direction of wave propagation. The particles do not move along with the wave; they simply oscillate up and down about their individual equilibrium positions as the wave passes by.

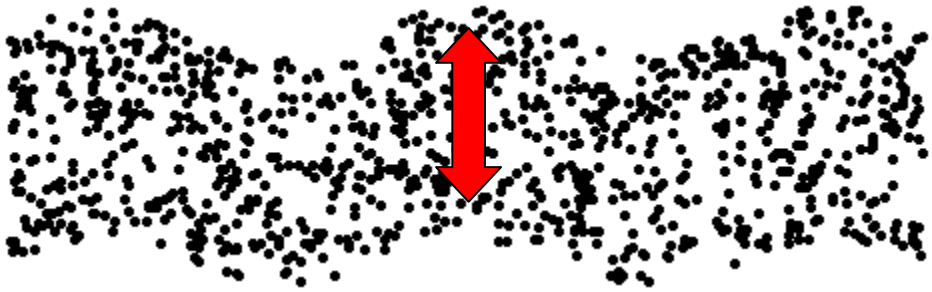

Figure 1.12 Transverse wave (or shear wave) propagating from left to right with the particle displacement perpendicular to the direction of the traveling wave. The red arrow denotes particle displacement.

Unlike the bulk waves just described, surface waves involve a combination of both longitudinal and transverse motions. Figure 1.13 depicts a typical ocean wave. As the name intuitively describes, ocean waves in elastic media are analogous to surface waves one might see crashing on a sandy beach or propagating in a bathtub. In the figure, the wave is propagating from left to right; however, the particle displacement takes a clockwise elliptical path which is much different from the linear path found in the longitudinal and shear waves. Note that the radius of the circle that defines the particle path decreases as the penetration depth into the surface increases.

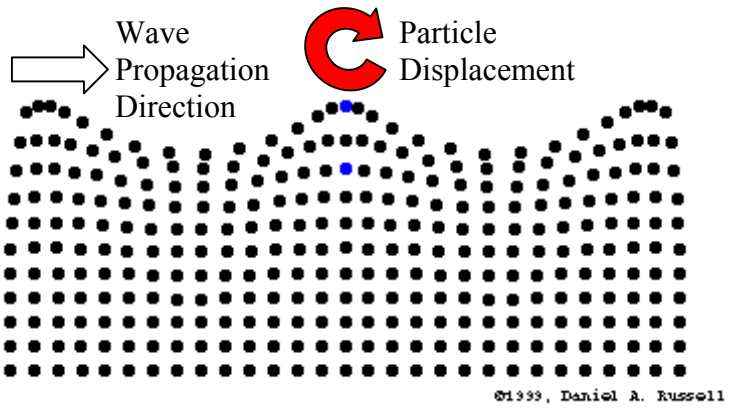

Figure 1.13 Schematic description of an ocean wave where the acoustic wave propagation is from left to right, and the particle displacement is clockwise.

Another example of waves with both longitudinal and transverse motion are Rayleigh waves (Figure 1.14). Rayleigh waves are different from ocean waves in one important way. In an ocean wave, all particles travel in clockwise trajectory. In a Rayleigh wave, particles at the surface trace out a counter-clockwise elliptical path. As the depth into the solid increases, the width of the elliptical path decreases to zero until a depth of more than 1/5th the acoustic wavelength where particles begin to trace out a clockwise elliptical path[93]. Rayleigh waves are associated with earthquakes and

subterranean movement of magma, as well as with other sources of seismic energy such as explosions.

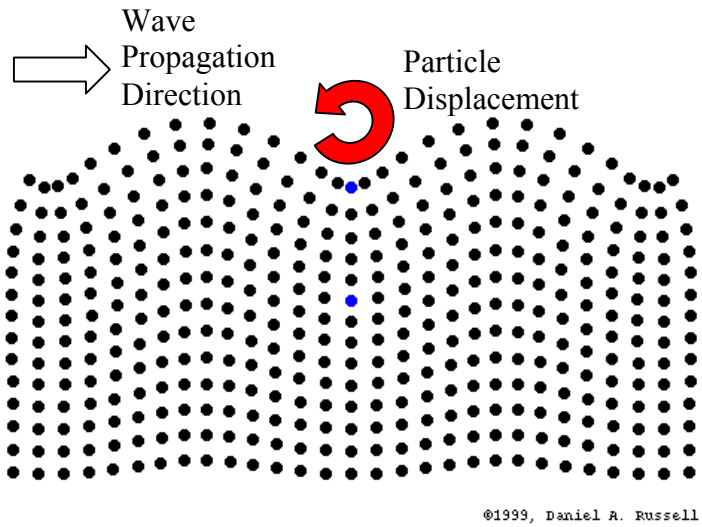

Figure 1.14 Schematic description of a Rayleigh wave where the acoustic wave propagation is from left to right, and the particle displacement is counter-clockwise at the surface and clockwise in the interior of the bulk.

In addition to the acoustic waves described above, there are other wave types known to propagate in elastic media: Love waves[94], Lamb waves[95], Stoneley waves[96] and flexural plate waves[97], to name a few. Each is unique in its manner of propagation and each has unique applications. However, they will not be addressed further.

In the next set of sub-sections, a self-consistent set of equations that describe the propagation of mechanical strain in a one-dimensional solid will be given. This will be used to build the three dimensional equation of motion (the Christoffel equation). Finally, the piezoelectric contribution to acoustic stiffening will be presented.

1.5.1 Mechanical Equation of Motion in One-Dimension

A self-consistent set of equations that describe the propagation of mechanical strain in a 1D solid is derived in this section. Just as in Maxwell's equations for electromagnetics, there are a set of four relationships between four mechanical variables that are required for characterizing mechanical motion in elastic media. The four variables are stress (*T*), strain (*S*), particle displacement (*u*) and particle velocity (*v*). The four necessary equations are as follows:

1) Newton's 2nd Law:

Consider a slab with cross-section dA and dimensions dx and dy. Also consider two apposing traction forces T_1 and T_2 that are opposite but not equal resulting in a net force on the slab normal to the cross-sectional area. Describing the internal coupling as springs,

$$\begin{array}{ccccc} dF & = & m & + & a \\ \Downarrow & & \Downarrow & & \Downarrow \end{array}$$

$$\frac{\partial T}{\partial z} dzA = \rho A \Delta z + \frac{\partial^2 u}{\partial t^2}$$

or

$$\frac{\partial T}{\partial z} = \rho \frac{\partial^2 u}{\partial t^2} \tag{1.28}$$

where ρ is density in kg/m^3.

2) Particle Velocity:

$$v = \frac{\partial u}{\partial t} \tag{1.29}$$

which can be seen as the time derivative of particle displacement.

3) Strain:

The gradient of the particle displacement with respect to position (spatial rate of change)

$$S = \frac{\partial u}{\partial z} \tag{1.30}$$

This equation is only valid if strains are small, which may not be realistic in some practical cases.

4) Hooke's Law:

$$T = cS \tag{1.6}$$

This equation was addressed extensively in section 1.3.1 and defines the properties of connected springs. For given stress components, a stiff spring results in a relative small strain whereas a compliant spring results in a large strain. These four equations enable the solving of the four variables listed above. There are two fundamental physical laws, (1.28) and (1.30) and two constitutive equations (1.29), (1.6).

By taking the derivative of (1.29), (1.28) can be simplified to $\frac{\partial T}{\partial z} = \frac{\partial u}{\partial t}$.

Differentiating $S = \frac{\partial u}{\partial z}$ with respect to *t* and using (1.6)

$$\frac{\partial S}{\partial t} = \frac{\partial u^2}{\partial t \partial z} = \frac{\partial v}{\partial z} = \frac{1}{c}\frac{\partial T}{\partial t} \tag{1.31}$$

This set of equations can now be solved to give the 1D wave equation. Differentiating (1.31) with respect to *t* and (1.28) with respect to *z* gives

$$\frac{\partial^2 v}{\partial z \partial t} = \frac{1}{c}\frac{\partial^2 T}{\partial t^2} \text{ and } \frac{1}{\rho}\frac{\partial^2 T}{\partial z^2} = \frac{\partial^2 v}{\partial z \partial t}$$

Since the terms with cross derivatives are equal,

$$\frac{1}{\rho}\frac{\partial^2 T}{\partial z^2} = \frac{1}{c}\frac{\partial^2 T}{\partial t^2} \tag{1.32}$$

Equation (1.32) is the 1D wave equation with the solution v_a, which is the phase velocity of the acoustic wave shown in (1.33)

$$v_a = \sqrt{\frac{c}{\rho}} \tag{1.33}$$

In the 1D acoustic system, it can be seen that the solution is a plane wave with the acoustic polarization in the direction of the wave propagation (longitudinal wave). In a 3D system, three possible acoustic polarizations will result as solutions to the equation[82].

1.5.2 Three Dimensional Christoffel Equation

The 3D wave equation is generally referred to as the Christoffel equation. It yields three solutions, the properties of which are determined by the relationship between propagation direction and the stiffness matrix. To start, it is necessary to expand the definitions of (1.28) and (1.30) by considering the 3D physical equations where Newton's law is $\nabla T = \rho \frac{\partial^2 u}{\partial t^2}$, and the definition of strain becomes $S = \nabla_s u$. The constitutive relationships remain the same; however, things become more complex now that it is necessary to consider the full 6x6 stiffness tensor as derived above in section 1.3.1.

First, manipulation of these equations using the constitutive relations to form the wave equation is performed. Each is written in terms of *T* and *v*.

$$\nabla T = \rho \frac{\partial v}{\partial t} \tag{1.34}$$

$$\nabla_s v = \frac{\partial S}{\partial t} = s : \frac{\partial T}{\partial t} \tag{1.35}$$

Differentiating (1.34) with respect to *t* and multiplying (1.35) by *c* gives:

$$\nabla \frac{\partial T}{\partial t} = \rho \frac{\partial^2 v}{\partial t^2} \tag{1.36}$$

$$c : \nabla_s v = c : s : \frac{\partial T}{\partial t} = \frac{\partial T}{\partial t} \tag{1.37}$$

Since *c* is simply the inverse of *s*, *c*:*s* = 1 (the colon symbol denotes matrix multiplication). Substituting $\frac{\partial T}{\partial t}$ from Equation (1.37) into (1.36) results in

$$\nabla \frac{\partial T}{\partial t} = \nabla c : \nabla_s v = \rho \frac{\partial^2 v}{\partial t^2} \tag{1.38}$$

which is the wave equation in 3D. Next, it is possible to derive an equation of identical form for the particle displacement *u*. If *c* and *v* are scalars with particle velocity in the Z direction, (1.38) reduces to,

$$\nabla \cdot c : \nabla_s v \rightarrow c \nabla \cdot \nabla v = c \nabla^2 v = c \frac{\partial^2 v}{\partial z^2} = \rho \frac{\partial^2 v}{\partial t^2}$$

which can be written in a more convenient 3x6 matrix where $\nabla_s \rightarrow \nabla_{Ij}$ $I = 1$ to 6, $j = 1$ to 3. The expression $c : \nabla_s v$ is a 6x6 matrix, making $\nabla \cdot (c : \nabla_s v)$ a vector.

Therefore, the 3D wave equation reduces to

$$\nabla \cdot c : \nabla_s v = \rho \frac{\partial^2 v}{\partial t^2} \rightarrow \nabla_{iK} c_{KL} \nabla_{Lj} v_j = \rho \frac{\partial^2 v_i}{\partial t^2} \tag{1.39}$$

which contains three summations over the dummy indices *j*, *K*, *L* where ∇_{Lj} is the 6x3 matrix in (1.40) and ∇_{iK} is simply the transpose.

$$\nabla_{Lj} = \begin{bmatrix} \frac{\partial}{\partial x} & 0 & 0 \\ 0 & \frac{\partial}{\partial y} & 0 \\ 0 & 0 & \frac{\partial}{\partial z} \\ 0 & \frac{\partial}{\partial z} & \frac{\partial}{\partial y} \\ \frac{\partial}{\partial z} & 0 & \frac{\partial}{\partial x} \\ \frac{\partial}{\partial y} & \frac{\partial}{\partial x} & 0 \end{bmatrix} \tag{1.40}$$

∇_{Lj} can be simplified by considering the time and space dependence of propagating acoustic waves. Unlike electromagnetic waves where displacement, electric field, magnetic field and induction are all in phase, in acoustic systems particle displacement is out of phase with particle velocity. An arbitrary plane wave propagation direction $\hat{L}$ is considered and can be written as,

$$\hat{L} = l_x \hat{i} + l_y \hat{j} + l_z \hat{k} \tag{1.41}$$

where l_x, l_y and l_z are the projections of the unit vector $\hat{L}$ on three Cartesian axes. The 3D time and space dependant phase relationship is written as,

$$v \propto e^{j(\omega t - k \hat{L} \bullet \bar{r})} \tag{1.42}$$

where $\hat{L}$ is given by (1.41), $\bar{r} = x\hat{i} + y\hat{j} + z\hat{k}$ and $k = \frac{\omega}{v_a}$. Performing the operation $\hat{L} \bullet \bar{r}$, (1.42) can be written as:

$$e^{j(\omega t-k\hat{L}\bullet\bar{r})}=e^{j(\omega t-k(l_x x+l_y y+l_z z))} \tag{1.43}$$

Now it is simply a matter of differentiation to obtain

$$\frac{\partial}{\partial x}(e^{j(\omega t-k\hat{L}\bullet\bar{r})})=-jkl_x e^{j(\omega t-k(l_x x+l_y y+l_z z))}$$

By substituting (1.43) back into the derivative,

$$e^{j(\omega t-k\hat{L}\bullet\bar{r})}=-jkl_x v \tag{1.44}$$

Recalling (1.40), the *L* matrix in (1.45) has the same form as the gradient operator matrix and each of its components represents a propagation direction of the acoustic wave.

$$\nabla_{Lj}\rightarrow -jk\begin{bmatrix} l_x & 0 & 0 \\ 0 & l_y & 0 \\ 0 & 0 & l_z \\ 0 & l_z & l_y \\ l_z & 0 & l_x \\ l_y & l_x & 0 \end{bmatrix}=-jkl_{Lj} \tag{1.45}$$

Next, (1.39) can be rewritten as

$$\nabla_{iK}c_{KL}\nabla_{Lj}v_j\rightarrow -(k^2 l_{ik}c_{KL}l_{Lj})v_j=-k^2\Gamma_{ij}v_j=-\rho\omega^2 v_i \tag{1.46}$$

where, $\Gamma_{ij}=l_{ik}c_{KL}l_{Lj}$ is the Christoffel matrix. This matrix is 3x3 with elements that depend solely on the propagation direction of the wave and the stiffness constants of the crystal. Solving the Christoffel equation involves solving an eigenvalue problem where the three eigen solutions are the three acoustic velocities of the possible propagating waves. The three corresponding eigenvectors are called the acoustic polarization and are simply the particle direction[82].

1.5.3 Piezoelectrically Stiffened Christoffel Equation

The presence of piezoelectricity in crystals has an effect on the propagation characteristics of acoustic waves in elastic media. It is possible to develop the Christoffel matrix for piezoelectric materials and show the dependence of piezoelectricity on crystal orientation. Of the four necessary acoustic equations, all remain the same except for Hooke's law. Since any stress applied to the crystal results in an electrical polarization, it is necessary to include the additional term as shown in the stress-charge form given previously in section 1.3.4.

$$\begin{aligned} T_I &= c_{IJ}^E S_J - e_{kJ} E_k \\ D_i &= e_{iJ} S_J + \varepsilon_{ik}^S E_k \end{aligned} \tag{1.22}$$

In addition, it is necessary to consider the three electrical equations in order to re-calculate of the Christoffel equation to include an electrical perturbation.

$$\nabla \times E = -\frac{\partial B}{\partial t} \text{ (Faraday's Law)}$$

$$\nabla \times H = \frac{\partial D}{\partial t} + J \text{ (Ampere's Law)}$$

$$B = \mu H$$

Using these equations enables the direct coupling of the acoustic wave equation to the set of electromagnetic wave equations in 3D (letting J=0).

First, the strain equation (1.35) is multiplied by the stiffness matrix under a constant electric field:

$$c^E \nabla_s v = c^E : \frac{\partial S}{\partial t} \tag{1.47}$$

Next, (1.22) is differentiated with respect to t:

$$\frac{\partial T}{\partial t} = c^E : \frac{\partial S}{\partial t} - e : \frac{\partial E}{\partial t} \tag{1.48}$$

Using (1.47)

$$\frac{\partial T}{\partial t} = c^E \nabla_s v - e : \frac{\partial E}{\partial t} \tag{1.49}$$

Differnetiating Netwon's law gives

$$\nabla \frac{\partial T}{\partial t} = \rho \frac{\partial^2 v}{\partial t^2} \tag{1.50}$$

(This is also equation 1.36 from above)

Substituting (1.49) into (1.50) results in:

$$\nabla \cdot c^E : \nabla_s v - \nabla \cdot e : \frac{\partial E}{\partial t} = \rho \frac{\partial^2 v}{\partial t^2} \tag{1.51}$$

Next, we consider the electromagnetic wave equation in 3D:

$$-\nabla \times \nabla \times E = \mu_o e \frac{\partial^2 D}{\partial t^2} \tag{1.52}$$

Using 1.22 gives,

$$-\nabla \times \nabla \times E = \mu_o \varepsilon^S : \frac{\partial^2 E}{\partial t^2} + \mu_o e : \frac{\partial^2 S}{\partial t^2} \tag{1.53}$$

Eliminating the strain term by substituting (1.35) gives the electromagnetic wave equation with an acoustic perturbation term:

$$-\nabla \times \nabla \times E = \mu_o \varepsilon^S : \frac{\partial^2 E}{\partial t^2} + \mu_o e : \nabla S\left(\frac{\partial v}{\partial t}\right) \tag{1.54}$$

Equations (1.51) and (1.54) are the two equations that couple the electric field E to the acoustic field v. In the absence of piezoelectricity $(e \to 0)$ they reduce to the uncoupled equations for the acoustic and electric fields.

The electrical coupling term from (1.51) is $\nabla \cdot e : \frac{\partial E}{\partial t}$. For plane waves[82],

$$\nabla \cdot e : \frac{\partial E}{\partial t} \rightarrow \nabla_{iJ} e_{Jk} \frac{\partial E_k}{\partial t} \rightarrow -jkl_{iJ} e_{Jk} \frac{\partial E_k}{\partial t} \tag{1.55}$$

The acoustic perturbation term in (1.54) is $\mu_o e : \nabla_S \frac{\partial v}{\partial t}$. The term can be seen to poses a 3X1 matrix as it must. Analagous to (1.55),

$$\mu_o e : \nabla_S \frac{\partial v}{\partial t} \rightarrow \mu_o e_{iI} \nabla_{Ij} v_j \rightarrow \mu_o e_{iI} \left(-jkl_{iJ}\right) v_j \tag{1.56}$$

It must be assumed that the presence of the acoustic wave does not cause electromagnetic radiation in the crystal. This assumption is called the *quasistatic approximation*. The assumption that there is no coupling to an electromagnetic wave with an acoustic wave and thus no acoustically-generated magnetic field implies that $\nabla \times E = 0$. Therefore, the electric field can be written as a gradient, $E = -\nabla\Phi$. The implication of this is that the electric field is continuously being generated by the propagation of the strain wave. Furthermore, assuming a plane wave, the spatial variation of the electric potential only varies in the direction of the acoustic wave stating that the electric field is in the direction of $\hat{l}$.

Setting the left side of (1.54) to zero, substituting $E = -\nabla\Phi$ into (1.51) and (1.54) and taking the divergence gives:

$$\nabla \cdot c^E : \nabla_s v - \nabla \cdot e : \frac{\partial \nabla\Phi}{\partial t} = \rho \frac{\partial^2 v}{\partial t^2} \tag{1.57}$$

and,

$$0 = \mu_o \nabla \cdot \varepsilon_S : \frac{\partial^2 \nabla\Phi}{\partial t^2} + \mu_o \nabla \cdot \left(e : \nabla_S \frac{\partial v}{\partial t} \right) \tag{1.58}$$

Next, converting to a plane wave,

$$-k^2\left(l_{iK}c_{KL}l_{Lj}\right)v_j + \rho\omega v_i = j\omega k^2\left(l_{iK}e_{Kj}l_j\right)\Phi \tag{1.59}$$

because $\nabla\Phi \to \left(l_j\Phi\right)\left(-jk\right)$ and,

$$0 = \omega^2 k^2\left(l_i\varepsilon_{ij}^S l_j\right)\Phi - j\omega k^2\left(l_i e_{iL}l_{Lj}\right)v_j \tag{1.60}$$

Equations (1.59) and (1.60) are a set of two equations with two unknowns, one acoustic (v) and one electric (Φ). Solving (1.60) for Φ gives,

$$\Phi = \frac{1}{j\omega}\frac{\left(l_i e_{iL}l_{Lj}\right)v_j}{l_i\varepsilon_{ij}^S l_j} \tag{1.61}$$

Substituting (1.61) into (1.59) gives the result we are looking for:

$$k^2\left(l_{iK}\left(c_{KL}^E + \frac{\left[e_{Kj}l_j\right]\left[l_i e_{iL}\right]}{l_i\varepsilon_{ij}^s l_j}\right)l_{Lj}\right)v_j = \rho\omega^2 v_i$$

where,

$$\Gamma_{ij} = l_{iK}\left(c_{KL}^E + \frac{\left[e_{Kj}l_j\right]\left[l_i e_{iL}\right]}{l_i\varepsilon_{ij}^s l_j}\right)l_{Lj} \tag{1.62}$$

This form is nearly identical to the uncoupled Christoffel equation from section 1.5.2 with a few extra terms from the piezoelectric and permittivity matrix included. It is said that these components *stiffen* the matrix. This form of the equation will be revisited towards the end of the thesis in Chapter 4[82].

1.6 Thesis Matter

Piezoelectric ZnO nanowires and nanobelts will be the nanomaterial of focus throughout this body of work. The following chapters will address some of the issues Feynman introduced during his speech to Caltech. Progress in the areas of manipulating small things will be demonstrated using novel techniques in Chapter 2. Some techniques utilize brute force manipulation through the physical contact of probe tips. Others more elegantly enable non-contact manipulation by using optically generated surface acoustic waves to push microstructures and nanomaterials into desired locations. Chapter 3 will demonstrate the first ever bulk acoustic resonator (BAR) based on bottom-up synthesized ZnO belts. In this chapter, many non-traditional fabrication methods will be introduced as necessary tools for fabricating the nanodevice. Device fabrication and testing will be presented along with one-dimensional modeling to confirm device performance. Chapter 4 will introduce a 2nd generation design for the bulk acoustic resonator. Here, slow, low yield nanofabrication will be abandoned for traditional photolithograpy in order to streamline the process and increase throughput. In this section a redesign of the device presented in Chapter 3 will result in freestanding nanobelt resonators. In addition, a novel approach for site-specifically growing nanostructures between two electrodes will be presented for the purpose of integrating nanomaterials directly into prefabricated MEMS, NEMS and CMOS systems without the need for manipulation. This can be seen as an advantageous solution to mass production of nanodevices. In Chapter 5, device performance of each nanoresonator type will be analyzed along with modeling to describe some of the hurdles limiting further success. Finally, concluding remarks and an outline for future work will be detailed for anybody wishing to continue this type of research.

CHAPTER 2

NANOMANIPULATION

Bottom-up synthesized nanomaterials have received a great deal of attention from the scientific community in recent years. Their unique optical and electronic properties are seen as promising components in a variety of novel applications such as field effect transistors[98], light emitting diodes[99], sensors[100], resonators[44] and power generators[101]. Some of the key scientific hurdles to overcome when building functional devices around nanomaterials are controllable handling, manipulation and assembly[102]. Some scientists have developed synthesis procedures in order to site-specifically grow nanostructures in desired locations via catalysis[91]. This technique is preferred yet sometimes limited to a vertical growth direction and not ideal when considering more complex device designs and geometries. Others have obtained control over the position of individual nanostructures by manipulating them post synthesis. The atomic force microscope (AFM) has been demonstrated as a useful direct-contact technique by applying lateral forces to the nanomaterial via a probe tip[103]. Alternating current dielectrophoresis has been used to separate metallic carbon nanotubes from semi-conducting nanotubes by aligning them between two electrodes[104]. Infrared optical traps have been used to transfer and assemble semi-conducting nanowires in a fluid environment[105]. Other techniques have been developed that utilize magnetic fields[106], Langmuir-Blodgett troughs[107] and micro-fluidic channels[108]; each is seen as a step forward in the nano-fabrication process.

This chapter deals with the techniques pioneered and utilized in order to build devices using ZnO nanobelts. Some of them involve direct contact between a probe tip and the individual nanostructure, while others utilize laser induced acoustic waves for non-contact manipulation of 1D microstructures and nanomaterials.

2.1 Direct Contact Manipulation of Nanomaterials

This section will highlight two direct contact techniques used to manipulate bottom-up synthesized nanobelts. The first, utilizes the build up of eletrostatic charge to generate attractive forces between the nanostructure and a tungsten probe. The second involves the "welding" of platinum (Pt) to a small probe in direct contact with a 1D nanostructure in order to create a physical bond by which to pick up the nanomaterial. The former is useful for manipulating large structures with thickness and width dimensions in the low micron to high nanometer range, while the latter is useful when manipulating extremely small nanomaterials. Each has its own advantages and limitations which will be addressed below. These techniques are synonymous with the STM manipulation experiments Eigler performed. However, instead of building devices one atom at a time, the materials are grown to atomic precision using large scale synthesis first and then integrated with other device components.

2.1.1 Electrostatic Manipulation

This technique was developed around the desire for an inexpensive process that required little training and a minimal amount of equipment for implementation. The technique utilizes two DC probes, an optical microscope, an insulating substrate and the as-synthesized nanomaterial.

First, 400nm of Si_3N_4 was deposited using PECVD onto a silicon wafer. The as-grown nanobelts/nanowires were scraped from the deposition substrate using a pair of fine tipped tweezers and allowed to freely disperse onto the nitride thin film. The wafer was then placed onto the probe station underneath the optical scope. Two tungsten DC probe tips model PTT-120/4-25 made by Cascade Microtech with a 12μm tip radius were fixed to Cascade micromanipulators and then positioned just above the wafer within the microscopes field of view.

The probe stage was moved in the X and Y directions until a suitable nanostructure could be identified for manipulation. Once the desired structure was sighted, one of the probes was lowered using the Z-position on the micromanipulator until it contacted the nitride film just behind the structure. With the probe in contact with the insulator, it was then skated forward until it achieved contact with the nanomaterial. With the probe in intimate contact with both the substrate and the nanomaterial, it was then pushed forward further to slide the nanostructure across the insulating surface in order to build up static charge. This is similar to the way a person would rub their shoes back and forth on fuzzy carpet. Due to the build-up of static charge resulting in coulombic attraction between the probe tip and the nanomaterial, the nanostructure would attach itself to the end of the probe. After moving a finite distance, the micromanipulator was retracted, causing the tip to skate backwards with the nanostructure in intimate contact (similar to what Eigler did by sliding atoms along the surface of nickel to build arrays of molecules). As the probe was raised from the substrate, the nanostructure remained secure, withdrawing it from the surface. Once this was done, the underlying substrate can be repositioned without disturbing the static bond between the probe tip and the nanostructure. Next, the new substrate on which the structure is to be deposited can be moved into the field of view just beneath the nanomaterial. The probe is then lowered into contact and positioned so that the nanostructure is set in its desired resting place. At this time the nanostructure is still in contact with the probe. Attempts were made to agitate the structure by scraping it across the substrate; however, mechanical forces were insufficient to detach it from the probe tip. In order to release the nanobelt a second probe was brought into contact with the free end of the nanostructure in order to discharge the built up static electricity. This is similar to touching a door knob after one has rubbed his or her feet on a shaggy carpet to generate a spark (one probe is the floor, the other probe is the door knob, the person with built up charge is the belt). Once this was done, the nanostructure remained on the surface and both probes were retracted

without disturbing it. In some cases, if the final resting position is not ideal, the probes can be brought in again in order to repeat the manipulation. If the surface on which the nanostructure was deposited is a good conductor, it may not be possible to pick up the nanomaterial again. This is sometimes advantageous if the operator of the probes simply wants to reposition the nanomaterial and not physically lift it. A series of video files were captured with a Moticam 2300 digital camera with 3.0 mega-pixel resolution in order to document the reproducibility of this technique. Individual frames from one of the movies are shown starting with Figure 2.1 and ending with Figure 2.18. Each frame is captioned to describe what is going on during the manipulation experiment.

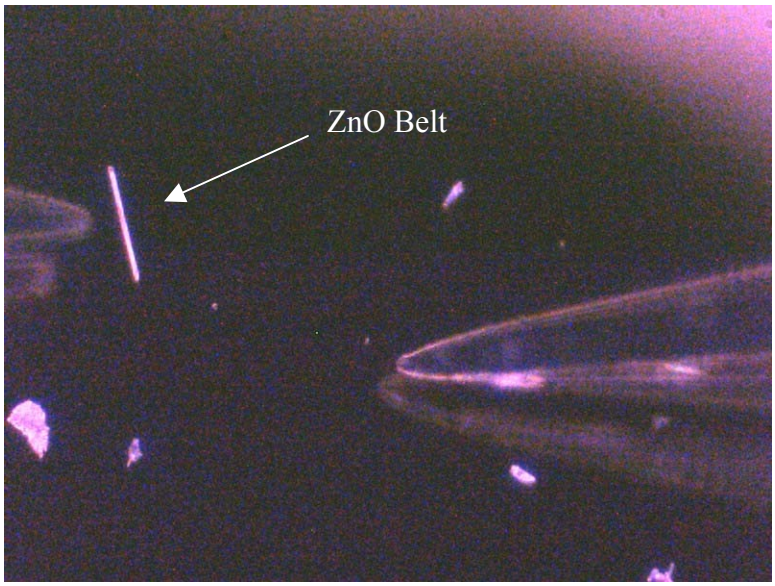

Figure 2.1 This is the first frame of the manipulation experiment. Both probes can be seen and each is freely suspended just above the nitride coated wafer. The probe on the left will be used to pick up the ZnO microbelt in the frame. There is some other contamination on the surface, but this can be ignored.

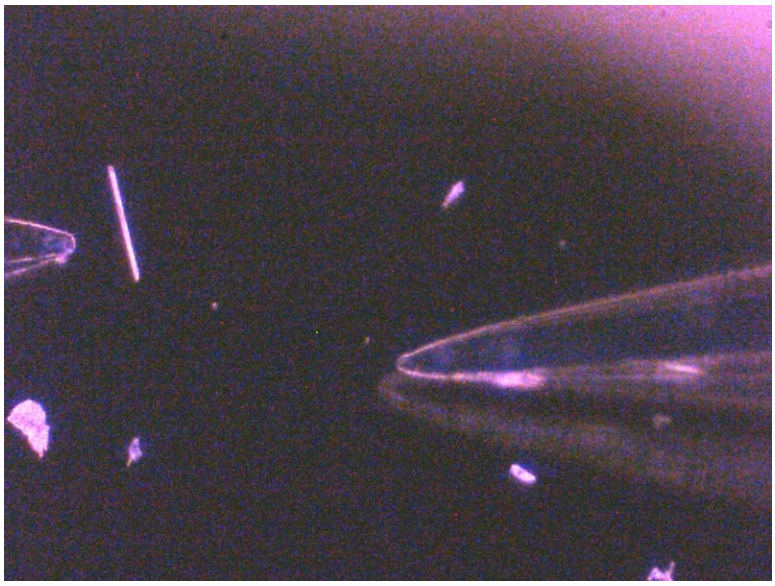

Figure 2.2 The probe is lowered until it is in intimate contact with the nitride layer. The right side probe is still hovering above the surface. It will not be utilized until the final step of manipulation.

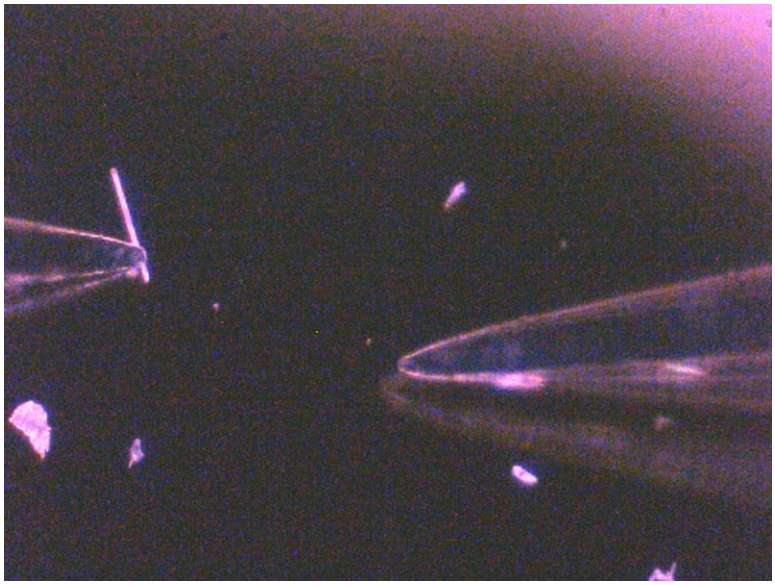

Figure 2.3 The probe is skated forward into contact with the ZnO belt. At this time the probe is in contact with both the nitride and the ZnO.

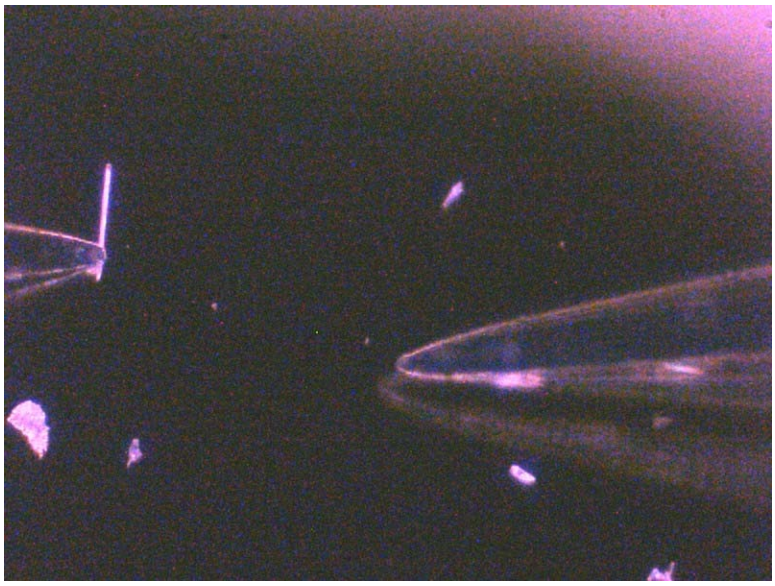

Figure 2.4 In this frame, the probe is kept in contact with the nitride and retracted in the X-direction in order to see whether or not the belt is stuck to the probe. Since the belt moves backwards with the probe, it is assumed that the coulombic attraction has attached the ZnO belt to the probe tip.

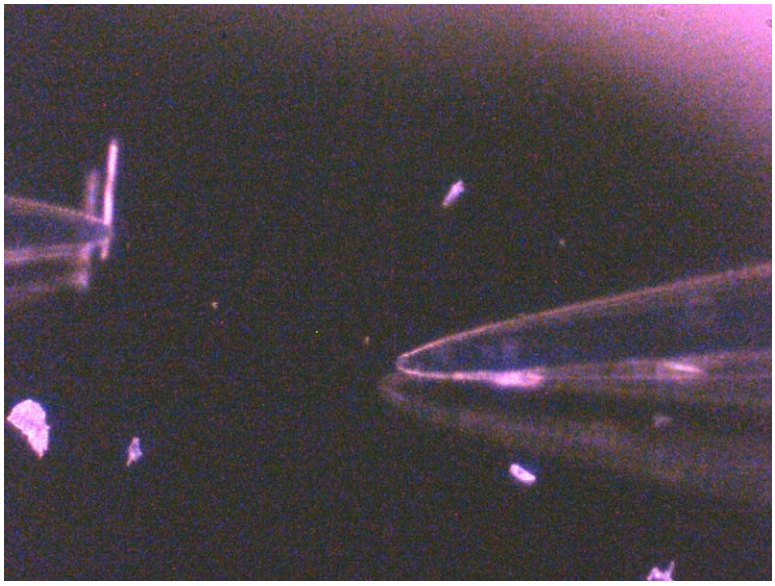

Figrue 2.5 The manipulator is raised in the Z-direction out of contact with the nitride. It is possible to see the reflection of both the belt and the probe off the surface beneath it. It can bee seen that the belt is clearly in contact with the tungsten probe.

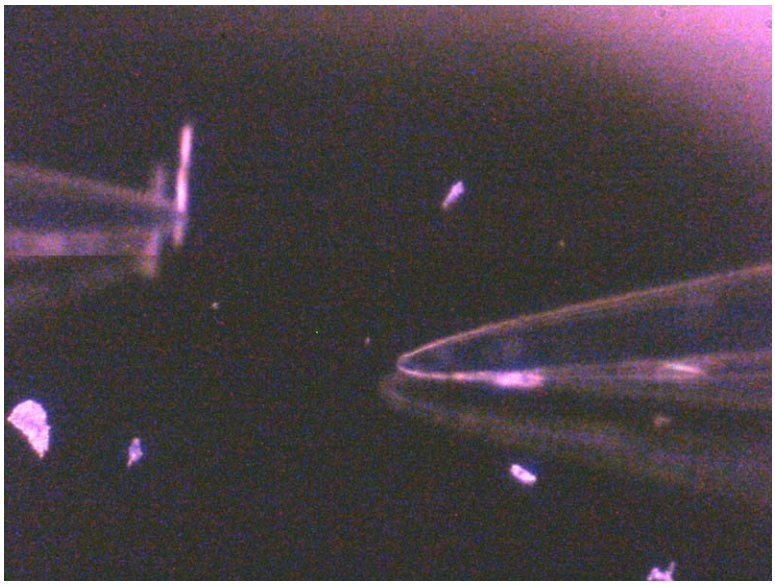

Figure 2.6 In this frame, the operator is agitating the manipulator back-and-forth violently in order to see if the belt can be detached. It is impossible to truly demonstrate this without a movie; however, this still is taken at the end of agitation to verify that the belt has remained in contact.

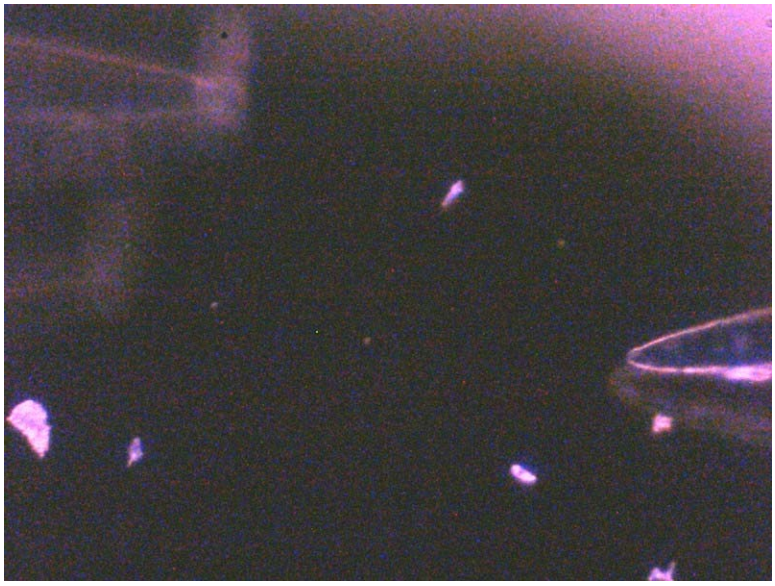

Figure 2.7 The micromanipulator is being raised further above the substrate. A faint reflection of the belt can still be seen as it is being raised.

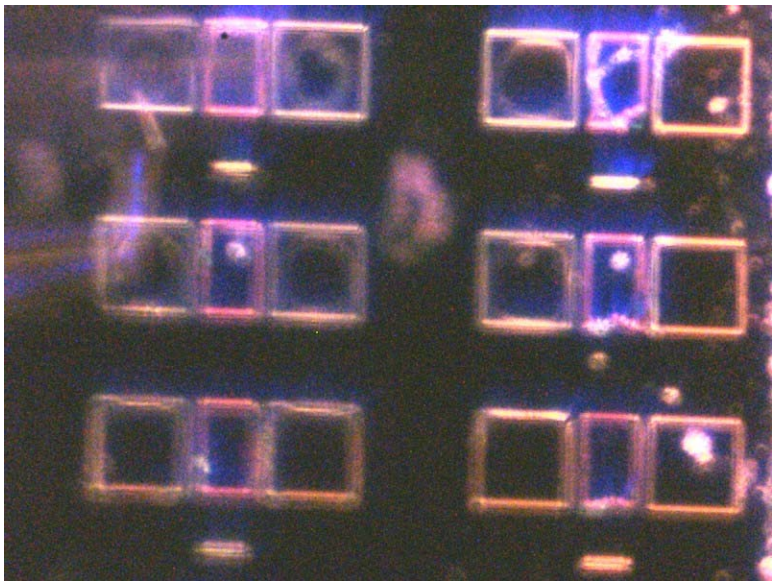

Figure 2.8 Once the probe has been moved far enough away from the surface, the substrate on which the belt will be deposited can be moved into the field of view. In this case the belt will be deposited on top of a series of electrodes in order to test certain functional characteristics of the ZnO belt. The device consists of six electrodes with a trench that has been etched into a SiO2 layer (three electrodes are above the trench; three are below). The nature of this device will be discussed in subsequent chapters 3 and 4.

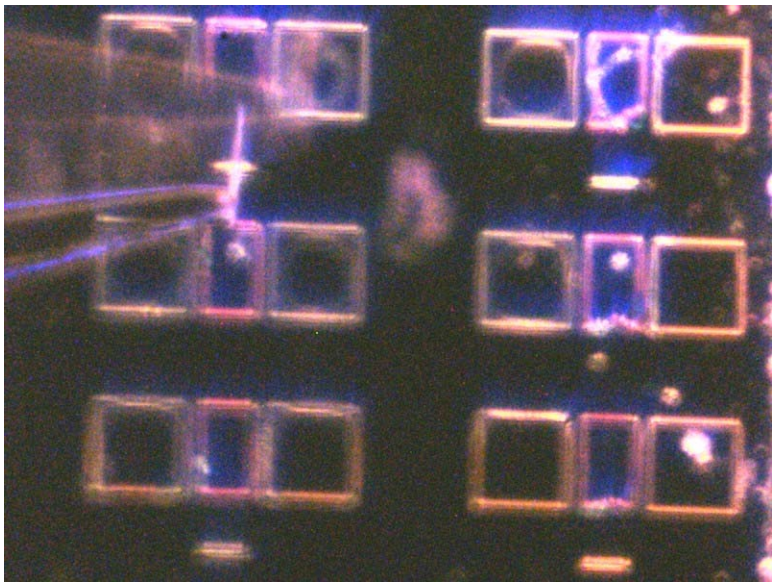

Figure 2.9 Here the micromanipulator is being lowered into contact with the device electrodes in order for the belt to be deposited into its final resting position.

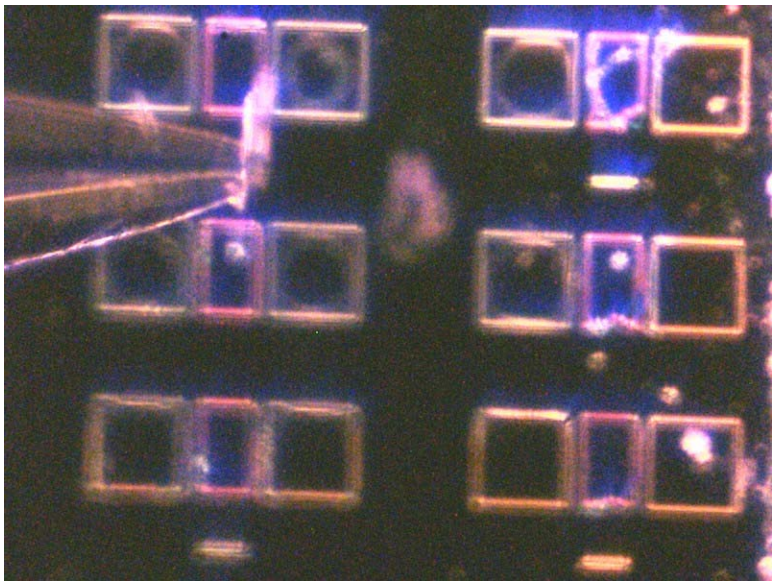

Figure 2.10 This is another intermediate step that shows the continued lowering of the manipulator along with the belt just before it finally touches down on the device pads.

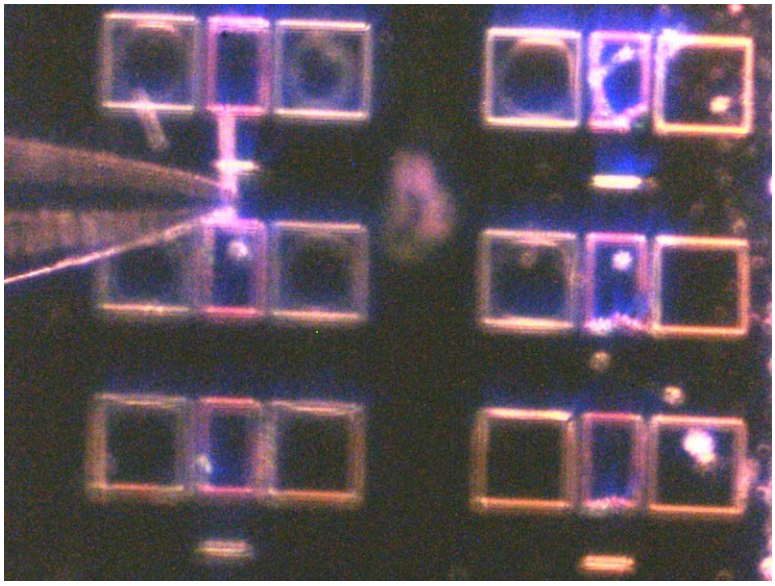

Figure 2.11 The belt is now in direct contact with the device pads though it is also still statically attached to the end of the tungsten probe.

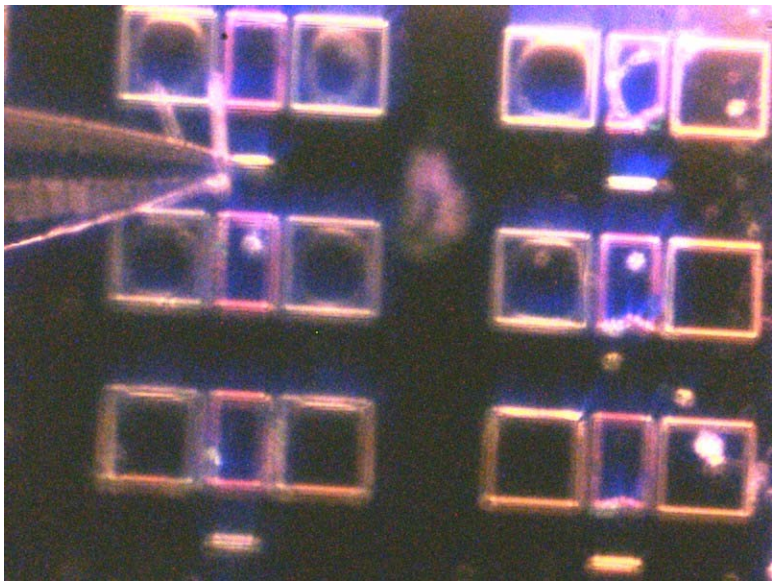

Figure 2.12 Here the probe is pulled back slightly so as to drag the belt across the surface of the electrodes. This was done in an attempt to mechanically strip the belt from the end of the probe. However, the mechanical forces were not strong enough since the belt is still in contact with the probe tip.

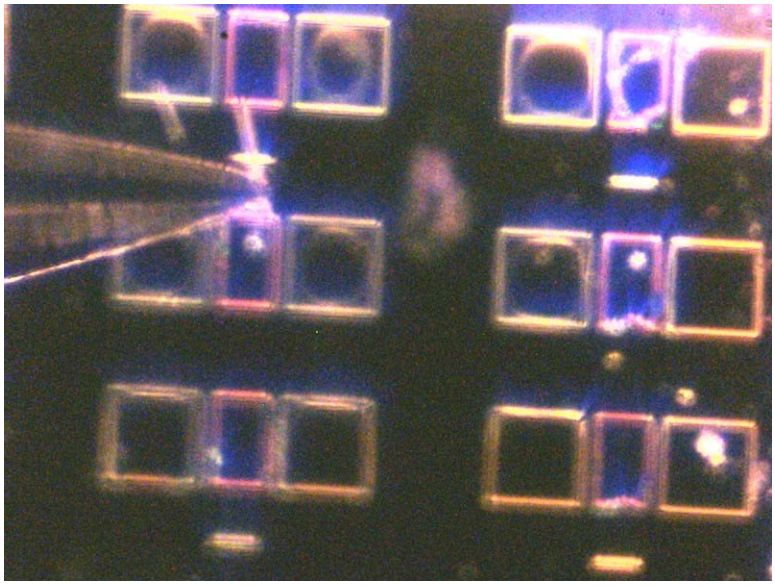

Figure 2.13 The probe is pushed forward again after attempting to remove it mechanically. It can be seen that the mechanical forces are capable of pivoting the belt around the contact point between the belt and the probe. As a result, the belt is no longer perpendicular to the device electrodes. However, since this is an acceptable position for

the belt, and it is not necessary that it be ideally configured for measurement purposes, it was left as is.

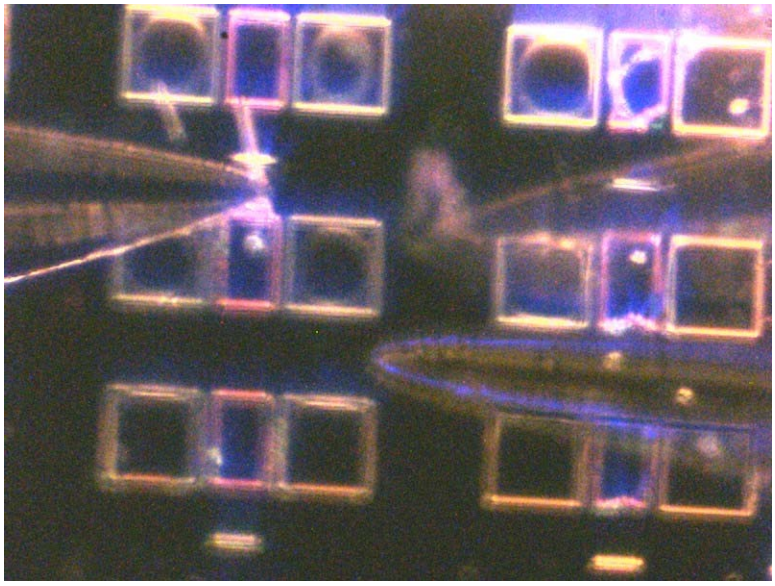

Figure 2.14 The second probe is being brought in from the right hand side. This probe was used to discharge the static electricity and release the structure.

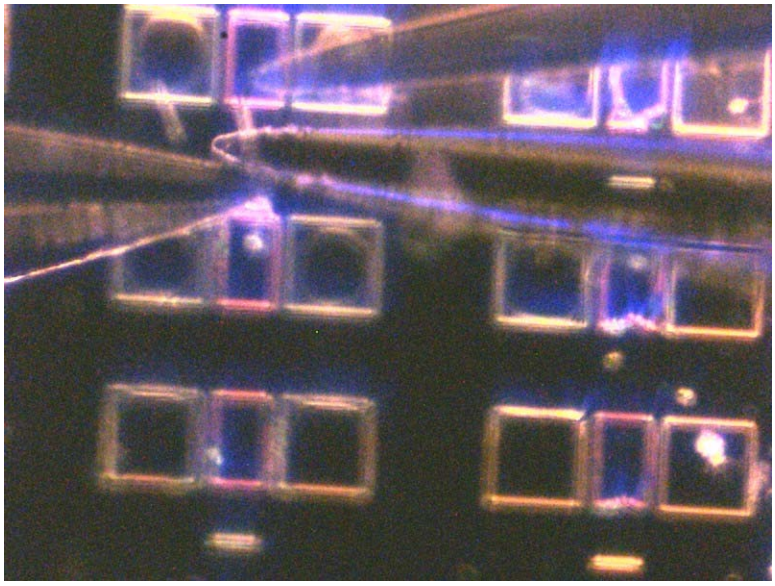

Figure 2.15 The second probe (discharge probe) is brought in closer to the belt. The actual probe and its reflection can be seen in this frame.

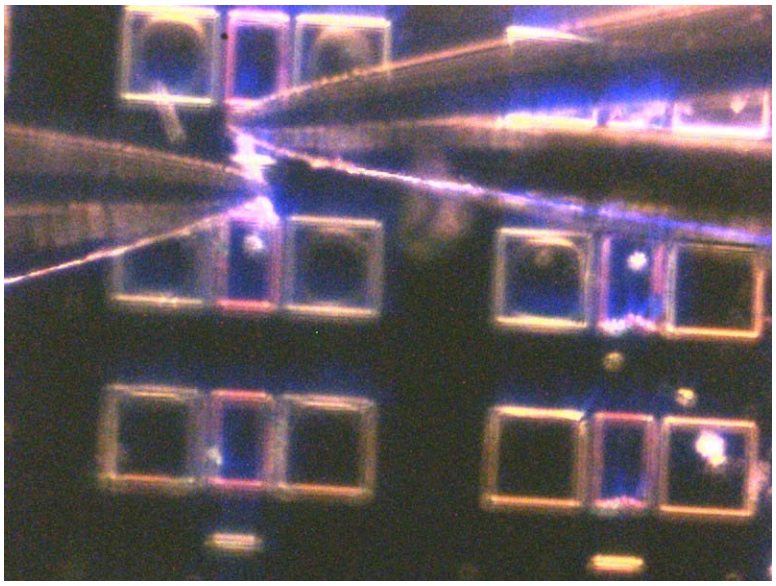

Figure 2.16 Both probes are now touching the ZnO. As a result, all three components should share the same potential. The belt should no longer be attracted to one (or either) of the probes.

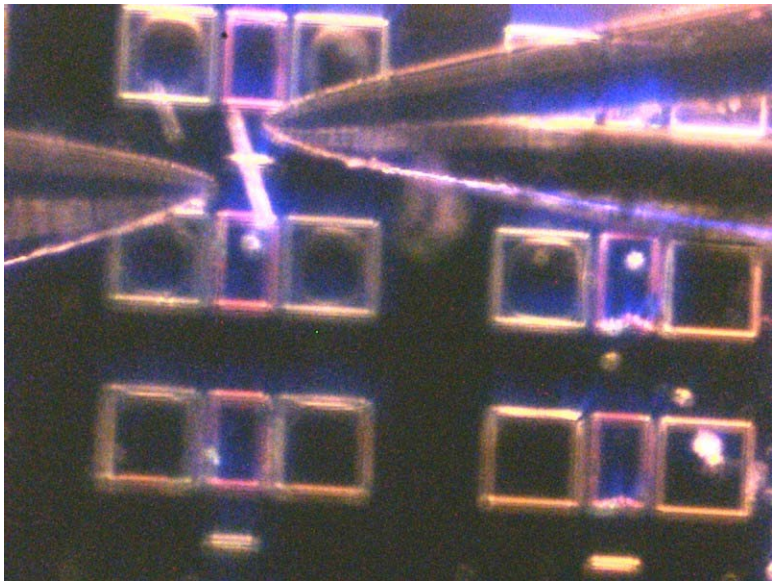

Figure 2.17 Both probes have been pulled back away from the ZnO nanostructure. It can be seen that the ZnO is sitting alone across a trench.

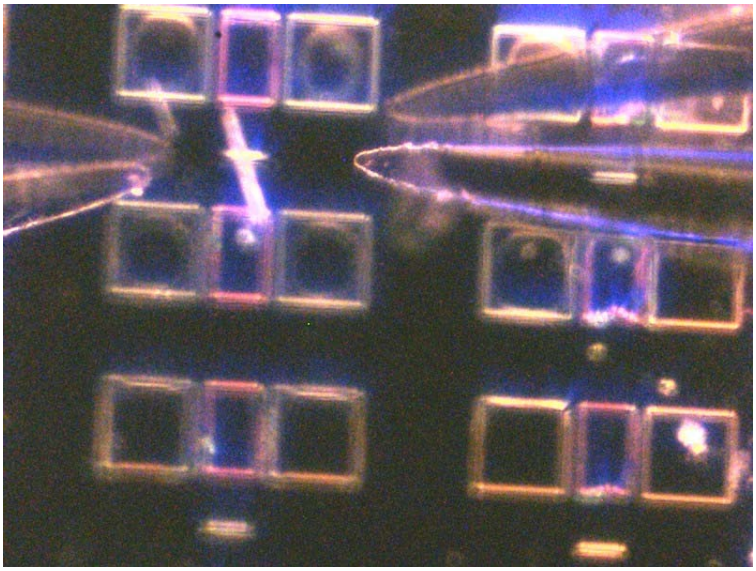

Figure 2.18 This is the last frame of the movie showing both probes suspended in air above the nanostructure they were used to manipulate.

One of the main drawbacks of this technique is that it utilizes direct contact for manipulation. As a result, the nanomaterials can be damaged, shattered, or contaminated, which can interfere with device functionality. In addition to contamination, this technique loses some of its utility when attempting to manipulate extremely small nanomaterials. The smallest nanostructure successfully demonstrated was approximately 700-800 nm wide. It is possible to go smaller; however, probes with a finer tip radius and an optical microscope capable of higher magnification would be necessary. It is the length of the nanostructure that is the limiting factor with this technique, not the diameter. When the nanobelt is shorter than the tip radius of the probe, picking it up is relatively easy; however, there is not enough surface area left to bring in a second probe to dissipate the charge. Probes with finer tip radii could provide a larger contact patch on the nanostructure to increase the usefulness of this technique. Cascade does make similar probes with a 60nm tip radius that would be more suited for manipulating nanomaterials. A technique utilized for manipulating smaller nanostructures will be discussed in the next section.

2.1.2 Focused Ion Beam Assisted Manipulation

One of the key limitations of the above technique has to do with the size of the structure capable of being manipulated. Another has to do with the lack of knowledge a researcher has about the nanomaterial being integrated into his or her device. As stated in Chapter 1, nanobelts provide a unique opportunity to study a variety of crystal orientations and confinement effects along different facets of the structure. In order to do this, some form of characterization is required before or after manipulation. If characterization is done after manipulation, the device is subject to a statistical chance that one orientation will be selected over another. Even though the crystal orientation can be characterized later, it limits control over a decisive direction for a research project. For commercial applications, if one orientation is deemed preferable relative to another, characterization prior to manipulation would be necessary.

The following technique utilizes a Hitachi HF-2000 field emission (200kV) transmission electron microscope (TEM) in conjunction with an FEI NOVA Nanolab 200 focused ion beam (FIB) microscope in order to successfully manipulate ZnO nanobelts. Synthesized ZnO nanobelts are first dispersed onto a copper TEM grid which is inserted into the TEM in order to record diffraction patterns and other crystallographic information. The nanobelts' locations are then mapped by comparing the real image in the TEM to the belts respective position recorded in a series of SEM micrographs. The copper grid is then transferred to the FIB, which is retrofitted with a Kleindiek micromanipulator probe station that was used to manipulate the nanobelts.

FIB is a tool that somewhat resembles the operation of a scanning electron microscope (SEM). However, while an SEM uses an electron beam to image the surface of a sample, the FIB uses a focused beam of gallium ions. A liquid metal gallium ion source (LMIS) is heated up until the gallium metal wets the tip of a tungsten filament. An electric field is applied to the end of the tip in order to ionize the gallium resulting in field emission of ions. The gallium ions are accelerated through a series of

electromagnetic lenses and focused onto the surface of a sample. Unlike SEM, FIB is inherently destructive to a sample. In addition to generation of secondary electrons, backscatter electrons and x-ray photons from the sample, when high energy ions strike the surface, atoms will also be sputtered away. This sputtering process is utilized as a tool for micromachining and nanofabrication at submicron dimensions.

In addition to its machining capabilities, FIB is also useful for depositing material via ion beam assisted chemical vapor depositions (CVD). FIB-assisted CVD occurs when a gas, in our case an organic platinum precursor supplied by FEI, is introduced inside the vacuum chamber and allowed to chemisorb onto the samples surface. By scanning a local area with the ion beam, the gas precursor reduces into Pt metal where the ion beam interacts. In addition to Pt, FIB has also shown to be useful for depositing other materials like, tungsten, silica, carbon and a variety of other insulating, semiconducting and conductive materials[109]. The FEI NOVA used in these experiments has an SEM column positioned vertical in the chamber in addition to the ion gun tilted 52^{o} relative to the electron gun—this is a dual beam system.

Inside the vacuum chamber, a Kleindiek micromanipulator was utilized to contact a nanobelt with a Picoprobe model T-4-10-1mm tip, and in conjunction with the FIB-assisted CVD, "weld" a bit of Pt between the tip and the nanobelt in order to create a physical bond. Once the bond was created, the nanobelt was lifted away from the copper grid and positioned just above a series of contact electrodes. Once the belt was in position, FIB was used again to mill the physical bond away, leaving the nanobelts in its desired location across the device electrodes. An example of the process is shown below in a series of SEM images that were taken during the manipulation experiment.

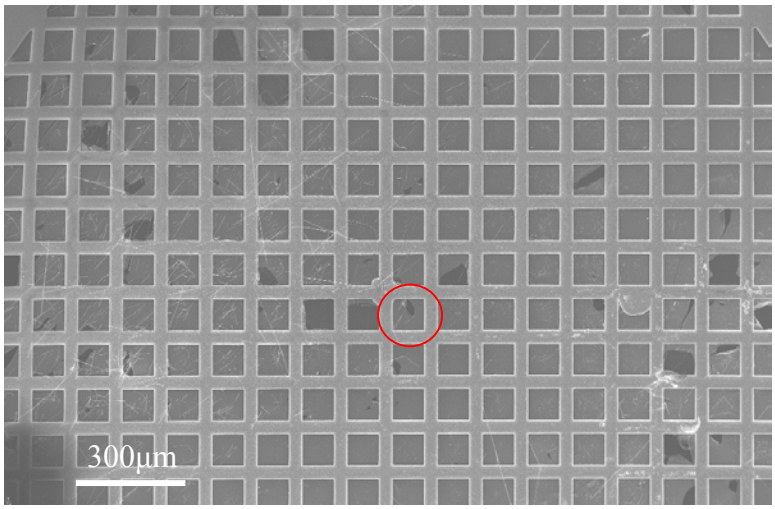

Figure 2.19 This is an SEM micrograph of the copper TEM grid with nanobelts dispersed across the surface. The red circle identifies the area from which two polar surface nanobelts lie, one of which will be successfully manipulated using the Kleindiek micromanipulator.

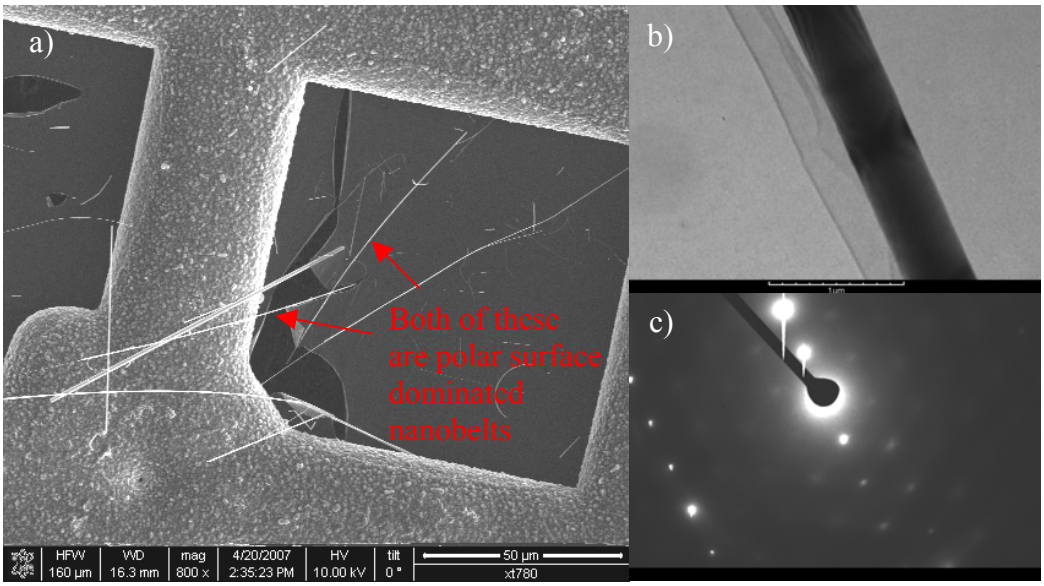

Figure 2.20 (a) Here is the region circled in the above image. Red arrows point to two polar surface belts. (b)TEM image from one of the nanobelts. (c) Diffraction pattern showing six-fold symmetry.

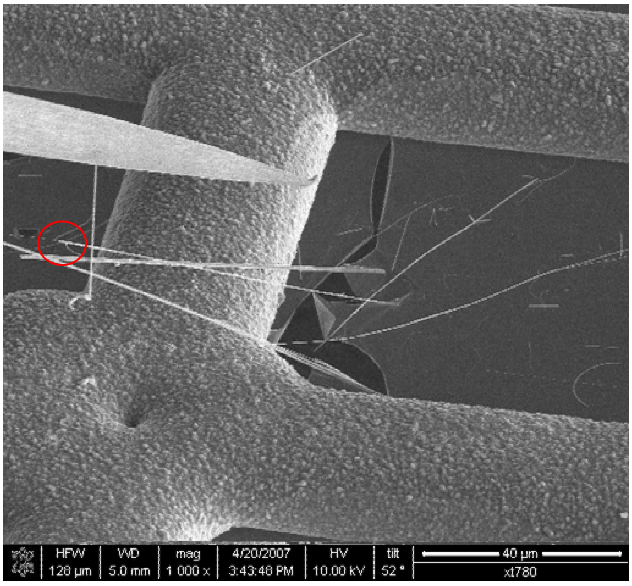

Figure 2.21 In this step the copper grid is tilted 52^{o} relative to the SEM column so that it is perpendicular to the ion gun for Pt deposition. This also enables more effective positioning of the probe since the SEM column can be used in conjunction with the ion beam to monitor the Z-position as well as the X and Y position of the probe. The red circle shows where the probe will contact the nanobelt in order to weld them together.

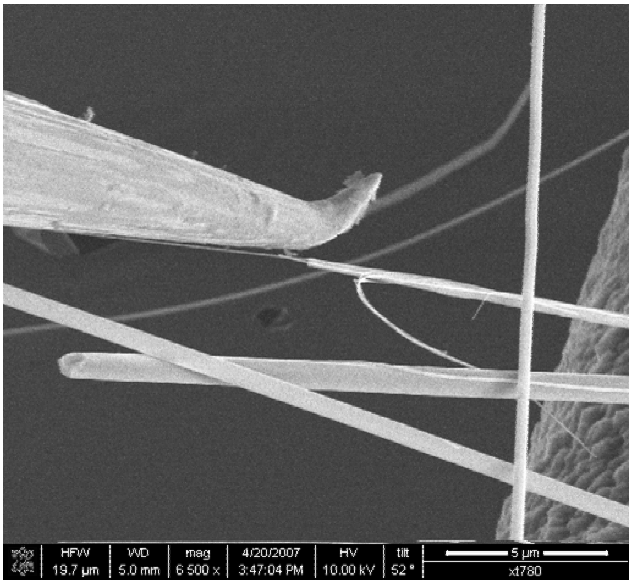

Figure 2.22 Zooming in on the back of the nanobelt, the probe has been positioned just to the side.

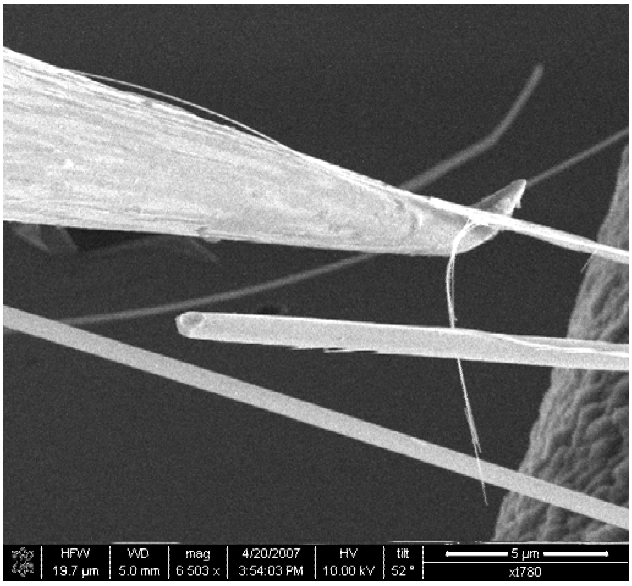

Figure 2.23 The probe is now in direct contact with the nanobelt. The slight hook in the probe is used to cradle the belt for Pt deposition.

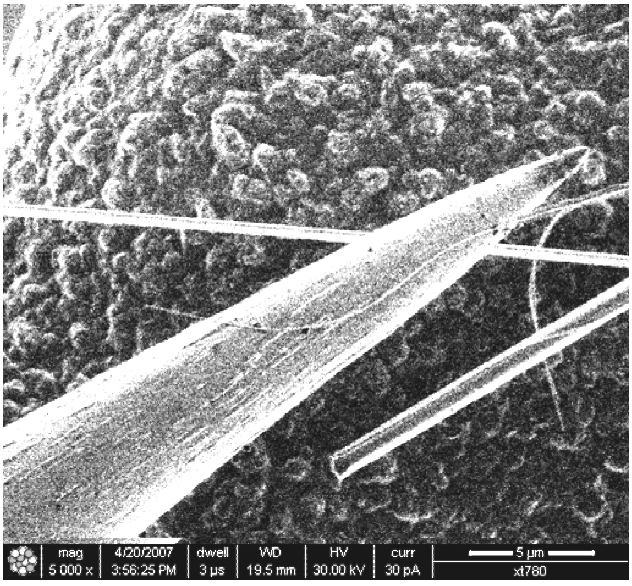

Figure 2.24 This is a low current ion beam image showing exactly where the probe is positioned relative to the nanobelt in the X-Y plane.

Since the SEM images from above are taken 52^{o} from normal, this snapshot was taken to ensure everything was lined up properly just before deposition. The ion beam snapshot was only taken while looking at a very small region of the belt. This was done to ensure

that no sputtering or contamination occurred in any regions of the belt that were to be used in the nanobelt device.

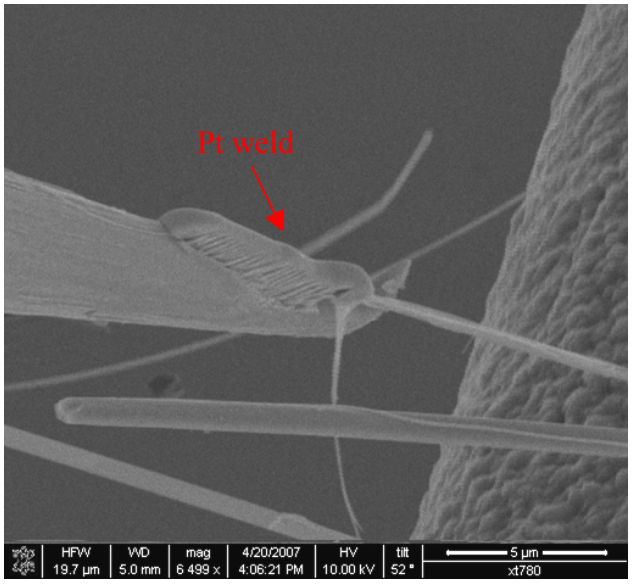

Figure 2.25 At this point the organic platinum precursor was introduced inside the chamber through a thin needle inserted just above the probe/nanobelt. A small rectangle of Pt was deposited using software to control the rastering of the ion beam. A thin weld of Pt can be seen connecting the nanobelt to the probe tip.

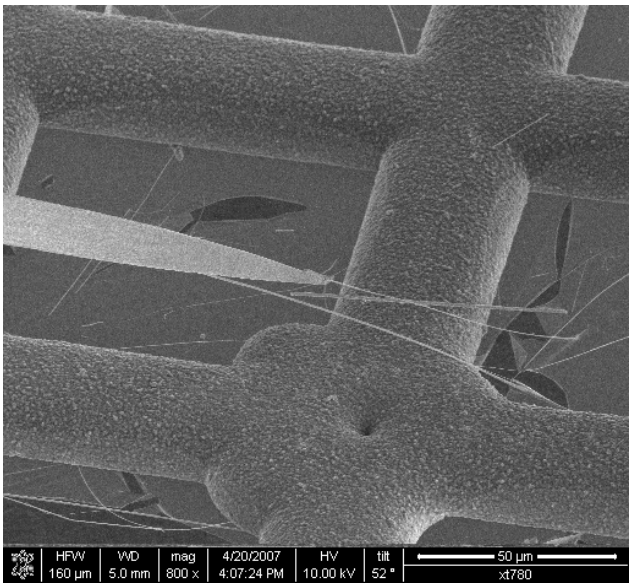

Figure 2.26 Here the magnification of the SEM was reduced in order to prepare to move the tip with the micromanipulator positioning system. As long as the belt is secured to

the probe tip, it will be possible to overcome any weak interaction forces between the nanobelt and the copper grid by lifting it away.

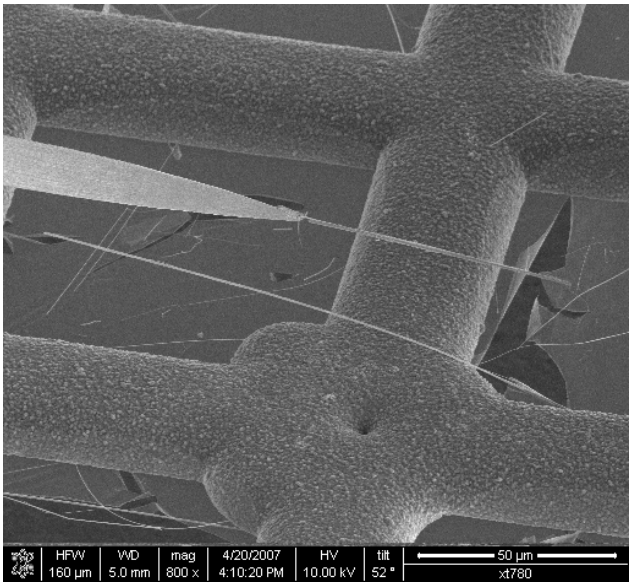

Figure 2.27 At this point the micromanipulator was retracted from the grid. The nanobelt caused a small piece of formvar film to tear back from the grid where the belt was weakly attached.

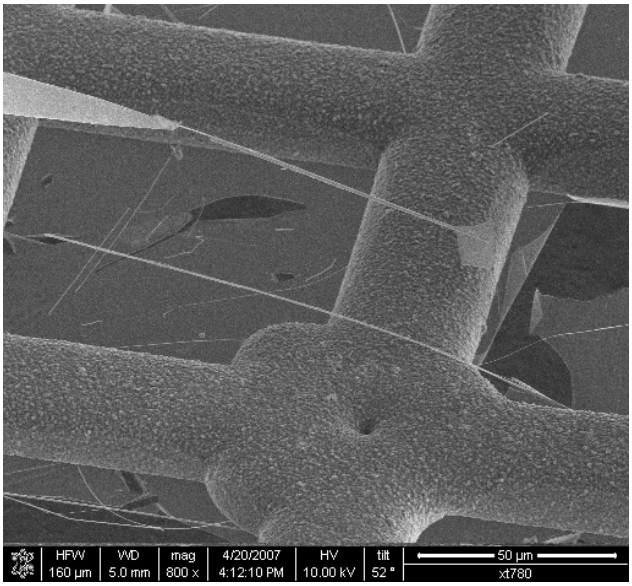

Figure 2.28 As the probe continues to retract, the formvar tears and a small square piece of polymer is observed to be stuck to the free end of the nanobelt.

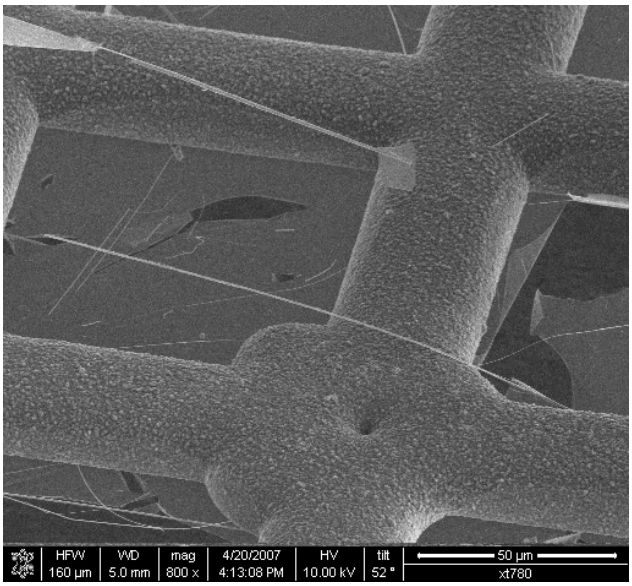

Figure 2.29 At this point, the nanobelt was no longer in contact with the copper grid and was completely free to be repositioned across the prefabricated device electrodes.

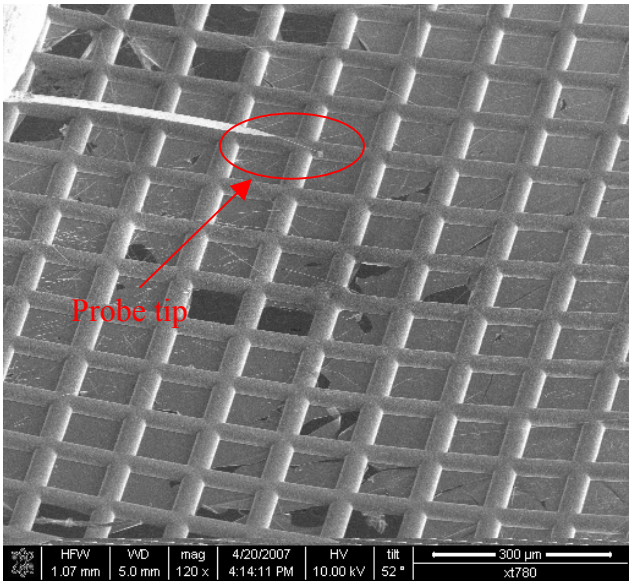

Figure 2.30 The speed of the manipulator was increased and was agitated violently to attempt to detach the nanobelt from the probe. This was done to test the robustness of this process.

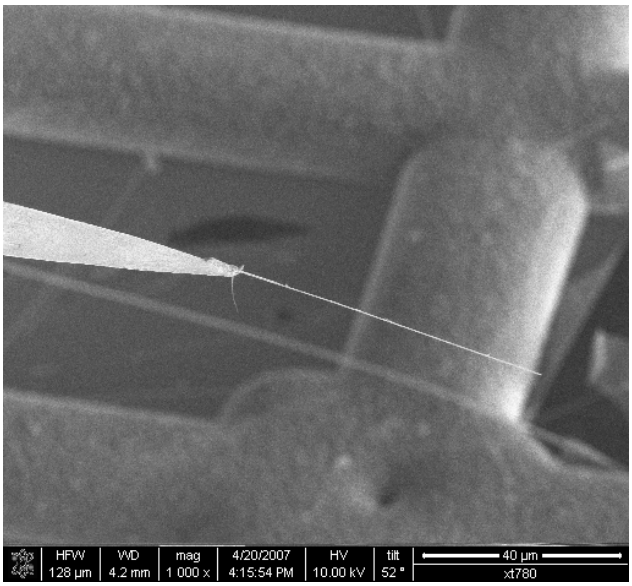

Figure 2.31 It seems that during the "wiggling" process, the small piece of polymer that was stuck to the free end of the belt was shaken loose.

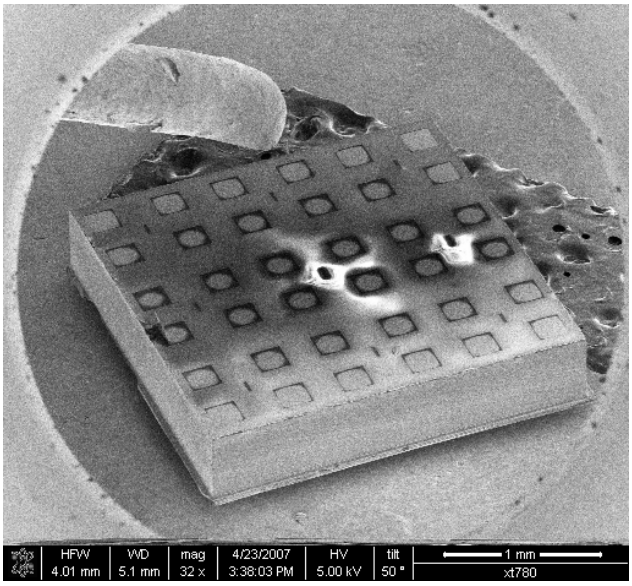

Figure 2.32 A 3X3 array of prefabricated device electrodes were positioned beneath the probe in order to complete the final steps of manipulation by severing the Pt weld.

Unfortunately, due to a severe amount of charging that occurred in the SiO_2 insulting layer that is a major component of this device architecture, it was difficult to obtain any images during this step in the process. The final image showing the nanobelt across two freestanding gold flaps can be seen below.

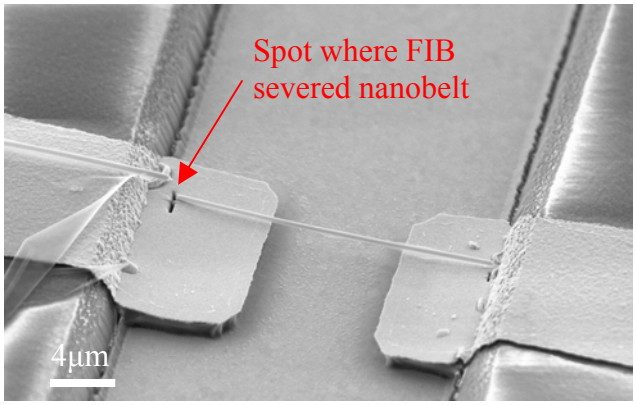

Figure 2.33 Here is the final resting position of the polar ZnO nanobelt. It is lying across two gold electrodes and ready for the final fabrication steps to prepare it for testing. A small mill line in the underlying gold electrode can be seen where the FIB was used to sever the nanobelt from the Picoprobe.

Very low beam currents (~10pA) were used and only the region being milled was ever imaged with the ion beam. The remainder of the nanobelt was kept out of the field of view of the ion beam in order to prevent any possible contamination from the gallium ion source. The actual utility of such a device will be discussed in subsequent chapters; only manipulation is being addressed here.

FIB-assisted CVD and milling has been demonstrated as a useful tool for manipulating nanostructures. Pre-characterizing the as-synthesized material in TEM prior to manipulation has been shown to complement this technique and enhance its utility. Unfortunately, there are still drawbacks that leave less brute force techniques to be desired. It is still a direct contact process, and possible contamination can be introduced into the system via the Picoprobe. In addition, while platinum metal only

decomposes where the ion beam interacts, the methyl platinum precursor ends up coating the entire area around the nanostructure even in regions outside the field of view of the SEM. It is unknown if these functional molecules have any effect on the surface properties of the nanobelt. If defects or vacancies are created, this would likely disrupt the natural electronic properties, resulting in measurable data that is false and device performance that is undesirable. Finally, this technique required a lenghty time commitment. Manipulating one structure could take a full day or longer since it requires the use of three sophisticated tools (TEM, SEM and FIB).

2.2 Non-Contact Manipulation of Nanomaterials

The nature of the techniques just described can introduce contamination or cause damage to the nanostructure. In addition to the techniques used above, others are also susceptible to contamination from an AFM probe tip or the viscous media used in dielectrophoresis and optical trapping. This becomes a concern when considering the high level of cleanliness necessary for maintaining high performance and yield in the MEMS, NEMS and CMOS systems being integrated with these nanomaterials.

2.2.1 Acoustic "tweezers" for Non-contact Manipulation

Impulsive Stimulated Thermal Scattering (ISTS) utilizes a pulsed laser along with beam-shaping optics in order to induce complex acoustic wave patterns in a thin film. Pulses of light from an excitation laser are focused through a series of lenses onto a beam-shaping optical mask (diffraction grating), causing the light to diffract into an array of line sources. The two primary diffraction orders then pass through an achromatic lens pair in order to focus the converging beams onto the sample creating an interference pattern on the sample surface. Absorption of the light in the surface layer of the film results in local heating and thermal expansion defined by the interference pattern. The thermal disturbances launch acoustic waves that consist of surface modes and bulk waves that travel into the interior of the sample[110]. Through the utilization of the diffraction

grating it is possible to control the propagation direction of an acoustic wave and tune its acoustic wavelength. This technique is typically used for the purpose of characterizing high frequency acoustic propagation in thin films[111]. Here, it has been adapted to generate acoustic waves in micro/nanomaterials in order to induce physical, controllable motion. This technique is non-contact and does not require the use of a liquid medium. Figure 2.34 schematically illustrates the ISTS tool.

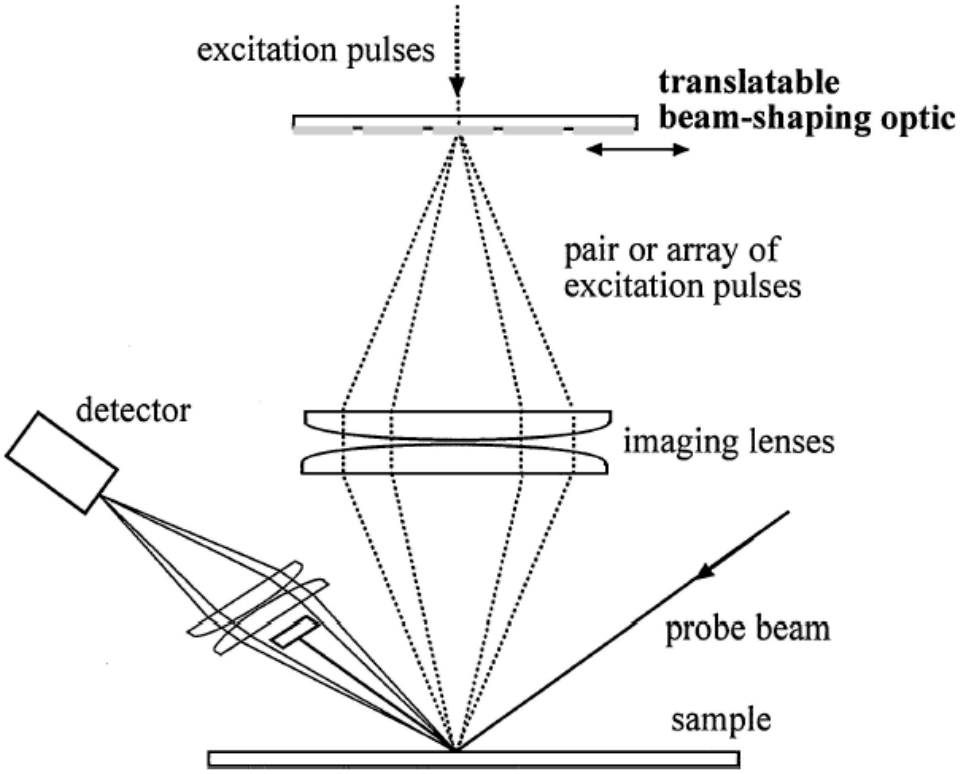

Figure 2.34 Schematic diagram of the ISTS tool.

2.2.1.1 Experimental Set-Up

For this specific experimental set-up, the excitation laser pulses with an average on/off frequency of 1500Hz and a pulse length of 500psec. The average power from the excitation laser is tunable from 0.97mW to 6.72mW. In order to optimize the behavior, copper is deposited as an optically absorbent thin film capable of efficiently absorbing

the 532nm optical wavelength of the excitation laser as heat. Unless otherwise specified, the intensity for all experiments was chosen to be 2.77mW since it was determined to be the maximum laser power that can be used without causing damage to the copper layer. Extremely high intensities will result in the melting of copper causing permanent and irreversible damage. This would be an undesirable effect when touting the non-destructive nature of this manipulation technique as a benefit. The ISTS tool used for these experiments enables acoustic wavelengths ranging from 5μm to 25μm. Unless otherwise specified, all results were obtained by fixing the acoustic wavelength at 8.2μm. An example of the line source spacing can be seen in Figure 2.35. This image was created by increasing the power of the excitation laser to the maximum 6.72mW in order to intentionally melt the copper and burn an image of the line source into the thin film. The SEM micrograph depicts the copper surface after re-solidification.

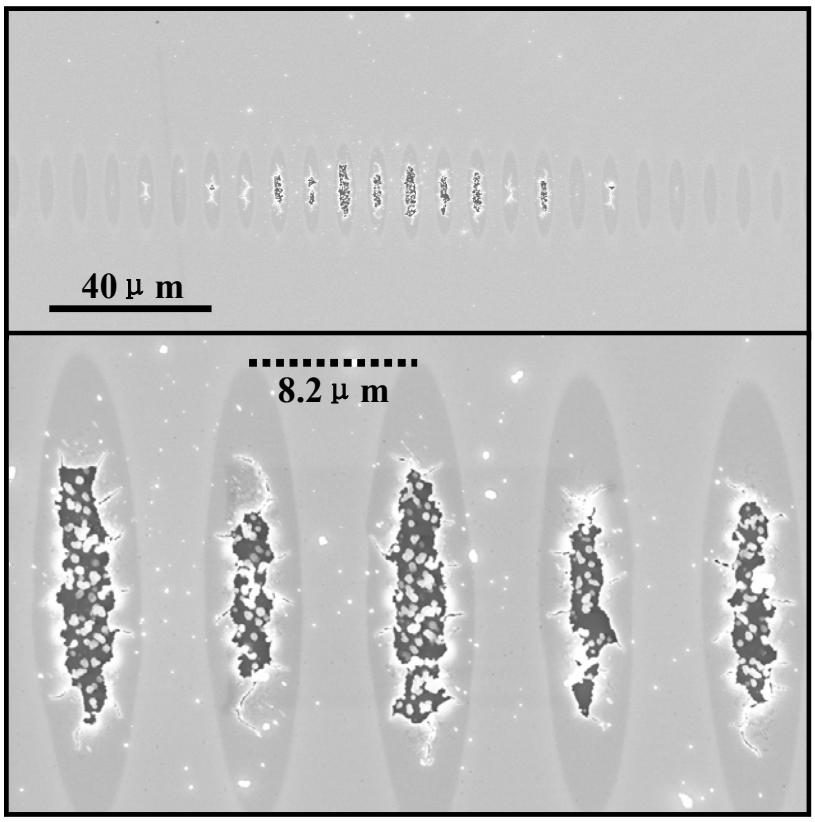

Figure 2.35 SEM micrograph of the line source used to generate the 8.2 micron acoustic response in the copper surface. This was burned in by the 6.72mW excitation laser.

ZnO nanobelts were used for the following experiments in order to demonstrate the usefulness of ISTS as a manipulation tool. Four substrates were prepared in order demonstrate the utility of the technique and prove the mechanism responsible for driving the manipulation. First, ZnO nanobelts were grown in a single zone tube furnace using a PVD process[112]. The bottom-up synthesized nanomaterials were then dry-dispersed onto a silicon wafer coated with 400nm of PECVD Si_3N_4. The Si_3N_4 layer was not necessary; such wafers were readily available for these experiments. Once the material was dispersed, 75 nm of Cu was sputtered on top in order to coat the surface of the nanobelts and the nitride wafer. The second sample was prepared much in the same way as the first; however, this time 75nm of aluminum was deposited instead of copper. The third sample was made by sputtering 75nm of copper onto the nitride-coated wafer prior to dry-dispersing the nanobelts. In this situation, only the nitride wafer was coated with copper while the uncoated nanobelts rested on the copper surface. The final wafer was created by removing some of the copper-coated nanobelts from the first wafer and placing them onto a bare nitride coated wafer. Once the samples were prepared, each was investigated separately with ISTS in order to quantify the behavior of the nanostructures.

The excitation beam in ISTS is fixed at a specific position inside the instrument (much like in SEM). The sample was placed on a stage capable of moving in the X, Y, and Z directions with a minimum controllable step size of 1.25μm. Z-positioning was used to ensure the wafer was set at the focal plane of the excitation laser, while X and Y movements were used to seek out appropriate nanobelts for testing as well as guide the manipulation experiment once one was identified. Each of the experiments were conducted in the following fashion: First, a burn pattern was made using the maximum power of the excitation laser. This defined the precise location of the line-source relative to a cross-hair at the center of the image. A belt was identified by scanning the surface with the optical microscope integrated with the ISTS. Once a candidate structure was

found, the stage was used to center the nanobelt in the path of the excitation laser. The excitation laser was turned on and allowed to interact with the belt, causing it to shift. The light source reflecting and scattering off the surface of the wafer/structure would created spots in the camera's image that agitated as long as the belt was moving. Once the diffracted light stopped agitating, it was determined that the structure had come to rest and the beam was turned off. The stage was moved to position the belt back into the path of the excitation laser for the next step in the manipulation process. A still image of the initial and final position was captured from the computer screen, or a movie file was used to record the entire experiment. Individual frames were used to analyze the results described below.

2.2.1.2 Results

All of the results, unless otherwise stated, were obtained using the first sample that had copper sputtered both on top of the ZnO belts, as well as the nitride substrate. Figures 2.36, 2.37 and 2.38 show a series of before, during and after images of a single microbelt as it was moved from left to right.

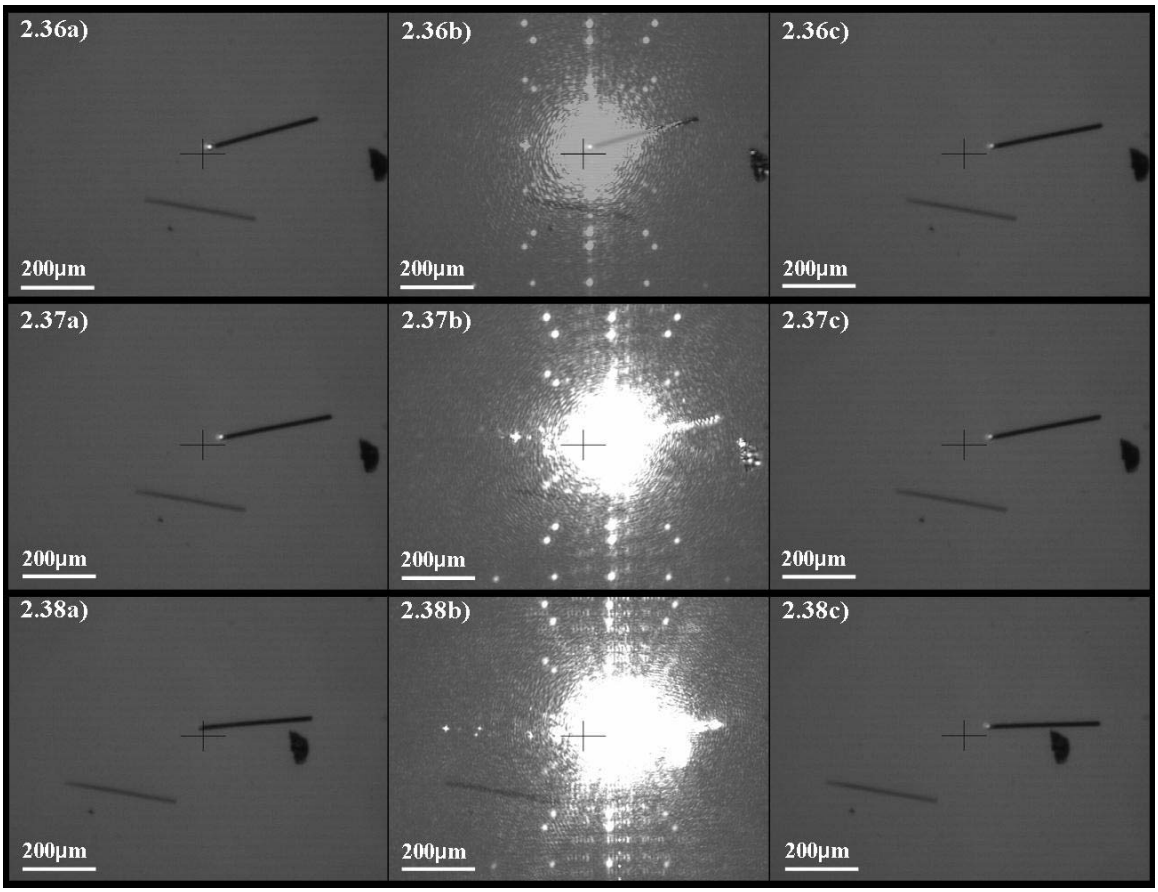

Figures 2.36, 2.37, 2.38 Three separate manipulations seperated into their individual steps. (a) Initial position of the belt prior to turning on the excitation laser. (b) Excitation laser is turned on and is generating acoustic waves. (c) Final position of the belt once the laser has been turned off.

Images 2.36a, 2.37a and 2.38a show the initial position of a ZnO belt prior to three subsequent manipulation experiments. 2.36b, 2.37b, 2.38b are snapshots of the beam once it's turned on and fired at the nanostructure. 2.36c, 2.37c, and 2.38c depict the final resting position of the belt in each experiment once the excitation laser was turned off. In order to continue pushing the belt across the surface, it was necessary to move the stage and reposition the belt underneath the beam. In Figures 2.37a and 2.38a, the belt's initial position was intentionally different from its position in 2.36a in order to determine if travel distance was fixed or if it depended on some other parameter. It can be seen when comparing figures 2.36c, 2.37c, and 2.38c that the total travel distance of the belt is dependent on its initial position. In 2.36c the belt moved ~62μm, in 2.37c it moved ~25μm, and in 2.38c it moved ~71μm, all while maintaining the power of the laser and acoustic wavelength constant. It is important to note that the final resting position in each of the experiments was the same relative to the cross-hair in the micrograph. An analysis of this behavior will be given below.

The next set of figures shows the same microbelt during six subsequent movements to the right, followed by six movements back to the left. In the series of images it can be seen how the microbelt shifts relative to two prominent features nearby. Red hash marks identify the previous position of the structure in each frame and are used to track the progress of the belt as it is pushed along.

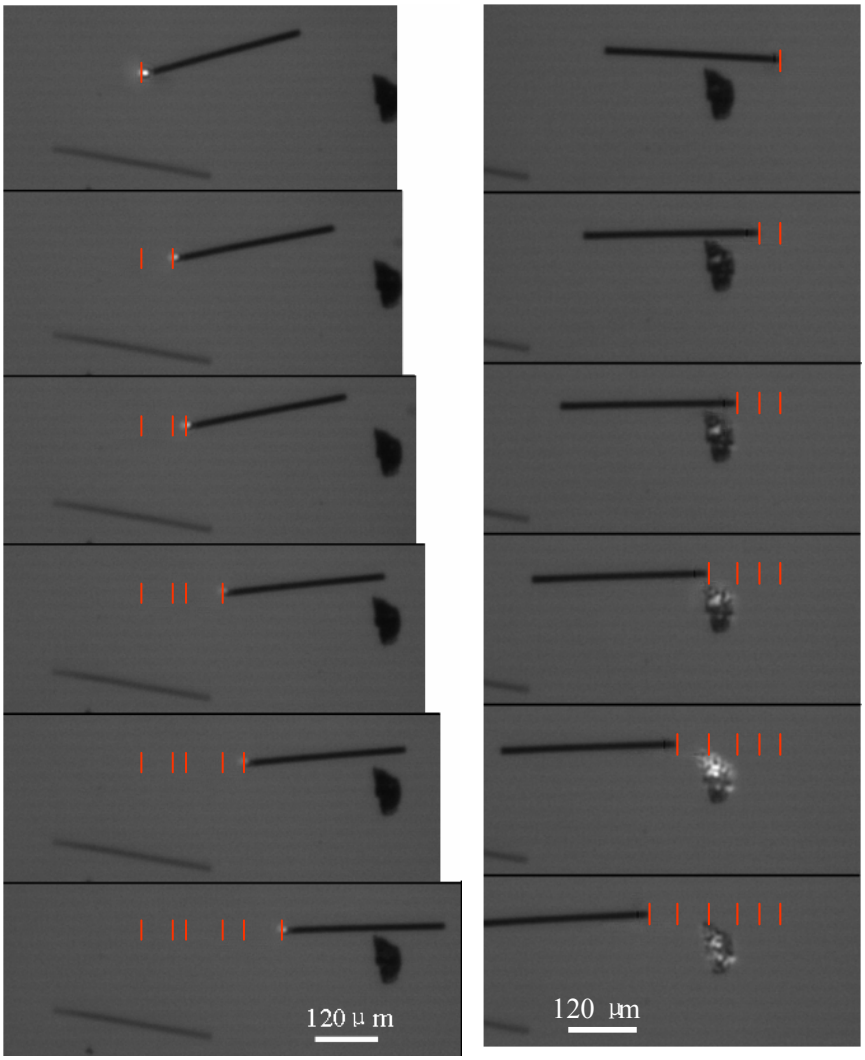

Figure 2.39 (a) Acoustic manipulation of the microbelt toward the right (b) Manipulating the same microbelt to the left.

In addition to the microbelt in Figure 2.39, other microstructures and nanobelts were successfully manipulated. The next figure shows two snapshots taken from a video that was used to capture the entire manipulation process. The power of the excitation laser was increased to the maximum 6.72mW in order to determine how acoustic intensity effected the overall travel distance. Only the initial and final positions are shown even though five steps were used to move it the total distance from Figure 2.40a to 2.40b.

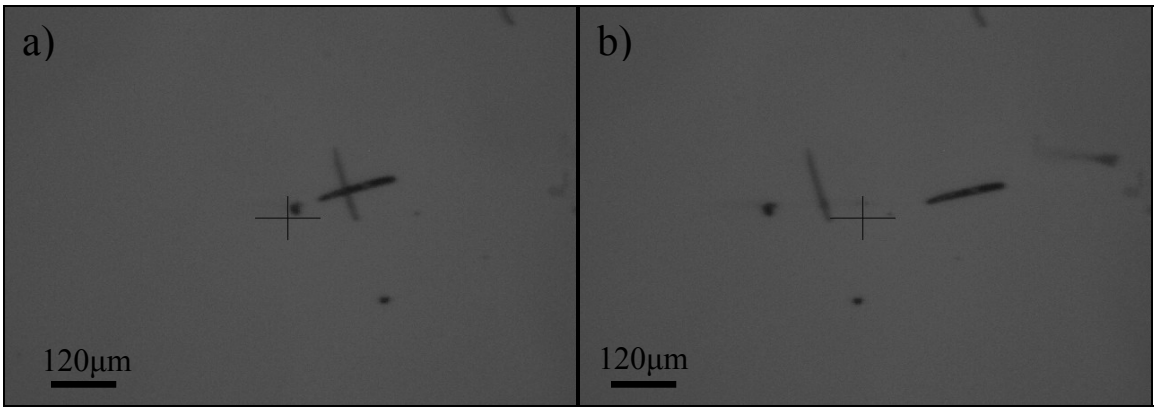

Figure 2.40 (a) Initial position of the microbelt. (b) Final position after 5 manipulation steps.

In Figure 2.40a, the microbelt makes a cross between itself and an outline it formed during copper deposition. It seems that the microbelt unintentionally rotated ~90^{o} during transfer of the wafer from the sputtering chamber to the ISTS stage resulting in the cross. Figure 2.41 is an SEM micrograph taken after documenting the experiment. Though it was possible to find its outline as well as burn markings created by the excitation source, the actual belt seemed to have moved once again during its transfer from the ISTS stage to the SEM and was unable to be located. The belt's measurements were taken from the outline's image and measured in the SEM to be ~ 5.7μm wide and ~135μm long.

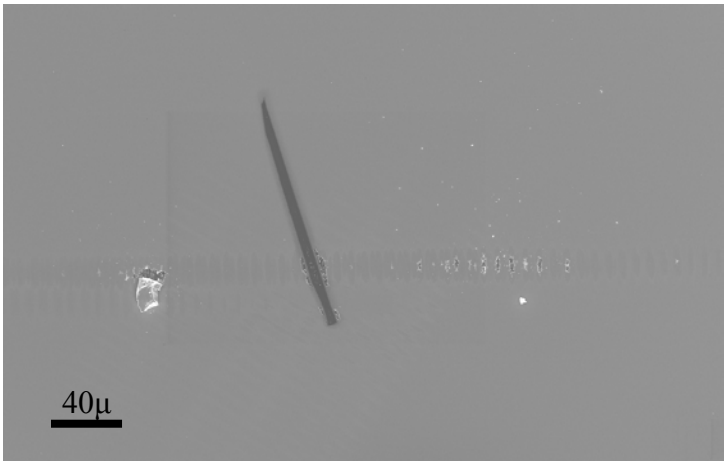

Figure 2.41 SEM micrograph of the copper shadow created by one of the microbelts manipulated using ISTS.

It should be noted at this point that control over the microbelt was only achieved from left to right in the horizontal plane and as long as the belt was parallel to the direction of acoustic propagation. Many attempts were made to position microstructures perpendicular to the acoustic field in such a way that only one free end was in the path of acoustic wave. This was done in an attempt to rotate the belt about a specific axis. Attempts to move the structure up and down in the vertical plane were also made; however, neither up and down control was obtained, nor was rotational control achieved.

In order to quantify the travel distance as a function of the excitation laser's power it is important to normalize the results. As stated above, the total distance traveled by the structure is not fixed by the intensity but is subject to its initial position relative to the total width of the acoustic field. Since the energy of higher order excitation spots are lower than the centermost ones, the intensity of the line source array drops off away from the center axis. As a result, the amplitude of the thermally-generated acoustic wave likely decreases as the structure moves towards the outer edges of the line source until there is no longer sufficient strain being generated to maintain motion. If a structure starts out at the edge of trailing acoustic energy, it will likely only move a short distance.

If its initial position is deep into the acoustic field, it will have to travel a great distance until it reaches the outer boundary. In addition, since the geometry and mass of the two structures discussed so far are not identical, they are not directly comparable. The travel distance will be defined as the distance from the centermost excitation spot to the final resting position of the trailing end of the structure. As a result, at 2.77mW of power, the belt moved ~60μm during one firing of the laser, while at 6.72mW it moved ~118μm. Figure 2.42 is a visual model of how acoustic waves are being generated in the nanostructure and resulting in mechanical motion.

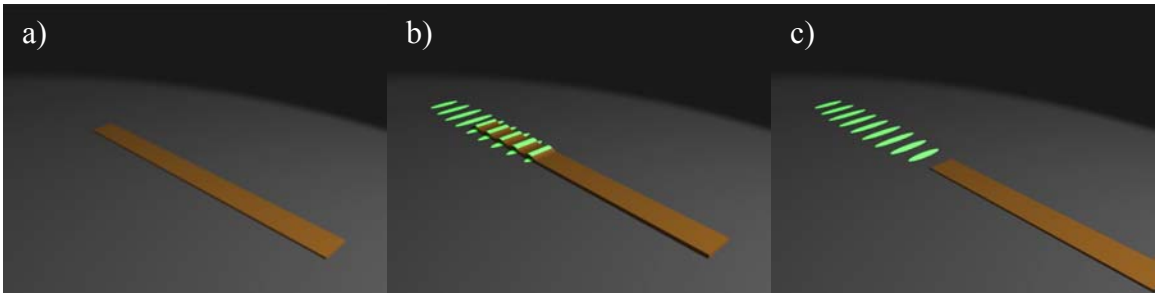

Figure 2.42 Model depicting how acoustic waves generated from the excitation laser induce motion in the structure. (a) Initial position of the belt before the excitation laser is turned on (b) Excitation laser is fired causing thermal expansion generating ripples in the structure (c) The acoustic wave pushes the belt until it is outside the acoustic field where it comes to rest.

In addition to large 1D microstructures, it was also possible to manipulate 1D nanostructures using this technique. Working with nano-sized belts resulted in a somewhat opposite behavior compared to that experienced with the microbelts. Up, down and rotational control was observed, yet no horizontal control was possible. In addition, movement in the up and down vertical plane required that the nanostructure be positioned perpendicular to the direction of motion, not parallel. Results from this are shown below while an analysis of the behavior is discussed in section 2.2.1.3.

Figure 2.43 shows two stills taken from a movie where a 1D nanobelt was manipulated. This time the structure runs perpendicular to the direction of motion and was manipulated a total of ~300μm in the vertical direction. Instead of turning the excitation laser on and off between movements, the laser was left on while moving the stage continuously in one direction. The following images were overlaid in such a way to compare features that remained idle while the nanobelt was being driven upward. Both the stationary features and the structure being manipulated are circled in each still to make this comparison more obvious. The moving structure is circled in white with some of the stationary features circled in black.

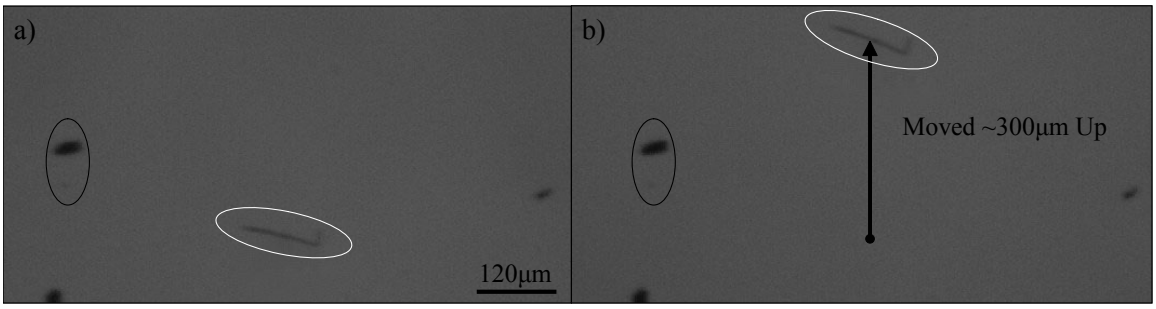

Figure 2.43 Overlay of images to demonstrate the manipulation of nanobelts in the vertical direction. (a) Initial position (b) Final position.

Figure 2.44 shows the same nanostructure, only this time its initial position was not directly perpendicular or parallel to the line source array, but rather up and to the right of it. This was done to see if it was possible to rotate the nanostructure as well as cause it to migrate in a direction other than parallel or perpendicular to the traveling acoustic wave. It can be seen from the figure that the nanobelt moved oblique in the X and Y plane closer to a small stationary particle nearby. In addition, it can be seen that the structure slightly rotated itself towards the particle.

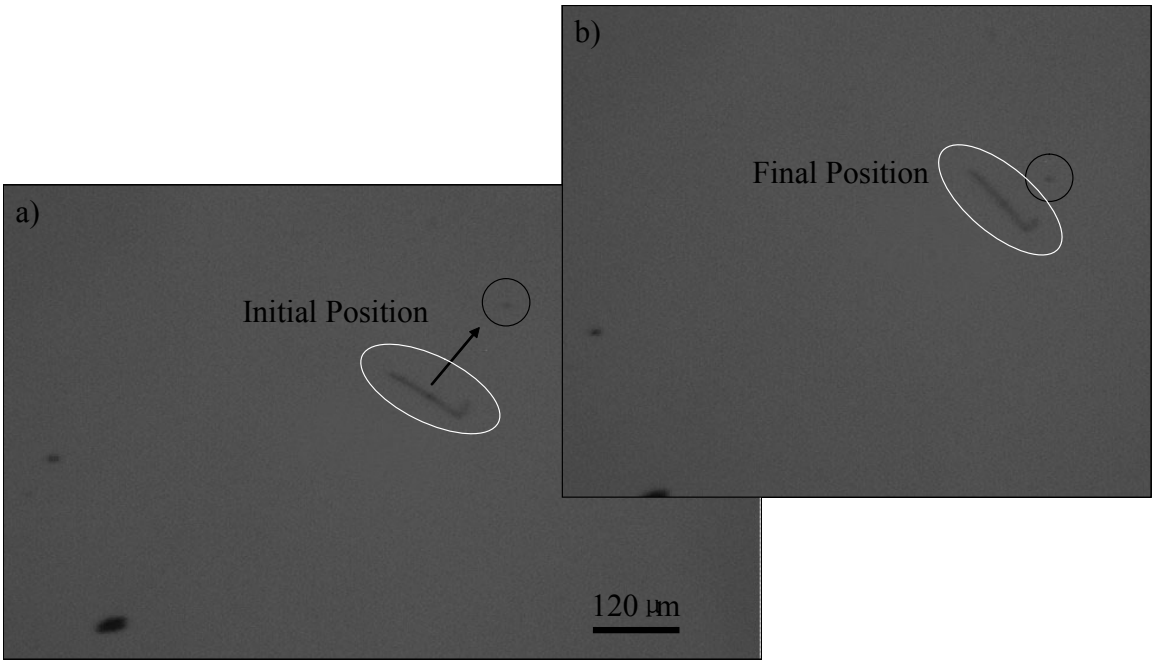

Figure 2.44 Nanostructure is pushed up and to the right. (a) Initial position (b) Final Position.

The same effect was achieved by positioning the nanostructure on the opposite side (up and to the left) of the acoustic field as shown in Figure 2.45. Notice that in this case the structure also rotates away in the opposite direction, as demonstrated in Figure 2.44.

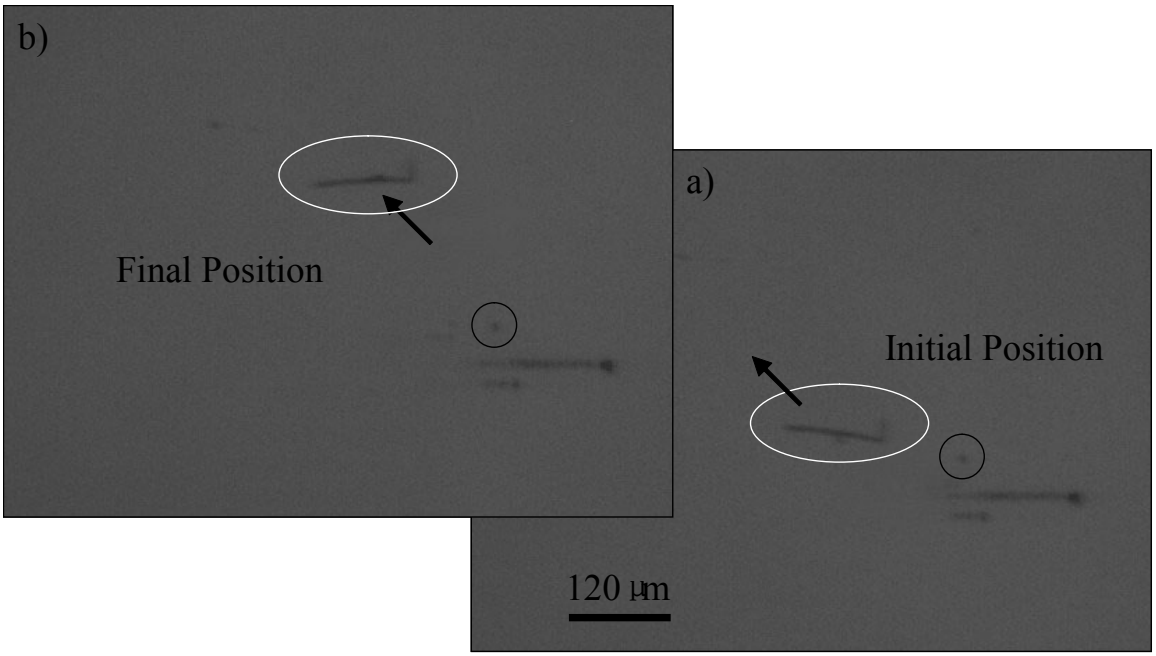

Figure 2.45 Manipulation and rotation of structure up and to the left, away from the acoustic field. (a) Initial position (b) Final position [Note that (a) is to the right of (b)]

After the experiment, the actual structure was identified in an SEM and can be seen in Figure 2.46. This was done by using burn marks as references when searching for the structure. The dimensions are somewhat inconclusive due to the way the structure is lying on the substrate. However, the width is assuredly sub-micron, with the thickness and width ranging somewhere between 300-600nm while the length is on the order of 100µm or more.

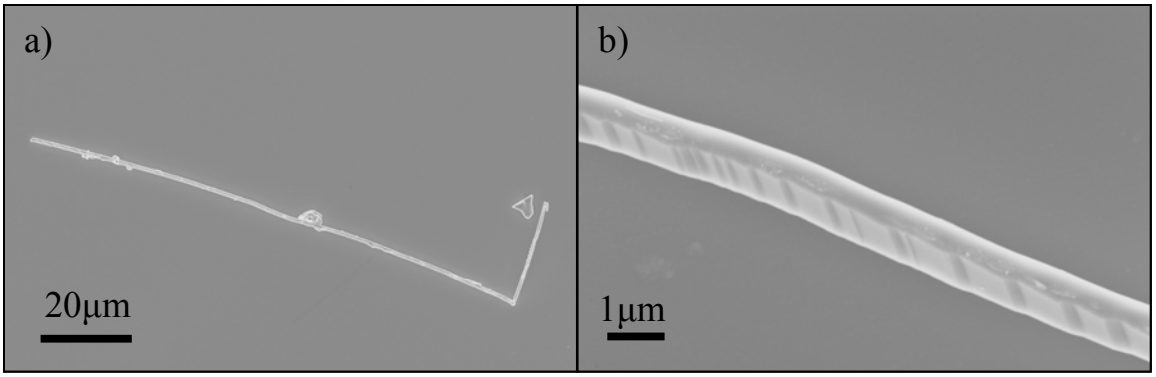

Figure 2.46 SEM images of the structure that was used in the above experiments.

The smallest nanobelt manipulated to date is shown in Figure 2.47. Unfortunately, it was never found in the SEM and the dimensions were never measured properly. Measurements taken from the optical image would put the length at ~20μm. Comparing the width of the belt to the structure from Figure 2.45 would result in a measurement decisively in the low nanometer range.

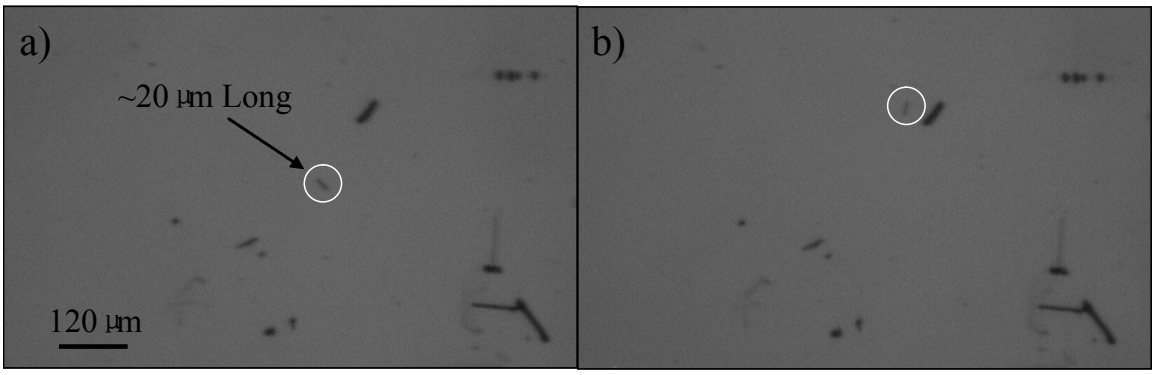

Figure 2.47 Smallest nanobelt manipulated to date.

2.2.1.3 Analysis and Discussion

One of the most immediate questions raised by these experiments is, "How can you be sure that the manipulation is acoustic in nature and not driven by photon momentum?" In order to prove that manipulation results from the propagation of acoustic waves and not momentum transfer from light, the same experiment was performed on a sample coated with 75nm of aluminum instead of copper. Due to its relatively high optical reflectivity, aluminum would be more likely than copper to convert photonic energy from the excitation laser directly into motion than. Recall that copper more readily absorbs green wavelengths. Looking at Figure 2.48, it can be seen when comparing the time dependent acoustic response in both copper and aluminum that there is more acoustic energy generated with the copper-coated materials than with aluminum-coated. As a result, the film in which the most prevalent motion was observed will indicate which behavior is dominant.

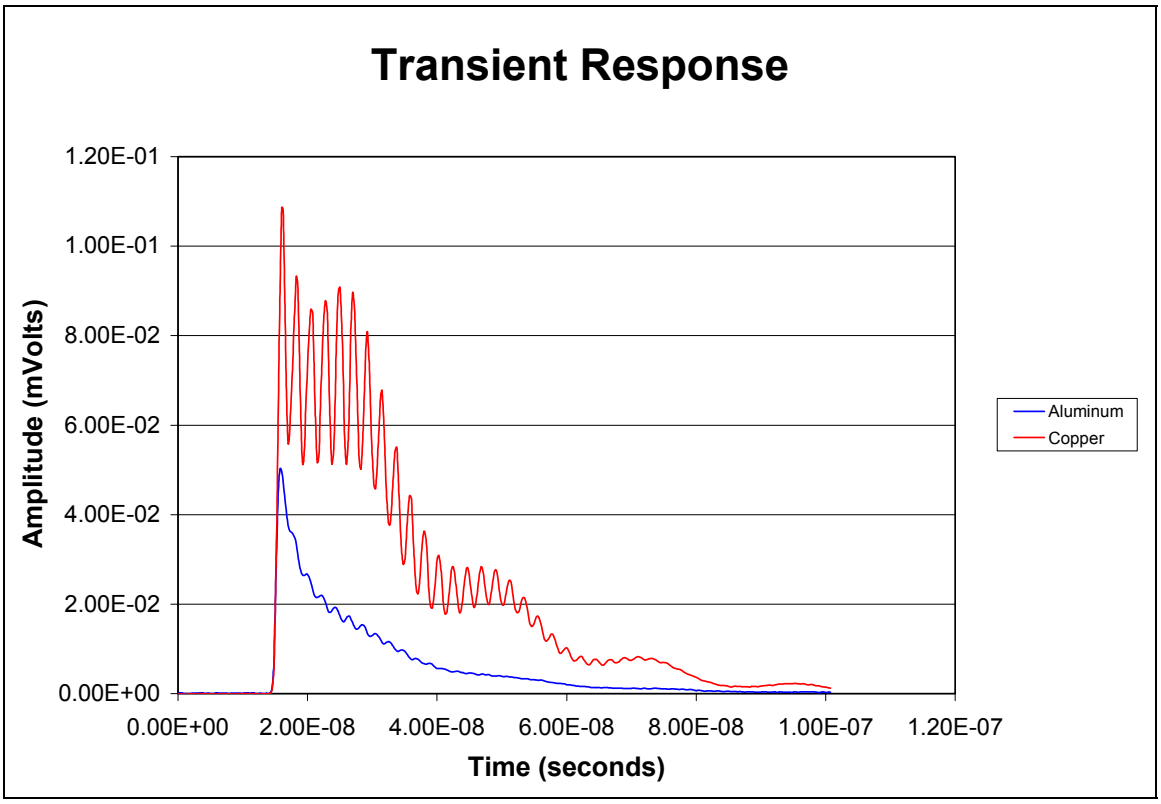

Figure 2.48 Acoustic response of copper thin films and aluminum thin fims on Si_3N_4.

No appreciable motion was observed in the Al coated ZnO belts. Even with the power of the laser increased to the maximum 6.72mW, the nanomaterials would only occasionally move very small distances and in an inconsistent and uncontrollable manner. This demonstrates that aluminum is not as efficient as copper when absorbing 532nm light as heat and generating acoustic waves. Since manipulation was more prevalent with copper coated belts than with the aluminum coated ones, acoustic waves must be the mechanism responsible. It should also be noted that even at the highest intensity, it was not possible to produce melting in the aluminum layer as was possible with the copper. Another consideration is that the excitation laser is positioned normal to the surface. Since there is little to no lateral component to the incident beam, any momentum transfer would simply push the belt into the substrate (assuming the belts have flat top surfaces).

Since each belt translation was observed to be reversible, the hypothesis of photon reflection from a unilaterally-slanted surface reflector was discarded.

Since the manipulation was determined to be driven by acoustic energy, questions about whether the acoustic waves are being generated in the underlying copper, in the nanostructure itself, or both still remain. The nanomaterial is clearly smaller than the spot-size of the beam, so either situation is possible. It is for this reason that the final two wafers (one with copper on the wafer but not on the belts; another with copper on the belts but not on the wafer) were evaluated. Since ZnO is transparent, it can not absorb sufficient photonic energy as heat from a 532nm laser. Any physical motion observed in the sample, with no copper coating the ZnO, would then be solely attributed to the acoustic waves generated in the underlying substrate. Many tests were performed at a variety of intensities and on a large number of nanostructures of varying size and shape. At no time was any movement observed in the uncoated ZnO belts.

The final substrate (with copper coated nanobelts dispersed on bare nitride) was designed to eliminate any acoustic waves in the support wafer and to isolate propagation to the nanostructure itself. This configuration did result in successful manipulation and, in some cases even more control was obtained when compared to the wafer with copper coating both the nanobelts and the wafer. This clearly indicates that acoustic waves traveling inside the nanostructure itself are responsible for manipulation.

It was mentioned above that two basic phenomena were observed using this technique. One was confined to large microbelts moving horizontally in the direction of acoustic propagation as defined by the line source array. The other resulted in smaller nanostructures moving in the vertical direction, perpendicular to their direction of orientation. First, it is necessary to realize that there are two consequences by which acoustic waves are generated from the excitation laser. The first was addressed above and is dictated by the diffraction grating that fixes the dominant acoustic wavelength and propagation direction. The second has not been addressed and has to do with the fact that

the excitation laser is pulsing at 1500Hz with a 500psec on time and a 666.67μsec off time. This on/off switching also generates a periodic heating and cooling that will result in thermal expansion and retraction in the surface layer. Since this behavior is not defined by the diffraction grating, any acoustic response is going to propagate radially in all directions from each line as if it were a point source. Since the length of time the laser pulse is actually on is much shorter than the time it is off, all acoustic waves will have dissipated prior to the onset of the next pulse. This can be treated as a source with a finite duration resulting in acoustic waves with an infinite bandwidth[113]. The acoustic waves generated laterally in the horizontal plane are reinforced to a wavelength of 8.2μm through the replication of point sources every 8.2μm. However the waves propagating in the vertical direction are not so reinforced and therefore a large spectrum of wavelengths are allowed to propagate in this direction.

Since the excitation laser launches a variety of acoustic modes, it is important to determine the likely mode responsible for manipulation. All types of longitudinal waves and love waves can be ruled since both the wave direction and particle displacement run parallel to the surface, lacking any perturbation manifesting as an in-plane force on the nanobelt. An in-plane shear wave is also not likely to result in manipulation since the particle displacement is only perpendicular to the surface, and there is no lateral force capable of driving the structure forward. The likely mechanism for generating acoustic manipulation is a Rayleigh wave. As discussed in Chapter 1, both Rayleigh waves and ocean waves have rotational particle displacements that exhibit both vertical and horizontal components. However, ocean waves aren't typically observed in solids.

Rayleigh waves have a surface particle displacement that is counter-clockwise relative to a wave propagating to the right and a clockwise rotation with a wave propagating to the left. For the purpose of this exercise, assume a Rayleigh wave is propagating to the right inside a ZnO belt. The ZnO nanobelt should be treated as an unbound surface as represented in Figure 2.49. The left side of the figure describes

Rayleigh wave propagation in bound solids, and the right side shows what it looks like in unbound solids (nanobelts). Also, for the purpose of this discussion, assume the acoustic response is driven by the spacing in the line source as described above for the larger structures.

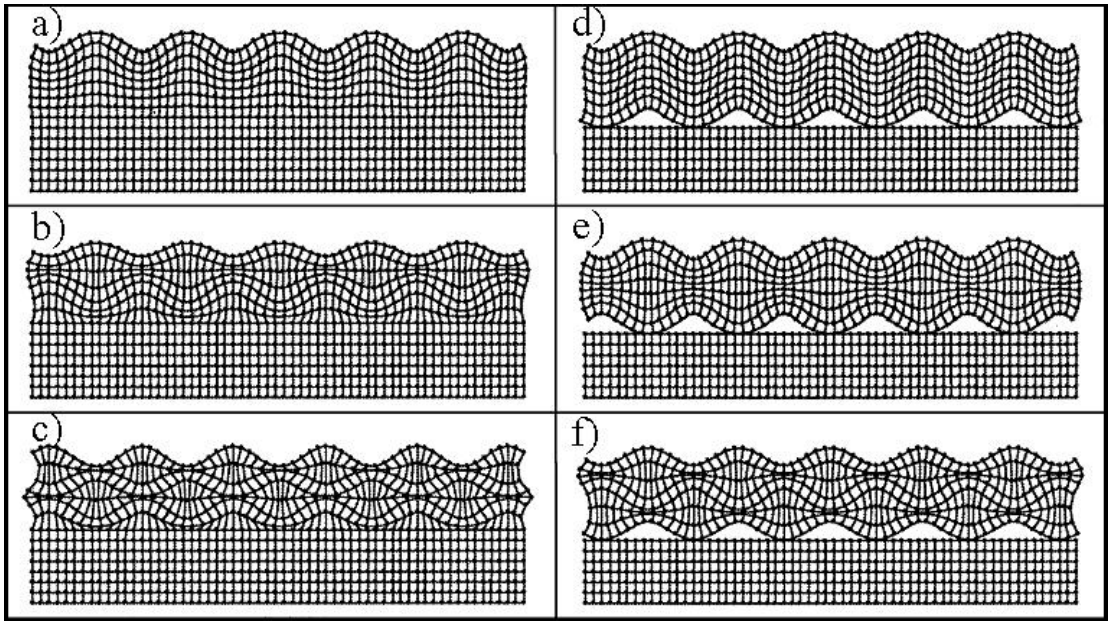

Figure 2.49 (a) Rayleigh waves propogating in a bound surface (d) Rayleigh waves propogating in an unbound surface. Images (b), (c), (e) and (f) are higher order harmonics of the same.

As one penetrates deeper beneath the surface of a propagating Rayleigh wave, the width of the particle displacement begins to decrease until a null point is reached at a depth of 1/5 the acoustic wavelength[114]. At this point the horizontal particle displacement inverts, generating a clockwise rotation described by an ocean wave at the lower free surface (in our case 1/5 of 8.2μm is 1.64μm). As long as the belt is thicker than 1.64μm, the underside of the structure in contact with the substrate is going to experience the anti-symmetric polarization clockwise rotation associated with an ocean wave. Since the particle displacement has surface normal and lateral retrograde components, an equal and opposite force will act on the belt propelling it forward. This

wave type is commonly observed in thin plates with free surfaces on either side and is also called an anti-symmetric Lamb wave[115]. The particle displacement can be seen in Figure 2.50.

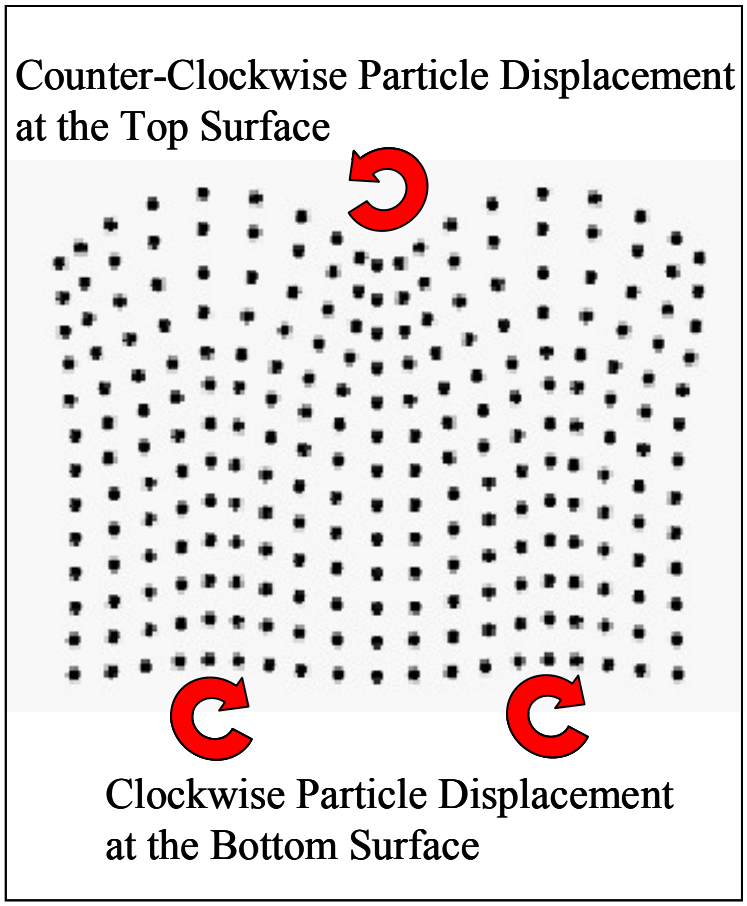

Figure 2.50 Rayleigh surface wave particle displacement in an unbound surface. This wave type is also called an anti-symmetric Lamb wave.

The reason only the large belts can be pushed horizontally by the line source is because belts with small dimensions are thinner than the 1.64μm necessary thickness to generate the appropriate particle displacement. They will still have a counter-clockwise rotation at the interface. Large belts oriented perpendicular to the propagation direction are thick enough; however, they are now too narrow and likely fit somewhere in between two crests of the acoustic wave.

The small nanobelts moving in the vertical direction are being driven by the point source created by the pulsating laser. Since there is a wide range of frequencies being generated, the higher end of the frequency spectrum has shorter acoustic wavelengths that are likely to be sufficient for generating Rayleigh/Lamb waves in the smaller structure. The lower the wavelength, the smaller the structure can be and still experience the ocean wave particle displacement at the interface capable of driving it forward. The reason the belt in Figure 2.44 and 2.45 was able to rotate and move oblique in the X-Y plane was due to the radial acoustic path of the acoustic pulse.

Even though only a few successful manipulation experiments were actually shown here, 10s of data points were documented to help draw these conclusions and ensure the above process was reproducible.

2.3 Conclusions and Future Work

Three techniques for manipulating bottom-up synthesized nanomaterials have been presented. The nature of the first two required direct contact between the structure and a physical probe. Electrostatic manipulation has shown to be useful as an inexpensive, simple technique easy enough to set up in any lab, though it is limited in its ability to work with smaller nanomaterials. Utilizing TEM in conjunction with FIB is significantly more sophisticated than a probe station and has shown to be very useful when manipulating small nanostructures, especially when some information about the crystal structure is also desired. This technique is still limited due to contamination introduced during the welding and milling process. Also, it requires a long time commitment to manipulate one structure.

A new technique for manipulating nanomaterials using surface acoustic waves has been developed. The technique is non-contact and does not introduce contamination like the first two. Both microstructures and nanomaterials can be manipulated using this tool. Work is currently being done to model the observed phenomenon and ensure that the

generalized Rayleigh/Lamb wave surface traction hypothesis is correct. Work is also being done to modify the instrument in order to incorporate multiple excitation beams and multiple diffraction gratings. Through the utilization of multiple beams along with additional beam shaping optics, an instrument could be envisioned whereby each beam would govern motion in a specified direction. One set of optics would control lateral movement of nanomaterials. Another set would control motion up and down, while a third would be designed for rotational control. Modeling will be performed in order to determine the grating geometries for generating the desired acoustic response. All optical gratings will be fabricated using traditional lithographic processing.

Work is also being done to identify a sufficient optically absorbent material other than copper. The need to deposit copper onto nanomaterials in order to achieve control over their position is one of the few limitations of this tool. Polymeric materials are being investigated as possible replacements. A polymer that could be spun on or otherwise deposited on the structure could easily be burned off in oxygen plasma once the final position is achieved[116].

CHAPTER 3

ACOUSTIC DEVICES

Below is a description of lumped circuit (RLC) resonators as well as piezoelectric resonators. Advantages of piezoelectric resonators over circuit resonators will be given as well as how modern technology has progressed with the desire to find replacements for the current piezoelectric resonators. The usefulness of resonators as mass sensors will also be presented along with the appropriate techniques for making measurements on resonant devices.

The first ever bulk acoustic resonator based on bottom-up synthesized ZnO belts will be discussed. The fabricated device was characterized using the vector network analysis. Both the first and third harmonics of resonance were observed at approximately 246.81 MHz and 270.44 MHz respectively. In addition, a 1-dimensional Krimholt-Leedom-Matthaei model (KLM) was utilized to predict the resonant frequency of the device and confirm the observed behavior.

3.1 Microwave Resonators

Resonators are useful in a variety of applications including filters, oscillators, amplifiers and frequency meters. Resonance can be defined as a state in which an alternating voltage and current traveling through a circuit are in phase; the capacitance and inductance values are equal (net reactance is zero) and the only quantity left is a pure resistance. The simplest of resonators is made up of lumped circuit elements in either series or a parallel. Since the capacitance and inductance cancel, resonance for a series circuit will be observed as a minimum impedance. A series resonant circuit can be seen in Figure 3.1, and the magnitude of impedance is plotted as a function of frequency.

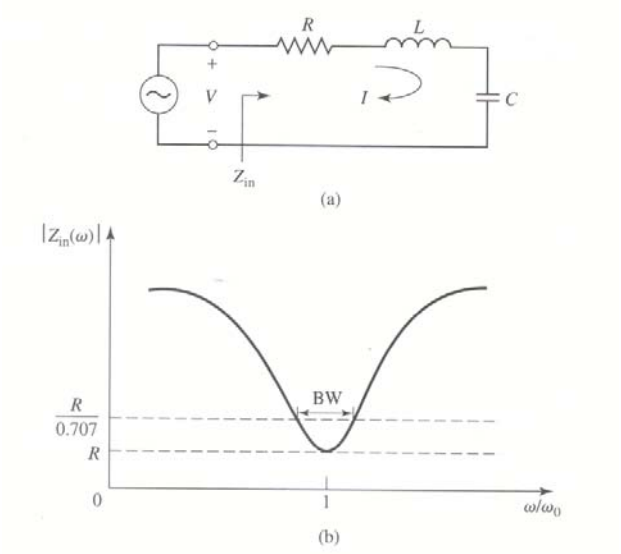

Figure 3.1 A series RLC resonant circuit and its response (a) A series RLC circuit. (b) The input impedance magnitude vs. frequency.

The input impedance of such a circuit is defined by the circuit elements, where

$$Z = R + j\omega L + \frac{1}{j\omega C} \tag{3.1}$$

and

$$P = \frac{1}{2}|I|^2 \left(R + j\omega L + \frac{1}{j\omega C} \right) \tag{3.2}$$

The Power dissipated by the resistor is determined to be

$$P_{loss} = \frac{1}{2}|I|^2 R \tag{3.3}$$

and the average magnetic energy stored by the inductor is

$$W_m = \frac{1}{4}|I|^2 L \tag{3.4}$$

as well as, the average electric energy stored in the capacitor is

$$W_e = \frac{1}{4}|I|^2\left(\frac{1}{\omega^2 C}\right) \tag{3.5}$$

Since resonance occurs when the average stored magnetic and electric energies are equal, the reactance terms cancel each other out, and impedance is simply equal to a pure resistance (Z = R). Therefore, the resonant frequency must be defined as:

$$\omega_o = \sqrt{\frac{1}{LC}} \tag{3.6}$$

Like a series RLC circuit, the parallel resonant circuit is displayed in Figure 3.2. The key difference between the two is that when the capacitance and inductance terms cancel, impedance is observed at a maximum in a parallel resonant circuit instead of a minimum.

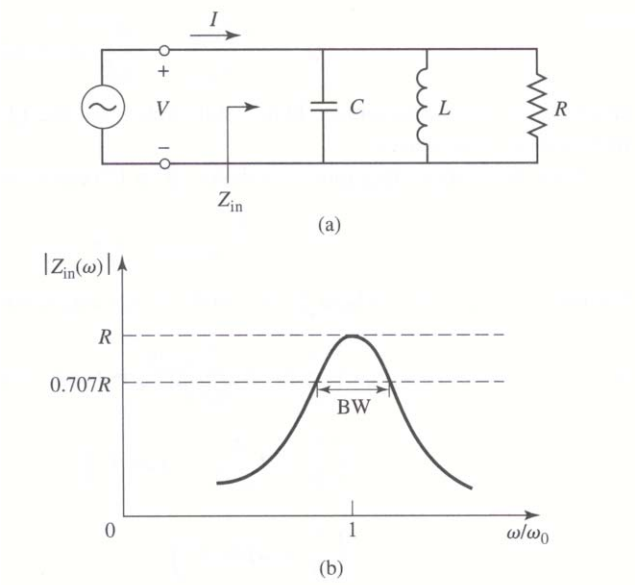

Figure 3.2 A parallel RLC resonant circuit and its response (a) The parallel RLC circuit. (b) The input impedance magnitude vs. frequency.

For the parallel case the inverse terms are additive. So,

$$\frac{1}{Z} = \frac{1}{R} + \frac{1}{j\omega L} + j\omega C \tag{3.7}$$

and

$$P = \frac{1}{2}|V|^2\left(\frac{1}{R} + \frac{1}{j\omega L} + j\omega C\right) \tag{3.8}$$

The Power dissipated by the resistor is

$$P_{loss} = \frac{1}{2}\frac{|V|^2}{R} \tag{3.9}$$

The average magnetic energy stored by the inductor is

$$W_m = \frac{1}{4}|V|^2\left(\frac{1}{\omega^2 L}\right) \tag{3.10}$$

and the average electric energy stored in the capacitor is

$$W_e = \frac{1}{4}|V|^2 C \tag{3.11}$$

Again, parallel resonance (or sometimes known as anti-resonance) occurs when the average stored magnetic and electric energies are equal and Z = R. Just like the series resonance, the parallel resonant frequency is also calculated to be

$$\omega_o = \sqrt{\frac{1}{LC}} \tag{3.12}$$

In order to characterize the quality of a resonant circuit a Q, or quality factor, is measured. Where,

$$Q = \omega\left(\frac{\text{average energy stored}}{\text{energy loss/second}}\right) = \omega\left(\frac{W_m + W_e}{P_l}\right) \tag{3.13}$$

Thus, Q is the measure of the loss of a resonant circuit—the lower the loss, the higher the Q. Since at resonance $W_m = W_e$,

$$Q = \omega_o\left(\frac{2W_m}{P_{loss}}\right) = \frac{\omega_o L}{R} = \frac{1}{\omega_o RC} \quad \text{(for a series resonance)} \tag{3.14}$$

$$Q = \omega_o \left(\frac{2W_m}{P_{loss}} \right) = \frac{R}{\omega_o L} = \omega_o RC \quad \text{(for a parallel resonance)} \tag{3.15}$$

It can be seen from the above equations that for a series resonance, Q increases as R decreases. Conversely, for a parallel circuit Q increases as R increases. Further treatment and assumptions about the relative circuits near resonance results in a simplification where the real power delivered to the circuit is one-half that delivered at resonance (for a more rigorous treatment see, Pozar 2005 3rd Edition). As a result the Q for any resonator is calculated to be

$$Q = \left(\frac{1}{BW} \right) \tag{3.16}$$

Where BW is the fractional bandwidth shown above in figures 1 and 2[117].

3.2 Bulk Acoustic Wave Devices

As stated before, piezoelectrics of low-loss, high dielectric constant materials can be used as bulk acoustic resonators (BAR). When these devices are placed into a transmission line they are indistinguishable, in principal, from the above described circuit resonators. The characteristic resonant frequency is dictated by the material properties as well as its geometry.

As mentioned, piezoelectric materials can be used as BARs in RF components. Applying an AC voltage to a BAR results in an acoustic oscillation. As the AC frequency is swept, a natural oscillation occurs where the amplitude reaches a maximum at a specific frequency (the resonant frequency). This behavior can be described as being analogous to a tuning fork. The high dielectric constant of these materials ensures that almost all of the electric field lines will be contained within the BAR; however, there can be some leakage through the sides and ends of the resonator[117]. The equivalent circuit for a BAR can be represented by a constant clamped capacitance in parallel with an acoustic motional arm. It is called the motional arm because it is these elements that are

associated with the large amplitude of vibrational motion caused by the piezoelectric effect. A suitable equivalent circuit, the Butterworth-Van Dyke model (BVD), is shown in Figure 3.3.

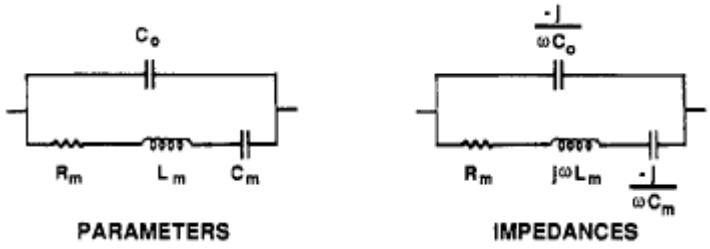

Figure 3.3 BVD equivalent circuit displaying both the parameters and impedances of the circuit elements.

The BVD takes into account both the series and parallel resonance observed in RLC resonant circuits. The values of the circuit element are derived in terms of the fundamental acoustic and electrical parameters (attenuation, phase velocity…) and can be calculated from the impedance values of the clamped capacitance and the motional arm[84, 118]. The admittance (Y) is thus given by the following:

$$Y = \frac{1}{Z} = \frac{1}{Z_m} + \frac{1}{Z_o} = \frac{1}{R_m + j\left(\omega L_m - \frac{1}{\omega C_m}\right)} + j\omega C_o \tag{3.17}$$

$$= \frac{1 + j\omega R_m C_o - \omega^2 L_m C_o + \frac{C_o}{C_m}}{R_m + j\left(\omega L_m - \frac{1}{\omega C_m}\right)}$$

where Z_m is the impedance of the motional arm and Z_o is the impedance of the clamped capacitance. Taking the inverse of admittance results in

$$Z = \frac{R_m + j\left(\omega L_m - \frac{1}{\omega C_m}\right)}{1 + j\omega R_m C_o - \omega^2 L_m C_o + \frac{C_o}{C_m}} \tag{3.18}$$

By multiplying the numerator and the denominator by the complex conjugate we get

$$Z = \frac{R_m + j\left(\omega L_m - \frac{1}{\omega C_m} - \omega^3 L_m^2 C_o + \frac{2\omega L_m C_o}{C_m} - \frac{Co}{\omega C_m^2} - \omega R_m^2 C_o\right)}{\frac{C_o^2}{C_m^2} + 1 - 2\omega L_m C_o + \frac{2C_o}{C_m} + \omega^2 R_m^2 C_o^2}$$

As mentioned before, the condition for resonance is satisfied when the reactance—the imaginary portion of the equivalent circuit (the portion in brackets)—is equal to zero. So,

$$0 = \omega L_m - \frac{1}{\omega C_m} - \omega^3 L_m^2 C_o + \frac{2\omega L_m C_o}{C_m} - \frac{Co}{\omega C_m^2} - \omega R_m^2 C_o \tag{3.19}$$

Solving the quadratic equation results in two solutions

$$\omega^2 = \frac{2L_m C_m C_o}{2L_m^2 C_m^2 C_o} \quad \text{and} \quad \omega^2 = \frac{2L_m C_m^2 + 2L_m C_m C_o}{2L_m^2 C_m^2 C_o}$$

The first root of the calculation is the series resonant frequency, and the second is the parallel (or anti-resonant) frequency, which can be simplified to

$$f_R = \frac{1}{2\pi}\sqrt{\frac{1}{L_m C_m}} \tag{3.20}$$

$$f_A = \frac{1}{2\pi}\sqrt{\frac{1}{L_m C_m} + \frac{1}{L_m C_o}} \tag{3.21}$$

It can be seen from the allowable solutions that anti-resonance will always be greater than resonance[84].

Bellow is a graphical depiction of a BAR as the swept frequency approaches and passes through resonance. In Figure 3.4, the magnitude of impedance (|Z|) as well as the phase angle of impedance (θ) is shown as a function of frequency.

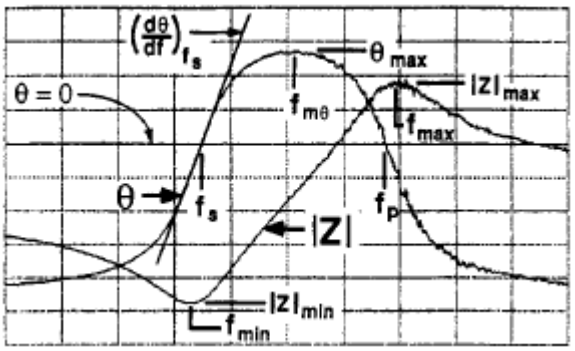

Figure 3.4 Display of a typical measurement of |Z| and θ as a function of frequency. The scale for θ is linear, while |Z| is on a log scale.

A Q can also be calculated for BAR using (3.16) treated above.

Since the behavior of the resonator is dependant on the properties of the crystal, we are able to relate each of the individual circuit elements to the stiffness, mass and loss of the system. C_o describes the behavior of the dielectric material and can be modeled as a simple a capacitor.

$$C = \varepsilon\varepsilon_o \frac{A}{l} \tag{3.22}$$

Where ε is the dielectric constant of the resonator and t is the thickness of the dielectric. This behavior dominates when the frequency sweep is significantly far from resonance.

The equivalent capacitance of the motional arm relates to the elastic stiffness of the resonator where ε is the piezoelectric constant, and *E* is the appropriate elastic constant.

$$C_{\mathrm{m}} = \frac{8\mathrm{A}\varepsilon^2}{\pi^2 tE} \tag{3.23}$$

The equivalent inductance of the motional arm is directly related to the mass of the resonator, which includes any coating on the surface (i.e. electrodes) and the fluid in contact with the surface. Where, ρ is the density of the piezoelectric, and

$$L_{\mathrm{m}} = \frac{\mathrm{t}^3\rho}{8\mathrm{A}\varepsilon^2} \tag{3.24}$$

Finally, the equivalent resistance describes the loss, or mechanical dampening associated with the device (r is the dampening coefficient) of which there are internal and external losses of electrical energy.

$$R_m = \frac{t^3 r}{8A\varepsilon^2} \tag{3.25}$$

First, electrical energy can be converted into thermal energy in the crystal (internal loss). Second, electrical energy can dissipate out of the crystal into a fluid (air, water…), which is in contact with the resonator (external loss). The latter loss mechanism depends upon the bulk properties of the "fluid" and the nature of the interaction.[118]

This raises the question, "What is the advantage of the BAR over a conventional resonant circuit?" The most important reason lies in the values, which conventional components would have to provide in order to simulate the behavior of the crystal. The simulation of C_0 would present no problem, but the simulation of other parameters is, in general, difficult. For example, the value of C_m in a typical 5-MHz AT-cut unit may be of the order of 0.01 pF. A capacitor of this size could scarcely be built, since its leads, if any, would probably have more capacitance than this. The value of L_m is of the order of 0.1H and R_m is perhaps 10 ohms. A coil having an inductance of 0.1H would ordinarily require many turns of wire on a ferromagnetic core. To construct such a coil with a resistance of only 10 ohms in a volume less than 0.5 cm^3 is probably unlikely[84].

Second, RLC resonant circuits are susceptible to changes in resonant frequency as a function of temperature. While a BAR is also susceptible, it is more stable over a broad temperature range. Also, certain crystal cuts result in orientations where an increase in thermal expansion of the crystal results in a proportional increase in the acoustic velocity, keeping resonance unchanged. This is how quartz watches are manufactured in order to prevent a thermal dependence on time. In addition, RLC circuits are fairly bulky while piezoelectric devices come in much smaller robust packages. Piezoelectric resonators are

cheaper, lighter in weight and are known to have much higher Q values than equivalent RLC resonator. To design a useful filter it takes an array of resonators in series or parallel for low-pass, band-pass and stop-band applications. This can become cumbersome in RF applications where small, portable devices are desired.[82, 84, 117-119]

In addition to applications in RF communications, BAR devices have been used as mass sensors. It is the direct piezoelectric effect that is the basis for force, pressure, vibration and acceleration sensors and the converse effect for actuator and displacement devices[120]. The use of piezoelectric BAR devices as gravimetric sensors has origins in the work of Sauerbey. Sauerbey demonstrated, under an AC field, the mass/frequency relationship between rigid layers attached to a quartz resonator and treated it as an equivalent mass change to the crystal itself[121]. The following equation demonstrates that the frequency change is directly proportional to the added mass:

$$\Delta f = \left[\frac{-2f_{\mathrm{ro}}^2}{A\sqrt{\rho_{\mathrm{q}}G_{\mathrm{q}}}}\right]\Delta m_{\mathrm{q}} \tag{3.26}$$

Where, Δf is the change in resonant frequency due to the added mass, f_{ro} is the unloaded resonant frequency of the resonator. ρ_q and G_q are the density and the shear modulus of the crystal. A is the surface area of the resonator and Δm_q is the change in mass[122]. This concept has been exploited extensively in the fabrication of chemically selective sensors, where a binding agent is incorporated onto a BAW device[123]. Since the description of this behavior, BAR devices have been used to quantify the thickness of sputtered metal[124], detect phase transitions[125], evaluate contamination in food[126], and sense viruses[127].

3.3 Thin Film Bulk Acoustic Resonators

Due to the growing need for high performance frequency control devices in wireless networks with low power consumption. A point has been reached where even the acoustic devices described above are considered bulky for RF applications. Subsystem miniaturization in cell phones, pagers, navigation systems, satellite communication and various forms of data communication are all pushing towards on-chip components instead of the off-chip quartz filters that are currently being used[128]. In particular there is a need for front-end filters that protect receivers from adjacent channel interference and output filters that limit the bandwidth of transmitter noise[129]. The most promising candidates for these applications are the solidly mounted resonator (SMR)[130] and the thin-film bulk acoustic resonator (FBAR)[131].

SMR and FBAR devices are very similar to the BAW devices described above; however, they are scaled down to operate in the GHz frequency range. It can be seen from Figure 3.5, the device consists of a thin piezoelectric film sandwiched between two electrodes. An RF signal applied through the thickness of the film produces mechanical motion, and fundamental resonance occurs when the film thickness equals $\lambda/2$ the input signal. Note that the SMR is fabricated on top of an acoustic reflector in order to prevent loss from being transmitted into the underlying silicon. In order for this to work, three or four pairs of acoustically dissimilar materials must be used. The FBAR deals with loss by creating a freestanding device as shown in Figure 3.5b. The creation of an air/crystal interface prevents interaction between the resonator and the underlying substrate[132]. Both of these devices are attractive since they can be fabricated to occupy the same or similar packages as high frequency integrated circuits. Both are seen as a promising replacement for ceramic devices used in mobile communications that operate between 200MHz and 6GHz.

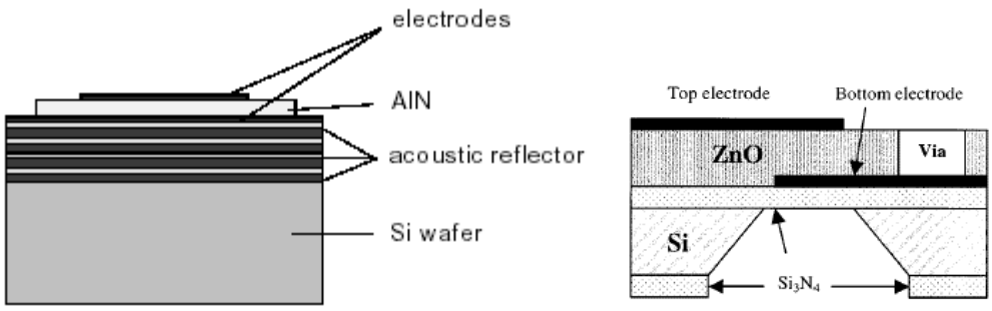

Figure 3.5 (a) Schematic view of an SMR (b) Schematic view of an FBAR.

The beam resonator, Figure 3.6, operates differently from an FBAR in that the flexural mode is excited[133]. This design uses a piezoelectric film to drive a silicon beam into oscillation. The vibration travels as a transverse wave through the beam to a piezoelectric film on the other side, which then converts the mechanical oscillation back into an electrical signal. This type of device is useful in lower frequency applications where a greater sensitivity to mass is desired. Beam resonators have the added benefit that the resonant frequency can be capacitively tuned using an additional electrode fabricated just bellow the resonator[134]. There are many promising applications of flexural modes resonators as a pressure, mass and chemical sensors[135, 136].

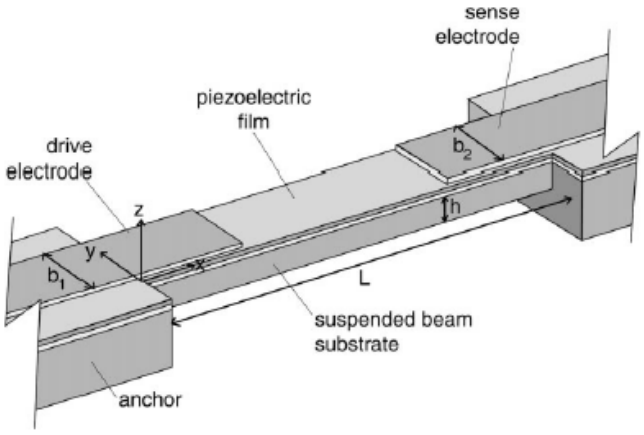

Figure 3.6 Schematic of a clamped-clamped beam resonator.

The piezoelectric materials currently being utilized are typically grown via sputter deposition. The results of this are low quality films made up of oriented grains with a high concentration of defects (Figure 3.7)[137]. ZnO is one of the more commonly utilized materials due to its ease of deposition; however, it is particularly sensitive to temperature, acids, bases and even water. As a result, other processing like cleaning, etching, metal layer patterning, passivation, reactive ion etching and the stripping of photoresist all degrade the quality of the ZnO[138]. High quality single crystals are desirable; however, micro-fabrication techniques result in poor material properties.

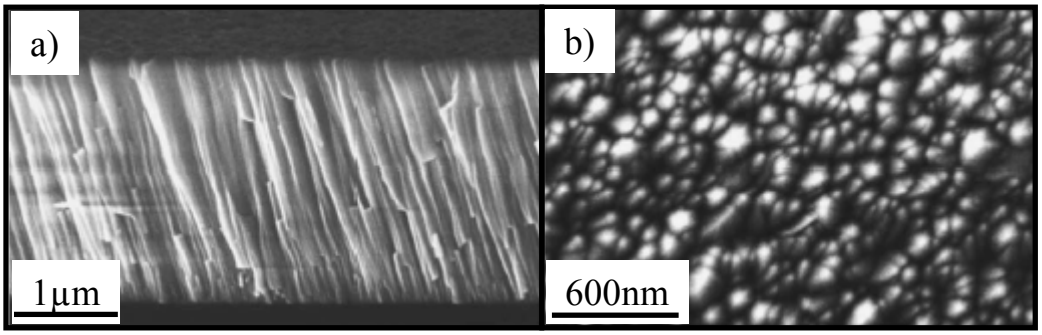

Figure 3.7 SEM micrographs of sputter deposited a ZnO film (a) Cross-section (b) Top View.

3.4 Network Analysis

Network analyzers have become one of the most important measurement tools for characterizing the performance of high-frequency components and devices, including resonators[139]. Vector network analysis (VNA) can accurately measure the effect a device under test (DUT) has on the amplitude and phase of test signals swept across a frequency range. The best way to describe the concept of network analysis is using the light wave analogy.

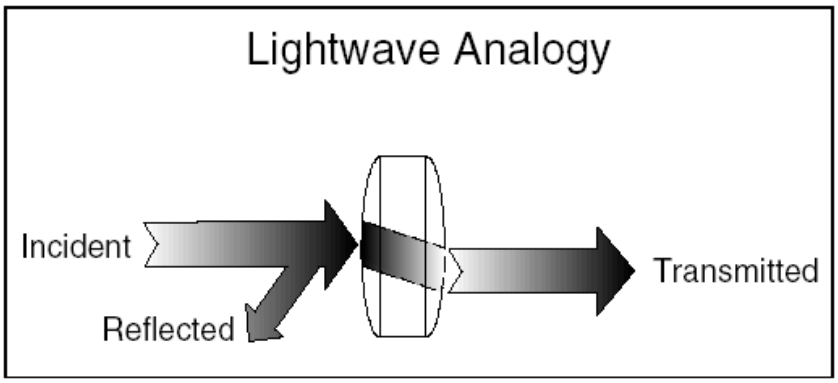

Figure 3.8 Light wave analogy as it relates to high-frequency device characterization using network analysis.

When light strikes a transparent lens, some of the light is reflected back, while most of it is transmitted through to the other side. If a lens has a mirrored surface, then a majority of the incident light will be reflected while little to no light will be transmitted through. Network analyzers act in very much the same way. Network analyzers measure the incident, reflected and transmitted energy off of a DUT during a frequency sweep. By taking the measurements as a ratio of the detected voltage to the incident voltage enables the use of reflection and transmission coefficients that are independent of variations in power as a function of frequency. Reflection measurement data is often shown as

$$\Gamma = \frac{V_{reflected}}{V_{Incident}} = \frac{Z_L - Z_o}{Z_L + Z_o} \tag{3.27}$$

where Z_L is the load impedance of the signal incident on the DUT from the network analyzer and Z_o is the characteristic impedance of the DUT. When Z_o and Z_L are equal, all of the incident energy is transmitted through the DUT and $\Gamma = 0$. When the Z_o and Z_L are not equal, some of the energy is reflected by the DUT and Γ is greater then zero. If Zo is equivalent to an open or short than $\Gamma = 1$.

The transmission coefficient (T) is defined as

$$\mathrm{T} = \frac{V_{transmitted}}{V_{Incedent}} \tag{3.28}$$

Whereby, if the transmitted voltage is greater than the absolute value of the incident voltage, then the DUT is said to have gain, where

$$\text{gain}(db) = 20\left(\log\left|\mathrm{T}\right|\right) \tag{3.29}$$

If the absolute value of the transmitted voltage is less than the incident voltage, the DUT is said to have insertion loss, where

$$\text{insertion loss}(db) = -20\left(\log\left|\mathrm{T}\right|\right) \tag{3.30}$$

Low-frequency device or network characterization is usually based on the measurement of admittance functions (Y and Z parameters). In order to completely characterize the unknown device, the measurements of Γ and T are taken as scattering parameters (S-parameters). The measured S-parameters are easily converted to polar coordinates or real and imaginary components of Y and Z parameters by use of a Smith chart.

The number of S-parameters that can be measured relates to the square of the number of ports for the DUT. If there is only one port, then only one S-parameter can be measured (S_{11}); if there are two ports, then four S-parameters can be measured (S_{11}, S_{21}, S_{12}, S_{22}) and so on. The convention for the numbering of S-parameters defines the first number following the S as the number from which the energy coming from the DUT enters the network analyzer. The second number defines the port at which the network analyzer sends the incident signal to the DUT. So, an S_{21}-parameter is measuring the signal being transmitted from the network analyzer from port 1, transmitted thru the device and detected by port 2. An S_{11}-parameter is a reflection measurement where the incident signal is sent from port 1, reflected off of the DUT and sensed by port 1[140].

3.5 Krimholt-Leedom-Matthaei (KLM) Model

To assist with the measurements it is necessary to use a model in order to predict the location of resonance based on the geometry and material properties of the nanobelt. It can sometimes be difficult to locate resonance in a large frequency sweep, and modeling can help identify a frequency range in which to start looking. This model will also be used to validate the test results from a nano-resonator. To do this, a 1-dimensional KLM model will be employed.

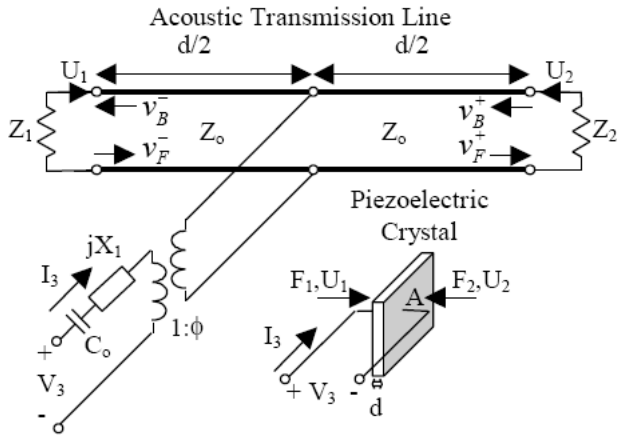

Figure 3.9 The KLM model of a piezoelectric transducer.

The KLM model is depicted in the above Figure where, V_3 and I_3 are the voltage and current applied to the piezoelectric crystal. The converse piezoelectric effect results in a force F and acoustic velocity U that is felt at the respective faces. The velocities of the wave inside the crystal are $\pm$ v_B, v_F, where the subscript F indicates a forward traveling wave propagating towards interface 2, and subscript B indicates a backward-traveling wave propagating towards interface 1. The $\pm$ defines waves propagating in the right and left half of the crystal. The model input parameters include the thickness of the crystal d, the contact area of the electrodes applying a stimulus to the crystal A, and the characteristic load impedance of transmission line, Z_o. Impedances Z_1 and Z_2 are the

respective impedances of the backlayers, or the medium, into which the crystal is oscillating (in our case, air).

In order to complete the model, it is also necessary to include a capacitor, C_o, that results from dielectric properties of the material; impedance X_1, and a transformer with the ratio (1:Φ) that converts the electrical signal into the appropriate acoustic values. The values for these parameters are

$$Z_o = \rho c A$$
$$C_o = \frac{\varepsilon A}{d}$$
$$X_1 = \frac{h^2}{\omega^2 Z_o} \sin\left(\frac{\omega \cdot d}{c}\right)$$
$$\phi = \frac{\omega Z_o}{2h} \operatorname{cosec}\left(\frac{\omega \cdot d}{2c}\right)$$

where ε is the permittivity of the piezoelectric, absent an applied voltage, h is the piezoelectric pressure constant for the crystal, ρ is the density, and c is the speed of the sound waves in the crystal. From this, it is possible to calculate the input impedance from the model parameters as done above with the BVD circuit parameters[141].

The key advantage of this model results from its ability to predict higher order harmonics, while the BVD is only able to predict the primary mode of resonance. This model has been utilized as a MatLAB computer simulation which will be described in the following section.

3.6 Bulk Acoustic Resonators Based on ZnO Microbelts

The bottom-up approach of nanotechnology has yielded many high quality, single crystal, and defect free structures like the nanobelt[57]. Piezoelectric nanobelts of ZnO become attractive in these applications because of their perfectly faceted, free-standing, beam-like geometry, making them ideal candidates as SMR, FBAR, and beam resonators[85]. However, handling nanobelts can be cumbersome when attempting to manipulate these materials into useful devices. In addition, the current operational frequency range for devices that utilize electro-mechanical filters are between 200MHz

and about 6GHz. In order to fabricate devices that operate within this range, films on the order of 500nm-15μm thick are desired.

Work accomplished thus far has utilized the process of nanotechnology to synthesize larger structures for the above mentioned radio frequency (RF) applications and incorporate them into a working resonator. While the materials were synthesized using a bottom-up approach, traditional fabrication techniques were employed to manufacture other components of the resonator, like the support substrate, ground pads and contact electrodes. Network analysis was implemented to measure the scattering parameters (S_{11}) and fully characterize the working device[142]. A one-dimensional KLM model was also used to compare predicted resonant frequencies to those that were measured experimentally[141].

3.6.1 Experimental Method

The ZnO nanobelts were grown using a single zone tube furnace. The furnace was operated for a period of 12 hours in order to increase the size of the nanobelts per our application; typical width dimensions of the belts varied between 5 and 30 μm, while the thickness ranged from a few hundred nm up to 5 μm thick. In some cases the nanobelts were grown up to a centimeter long. As mentioned before, these large nanobelts will resonate in a frequency range suitable for modern RF communication systems.

A (100) oriented silicon wafer was chosen as the support substrate for device fabrication. PECVD was used to deposit 400nm of Si_3N_4 onto the surface to provide an electrically insulating barrier between the device and the low resistivity silicon substrate. Thermal evaporation was then used to deposit 2000 Å of aluminum. An electron beam sensitive negative resist (ma-N2410) was spun onto the aluminum surface at 4000 RPM to obtain a thickness of approximately 1μm. The wafer was then cured at 90^{o}C on a hotplate and subsequently diced into small chips approximately 1cm^2. A JEOL JSM-5910 SEM, modified with a J.C. Nabity Nanometer Pattern Generation System (NPGS),

was used to pattern the contact electrodes for the device into the resist via e-beam lithography (Patterns were designed using DesignCAD LT2000). The chip was subsequently developed with a 2.5% tetramethyl ammonium hydroxide (TMAH) solution for 90 seconds and rinsed with deionized water (DI). After the pattern was inspected with an optical microscope, an aluminum etchant made up of acetic, phosphoric and nitric acid was heated to 50^{o}C and used to remove the unwanted metal and define the large contact pads. The remainder of the resist was then dissolved in acetone and rinsed with isopropanol (IPA) and DI. The electrodes were inspected again to ensure the desired features were achieved and free from contamination.

The next stage of processing involved manipulating the as-synthesized nanobelts appropriately between the ground pads and the drive/sense electrode. First, ZnO nanobelts were dispersed onto the surface of a clean silicon chip. A long thin glass capillary that had been pulled to a fine point was fixed to a set of Cascade Microtech MPH series micromanipulators. Under an optical microscope with a large working distance, the manipulators were carefully operated in order to identify a nanobelt appropriate for testing. The capillary interaction forces between the tip of the glass rod and the nanobelt resulted in a weak adhesion sufficient to lift the nanobelt off of the surface of the silicon and redeposit it in between the electrodes. Figure 12 shows a schematic of the as fabricated device electrodes and the perceived manipulation of a nanobelt into position in between. Figure 12b and 12c are SEM micrographs of a successful manipulation.

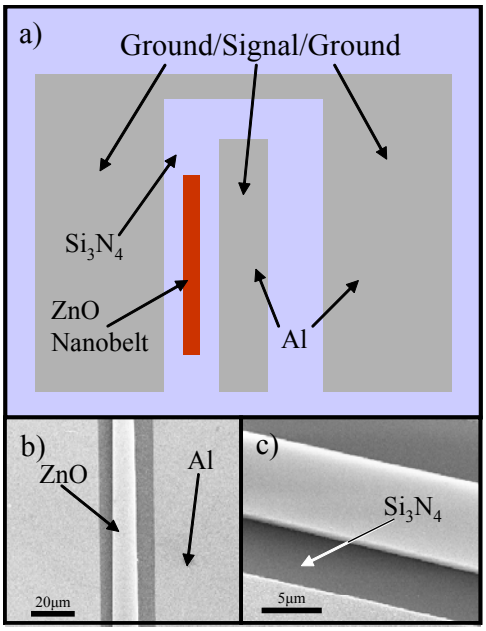

Figure 3.10 (a) Schematic of ground electrodes and position of nanobelt prior to establishing contact (b) SEM micrograph of nanobelt between electrodes (c) close-up of side facets.

In order to make contact to the nanobelt, an FEI NOVA dual-beam, focused ion beam microscope (FIB) was used. Typically, FIB is used for milling into a sample by accelerating gallium ions toward the sample's surface. Deposition of metal (instead of milling) can occur using an ion-beam-assisted-CVD of an organometallic precursor. In our case, a methyl platinum gas was introduced into the chamber using a small capillary that suspends just above the sample. Gas molecules adsorb on the surface but only decompose into platinum metal (Pt) where the ion beam interacts[143]. A software package was used to control the position of the ion beam in order to deposit Pt on the side facets of the belt. Thin Pt leads were then deposited to connect the electrodes on the belt to the large Al contact pads. The deposited Pt electrodes, along with the lead wires that connect the belt to the contact pads, can be seen in Figure 13b and 13c.

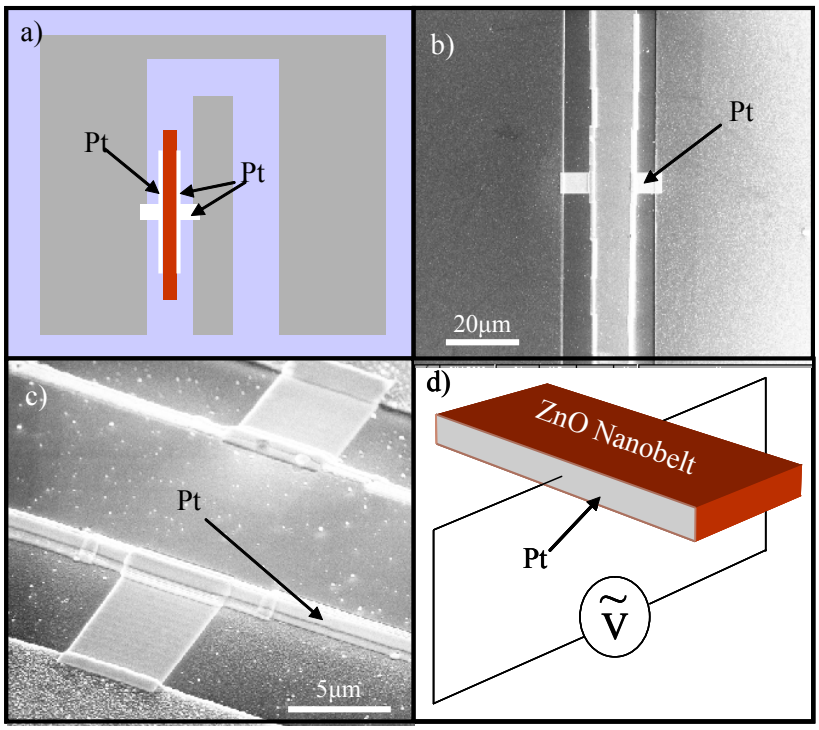

Figure 3.11 (a) Schematic of resonator before testing (b) SEM micrograph of nanobelt resonator (c) Close-up of side facets and lead wires (d) Depiction of stimulus applied through the thickness of the nanobelts.

For characterizing the device and measuring the resonant frequency of the ZnO resonator, an Agilent ENA series 5071B network analyzer was used. Cascade Microtech Infinity ground-signal-ground (GSG) probes with a 150μm pitch were utilized to make the on-wafer measurements. Phase-matched K-Type 3.5mm cables send the signal from the NA to the probes and back to the NA for analysis of the S_{11}-parameters. In order to isolate the system and remove as many random errors as possible, the entire measurement was performed on a Herzan TS-140 active isolation table.

In order to ensure a high quality signal it is common to first calibrate the network analyzer using vector error correction. A calibration standard consisting of an open, short and load (50 ohms) was used to quantify imperfections in the test equipment. The systematic errors were then stored in the network analyzer and an error model was

calculated to remove the effects from the subsequent measurement. This enables a full calibration all the way to the probe tips. However, in addition to the testing equipment, additional systematic errors are introduced through contact resistance and pad parasitics of the fabricated device. An additional method, response calibration, was performed to remove any systematic errors created by these fixtures. To do this, a set of bare electrodes, absent the nanobelt, were contacted and the data was stored in the network analyzer's memory. The trace was then displayed as "data divided by memory" to normalize the signal. The probes were then raised and positioned into contact with the actual device. This additional process allowed calibration of the entire system all the way to the resonator[144].

3.6.2 Results

Figure 3.12 is a plot of the data from the NA displayed as the magnitude of impedance (|Z|) in blue, and the phase angle (θ) in red as a function of frequency.

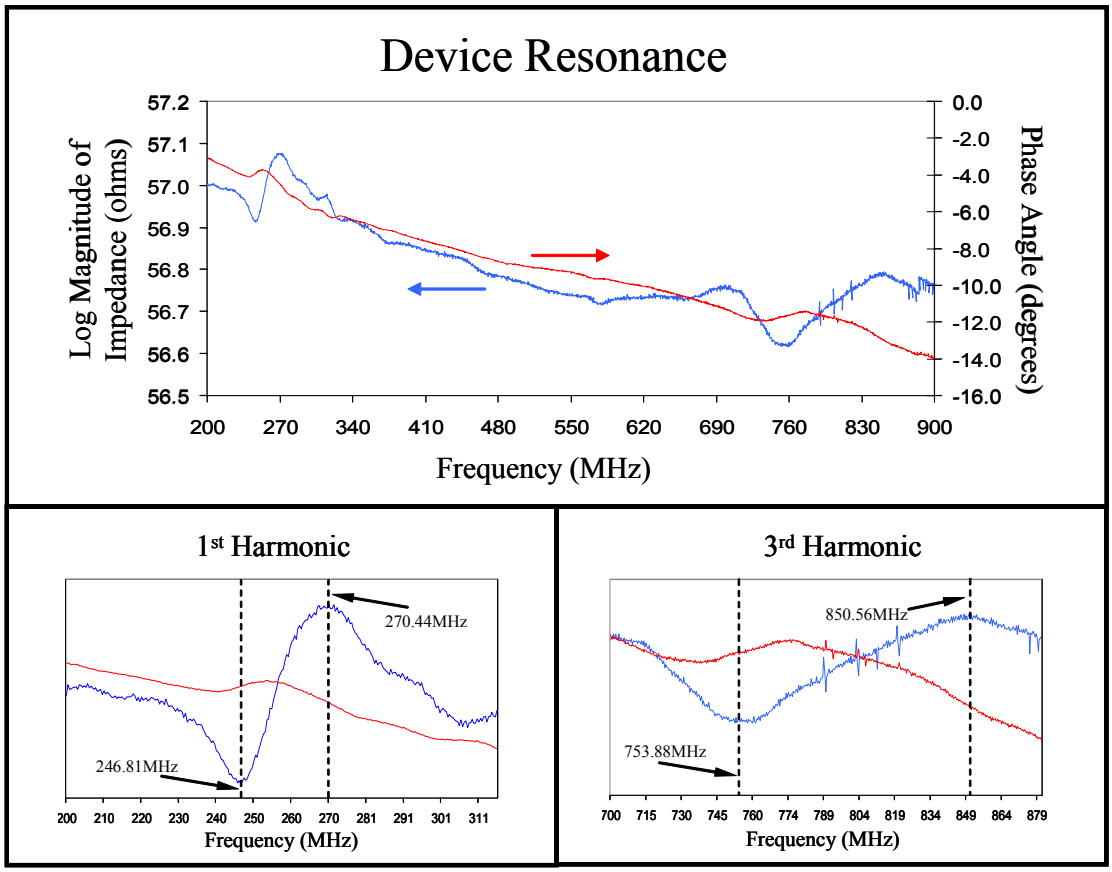

Figure 3.12 Plots of magnitude (|Z|) and phase angel (θ) of impedance. The full frequency sweep from 200MHz to 900MHz is shown as well as the zoomed-in portions of the 1st and 3rd harmonics.

The primary mode of resonance and anti-resonance is observed at 246.81 MHz and 270.44 MHz respectively. No quality factor (Q) was calculated, however, it can be seen that the very large bandwidth at resonance and anti-resonance is the result of a lossy, low Q device. This results primarily from the interaction between the nanobelt and the underlying substrate. Due to manipulation, the nanobelt cannot be considered to be in intimate contact with the support substrate, nor can it be considered to be free standing.

This quasi-substrate/nanobelt interaction gives rise to an additional dampening mechanism other than the traditional dampening caused by ambient conditions in the environment. In addition, it can be seen that there is a taper in the belt. The width varies from 11.9 μm at one end of the device to 12.3 μm at the other. This asymmetry will broaden the resonant peak creating a resonance that is averaged across the thickness variation rather than defined at a specific dimension. In addition to the 1st harmonic, we are also able to identify the 3rd at a factor three times the primary peak (753.88MHz). It is common in lossy systems for subsequent harmonics to exhibit even lower Q behavior, which is why the higher order mode appears even broader than the 1st. However, the existence of the third mode is a strong indication that the piezoelectric resonator is working properly.

In order to ensure that the measured signal is coming from a working device, a 1-dimensional KLM computer simulation was used to predict the resonant frequency based on a series of inputs. The parameters are thickness (chosen to be 12.1 μm), density, acoustic velocity, dielectric constant, coupling coefficient, quality factor, as well as the load impedance (50 ohms) and the acoustic impedance of the back layers, which were assumed to be air. All of the material properties were taken as bulk values for ZnO. Results are displayed in Figure 3.13, and it can be seen that the theoretical results are in good agreement with the experimentally measured values.

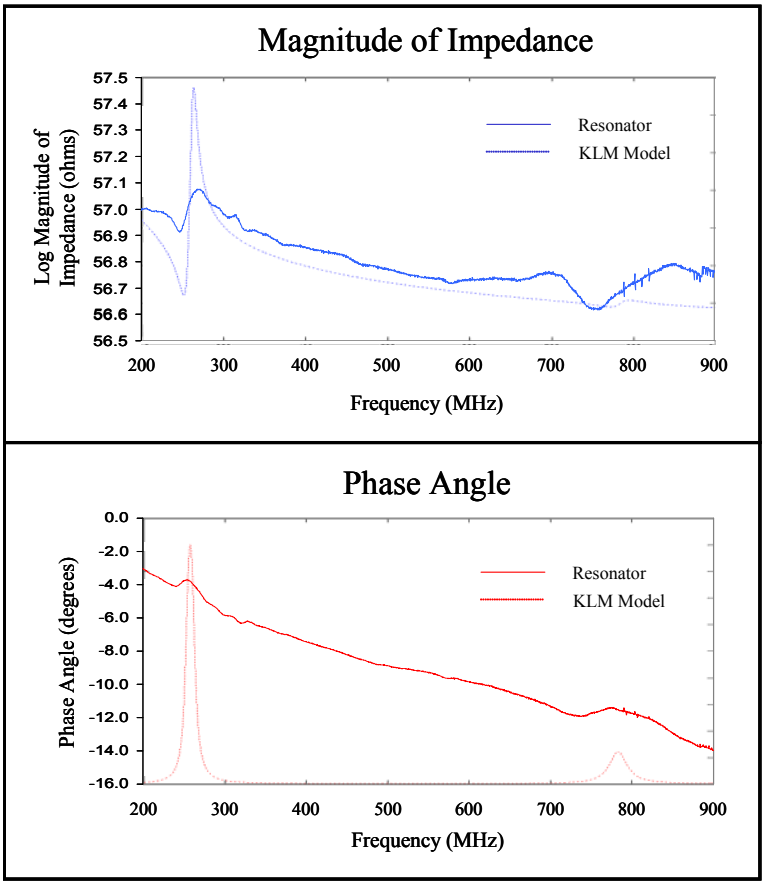

Figure 3.13 Experimental data plotted along with the predicted traces calculated from the KLM model confirming the results from the working device.

From the above experimental data it is also possible to calculate the coupling coefficient from the values of resonance and anti-resonance. The electromechanical coupling constant describes the efficiency in which mechanical energy is converted into electrical energy (or visa versa) and is related to the piezoelectric coupling constant, K^2, by,

$$k_t^2 = \frac{K^2}{1+K^2} \tag{3.31}$$

$$K^2 = \frac{{e_{33}}^2}{c_{33}\varepsilon_r} \tag{3.32}$$

where k_t^2 is the electromechanical coupling constant. The theoretical K^2 and k_t^2 values for a longitudinal wave traveling along the c-axis of ZnO are 8% and 7.4%, respectively

[145]. It is important to note that the frequency separation between resonance and anti-resonance (Figure 4.16) is intimately linked to the electromechanical coupling constant [145] for the first harmonic.

$$\omega_A^2 - \omega_R^2 = 8k_t^2\left(\frac{v_a}{d}\right)^2 \quad \textbf{(3.33)}$$

k_t^2 was calculated in this device to be 0.6%. When compared to a theoretical value of 7.4%, the electrical component of the ZnO belt is loosely coupled to its mechanical counterpart. It is important to note that the frequency stability among piezoelectric crystals increases as K^2 and therefore k_t^2 decreases. Physically this means that if the piezoelectric coupling coefficient is small, changes in the parameters of the electric circuit have minimum effect upon the mechanical properties of the resonator [84].

3.6.3 Initial Design Improvements

This initial result is exciting, yet there are a few ways the above design may be improved upon. First, the large impedance is attributed to the contact area of the electrode. The nanobelt is very thin, and while the length of the contact electrode is very long (~110 μm), the resultant contact area is still very small. The large impedance that results could make it challenging to identify resonance as we begin to work with smaller and smaller belts. Reducing the contact area further could cause the signal to be buried in the background noise, preventing confirmation of a working device. In order to deal with this issue, an attempt has been made at increasing the contact area by making contact to the top and bottom faces of the belt instead of the side facets. Figure 3.14 shows a schematic of the 1-port transmission design.

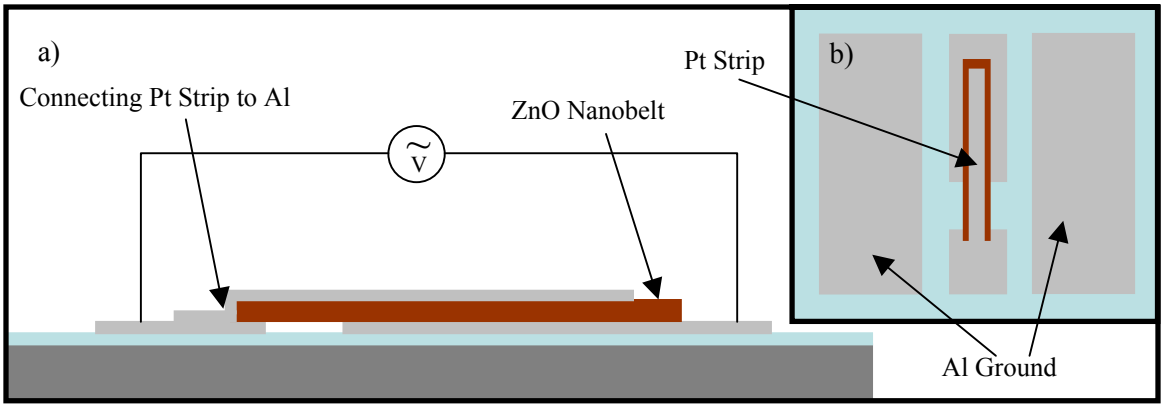

Figure 3.14 Schematic of SMR/FBAR designed to increase the contact area of the electrodes (a) Device cross-section (b) Top view of device.

The contact electrodes for this configuration are manufactured using the experimental procedure described above (e-beam lithography, etching…); only the design has been modified to achieve resonance through the thickness of the nanobelt instead of "width." This time the belt is manipulated to span two center electrodes so that the bottom of the belt is in direct contact with both Al pads. The FIB is then used to deposit a thin Pt strip down the length of the belt to act as the top electrode. At one end, Pt is deposited down the side-wall of the belt to establish contact between the Pt strip and one of the large Al contact pads as shown in Figure 3.15a. As a result, the contact area is increased, and resonance should be observed at much higher frequencies. This design could be considered to be an SMR without an acoustic reflector. Good data has yet to be obtained from this design for reasons to be described in a moment.

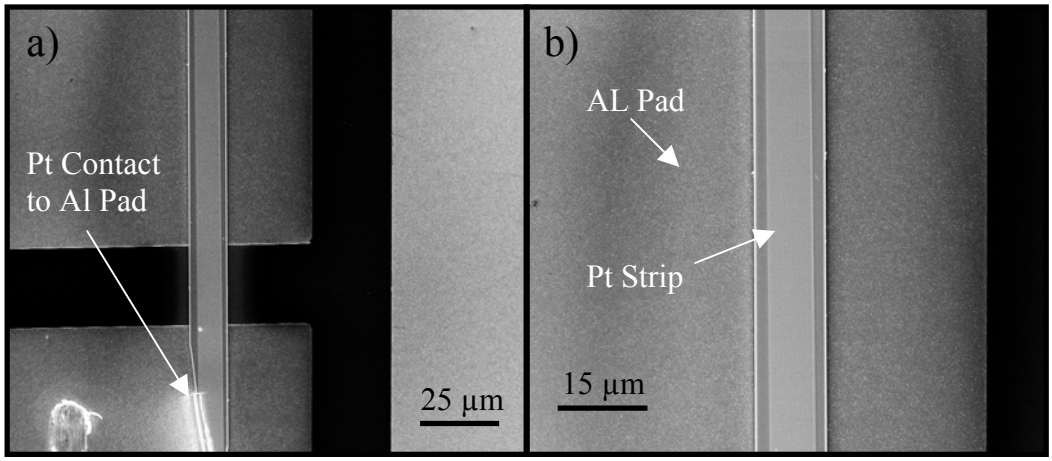

Figure 3.15 Nanobelt SMR (a) SEM of as fabricated device (b) close-up of device.

In addition to the nanobelt SMR, preliminary studies on ZnO nanobelt beam resonators are also being pursued for mass and chemical sensing applications. In order to fabricate this type of device, it is necessary to mill or etch a trench beneath the belt to eliminate any losses associated with substrate/resonator interaction. Again, the design of the device has been modified into a two port transmission configuration. In Figure 3.16, a cross-section and top-view schematic illustrates an early attempt.

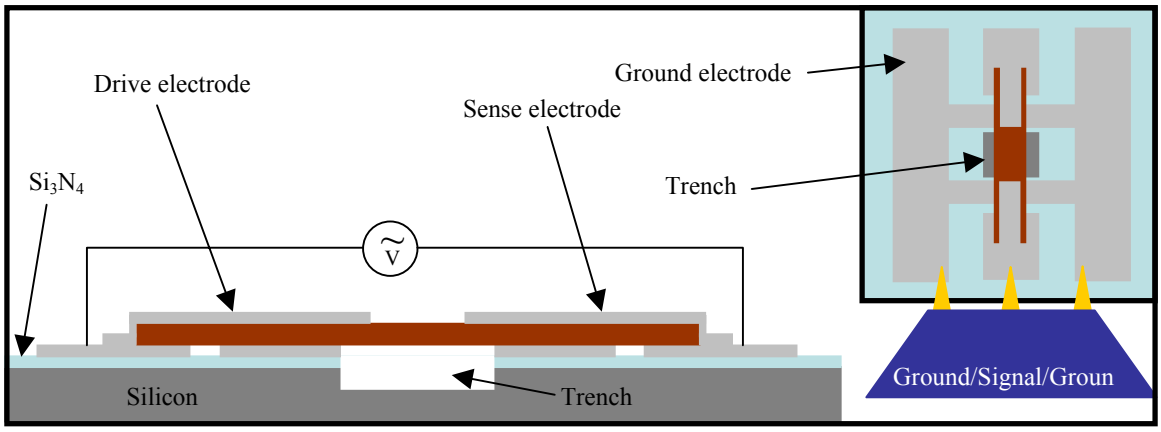

Figure 3.16 Schematic of beam resonator (a) Device cross-section (b) top view of device.

It can be seen that an "H-like" pattern is used as the ground electrode and contact between the drive/sense electrodes are established using the FIB (just like SMR design). In the following figure a few early attempts are displayed.

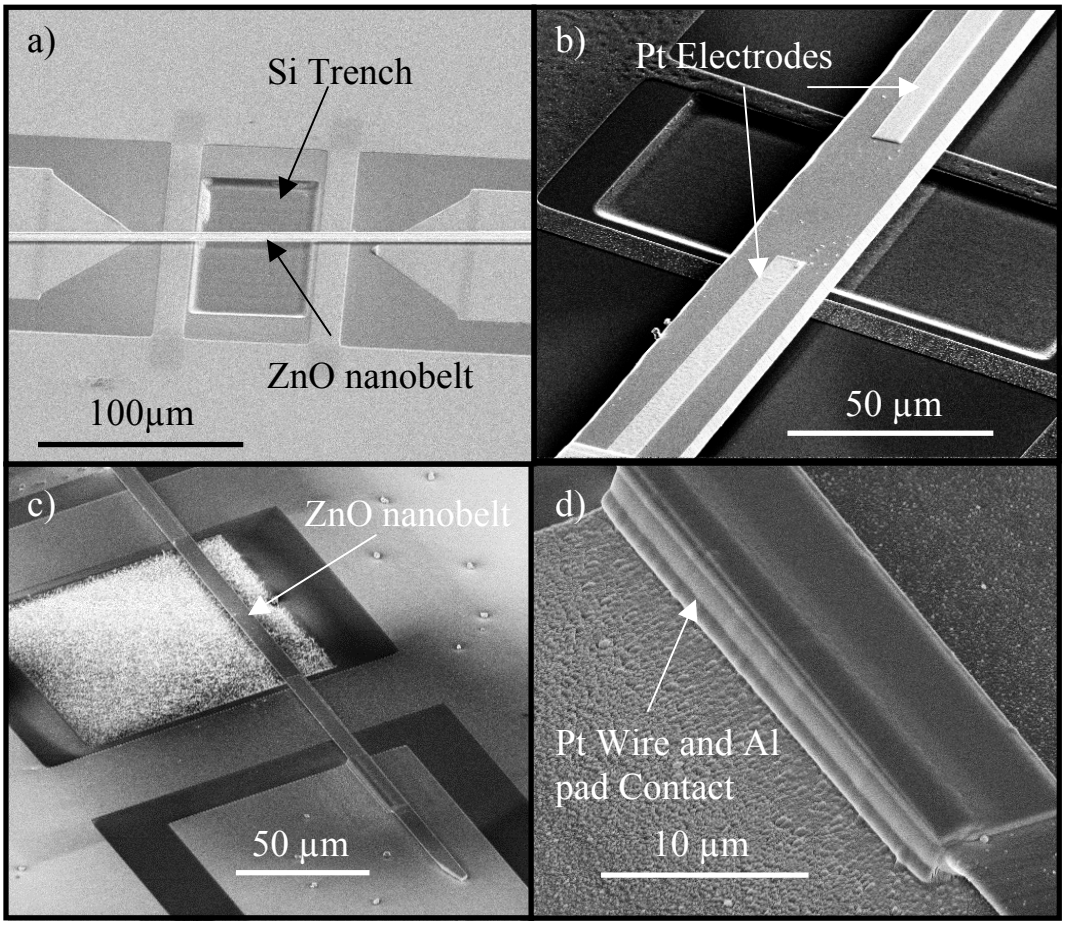

Figure 3.17 Clamped-clamped beam nanobelt resonator (a) Nanobelt manipulated across the prefabricated electrodes (b) Drive/sense electrode fabrication using FIB (c) Completed device (d) SEM micrograph showing the contact established between the top electrode and the Al contact pad.

Results have yet to be obtained from either of these designs due to poor contact between the bottom Al electrode and the nanobelt. The top electrode poses no issue since the ion beam CVD creates a good bond between the Pt and the ZnO. However, subsequent to

manipulation there is nothing to establish a successful bond between the nanobelt and the underlying ground pad, figure 21. A few annealing procedures have been implemented to create a diffusion of metal into the ZnO. However, since the two components are not in intimate contact, there is no interface for diffusion to take place.

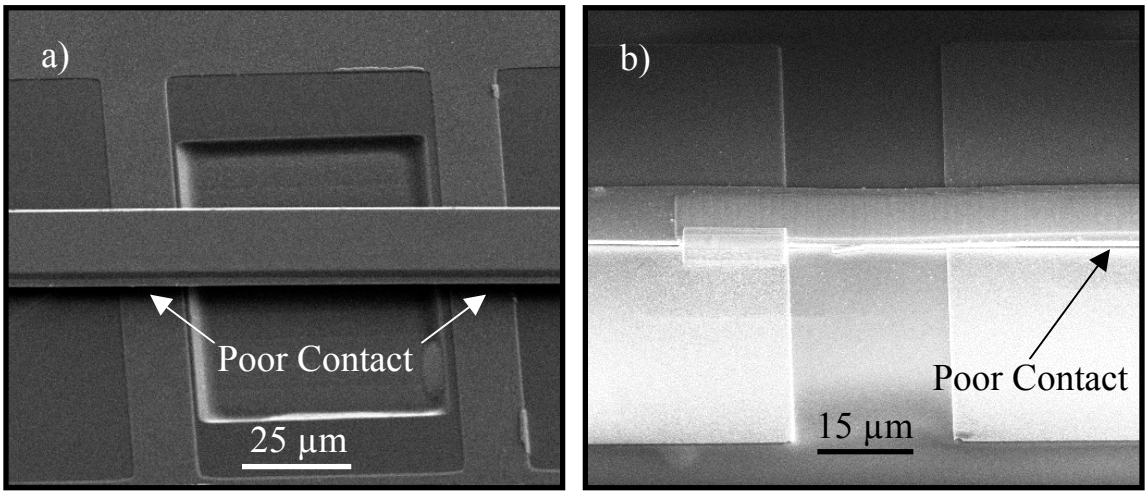

Figure 3.18 SEM images showing the lack of contact between the ground pads and the ZnO nanobelt (a) beam resonator (b) SMR/FBAR design.

3.7 Conclusions and Further Work

In conclusion, a new approach to resonator fabrication utilizing ZnO belts has been demonstrated. A union between the bottom-up synthesis of nanotechnology and MEMS/NEMS fabrication techniques has resulted in the first ever bulk acoustic resonator based on ZnO belts. A model was presented that explains the location of the resonant peaks as well as the breadth. While the above design resulted in a low Q device, proof has been shown that the piezoelectric properties of ZnO belts can be exploited, and further studies will confirm the benefits of a high quality single crystal.

The following chapters will deal with streamlining fabrication and scaling down of the process to work with smaller nanobelts. FIB will no longer be used as a major tool in fabrication. It is an inherently slow process and only capable of producing one device

at a time. Since most of the device architecture is fairly large, a series of photolithography masks will be designed in order to mass produce the basic components of the device (electrodes and support substrate). Manipulation will be necessary, though alternative techniques will be explored in order to make sufficient contact between the nanobelts and the underlying electrodes.

One of the techniques will focus on the direct synthesis of the piezoelectric nanostructures laterally between two free-standing electrodes. This technique could eliminate the need for any post-synthesis manipulation and could result in the mass production of nanodevices.

It will also be necessary to expand upon the one-dimensional model presented here in order to describe the resonant behavior of nanobelts in three dimensions. A treatment of the Hook's law in the calculation of the Christoffel matrix will be used to expand this model and demonstrate how reducing the frequency determining dimension will shift the resonant frequency of the device. Other geometries, like the beam resonator, and the exploration of lateral field excited acoustic waves in nanobelts will be discussed as well.

CHAPTER 4

FREE-STANDING ZNO NANOBELT RESONATORS

(2ND GENERATION)

The first ever bulk acoustic resonator based on bottom-up synthesized ZnO belts was demonstrated in Chapter 3. While this result is interesting, there is a great deal of room for improvement with regards to design, fabrication and device performance. As a result, Chapter 4 will focus on four main thrusts: 1) Develop a new fabrication scheme that eliminates the need for non-traditional fabrication techniques like e-beam lithography and FIB and design a process flow that is based solely on the well established methods of photolithography. 2) Scale down the device to work with nano-sized belts in order to study their possible change in properties and push the limits of their sensing capabilities. 3) Realize freestanding nanobelt resonators for high frequency FBAR and low frequency beam resonator applications. Specific device architectures will be fabricated in order to benefit from the characteristic that nanobelts grow naturally freestanding. Capitalizing on this will result in low loss/high Q devices. 4) Develop a new synthesis scheme to site-specifically grow individual ZnO nanowires between two electrodes. Achieving this will eliminate the need for nanomanipulation and result in a process that is completely integratable with a traditional process flow.

One of the key barriers to commercialization of any nanodevice is mass production. While the nanoBAR is the focus of this thesis, mass production would impact the field of nanotechnology as a whole and be applicable to a variety of functional nanodevices. Photolithography will be used to fabricate the device architecture while hydrothermal techniques as described in Chapter 1 will be utilized for synthesis.

4.1 Resonator Redesign

One of the limitations in fabricating a resonator using a top-down approach is the large acoustic impedance mismatch that must exist on both sides of the piezoelectric element. This requires the inclusion of a Bragg reflector on the bottom side of the piezoelectric (SMR) or an air/crystal interface under the resonator (FBAR)[146]. If one chooses to make an air/crystal interface on both sides of the piezoelectric, aggressive processing techniques are required to etch sacrificial layers from underneath the piezoelectric which can cause stress and degradation in the film[146]. As stated, one of the key advantages of ZnO nanobelts is that they are naturally grown to be freestanding. By pre-processing the air/crystal interface prior to laying down the ZnO nanobelt, increased device performance could be realized.

Another way to limit the effects of loss is to utilize the lateral field excitation (LFE) of BARs instead of the thickness excitation (TE) as presented in Chapter 3. Lateral field excitation in resonators is also known as an "electrodeless" technique because the electrode layers are not in the acoustic path[82]. Figure 4.1 shows an LFE resonator fabricated on top of an acoustic reflector. In this configuration the electric field between the two electrodes runs perpendicular to the acoustic wave. This makes LFE devices better suited for sensing applications since the metal electrodes that are usually responsible for acoustic wave scattering are no longer in the acoustic path[147]. In theory, LFE resonators experience higher coupling coefficients and higher Q's when compared to TE devices at all frequencies[82, 148]. This type of excitation along with TE nanoresonators will be the focus of this chapter.

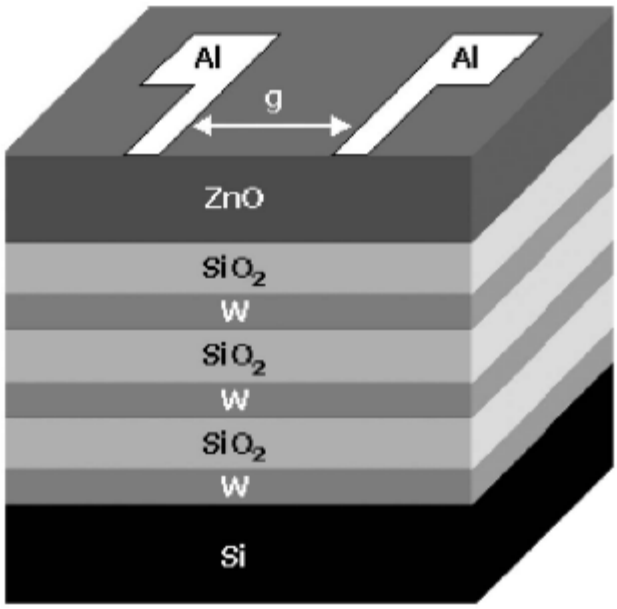

Figure 4.1 Depiction of LFE-SMR[147].

4.1.1 Fabrication

Two distinctly unique processes for fabricating freestanding nanoBARs are described below. The first process enables mass production of the device support architecture using photolithography to help streamline the process resulting in an LFE device. No e-beam or FIB will be required for any step in the process flow; however, individual manipulation of nanobelts is required. The second process involves growing nanowires site-specifically between two electrodes resulting in a TE design. In addition to elimination of non-traditional nanofabrication techniques, this technique would also remove any need for post-synthesis manipulation. Integrating bridged nanowires directly into prefabricated device architecture would be a dramatic leap in the mass production of nanodevices and a step toward commercial nanosystems based on individual 1D nanostructures.

4.1.1.1 Free-Standing Fabrication Utilizing Manipulation

In order to fabricate freestanding nanobelt resonators, a new approach was envisioned to work out the contact issues described at the end of Chapter 3. The FIB has proven to be a very useful tool since it provides a great deal of freedom when designing and prototyping devices. However, certain steps within the process become time consuming (milling large holes and fabricating large contact pads) when compared with alternative techniques. A new process was designed in order to eliminate the need for non-traditional nanofabrication in favor of a traditional photolithography process flow. These devices were designed to incorporate trenches and contact pads into the pre-fabricated support substrate. Patterning, lift-off, dry-etching and wet-chemical etching were used along with some of the manipulation techniques (described in Chapter 2) in order to build the next generation of nanoresonators. New chemicals were also investigated as alternatives to the strong acids and bases used in CMOS and MEMS processing in order to prevent the ZnO nanobelts from being etched.

In order to utilize photolithography exclusively in this redesign, some creative processing solutions were required. The photolithographic process is used in the semiconductor industry to transfer circuit patterns onto a semiconductor wafer. This is done by projecting light through a patterned reticle (or mask) onto a silicon wafer covered with a photosensitive polymer (photoresist). The mask is made up of a glass plate with a layer of chrome on one side. The chrome areas block the light, thereby preventing unwanted regions of the resist from being exposed. In order to deposit the photoresist on a wafer, spin-coating is employed by rotating a wafer at high speed in order to spread the fluid by centrifugal force until a uniform thickness is achieved. The speed at which the spin-coater rotates and the viscosity of the resist will dictate its ultimate thickness. Belts dispersed or manipulated onto specific locations prior to spin-coating are likely to shift their position once spin-coating commences. To deal with this, the electrode material will be sputter deposited on top of the nanobelts to pin them down.

Subsequent patterning will define the electrode regions on top. This will be discussed in greater detail below in the process flow outline[149].

From Chapter 3 it should be noted that the resonator is not just the active piezoelectric material, but includes all of the device fixtures coupled to it. Therefore, a novel approach for achieving a freestanding resonator (along with the electrodes) was required. A full description of the process flow is given below.

A 500 μm thick, 4" (100) silicon wafer was treated and cleaned by soaking it in acetone for 5 minutes. After soaking, the wafer was rinsed subsequently with isopropyl alcohol (IPA), methanol and finally de-ionized water (DI). The wafer was blown dry with nitrogen and baked at 115^{o}C on a hotplate for two minutes to remove any excess moisture.

Figure 4.2 Bare silicon wafer after cleaning, prior to metallization.

A thin 10nm layer of titanium (Ti) was e-beam evaporated on top of the silicon in order to act as an adhesion layer for 200nm of Au which was subsequently deposited.

Figure 4.3 200nm of Au deposited on top of the silicon wafer.

Plasma enhanced chemical vapor deposition (PECVD) was used to deposit a 3 μm thick film on top of the Au layer. PECVD uses reactant gases; in this case, 5% SiH_4 in helium was chemically reacted with N_2O in a Unaxis PECVD chamber at a pressure of 900 mTorr. The ions in the plasma are in an excited state and easily react with the silicon wafer.

Figure 4.4 SiO_2 insulation layer deposited using PECVD.

1827 Shipley photoresist was spun onto the surface of the SiO_2 at 1000 RPM in order to achieve a film thickness of approximately 5μm. A Quintel Corporation Ultra μ line series mask aligner with a UV wavelength of 405nm was operated at 200mJ/cm^2 in order to transfer the necessary pattern from a chrome reticle (designed in AutoCAD and built by PhotoSciences) into the photoresist. After the exposure was complete, the pattern was developed in MF-319 developer for 2 minutes to reveal the pattern. The wafer was then rinsed with DI and hard baked at 115^{o}C for 4 min. The pattern defines five square regions which were dry etched to reveal the underlying gold layer.

Inductively coupled plasma etching (ICP) is a dry etch process that uses reactive ions to anisotropically etch away the insulator from the open regions in the photoresist. Each of the ions reacts chemically and there is no physical bombardment of the surface, as in sputtering.

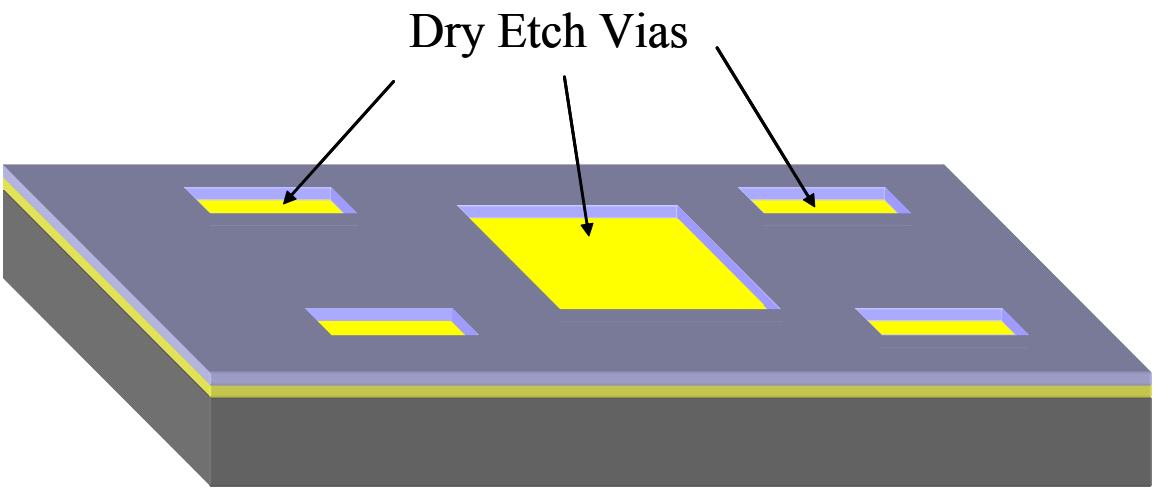

Figure 4.5 Trenches etched into the SiO_2 layer to reveal the underlying Au.

Next a 2.7μm layer of Shipley 1827 photoresist is spun across the surface of the wafer at 3000 RPM to fill the trenches and planarize the surface. It is necessary to step away from the process flow for a moment to discuss a problem that typically plagues the photolithographic process and explain how it is being exploited here as an advantageous solution. When spin-coating into deep pits in a wafer, the thickness of the resist inside the pit is not equivalent to that on the surface. One of the characteristics of a quality resist is that during spin-coating, it does not conform to surface features but eliminates any roughness by filling in voids and planarizing the wafer to form a new surface. Figure 4.6 depicts this phenomena using Shipley 1827 photoresist spun at 3000 RPM to achieve a resist thickness of 2.7μm.

Figure 4.6 Depiction of how photoresist planarizes a surface with 3μm deep features affecting the thickness in these regions. The model here is for Shipley 1827 resist spun at 3000 RPM.

A 2.7μm thick layer of Shipley 1827 resist requires a 200mJ/cm^2 dose in order to properly transfer the pattern in a reticle to the polymer layer. The average intensity of the mask aligner in this case is 25mW/cm^2, which means that the length of time necessary to successfully transfer the pattern is eight seconds. Since the resist inside the pit is 5.7μm and the resist on other regions of the wafer is the desired 2.7μm, the deep regions in the wafer will be underdosed, and the photoresist will remain behind after development. This is depicted in Figure 4.7 below.

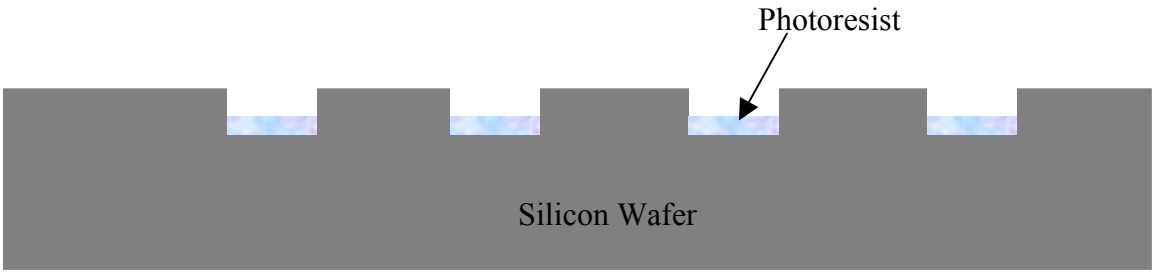

Figure 4.7 Depiction of how resist can be left in deep pits and trenches when underdosed.

This behavior is usually considered disruptive to further processing; however, it was used to our advantage by intentionally under-dosing the photoresist inside the trench so that it would act as a sacrificial layer during fabrication. Once fabrication is complete, O_2 plasma can be used to burn out the unwanted polymer, leaving a self-supporting structure above the trench.

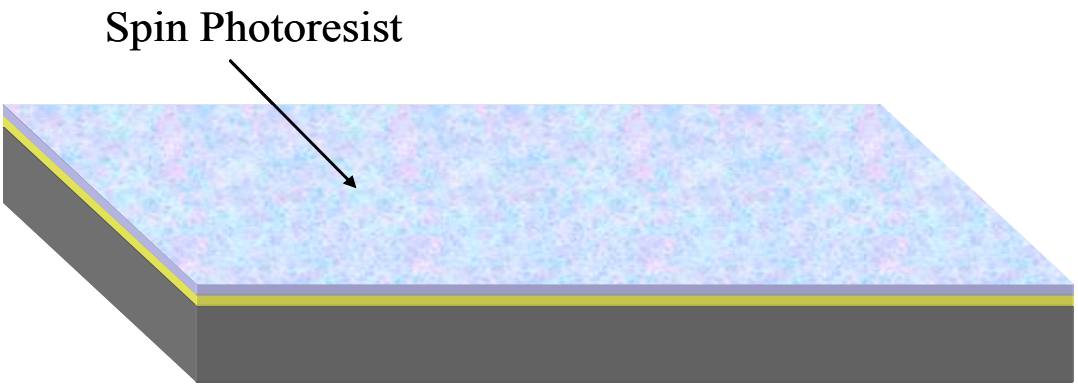

Figure 4.8 Photoresist spun across the surface to fill the deep trenches and planarize the surface.

Moving along with the actual process, at this point, the wafer is diced into small chips with nine individual devices in a 3X3 array. Each chip is about 2mm X 2mm in size. This was done so that it was not necessary to manipulate 1000's of belts before being able to complete the process. This way it is possible to manipulate a few belts at a time to finish out the process in order to optimize any unforeseen problems that might arise during testing. This is the 3X3 array depicted in Chapter 2, Figure 2.32.

Next, individual chips (no mask) are exposed under the UV lamp at 300mJ/cm^2 to under-dose the photoresist. The chip is developed in MF-319 developer in 30 second time intervals in order to inspect the surface and monitor the progress in between. As a result, photoresist deposit fills only the trench cavities created by the ICP process.

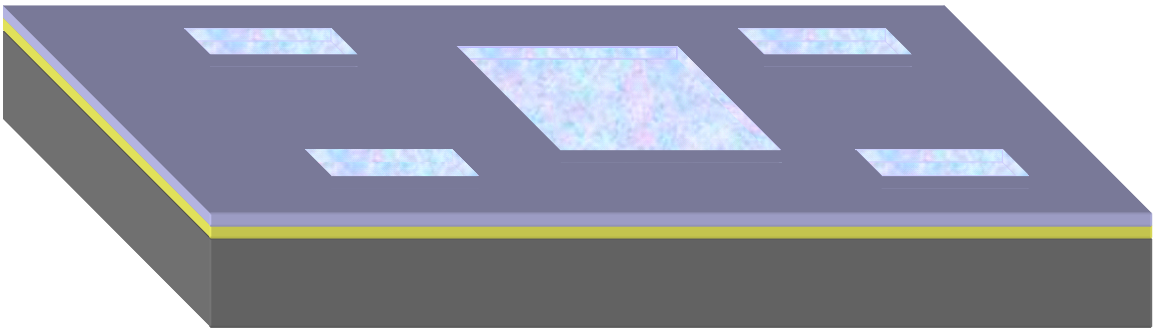

Figure 4.9 In this figure it can be seen how photoresist is left to fill the cavities created by the ICP.

Next, manipulation was accomplished by using one or all of the three techniques described in Chapter 2. Since the surface is planar relative to the surface oxide, the nanobelt is sufficiently supported across the gap.

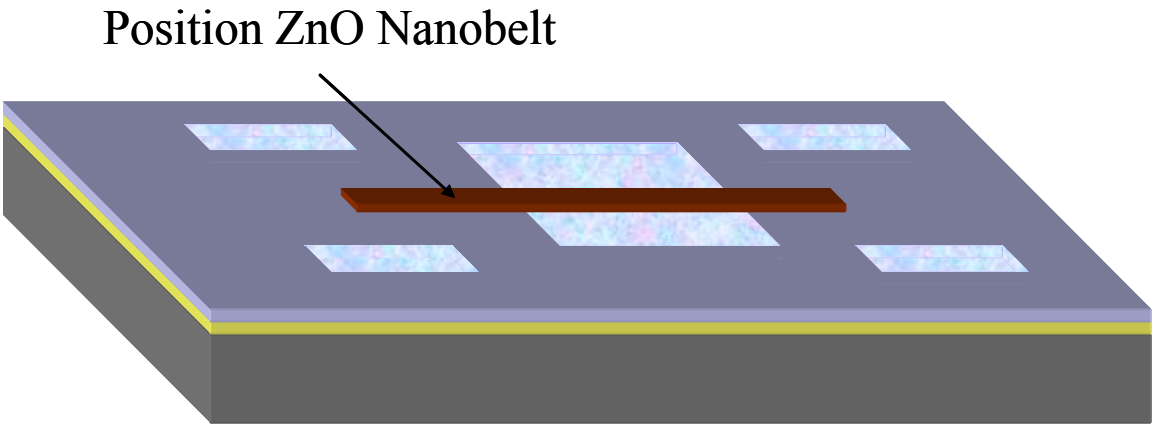

Figure 4.10 Figure showing the nanobelt lying across the trench filled with photoresist after manipulation.

Next, 200nm of aluminum was sputtered on top of the nanobelt to pin it for spin-coating. The aluminum layer was also patterned in the next step to serve as the drive and sense electrodes.

Figure 4.11 Sputtering of aluminum to conformally coat the belt and wafer.

Photoresist was spun again at 3000 RPM and the chip was realigned in the mask aligner to define the electrode regions on either side of the nanobelt. A 10g $K_3Fe(CN)_6$:1g KOH: 100ml DI solution was used as an aluminum etchant since it is capable of etching aluminum preferentially without attacking the ZnO.

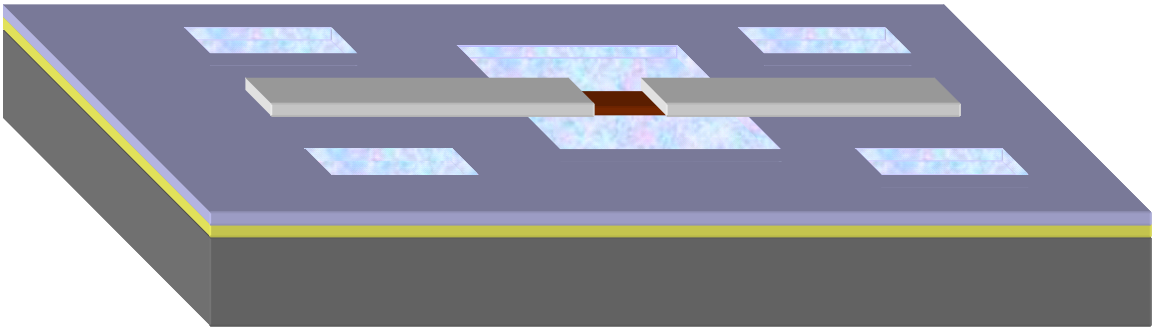

Figure 4.12 Aluminum drive and sense electrodes patterned on top of the nanobelt for lateral field excitation of the ZnO.

Finally, O_2 plasma was used to burn away the remaining polymer, defining a nanobelt resonator freely suspended across the gap.

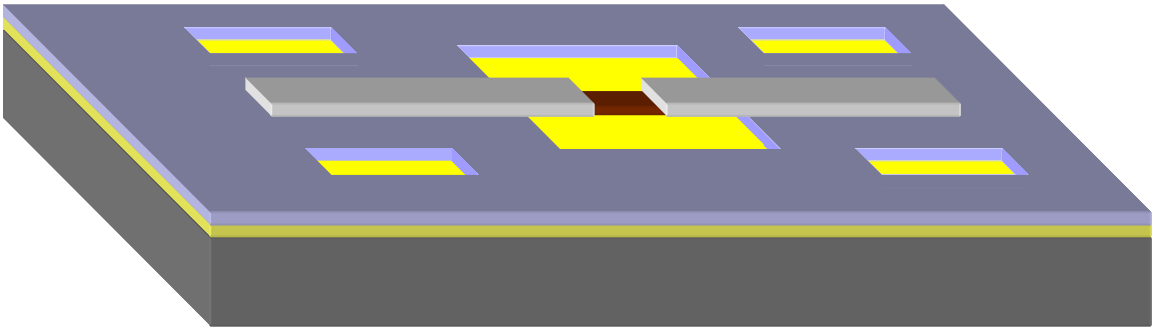

Figure 4.13 Free-standing nanobelt resonator.

The figure below depicts the device architecture fabricated excluding the step to include a nanobelt. This was done to insure the polymer sacrificial layer did its job in keeping all electrical contacts open. The small gap that was intentionally fabricated between the drive/sense electrodes and the underlying ground that runs beneath the SiO_2 can be seen. Even though it is difficult to confirm this with an optical/SEM image, a

voltmeter was used to probe the electrical circuit and each of the three electrodes measured open, indicating that no short had been created by the process.

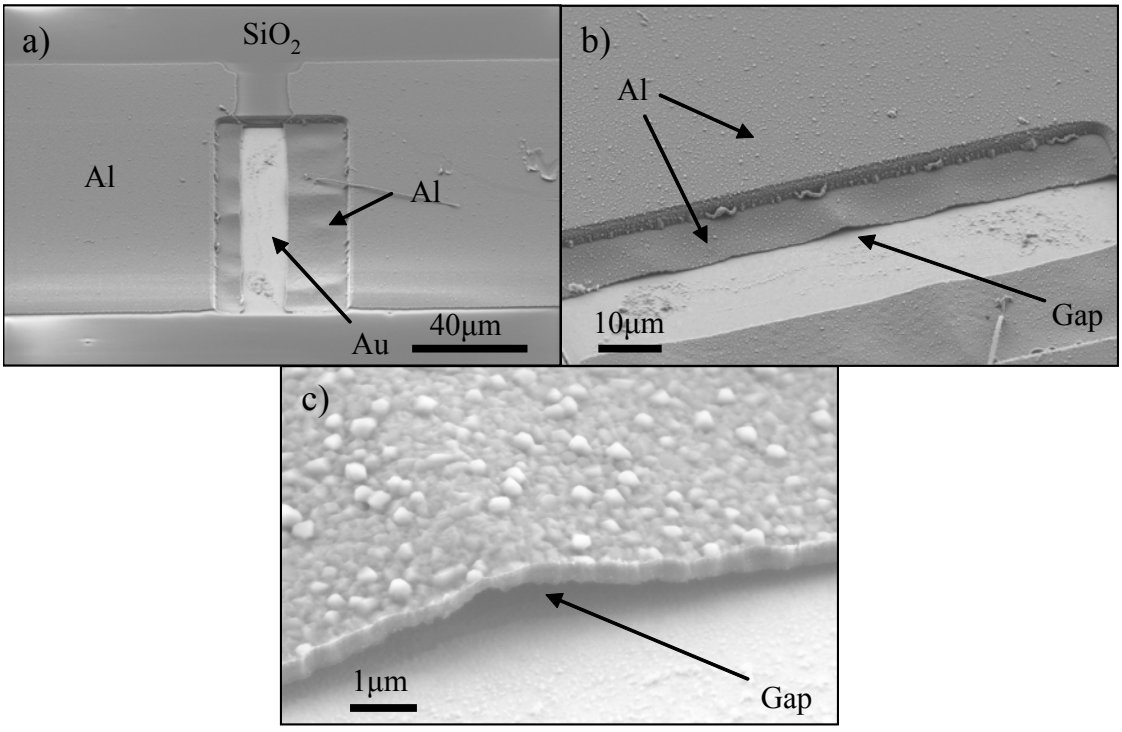

Figure 4.14 Series of images depicting the gap created between the drive/sense electrodes and the ground. (a) Tilted side view (b) Showing the aluminum flap suspended over the trench (c) Close-up to show the gap between the aluminum and gold.

Since the process has been demonstrated to be useful, it was then implemented along with manipulation to fabricate working nanobelt resonators. Figure 4.15 depicts an actual device where a ZnO belt has been successfully integrated into the prefabricated architecture. All electrodes were tested again and still remained open from each-other.

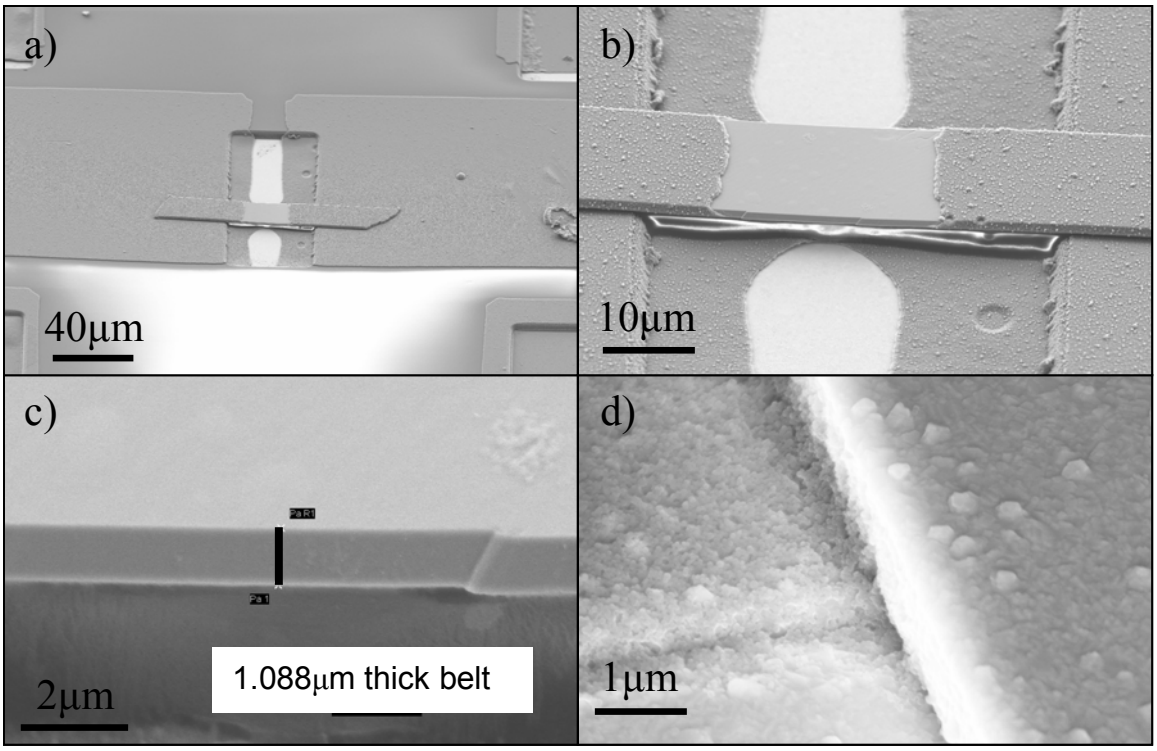

Figure 4.15 Integration of a ZnO belt into the device architecture. (a) ZnO belt integrated in between the electrodes. (b) Zoomed in view of the same. (c) Side view of belt showing the C-plane which is determined from the side faceting. (d) Close-up of the aluminum connecting the belt to the contact pad.

It can be seen from Figures 4.15b and 4.15c that the belt has stacking faults on the side facets indicating that this is the $[01\bar{1}0]$ fast growth direction.

In some cases the nanowires were placed on top of the electrodes, as in Figure 2.33. The figure is re-shown here to refresh the reader. Both of these configurations result in the lateral field excitation of ZnO nanobelts.

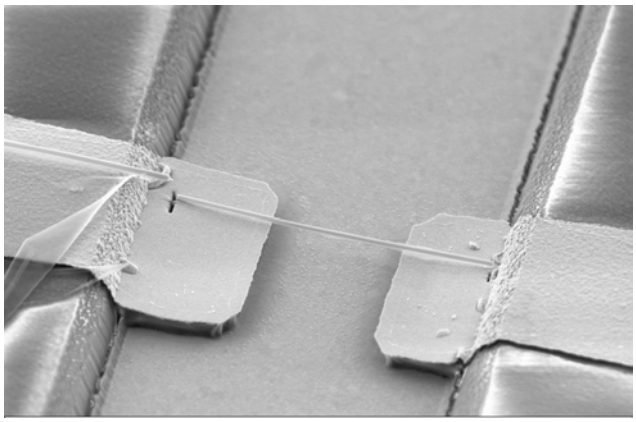

Figure 4.16 Polar surface dominated nanobelt spanning two freely suspended electrodes.

Discussion on testing these devices will be presented in the results section. First, the processing method for growing nanowires site-specifically between two electrodes will be introduced so that all the results may be addressed at the same time.

4.1.1.2 Mass Production Without Manipulation

The above process enables fabrication of resonators using nanobelts, but it only allows for fabrication of one device at a time. For these new devices to have any real commercial implications it is necessary to consider the cost of manufacturing. Manipulation of individual nanostructures would be cost-prohibitive to any commercial applications these systems might have, making a bulk process necessary. Some people have attempted to deal with this by growing nanostructures in desired positions or aligned arrays[150]. Others have looked to new techniques like dip-pen lithography[151] and micro-contact printing[152] of functional molecules to assist with alignment. However, it ultimately forces re-tooling of a FAB and benchmarking of a process in order to incorporate these techniques into an assembly line.

Using mainstream techniques like photolithography to manufacture nanodevices, makes the utilization of nanowires in MEMS/NEMS and CMOS systems more readily integratable. A technique to grow ZnO nanowires site-specifically between two

electrodes will be explored for the mass production of nanoresonators. This technique benefits from full CMOS and MEMS process flow integration of nanomaterials into prefabricated device architecture, making the need for post-synthesis manipulation obsolete.

There has been some recent success in bridging individual Si nanowires using MOCVD to grow them across a microscale trench on a Si or silicon on insulator (SOI) substrate [153, 154]. The PVD process described in Chapter 1 has also been used in conjunction with a ZnO seeding layer to laterally grow ZnO nanowires across a Si trench [155]. Unfortunately, the high temperatures required for these deposition techniques limits their application in many areas where high temperatures could induce unwanted oxide formation, degrade metal contacts and initiate diffusion of localized dopants into unwanted regions of a device. Using a low temperature process like hydrothermal synthesis can be seen as an ideal solution when designing devices with these constraints in mind. In addition, hydrothermal synthesis can be advantageous when considering the integration of nanomaterials with polymer substrates for applications in flexible electronics [75, 76, 156].

In this section, hydrothermal synthesis is demonstrated for growing similar structures at much lower temperatures (60-80^{o}C). Large-scale, laterally bridged ZnO nanowires with diameters ranging from 50nm to 1μm have been successfully grown across a trench, in between two gold electrodes, with a separation distance of 500nm and 10μm. The process began with the deposition of 100nm of SiO_2 on a 4-inch silicon wafer (*p*-type, <100>, 0.01 Ω.cm) (Figure 4.17) by way of PECVD. Lithography was used to pattern AZ5214 negative photoresist. The pattern was subsequently transferred into SiO_2 via dry etching using a Plasma-Therm ICP etcher. The Bosch process was then employed to fabricate deep trenches (~100μm or more) into the underlying silicon utilizing the SiO_2 layer as a hard mask. Next, a 100nm-thick gold coating was deposited via sputtering onto the wafer to conformally coat the surface and the side walls of each

trench. Finally, the top SiO_2 layer was lifted off using hydrofluoric acid (HF), taking the surface gold layer with it. A second substrate was fabricated in a similar fashion to the first, only a ZnO seeding layer was deposited to coat the inner wall of the trench as well.

The growth of ZnO nanowires was initiated by suspending either the substrate coated with gold or one with ZnO seeds in a Pyrex glass bottle filled with an equal molar aqueous solution of zinc nitrate hexahydrate ($Zn(NO_3)_2.6H_2O$, 0.01 M) and hexamethylenetetramine ($C_6H_{12}N_4$, 0.01 M) at 80°C. The reaction time ranged from 1-4 hours for both substrates. After synthesis was complete, the substrates were removed from the solution, rinsed with de-ionized water, and then dried in air at 65°C overnight. Figure 4.17 shows a schematic diagram of the synthesis strategy.

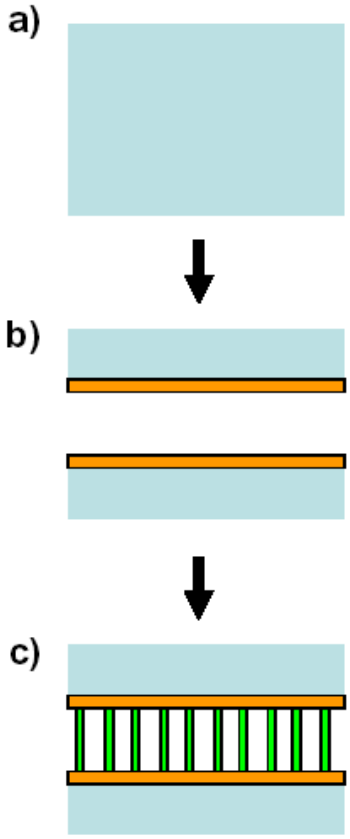

Figure 4.17 Fabrication and growth processes for growing bridged nanowires across trenched electrodes[157].

Figure 4.18 is a set of SEM images of the as-grown nanowires on the gold-coated substrate. The left part of Figure 4.18a shows the nanowires selectively growing from one of the side-walls of the gold electrodes at 10μm separation distance, but without touching the opposite side. By increasing the growth time, the nanowires grew longer and eventually touched the second gold electrode (Figure 4.18b).

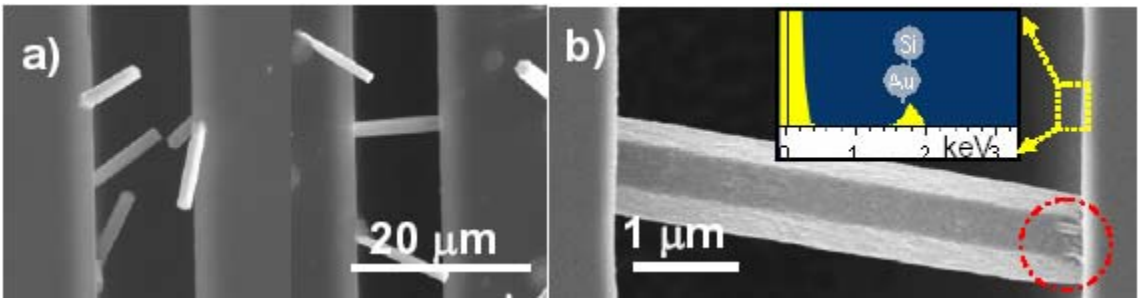

Figure 4.18 SEM images showing various configurations of as-grown nanowires bridging across Au/Si electrodes[157].

The diameter of the wires were measured to be ~2μm. From the magnified SEM image in Figure 4.18b, it can be seen that the wire grew across the trench from right to left, as shown by the rooted region on the right side of the trench. An inset of an EDS spectrum taken from the side wall confirms the existence of the gold layer on Si.

Using a ZnO seeding layer enabled a large scale, well aligned array of nanowire bridges. Figure 4.19 is a set of SEM images showing horizontally aligned nanowires across a 500nm trench array. In Figures 4.19a and 4.19b, sparsely grown ZnO nanowires span across each trench, forming a network of horizontal nanowire bridges. These nanowires have a uniform diameter of ~50nm. As the growth time increased, the densities of the nanowire networks also increased, as indicated in figures 4c and 4d. Figure 4.19f is a magnified SEM image showing the densely packed nanowire bridges embedded in two trenches. A 50nm ZnO seed layer can be seen as indicated by the orange arrow[157].

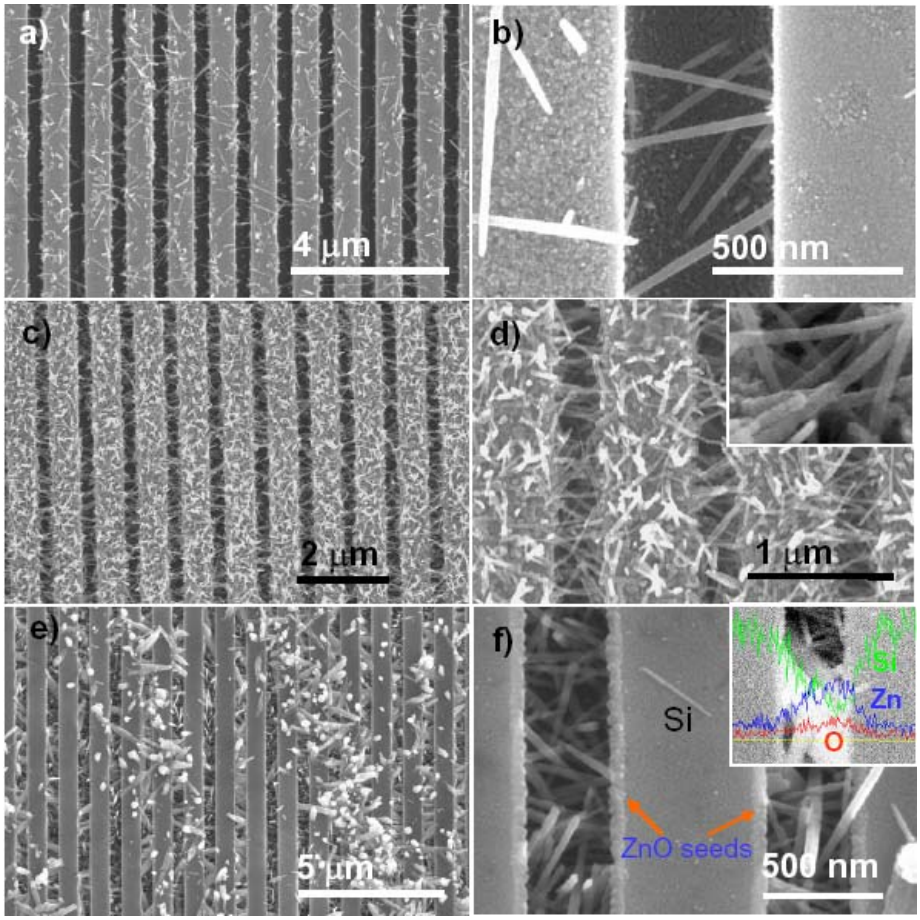

Figure 4.19 Bridged ZnO nanowire arrays across a 500-nm nanotrench array with different densities, where (a) and (b) are the most sparse ones, (c) and (d) are the dense ones, and (e) and (f) are the dense ones after removal of the ZnO nanowires from the top of the trenches.

This technique is simple and results in large networks of nanowires growing across a gap in between two electrodes. Expanding on this technique, a new methodology was developed to physically pattern the inner walls of a trench with specific dimensions with the intent to locally control the position of a single nanowire. To do this, further understanding of the synthesis mechanism is required.

Figure 4.20 shows a flat gold-coated deposition substrate (with no trenches) that was lowered into the synthesis vessel and fixed perpendicular to the liquid surface. This was done to determine the optimal depth inside the solution for growing ZnO nanowires. It can be seen from the figure that the highest density growth is obtained directly at the gas/solution interface where a thin line of dense wires can be seen to precipitate. The nucleation density quickly drops off just below the liquid surface and continues to decrease deeper into the solution. As a result, a new growth substrate was designed and fabricated in order to benefit from the high density synthesis that results at the interface. To do this it was necessary to etch through an entire wafer from the backside so that the inner walls of the trench were exposed to both the liquid and gas regions.

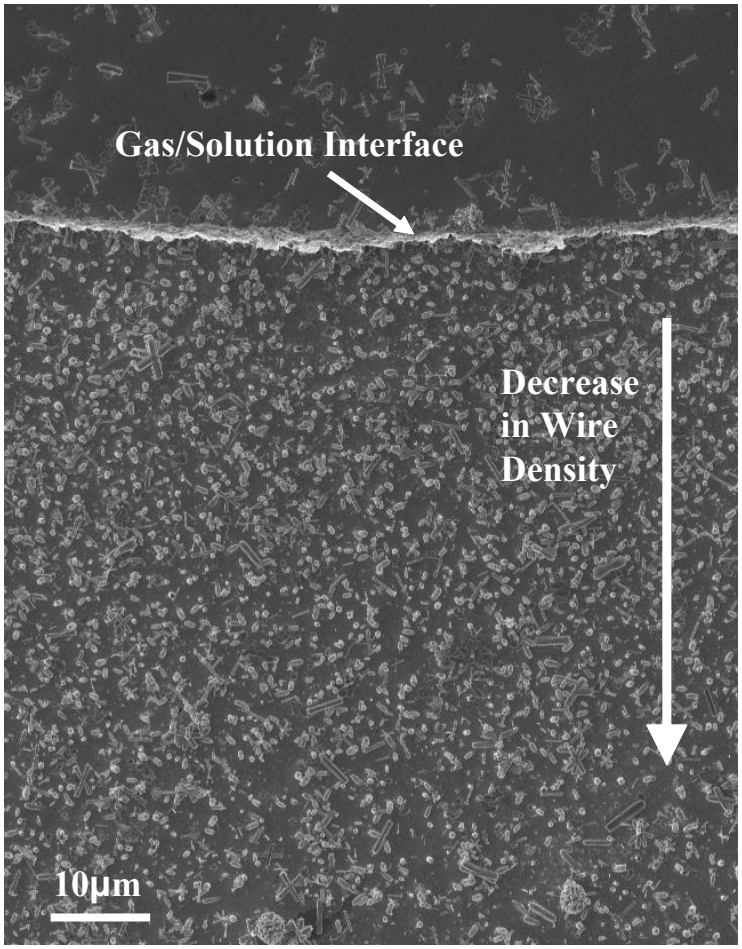

Figure 4.20 Gold deposition substrate showing nanowire density as a function of depth in the synthesis solution.

The following process flow began with a double-sided polished (100) wafer and is outlined schematically starting with Figure 4.21 and ending with Figure 4.32. Having both faces of the wafer polished smooth was necessary since photolithography was performed on both sides. Next, a 3μm thick film of SiO_2 was deposited on top of the Si using PECVD. The wafer was flipped over and deposited with 400nm of Si_3N_4 via PECVD on the back side. Both sides of the wafer were spun with 1827 photoresist at 3000RPM, and photolithography was used to pattern large square openings in the photoresist on the backside nitride layer. Buffered oxide etchant (BOE) was used to etch through and transfer the pattern to the nitride thin film to create a nitride hard mask for wet etching through a 500μm thick Si wafer. Photoresist was spun on the front side of the wafer to protect the 3μm oxide layer from being etched by the BOE. Once the pattern was transferred, the photoresist was stripped in acetone and the wafer was inspected for defects. Next, the wafer was fixed inside a tan wafer holder with an opening on one side and the nitride layer facing out. The wafer was secured using a series of plastic bolts and rubber o-rings to prevent KOH from leaking through to the other side and contaminating the oxide layer. A large bath of 45% KOH etching solution was heated on a hotplate and stirred with a magnetic stir bar until the solution temperature reached 80^{o}C. Once the bath had reached the desired temperature, the tan holder, along with the wafer, was submerged into the solution and secured for a period of 24-36 hours for anisotropic etching of Si. The last five hours of the etching process was monitored closely to identify when the through-etch had come to completion. Once finished, the holder was taken out of the KOH, the wafer was then removed from the holder, rinsed with DI, blown dry with nitrogen, and inspected for defects that might limit further processing. At this point, the oxide layer formed 1000s of individual membranes on the other side with dimensions of 150μmX150μm square. Also, alignment marks patterned on the back side had also etched through so that they were visible from the front. Assuming that the through-etch was successful, all membranes were intact, and alignment marks visible, the wafer was

flipped to the front side and spun with 1827 resist at 1000RPM to achieve a resist thickness of ~5.7µm. The wafer was then positioned inside the mask aligner to transfer the next pattern from a reticle into the photoresist. This opened a series of rectangles at the center of the freestanding membrane. There were six regions on the wafer and each was defined by the mask to have different rectangular dimensions. Each had an equivalent length of 100µm but varying widths of 150µm, 100µm, 50µm, 25µm, 10µm and 5µm. Once the pattern was revealed in the photoresist, the wafer was transferred to the ICP etcher in order to etch through the oxide. This created a series of trench walls that could then be reached from both sides of the wafer. Next, a thin gold layer was sputter-deposited on top of the wafer to coat the surface as well as the inner side walls. SEM micrographs of the as-fabricated substrate can be seen in Figure 4.27. A full representation of the masks designed for this process can be seen in Appendix A.

Figure 4.21 Step1—Double-sided polished Si wafer.

Figure 4.22 Step2—3µm thick film of SiO_2 is PECVD deposited on the top-side.

Figure 4.23 Step3—PECVD nitride is deposited on the back-side.

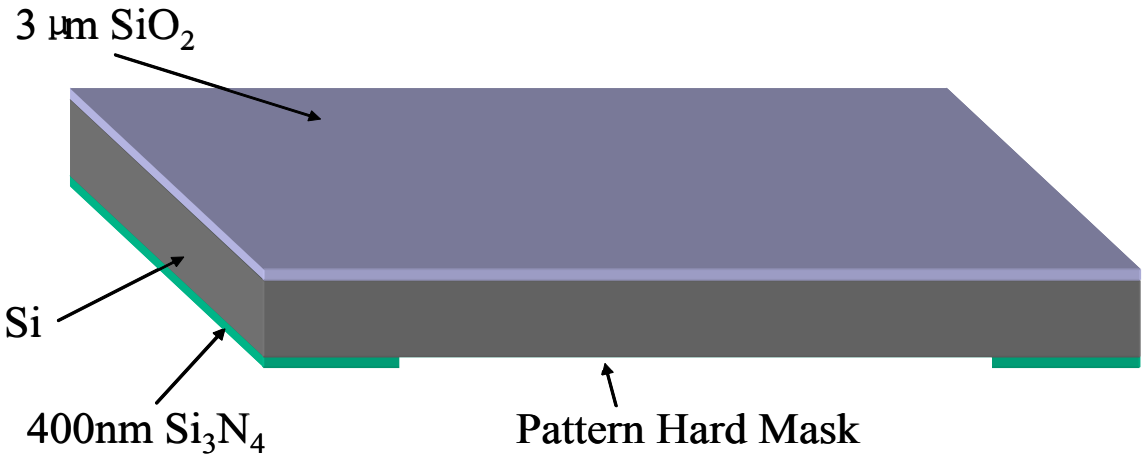

Figure 4.24 Step4—PECVD nitride is etched in BOE on the back-side.

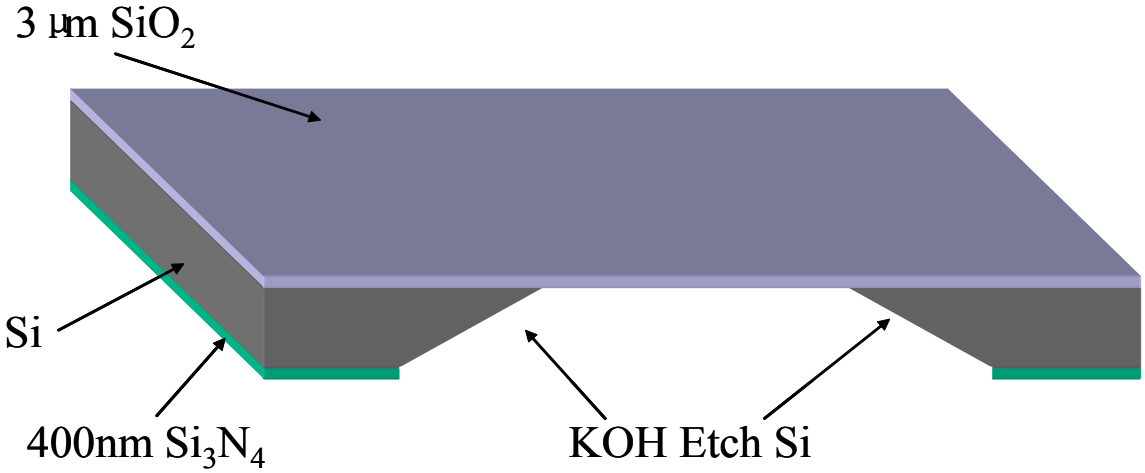

Figure 4.25 Step5—Wet chemically etched Si with 45% KOH solution to create freestanding SiO_2 membranes.

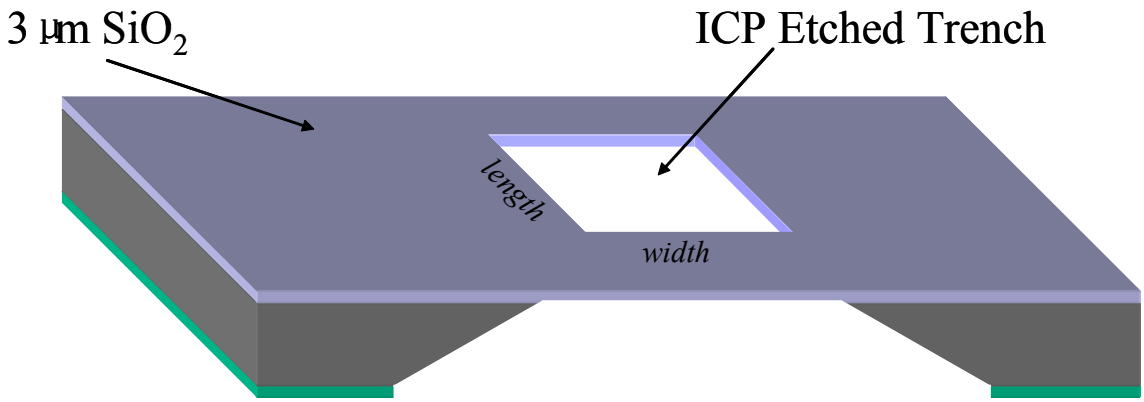

Figure 4.26 Step6—Trench etched into the oxide membrane to create an opening that could be reached from both sides.

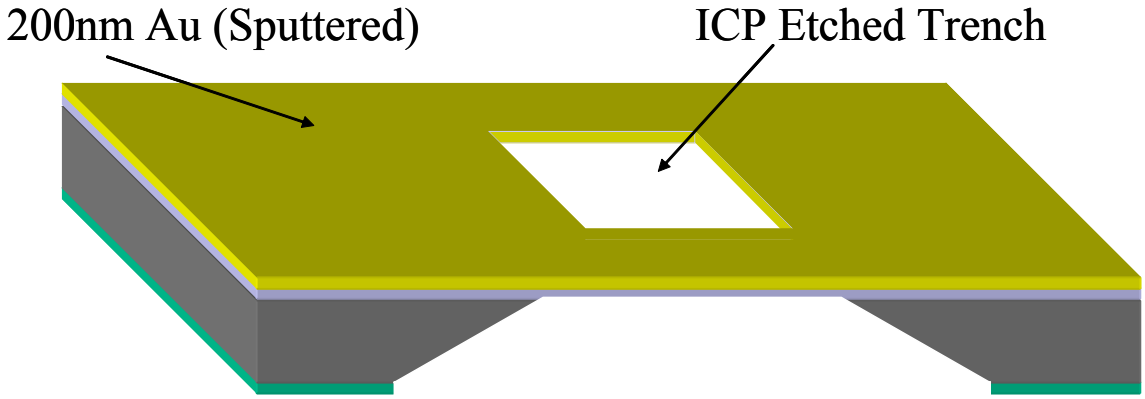

Figure 4.27 Step7—200nm sputtered gold layer coats the top surface as well as the inner walls of the trench.

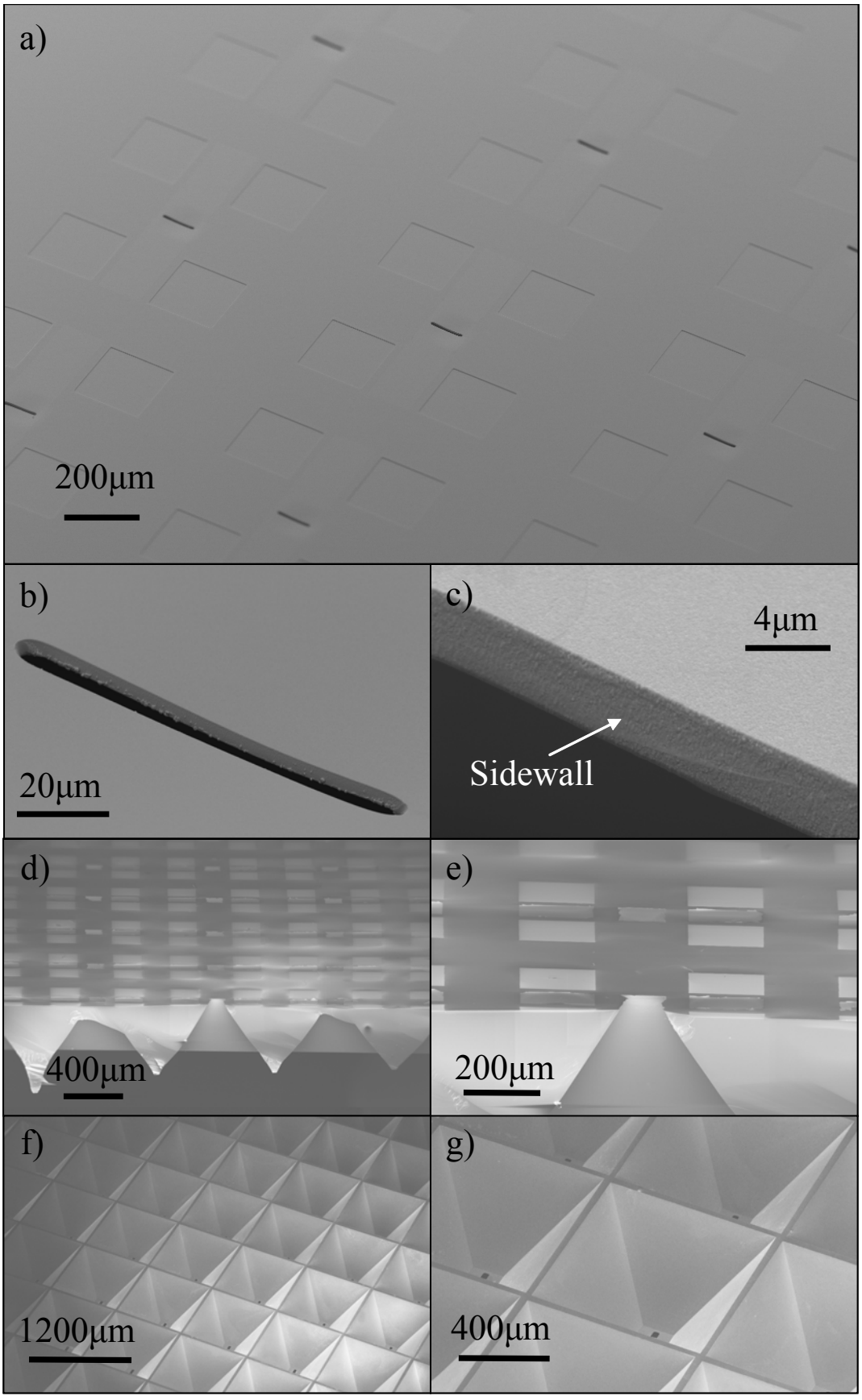
a)
200µm
b)
20µm
c)
4µm
Sidewall
d)
400µm
e)
200µm
f)
1200µm
g)
400µm

Figure 4.28 SEM micrographs of the fabricated substrate. a) Topside showing multiple trenches. b) Close-up of a single trench. c) Close-up of a Au trench sidewall. d) Cross-section of the substrate. e) Close-up of (d). f) Backside showing the Si through etch. g) Close-up of a few membranes seen from the back of the wafer.

At this point the sample is ready for synthesis; however, further processing can add additional functionality by patterning a thin gold strip inside the trench that runs back to large contact pads. To do this, 1827 resist is spun across the surface of the substrate. Due to the high viscosity of the resist, a self-supporting polymer meniscus spans the etched trench at the center of the membrane. As a result, the resist coats the inner walls of the trench, protecting the gold layer from further processing. The substrate is then exposed to UV light to pattern the photoresist on the surface as well as inside the trench. Figure 4.29 shows optical microscopy images of a polymer bridge that spans the trench at the center.

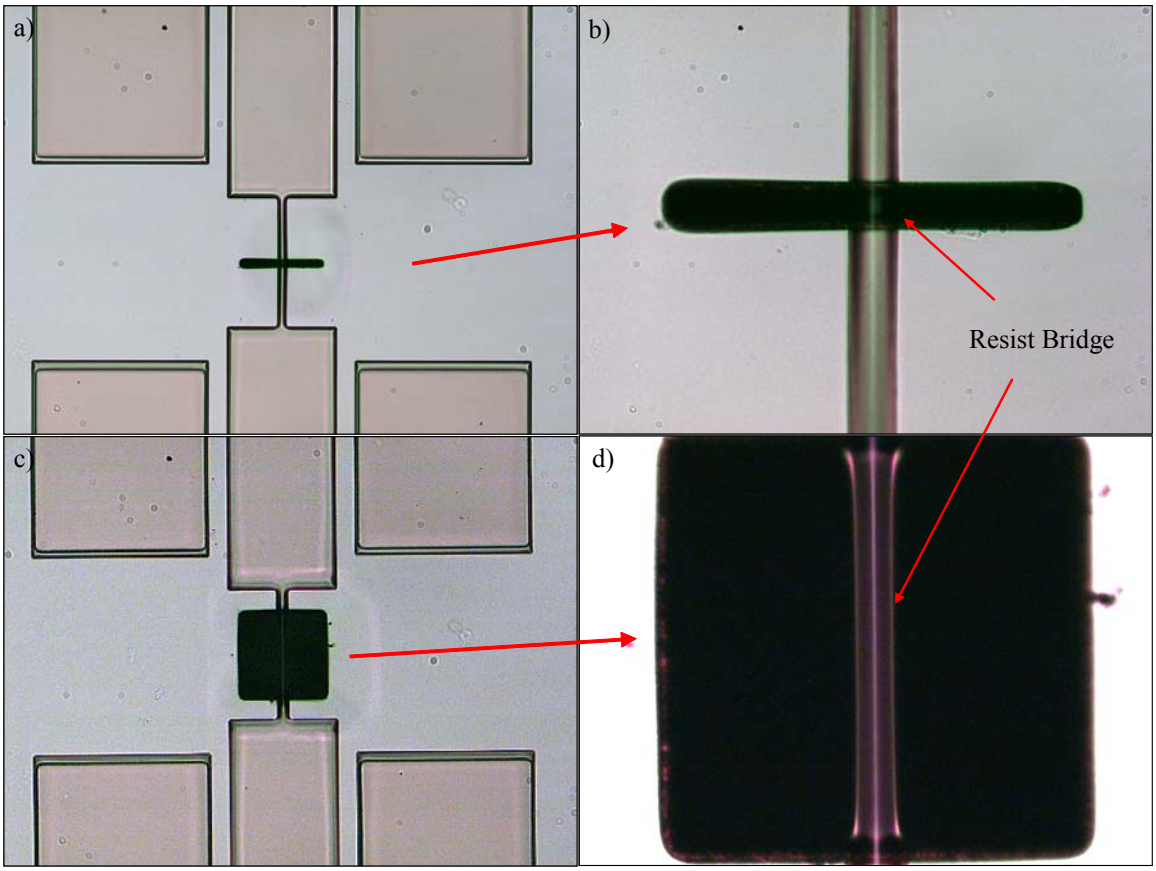

Figure 4.29 Step8—Resist bridge spanning a 10μm gap (a and b) and a 100μm gap (c and d). It can be seen that the resist coats the side walls of the trench only in the center where it spans.

The result is a pattern that protects the inner Au wall at the center of the trench so that the unprotected regions to the left and right can be etched using a potassium iodide gold etchant solution (4g KI:1g K_2:40ml DI) with an average etch rate of 0.5-1.0 μm/min[25]. A schematic of the processing step can be seen in Figure 4.30 along side actual SEM image of the result.

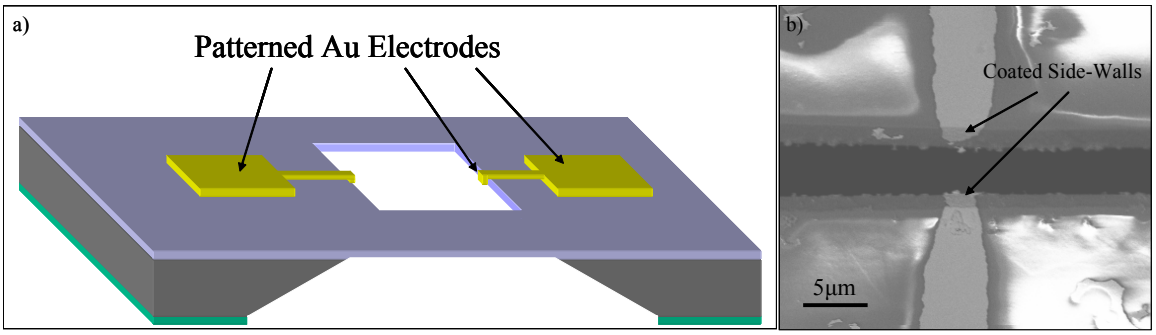

Figure 4.30 Step9—(a) Schematic of process for patterning the inner trench walls by etching the gold layer with KI (b) SEM micrograph of the actual fabrication.

With the inner walls of the trench coated with gold, the substrate can be positioned inside the synthesis vessel in such a way that it floats upside-down on top of the solution, as shown in Figure 4.31. This will put the two side walls right at the gas/solution interface resulting in growth in the trench as shown in Figure 4.32. Different experiments may be performed by controlling the concentration of ions in solution, temperature, time, and substrate depth to control the density of the nanowire deposition.

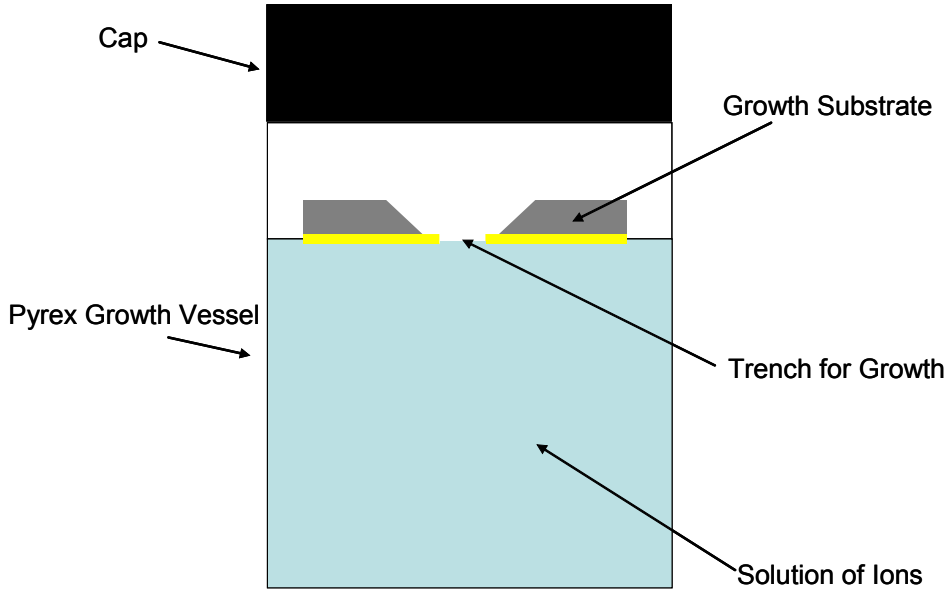

Figure 4.31 Synthesis vessel with as-fabricated substrate turned upside-down inside the bottle to generate nucleation and growth of nanowires at the interface, between the trench walls.

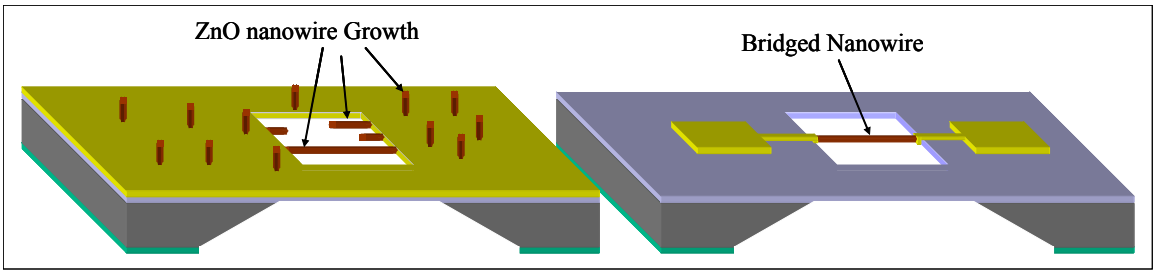

Figure 4.32 Schematics of the expected results using either substrate for synthesis.

Initial synthesis results can be seen in the following set of images. In the first series, the deposition substrate is submerged slightly below the water line so that the cups on the backside of the wafer are also filled with the synthesis solution. This was done to more closely resemble the synthesis conditions of the bridged growth observed in the earlier experiments in order to ensure reproducibility before altering the experiment conditions further. Bridged growth can still be achieved using the new design.

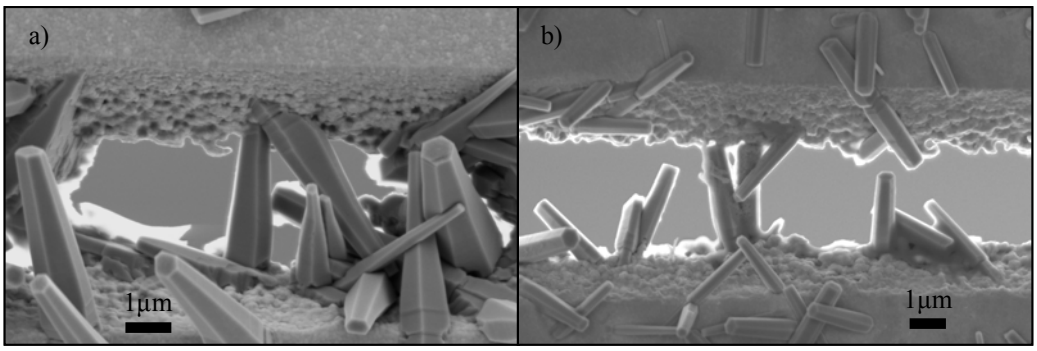

Figure 4.33 Figure showing ZnO nanowires spanning a 5μm trench to contact both side walls.

Conducting synthesis on the patterned substrates resulted in preferential nanowire nucleation and growth on the gold regions over SiO_2, as shown in Figure 4.34. There is some growth on SiO_2; however, it is much less dense and little bridging is observed. This could be important for large-scale fabrication of nanodevices given that only the wires in direct contact with both electrodes will be incorporated into the function of the

nanodevice. If the gold contacts can be made small enough to nucleate a single nanowire, synthesis can be allowed to take place in other regions without interfering with device performance.

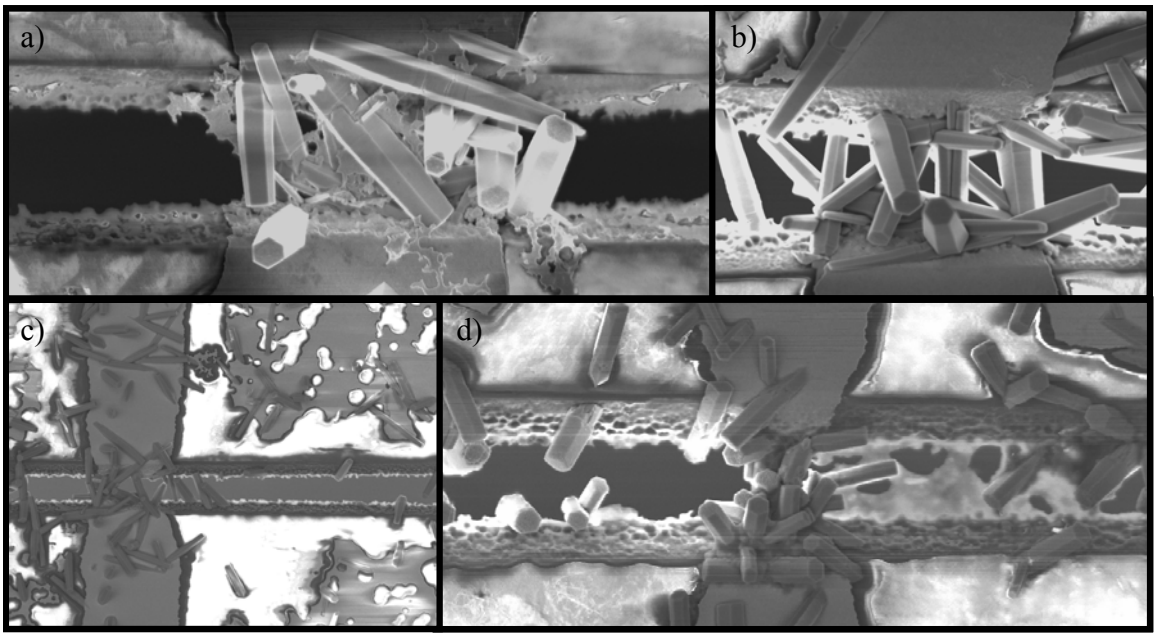

Figure 4.34 Four SEM micrographs showing preferential nanowire nucleation and growth on gold relative to SiO_2.

In one instance it was possible to nucleate a single wire from one side to the other (Figure 4.35) without generating other high density growth to block its path. The nanowire was actually growing from one trench wall into a small gold agglomerate that formed as an artifact on the other side. It would seem that this small piece of gold was unetched in the KI solution during fabrication resulting in the defect. Fortunately, sufficient contact was made between the sidewall and the agglomerate, which was confirmed by the conductivity measurements made on the individual nanowire (as shown in Figure 4.35b).

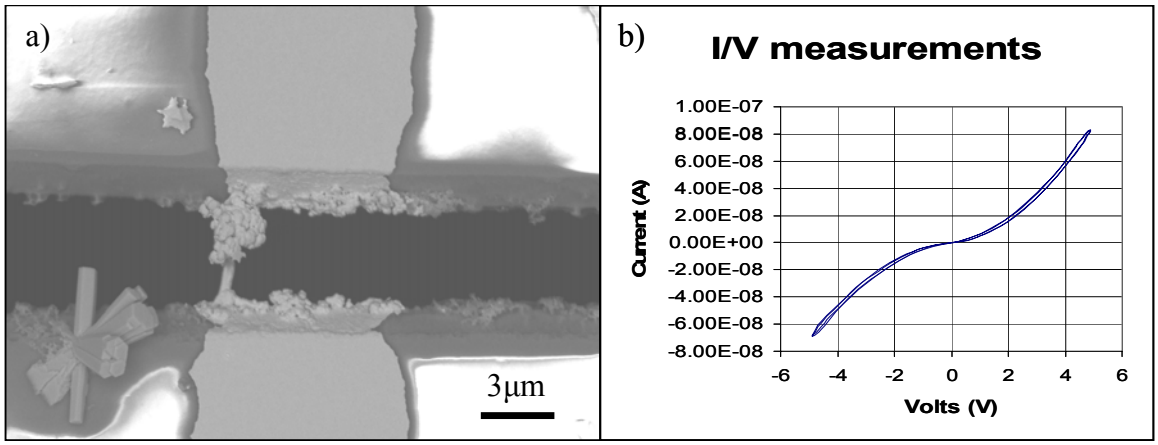

Figure 4.35 (a) Single nanowire grown between two patterned electrodes (b) I/V measurements from the wire.

The measurement was taken by probing the sample with the same tungsten probes used for manipulation in Chapter 2. Both probes were connected through a signal generator to a picoammeter. The signal generator supplied a 0.5Hz triangle wave with an amplitude of 5V. While sweeping the voltage, the current was measured through the picoammeter[158].

It can be seen from Figure 4.34 that the nanowires do not typically grow completely perpendicular to each of the sidewalls. The result in Figure 4.35 is a fortuitous occurrence that has not yet been replicated. The nanowires grow randomly and in a weed-like fashion, likely due to sidewall surface roughness. Since ICP did not reproducibly generate sufficiently smooth sidewalls, a few membranes were purposefully fractured with a tungsten DC probe tip. They were punctured in such a way as to preserve the left side of the trench that was fabricated by ICP while a clean break was generated in the glass membrane on the right side, resulting in a smooth sidewall. Once this was done on a series of membranes, gold was sputtered to coat both the rough trench wall and the smooth trench wall. This is not a common procedure that should be worked into a process flow, but it is useful for determining the effect of surface roughness on

synthesis. It is clear from Figure 4.36 that surface roughness plays a large role in whether or not the nanowires grow perpendicular to the surface.

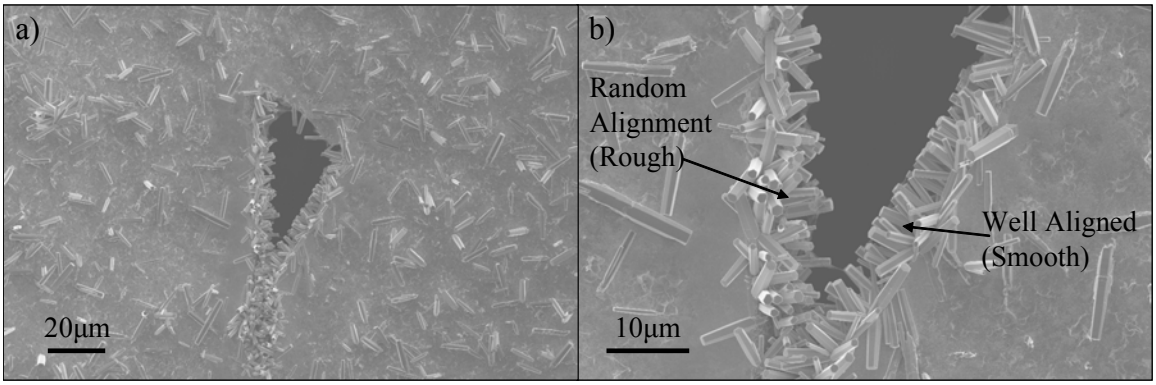

Figure 4.36 Intentionally-broken membrane used to demonstrate the effect of surface roughness on growth orientation of the nanowires.

Surface roughness is going to be an important parameter to control in order to achieve high device yield using this technique since the more nanowires growing perpendicular, the higher the likelihood they will bridge.

It should be observed that the density of nanowire growth inside the trench is much higher than that on the surface of the membrane. For this synthesis run, the membrane was still submerged slightly below the liquid level. Positioning the trench at the gas/liquid interface resulted in a high density, continuous network of nanowires growing between all four side-walls of the trench (Figure 4.37). The conductivity of this thin film of nanowires was measured and is shown in Figure 4.38.

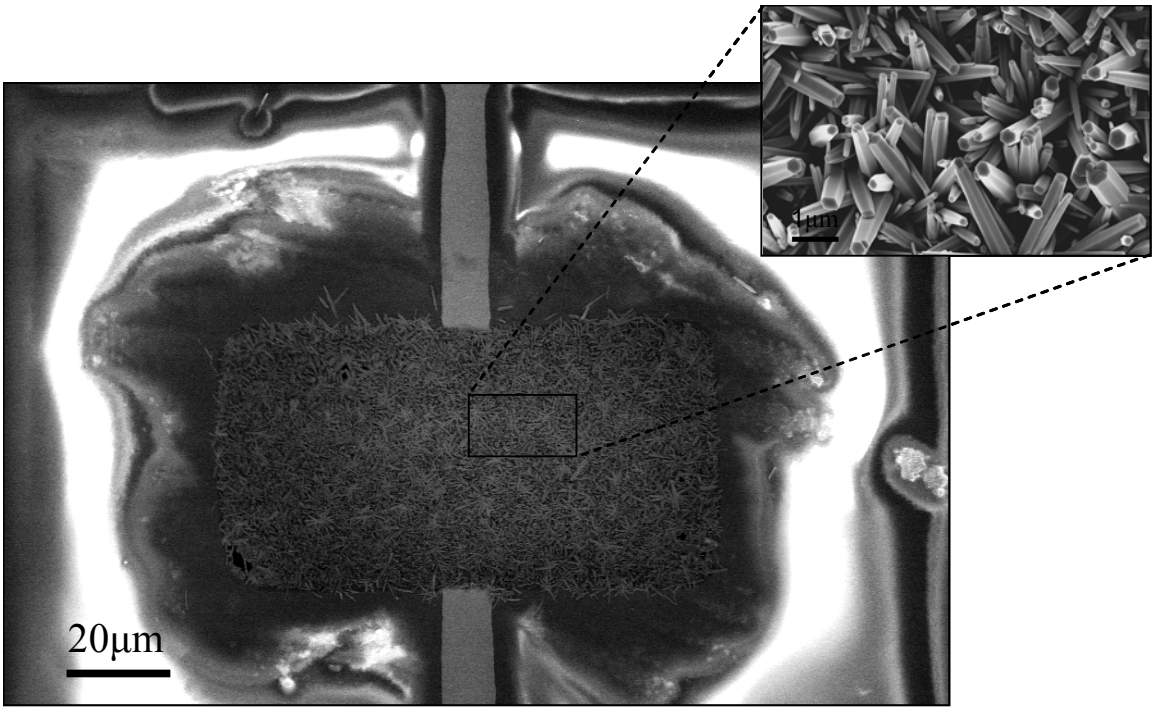

Figure 4.37 Fully-dense network of nanowires growing from one side of the trench to the other. No nanowires can be seen growing on the surface.

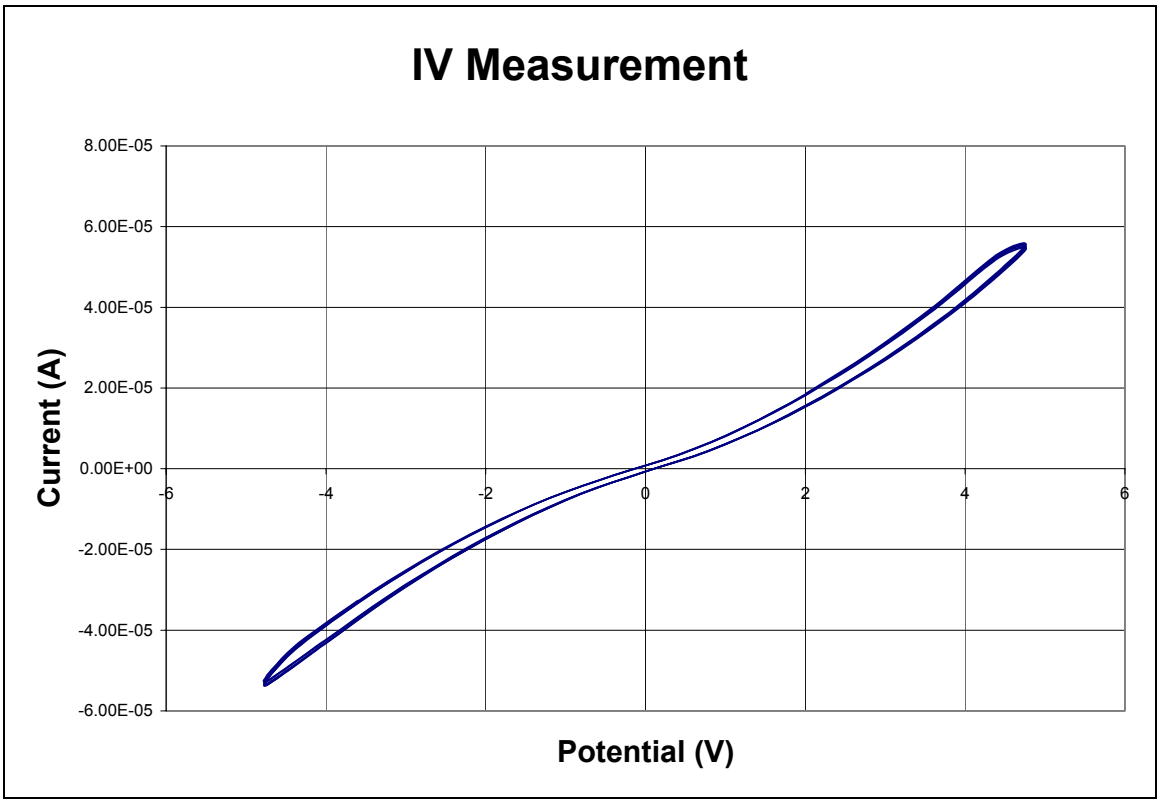

Figure 4.38 I/V measurement of fully-dense nanowire network shown in Figure 4.37.

It can be seen in Figure 4.33 that the wires nucleate and grow on oxide just as readily as gold, which was observed on all sidewalls.

4.1.2 Results from Network Analysis

The resonance of many devices fabricated in section 4.1.1.1, as well as some of the bridged nanowires that were grown in section 4.1.1.2, were characterized using vector network analysis using the same methods presented in Chapter 3. A compilation of the data can be seen in Figure 4.39. Images (a), (b), (c), (d) are all S_{11} reflection measurements on devices fabricated above in 4.1.1.1; (e) and (f) are S_{21} transmission lines from the bridged wire grown in 4.1.1.2 (Figure 4.34a). Unfortunately, none of the data from any of these devices fits the 1D KLM model presented in Chapter 3. In order to see if the resonance data is a result of some unusual propagation direction, the 1D

model will be expanded into 3D using the piezoelectrically-stiffened Christoffel matrix as outlined in Chapter 1.

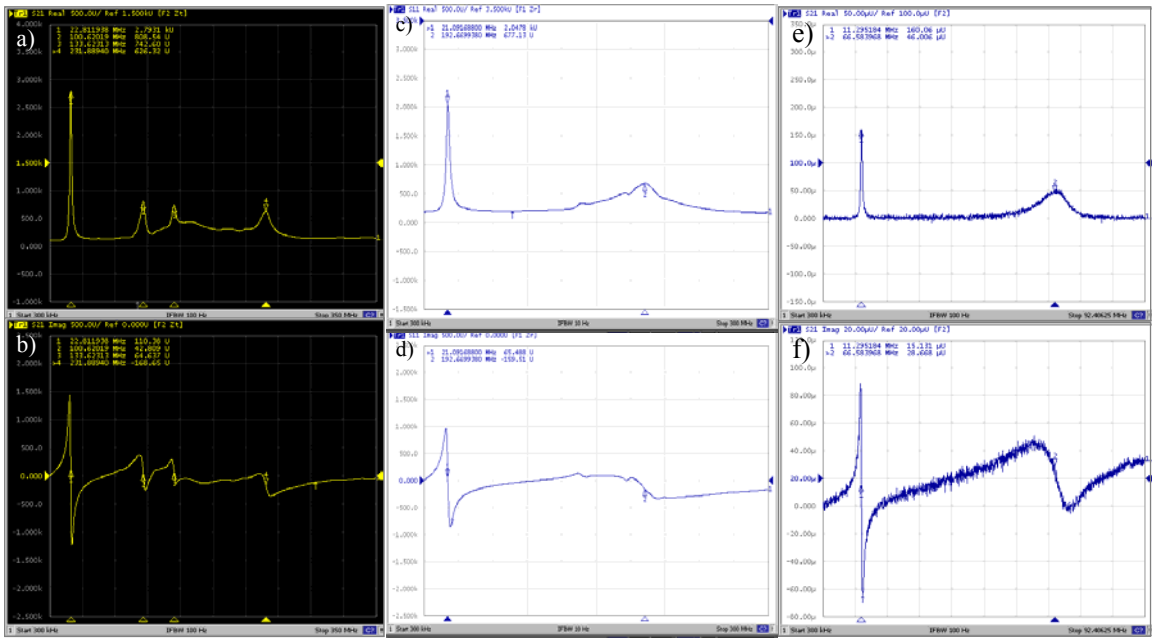

Figure 4.39 Compilation of resonance data measured from a series of devices fabricated in section 4.1.1. (a) Real portion of impedance from one of the devices. (b) Imaginary portion of impedance from the same device as in (a). (c) Real portion of impedance from another device. (d) Imaginary portion of impedance from the same device as in (c). (e) Real portion of impedance from one of the other devices. (f) Imaginary portion of impedance from the same device as in (e).

4.1.3 Three Dimensional Christoffel Model

A simulation of the 3D piezoelectrically-stiffened Christoffel equation, as presented in Chapter 1, is utilized here to expand on the 1D KLM model by calculating the three possible Eigen solutions. All bulk values for ZnO, as outlined in Table 1.5, were utilized for the calculation. A data manipulation software package (MatLAB) was used due to its efficiency in handling matrix multiplication. The actual code for the piezoelecrically-stiffened case (Equation 1.47) can be seen in Appendix B in case one is interested in reproducing the results presented here.

$$\Gamma_{ij} = l_{iK}\left(c^{E}_{KL} + \frac{\left[e_{Kj}l_{j}\right]\left[l_{i}e_{iL}\right]}{l_{i}\varepsilon^{s}_{ij}l_{j}} \right) l_{Lj} \tag{1.47}$$

First, code was written to calculate the acoustic velocity of the three allowable solutions in 2D by defining a (001) reference direction and solving (1.47) in that direction (this is the C-direction). Next, the Y-axis rotation matrix was applied by rotating in the X-Z plane around the Y- axis one degree at a time while re-solving the equation at each degree step along the way. This process was repeated until 360 directions resulting in 1080 solutions (three solutions per direction) were calculated.

$$\begin{bmatrix} \cos\phi & 0 & \sin\phi \\ 0 & 1 & 0 \\ -\sin\phi & 0 & \cos\phi \end{bmatrix} \quad \text{(Y-axis rotation matrix)}$$

Next, an X-axis rotation matrix was applied to the solver in order to now rotate one degree in Y-Z plane, re-solving all 1080 solutions in the new X-Z plane.

$$\begin{bmatrix} 1 & 0 & 0 \\ 0 & \cos\theta & \sin\theta \\ 0 & -\sin\theta & \cos\theta \end{bmatrix} \quad \text{(X-axis rotation matrix)}$$

The calculated direction was rotated again in the Y-Z plane and continuously solved for 180 total rotations in each new X-Z plane until a full three dimensional representation of each solution could be reconstructed. A large scale graphical representation of the three solutions to the problem can be seen in Appendix B. Figure 4.40 shows each solution on a smaller scale along with the relative orientation of the ZnO crystal as applied to the problem. There is one longitudinal wave, which is the fastest propagating solution, and two slower propagating shear waves. The 3D surfaces generated by the model are presented in the following three figures. The units of each axis are in meters per second

and a contour of each solution in the X-Z plane can be seen at the base of each figure.

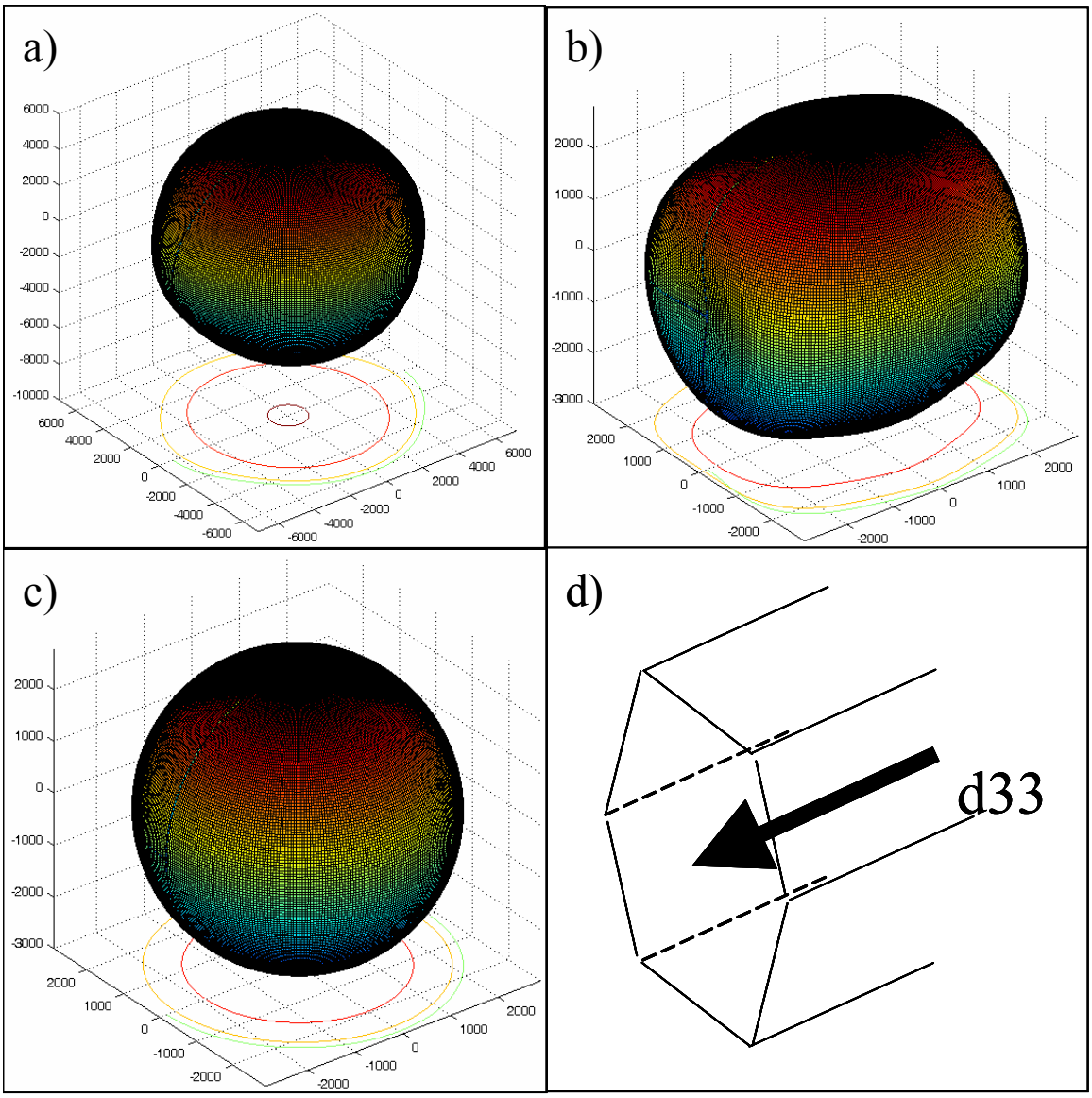

Figure 4.40 All solutions from above (a) longitudinal (b) shear 1 (c) shear 2; represented along with a depiction of (d) the ZnO crystal orientation as it relates to the 3D simulation.

Even once the solutions from this calculation was integrated with the KLM model presented in Chapter 3, no reasonable predictive result matched that which was measured experimentally by the network analyzer. Thus, it is likely that the resonance peaks measured are not acoustic and come from some other fixture in the test set-up. To

determine what is actually contributing to the resonance measurement, the entire device architecture must be modeled. This will be addressed in Chapter 5.

4.1.4 Summary and Conclusions

New methods for fabricating nanodevices using ZnO nanobelts have been introduced. Non-traditional fabrication techniques, such as e-beam lithography and FIB, have been replaced with a traditional process flow capable of utilizing photolithography for all of the fabrication. A few novel fabrication steps were implemented, for example, underdosing photoresist to act as a sacrificial layer.

The result from growing bridged nanowires site-specifically between two electrodes is promising. Future plans for this type of synthesis include the following: pursue a deeper understanding of the hydrothermal nucleation process to control the size, shape and growth direction of ZnO nanowires on gold; use resist or other poisoning agents as a masking layer to prevent synthesis on the unwanted SiO_2 regions; investigate functional molecules that could be used to initiate nucleation and enhance the growth process on gold; use patterned ZnO seeding layers to assist the synthesis process.

Obtaining control over this technique could be important in eliminating the need for nanostructure manipulation. Even though the specific device targeted in this thesis was unsuccessful, achieving the goal of integrating nanowires with other CMOS and MEMS devices would be a large leap for the future of nanotechnology.

Unfortunately it seems that there are issues when scaling the BAR down to work with ZnO belt dimensions in the nanometer range. A series of techniques to de-embed the resonator by storing data from a dummy device have been used to remove any of these impedance contributions. However, even with pad de-embedding, no acoustic signal was measured. An explanation of reasons will be presented in Chapter 5.

CHAPTER 5

IMPEDANCE MODELING

An attempt to scale down the above acoustic resonator to work with nano-sized belts has been unsuccessful. Experimental data from a number of devices fabricated using a variety of approaches does not match the 1D KLM model developed in Chapter 3. The 1D model was expanded to 3D using the piezoelectrically-stiffened Christoffel equation to describe all possible acoustic velocities and propagation directions in ZnO. Still, the measured resonance values are orders of magnitude lower than what was predicted by either model. In this section, an equivalent circuit model along with finite element analysis (FEA) is presented to explain where the observed resonance originates from. Suggestions on how to move forward with this project are outlined in Chapter 6.

5.1 Resonator Equivalent Circuit

To do this, it is first necessary to break down the device architecture into its individual components. Each component can be described by an equivalent circuit as shown in Figure 5.1.

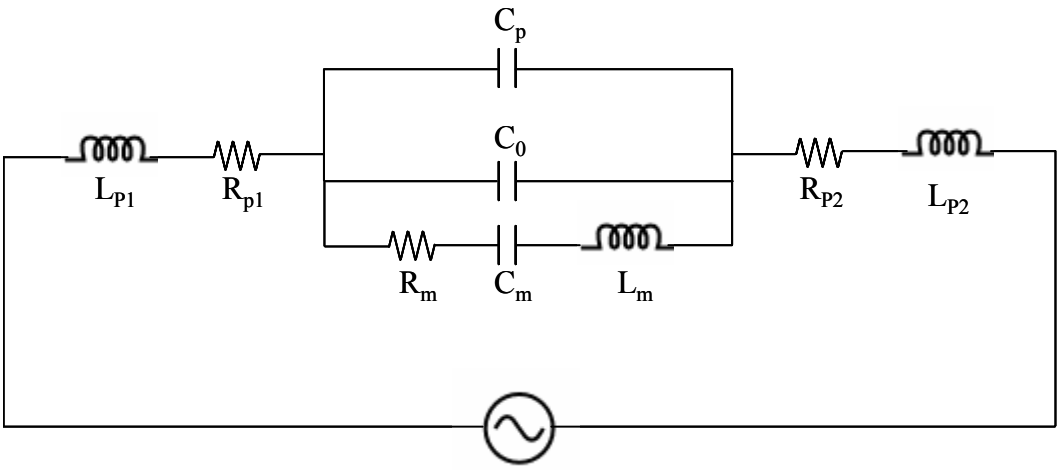

Figure 5.1 Equivalent circuit model describing the as fabricated nano-BAR.

Where C_o is the capacitance of the ZnO nanobelt everywhere but at resonance and R_m, C_m, L_m makes up the motional arm as described in Chapter 3. C_p is the parasitic capacitance attributed to the SiO_2 insulation layer acting as the support for the resonator. R_{p1} and R_{p2} is the resistance of the lead-wires and contact pads. L_{p1} and L_{p2} is the inductance of the thin metal layers at high frequency.

Since the resonance being detected by the NA is not attributed to the acoustic oscillation of the ZnO nanobelt, it is reasonable to assume that the nanobelt is only behaving like a dielectric. Making this assumption the circuit diagram of the device, as shown in Figure 5.1, can be simplified by eliminating the motional arm.

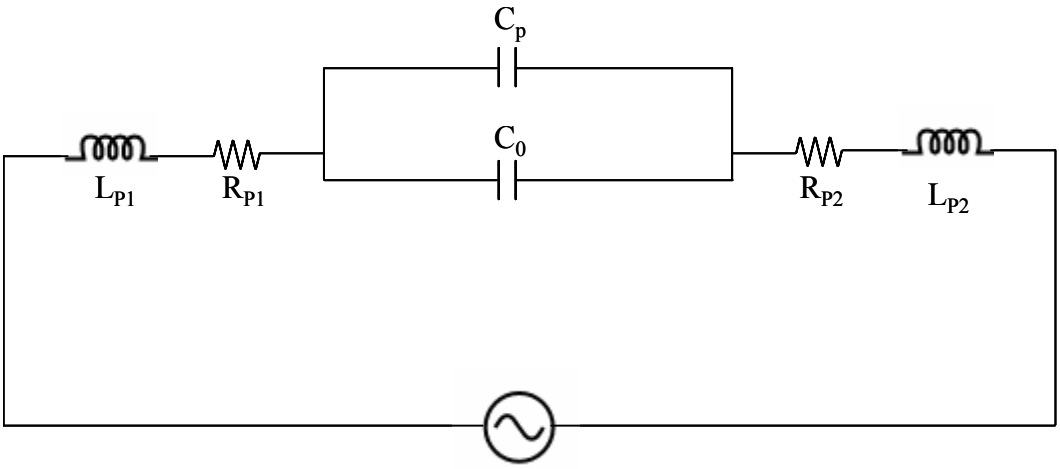

Figure 5.2 Simplified equivalent circuit model assuming the ZnO nanobelt is not resonating.

From here, it is necessary to calculate which of the two capacitors in the model has the lowest device impedance. Since the applied AC current will take the path of lowest impedance, this will be through the larger capacitance due to the inverse relationship $Z_C = \frac{1}{j\omega C}$. It is usually sufficient to relate two capacitors in parallel by using the $C = \varepsilon_r \varepsilon_o \frac{A}{l}$ relationship where C is the total capacitance, ε_r is the dielectric

constant, ε_o is the permittivity of free space, A is the area of each plate or electrode, and l is the distance between the plates. However, this equation is only applicable if l is very small in relation to the area of the plates. Due to the size of the nanobelts and nanowires integrated into these devices, in some cases l is much larger than A, making this calculation invalid. In addition, the distance between the two electrodes is not fixed due to the lateral orientation of the contact pads, making l difficult to define without applying a set of differential equations. Therefore, finite element analysis (FEA) will be used to make an accurate calculation of the capacitance of each component given the true dimensions of the device.

5.2 Finite Element Analysis (COMSOL)

COMSOL, also known as FemLab, is a finite element analysis (FEA) modeling tool that breaks complex geometries down into discrete portions (finite elements) that are connected by nodes. This creates a structured grid called a *mesh* where equations of equilibrium, in conjunction with applicable physical considerations such as compatibility and constitutive relations can be applied to each element resulting in the construction of a system of simultaneous equations. The system of equations is solved for unknown values using the techniques of partial differential equations[159].

COMSOL was used here to create an accurate depiction of the device outlined in Chapter 4. The electrostatics model based on the differential form of Gauss's law was used ($-\nabla \cdot \varepsilon_r \varepsilon_o \nabla V = \rho_e$), where the divergence of the electric field $\vec{E}$ is related to the electric charge density ρ at any point in space[160]. Dimensions were defined to resemble the actual device as closely as possible while including a factor of safety that forced the model to generate the best possible case for a working nanobelt resonator. This resulted in the highest possible capacitance value for the nanobelts making certain dimensional assumptions.

First, the area being modeled only includes the footprint of a single device. All other devices that would normally surround it were not included in the model even though they are likely contributing to the parasitic. The geometric model of the device is shown in Figure 5.3.

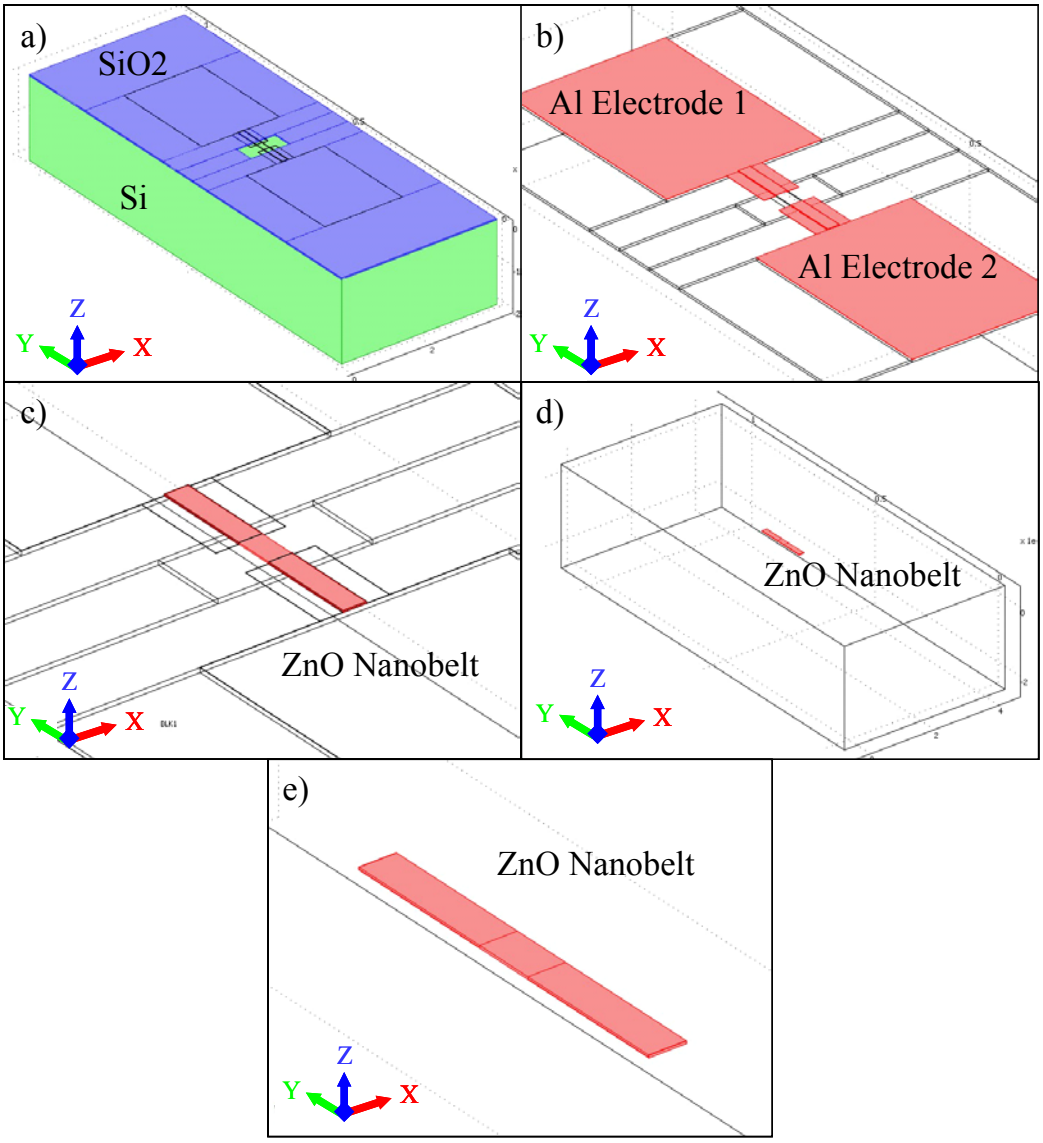

Figure 5.3 Simulated geometry of ZnO nanobelt in parallel with underlying parasitics (a) Model of the silicon wafer is highlighted in green, SiO_2 is in Blue. (b) Both aluminum electrodes are shown in red. (c) ZnO nanobelt spanning the trench and pinned under each electrode (d) This is the model of the nanobelt without the device parasistics, suspended in air (e) Close-up of ZnO nanobelt suspended in air.

The silicon wafer base was defined to be 1050 long (y-direction) X 400μm wide (x-direction) X 200μm thick (z-direction) according to the axes in the figure. The SiO_2 insulation layer has the same length and width of the silicon portion; however, it is only 3μm thick, which is the actual thickness in the device (Figure 5.3a). At the center there is trench modeled in the SiO_2, 3μm deep (opening to the silicon layer), 100μm wide and 25μm long. On top of the trench is a ZnO nanobelt (Figure 5.3c). The nanobelt's length if fixed at 150μm for each model even though the width and thickness are scaled down to the nanometer range. However, the aspect ratio of the width-to-thickness is fixed at 15:1 as the nanobelt is scaled down as well. This ratio is on the high end of what is typically observed. Also, as the belt gets smaller in the width and thickness dimensions, it will also get shorter. Fixing these dimensions was done to give the belt a larger surface area for electrical contact, resulting in a factor of safety for the calculation. The flaps that hang over the trench, as depicted in Figure 4.14 and 4.15, are also modeled here and are designed to conformally coat the belt; however, they do not run the full width of the trench and they are assumed to be at the same height as the nanobelt (Figure 5.3b). As seen in Figure 4.15, this is not actually the case, and the aluminum electrodes get much closer to the gold underlayer. Since this effect would only compound the problem and push the parasitic capacitance even higher, not including it is another factor of safety for the calculation. An air box was also placed around the geometry in order to simulate the electric field that might be generated between the electrodes through air.

Once the geometry was defined, the boundary conditions were set. Each electrode is defined by the $Q = C \cdot V$ charge relationship. The dielectric constants for each material were taken from a library of values stored in COMSOL: 8.3 for the ZnO nanobelt, 4.2 for SiO_2, 11.7 for silicon and 1.0 for air. The materials were assumed to be isotropic and based on the linear constitutive relationship $D = \varepsilon_r \varepsilon_o E$ where D is the dielectric displacement. To ensure continuity of the electric field lines, $n \cdot (D_1 - D_2) = 0$

is used to set the boundary between two dielectrics and $n \cdot D = 0$ sets the continuity condition of electric field lines outside of the device in air. Once the boundary conditions are set, the mesh can be generated.

Figure 5.4 shows the mesh that was generated by COMSOL to simulate equilibrium between nodes. The mesh is coarse in regions were there is not a lot of detail. In regions close to the electrode layer and near the belt where small dimensions exist, the mesh is finer in order to more accurately represent the detail in those regions.

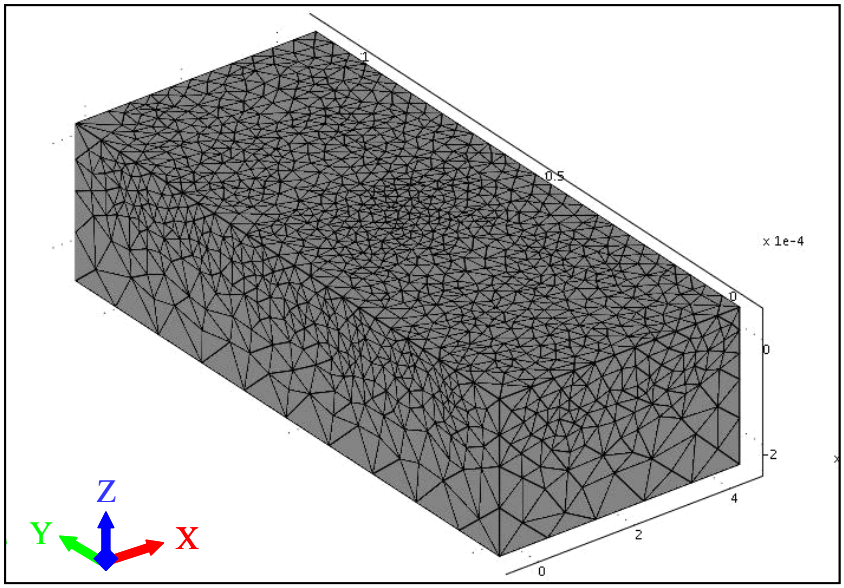

Figure 5.4 Mesh generated by COMSOL.

The model can be solved to calculate the potential distribution through the device. Vertical and horizontal slices through the device center are used to portray the visual result.

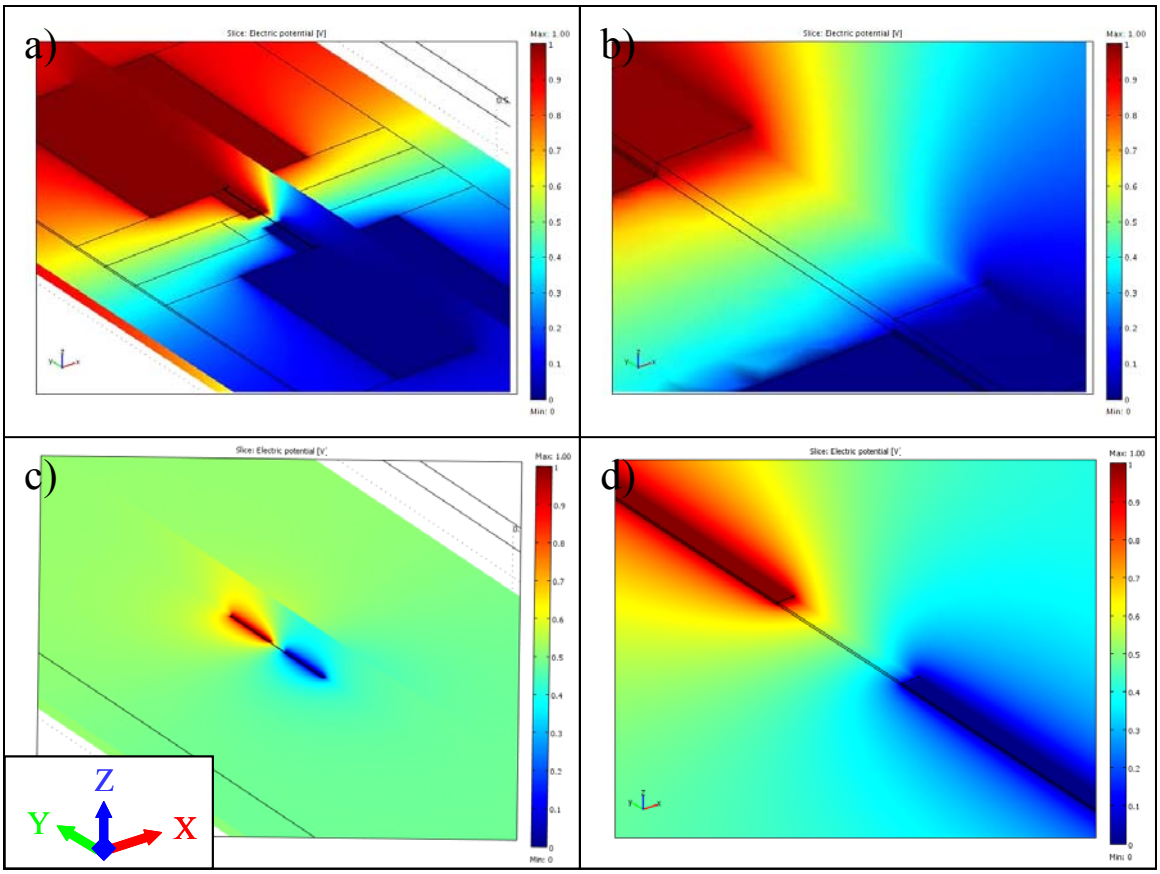

Figure 5.5 (a) Resulting potential distribution through the full device. (b) Close-up of a). (c) Potential distribution from the ZnO nanobelt. (d) Close-up of c).

Since this model was applied to a range of nanobelt dimensions, the C_o presented below will be for a moderately-sized belt with a width of 500nm, thickness of 33.33nm and length of 150μm. From the potential and the charge considerations, the capacitance can be calculated for the device support and ZnO nanobelts. The results are:

Capacitance of the Nanobelt $\boldsymbol{C_o = 3.55x10^{-16}F}$

Capacitance for Parasitics $\boldsymbol{C_p = 2.13x10^{-14}F}$

The result from the FEA calculation confirms that the parasitic capacitance of the device is much higher than C_o. The resulting impedance value is two orders of magnitude lower through the oxide layer than through the nanobelt. As a result, the circuit diagram shown in Figure 5.2 can be simplified again to the one in Figure 5.6.

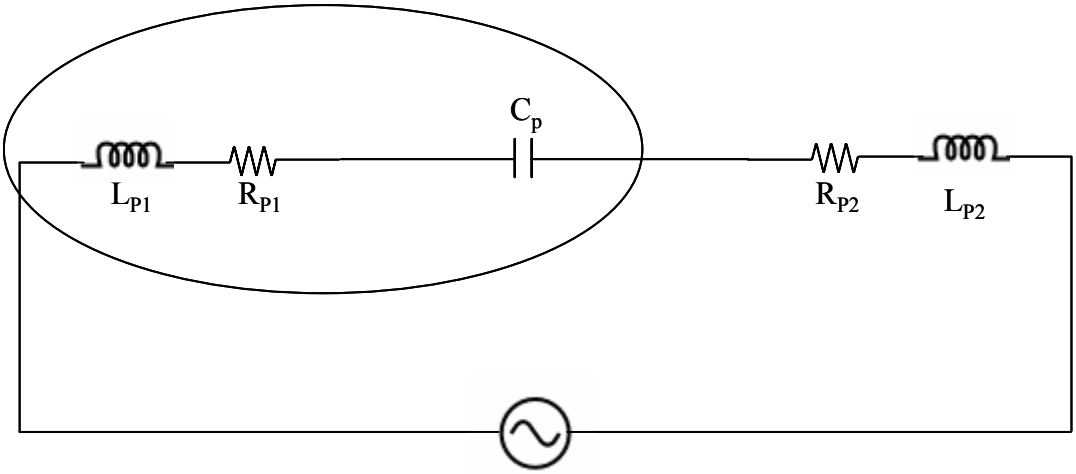

Figure 5.6 Simplified circuit diagram assuming C_p is orders of magnitude higher than C_o.

Given the new circuit diagram, it is now easy to see that the resonance measured by the NA could be attributed to the lumped circuit elements made up by the contact pads, lead wires and support substrate on which the resonator was fabricated. The impedance mismatch problems will only be compounded further by working with smaller nanobelts.

CHAPTER 6

CONCLUSIONS AND FUTURE WORK

6.1 Conclusions

Advancing the field of nanotechnology to incorporate the unique properties observed at the nanoscale into functional devices has become a major scientific thrust of the 21st century. New fabrication tools and assembly techniques are required to design and manufacture devices based on one-dimensional nanostructures. This body of work has contributed to three new techniques for manipulating nanomaterials post synthesis. Two of them involve direct contact manipulation through the utilization of a physical probe. The third uses optically generated surface acoustic waves to reproducibly control and assemble one-dimensional nanostructures into desired locations. The nature of the third technique is non-contact and limits contamination and defects from being introduced into a device by manipulation.

While the effective manipulation of individual nanostructures into device components is important for building functional nanosystems, commercialization is limited by this one-device-at-a-time process. A new approach to nanostructure synthesis was developed to site-specifically nucleate and grow nanowires between two electrodes. Integrating synthesis directly with prefabricated device architectures leads to the possible mass production of NEMS, MEMS and CMOS systems based upon one-dimensional nanomaterials.

The manipulation and synthesis accomplished here, was driven by the desire to realize nanosized bulk acoustic resonators for applications in high frequency electronic filtering as well as biological and chemical sensing. The first ever piezoelectric bulk acoustic resonator based on bottom-up synthesized belts has been demonstrated. Initial results were promising however scaling the device to sub-micron dimensions has posed some problems. Due to electronic limitations, studying material properties and quantum

confinement effects in piezoelectric oscillators has been unsuccessful. Unfortunately, the size of nanobelts results in large electrical impedances that limit performance.

Multiple models were developed within this body of work to assist with design and testing. Some of models were presented to verify the experimental results while others were designed explain the problems currently plaguing further investigations. The piezoelectrically stiffened Christoffel equation was implemented to describe all possible acoustic velocities in each direction within a three dimensional ZnO crystal. Finite element analysis was used to calculate impedance through multiple fixtures of the an equivalent circuit diagram based on the nanobelt BAR.

The work presented here has contributed new manipulation and synthesis techniques that can help other scientists advance their own research in nanotechnlogy. Successes and challenges in manufacturing BARs based on nanomaterials will help the scientific community make decisions as to the next steps with regards to future work.

6.2 Future Work and Recommendations

The electrostatic manipulation and FIB assisted manipulation techniques presented in Chapter 2 have proven their utility and there is no further work planned at this time. The non-contact acoustic "tweezers" method has generated promising data and much more is planned to understand and develop this technique further. First, modeling will be pursued to determine with more certainty whether or not the Rayleigh/Lamb wave hypothesis is the wave type responsible for driving the nanobelts. All experiments done to date have been at the acoustic wavelength of 8.2μm. Experiments will be designed to vary the acoustic wavelength and determine how this variable affects the manipulation process. More work will be conducted by varying the intensity of the excitation laser to quantify results from laser power in between the 2.77mW and 6.72mW power used above. Modifications are being planned to enhance the functionality of the ISTS tool by including multiple excitation lasers and multiple beam shaping optics. By altering the

interference pattern it should be possible to control other nanomanipulation trajectories. Materials other than ZnO nanobelts like carbon nanotubes, silicon nanowires will also be demonstrated with this tool. New optically absorbent materials that are more readily stripped will be investigated as a substitute for copper. A new excitation laser with an optical wavelength in the UV range will be considered for the manipulation of ZnO nanobelts without the need for a copper absorption layer.

Mass production of nanodevices based on an integratable synthesis process will continue to be researched. Investigating the process thus far has raised as many questions as it has answered with regard to the variables effecting site-specific nucleation and growth. Additional reticles will be designed to incorporate poisoning layers (polymers, functional molecules…) onto regions of the substrate where growth is unwanted. ZnO seeding layers and other metal layers will be investigated as potential nucleation sites for enhanced synthesis. Better control over side-wall roughness inside the trench will also be pursued to limit sporadic growth in any direction other than perpendicular to the side-wall.

Based on conclusions drawn from scaling down the BAR based on ZnO nanobelts, there are a few possible solutions that could still result in a successful device. First, it is possible to increase the over all capacitance of the nanobelt by incorporating multiple structure in parallel with eachother. This can be achieved in two ways. The first and easiest would be to grow a high density array of vertically aligned nanowires on top of a metal contact pad. Taking another electrode and sandwiching the nanowires in between could result in a parallel array of nanoresonators with a low enough combined impedance to resonate above the noise floor of the parasitic fixtures. Another way would be take the same structure designed in Chapters 3 and 4 and scale down the electrode dimensions. If it were possible to reduce the pad footprint to something smaller than the contact area on the belt, the parasitic impedance could be increased to a level where the optimal current path through the device under test is through the piezoelectric nanobelt or

nanowire. This is difficult since small nanosized contacts would be required to sufficiently probe the device.

Another possible solution could be to identify an alternative support substrate that has a lower capacitance. Since the lowest possible dielectric constant known in the universe comes from a vacuum, this is likely unattainable. The final recommendation could be to operate the device at elevated temperatures. Since ZnO exhibits hopping conduction, the impedance of the nanowire will decrease as temperature increases. Since the silicon based support exhibits band conduction, the impedance through the parasitics will increase as a function of temperature. An equilibrium temperature could be identified where the impedance through either component switches, resulting in a Z_o that is lower than Z_p. ZnO is a high temperature ceramic; however, the necessary temperature would still have to be low enough to not interrupt the contact resistance of the electrodes.

APPENDIX A

PHOTOLITHOGRAPHY MASK DESIGNS

The fabrication process outlined in Section 4.1.1.2 utilized three basic mask layers for photolithography. The first mask involves a series of square patterns that will be transferred into the nitride layer on the backside of the wafer in order to create a hard mask for KOH etching. The square dimensions were designed specifically around a 500µm wafer so that after the through etch, pits with 54.74^{o} sidewalls would result in a 100µm or 150µm square windows on the opposing side. Each square is spaced 50µm from each other. The first mask layer can be seen in Figure A.1.

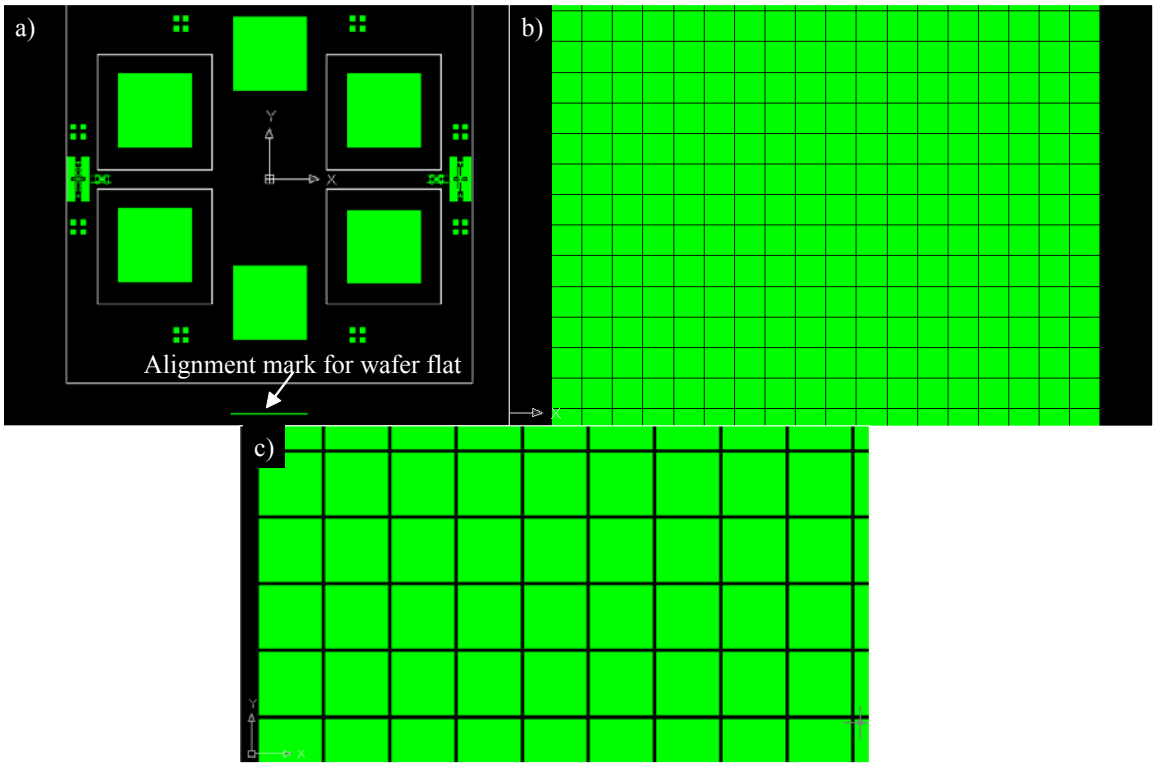

Figure A.1 First layer used to transfer the pattern into a nitride hard mask (a) Full view of 5x5 mask showing six distinct regions (b) A blow up view of one of these regions showing the individual squares. (c) Increased magnification of b).

First, it is important to note that there are six main regions on the wafer. Each consists of 300-400 devices. The full wafer is not used due to the through etch. Etching through the wafer will prevent further spin-coating since a good vacuum is needed to seal the wafer to a chuck while spinning. This would not be possible with holes in the wafer. The center region was left solid for this purpose. There is also a thin green line at the bottom of Figure A.1a. This line is used to align the flat of a (100) wafer. This is important so that the (111) planes are etched in accordance with the design.

The next layer can be seen in Figure A.2. This layer is used on the top-side of the wafer to reveal regions for ICP etching.

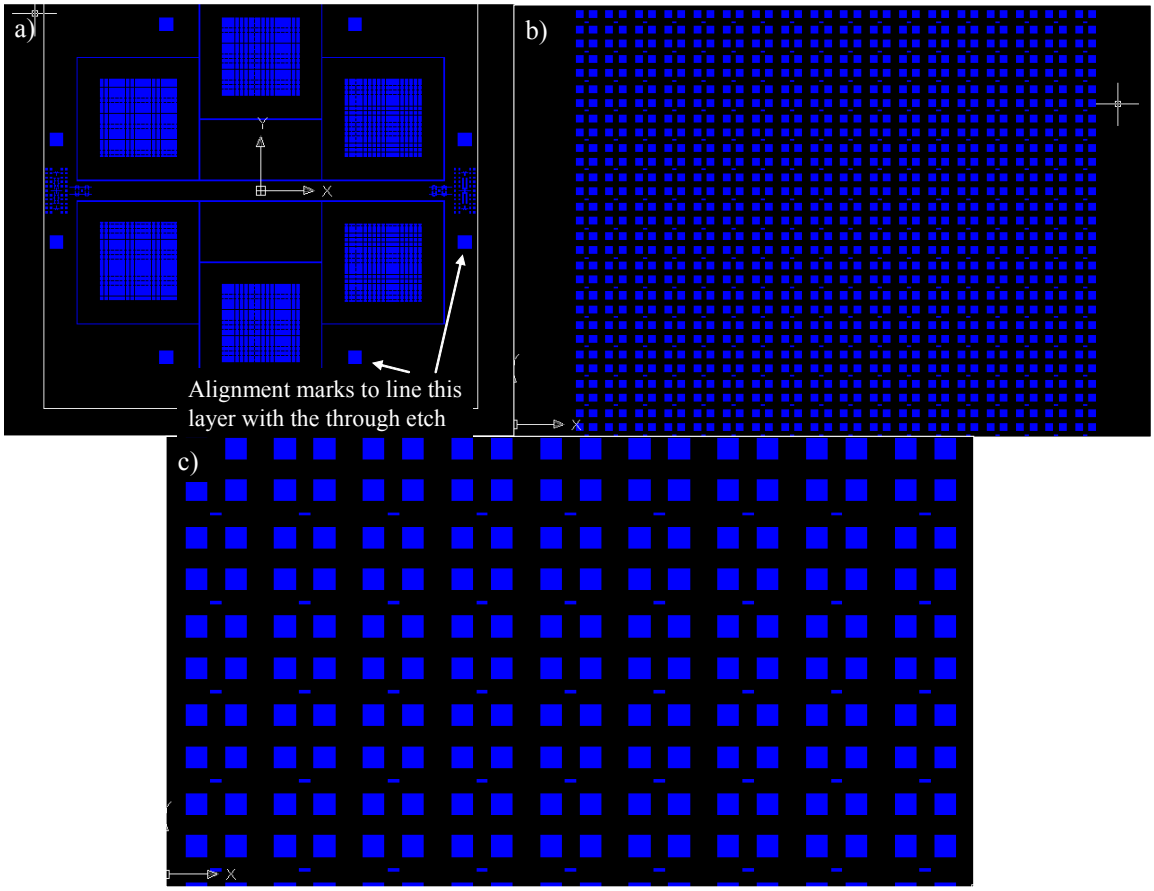

Figure A.2 Top-side mask for plasma etching a trench into the center of the membrane (a) full reticle view (b) increased magnification of one region (c) increased magnification to see individual trenches.

Since the mask aligner did not have backside alignment, it was necessary to design alignment features that would be etched through the backside in order to be seen on the topside. These alignment markings can be seen in Figure A.3.

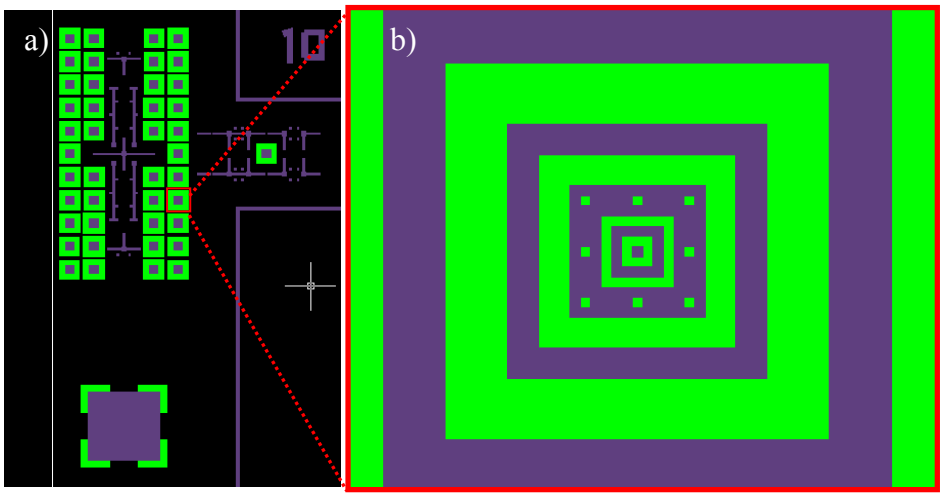

Figure A.3 Alignment marks to orient subsequent masks to the previous ones (a) Coarse alignment features (b) Fine alignment features.

The final mask in the series was used once the gold had been deposited and it was necessary etch unwanted gold regions away leaving thin strips inside the inner walls of the trench that run back to large contact pads. This is the step that creates the bridge of resist spanning the trench.

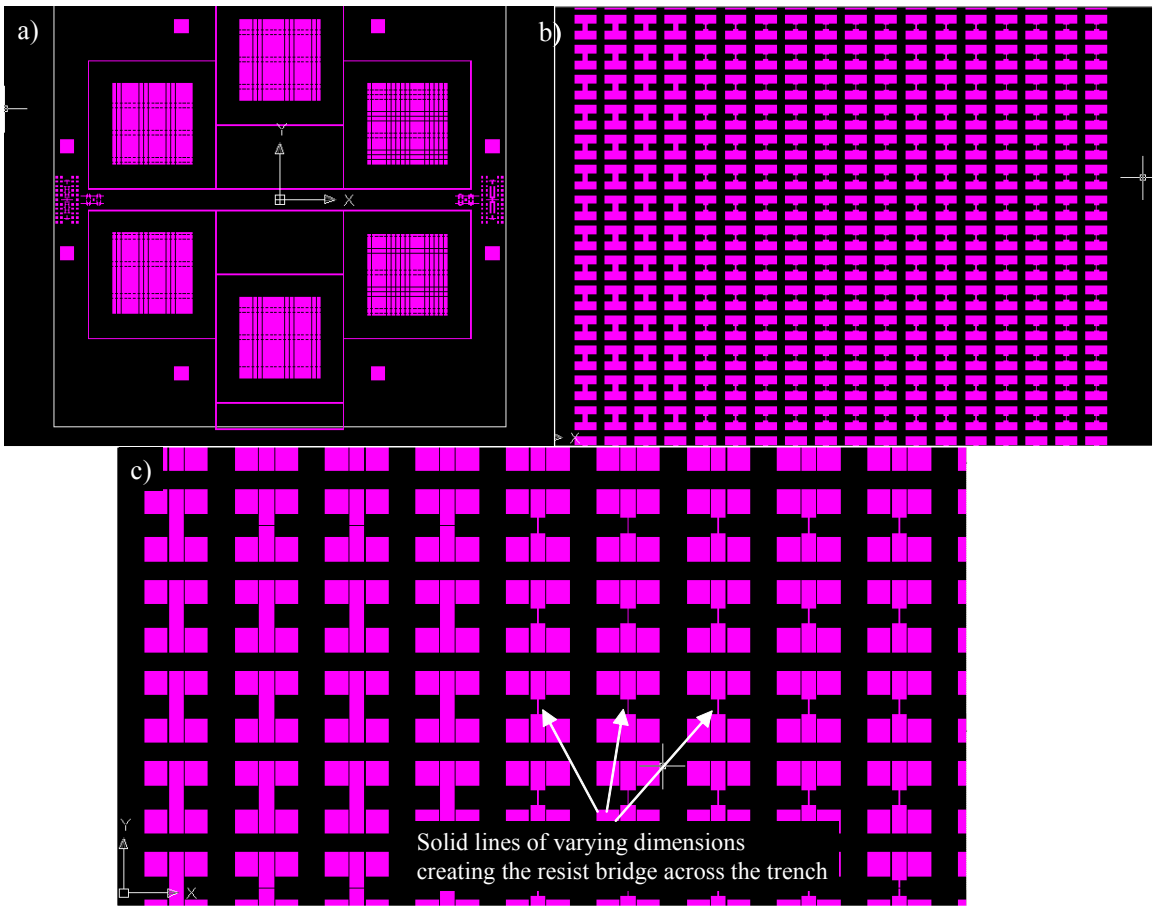

Figure A.4 Final mask layer used to etch Au with KI. (a) full view (b) one region magnified (c) magnified again to show the solid line designed to span the trench in order to create a self supporting strip of resist.

Figure A.5 shows how all of these masks work together.

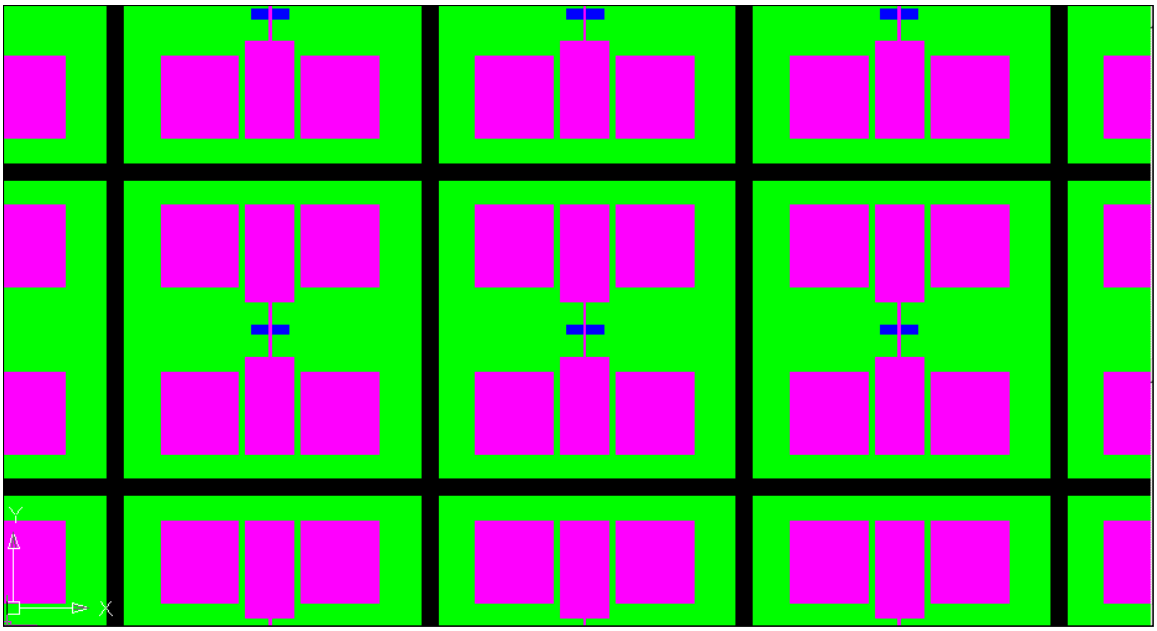

Figure A.5 Overlay of all layers to show how each works together to fabricate the desired product.

APPENDIX B

STIFFENED CHRISTOFFEL EQUATION

(3D MODEL MATLAB CODE)

This is the actual code used in order to simulate the three dimensional results presented in Chapter 4, Section 4.1.3. Any individual wishing to reproduce the results or modify the code for their own application need only copy it from below and run it in Matlab

```
%Acoustic velocity and slowness surface calculations using the
Christoffel Eq. for ZnO


%density of ZnO
rho=5.7*10^3;
%Stiffness Tensor
C=10^9*[210 121 105 0 0 0;121 210 105 0 0 0;105 105 211 0 0 0;0 0 0 43
0 0;0 0 0 0 43 0;0 0 0 0 0 44.5];
%Dielectric Constants
eps=8.85*10^-12*[8.6 0 0;0 8.6 0;0 0 10];
%Piezoelectric Coefficients
e=[0 0 0 0 -.48 0;0 0 0 -.48 0 0;-.57 -.57 1.32 0 0 0];
ref=[0;0;1];
theta=0;
phi=0;

%Stiffened Calculation
thetas = [];
phis = [];
for H=0:1:(180-1);
    theta=H*(pi/180);
    RMX=[1 0 0;0 cos(theta) sin(theta);0 -sin(theta) cos(theta)];
     for I=0:1:(360-1);
        phi=I*(pi/180);
        RMY=[cos(phi) 0 sin(phi);0 1 0;-sin(phi) 0 cos(phi)];

        l=RMX*RMY*ref;
        lp=[l(1,1) 0 0 0 l(3,1) l(2,1);0 l(2,1) 0 l(3,1) 0 l(1,1);0 0
l(3,1) l(2,1) l(1,1) 0];
        temp1=e'*l*l'*e;
        temp2=l'*eps*l;
        temp3=temp1./temp2;
        temp4=C+temp3;
        ch=lp*temp4*lp';
        [V,D]=eig(ch);
```

```
        %Extracts the index of the minimum and maximum values for
            plotting
        %for assigning appropriate shear and longitudinal velocities
        D2=sum(D);
        [mn,minidx]=min(D2);
        [mx,maxidx]=max(D2);
        vash1s(H*360+I+1)=sqrt(D2(minidx)/rho);
        vash2s(H*360+I+1)=sqrt(D2(6-minidx-maxidx)/rho);
        vlongs(H*360+I+1)=sqrt(D2(maxidx)/rho);
        thetas = [thetas theta];
        phis = [phis phi];

    end;
end;

% Convert cartesian data from spherical
[sh1x,sh1y,sh1z] = sph2cart(thetas,phis,vash1s);
[sh2x,sh2y,sh2z] = sph2cart(thetas,phis,vash2s);
[longx,longy,longz] = sph2cart(thetas,phis,vlongs);

% reshape converts 1-d matrices to 2-d matrices for the purpose of
plotting
% with surf function
figure
xxvlong=reshape(longx,360,180);
yyvlong=reshape(longy,360,180);
zzvlong=reshape(longz,360,180);
surfc(xxvlong,yyvlong,zzvlong);

figure
xxvsh1=reshape(sh1x,360,180);
yyvsh1=reshape(sh1y,360,180);
zzvsh1=reshape(sh1z,360,180);
surfc(xxvsh1,yyvsh1,zzvsh1);

figure
xxvsh2=reshape(sh2x,360,180);
yyvsh2=reshape(sh2y,360,180);
zzvsh2=reshape(sh2z,360,180);
surfc(xxvsh2,yyvsh2,zzvsh2);
```

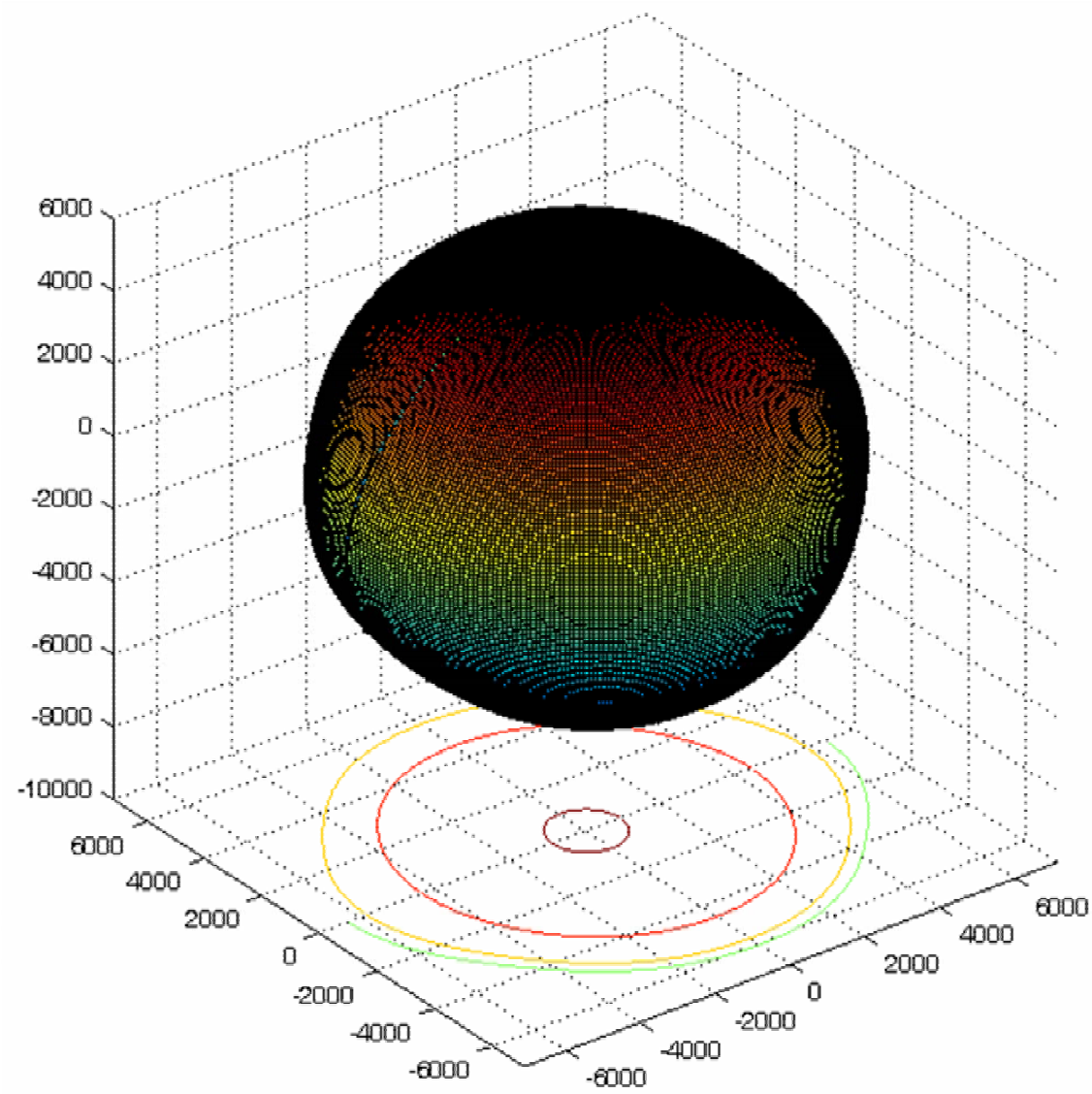

Figure B.1 First Eigen solution (a longitudinal wave).

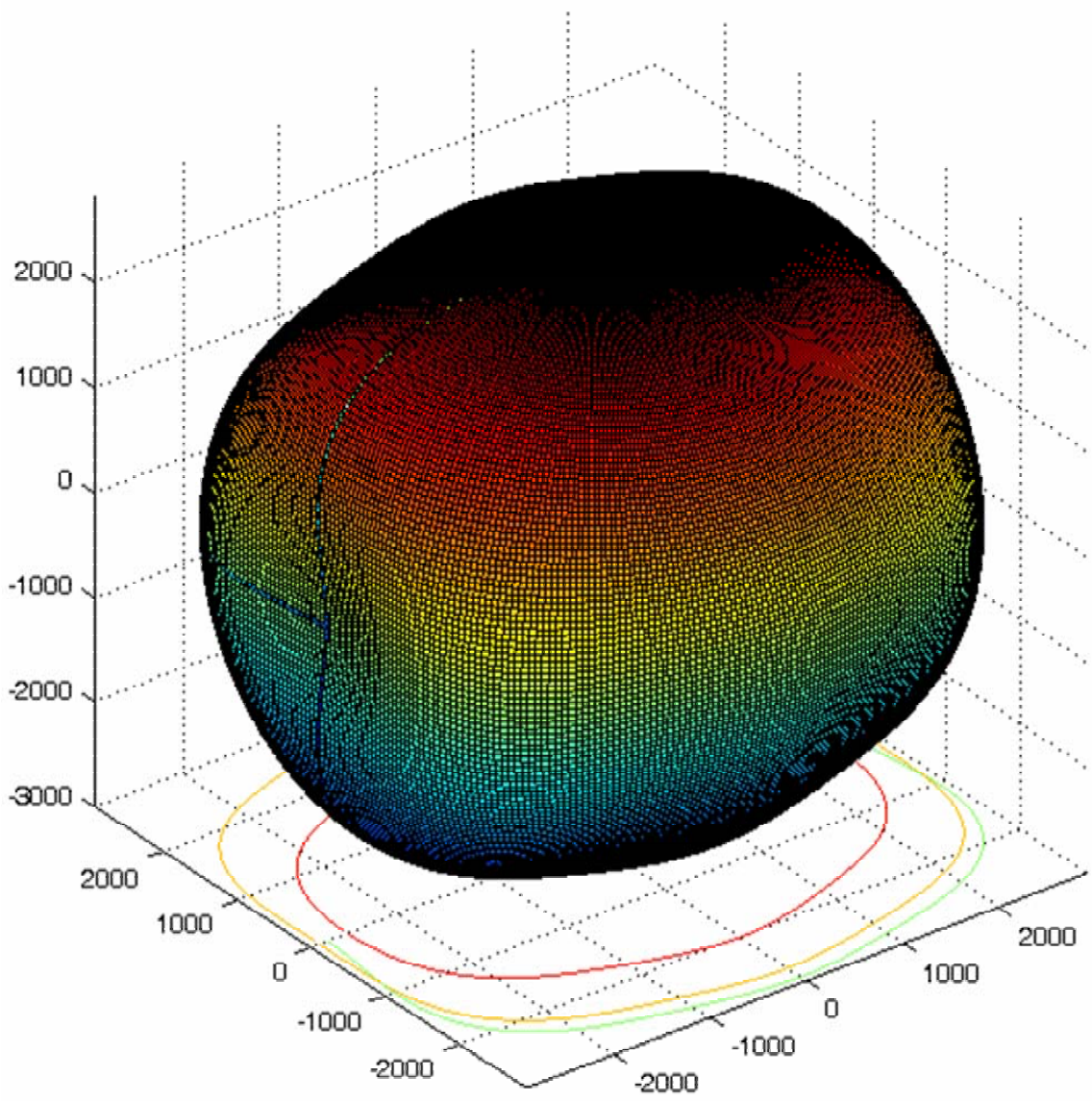

Figure B.2 Second Eigen solution (a shear wave).

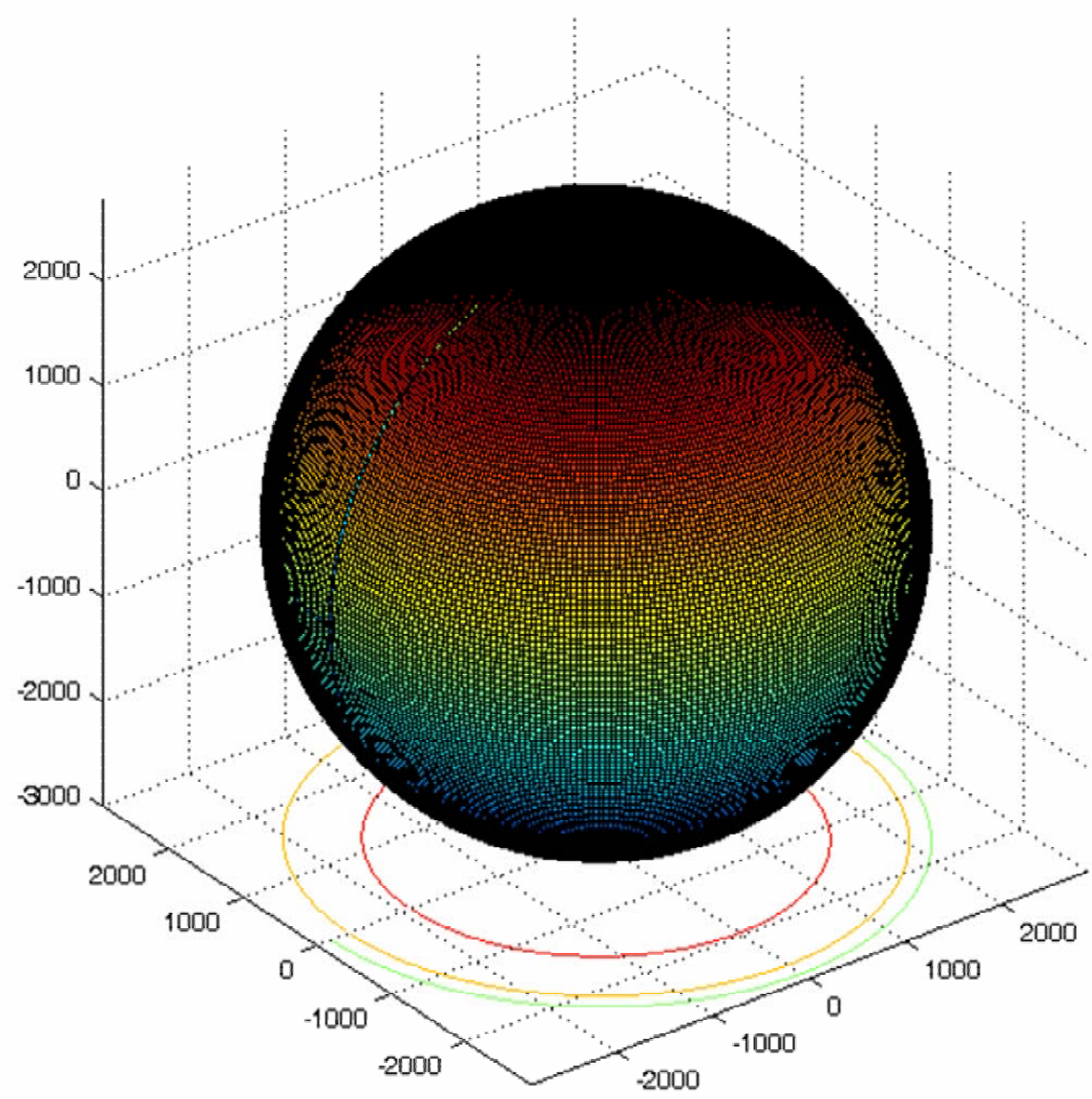

Figure B.3 Third Eigen solution (another shear wave)

REFERENCES

[1] R. P. Feynman, "There's plenty of room at the bottom: An invitation to enter a new field of Physics," A. P. S. A. Meeting, Ed. Pasadena, CA, 1959.

[2] J. M. Cowley and S. Iijma, "Electron-Microscope Image Contrast for Thin Crystals," *Zeitschrift Fur Naturforschung Part a-Astrophysik Physik Und Physikalische Chemie,* vol. A 27, pp. 445-&, 1972.

[3] G. Binning, H. Rohrer, C. Gerber, and E. Weibel, "Surface Studies by Scanning Tunneling Microscopy," *Physical Review Letters,* vol. 49, pp. 57-61, 1982.

[4] D. M. Eigler and E. K. Schweizer, "Positioning Single Atoms with a Scanning Tunneling Microscope," *Nature,* vol. 344, pp. 524-526, Apr 5 1990.

[5] D. M. Eigler, C. P. Lutz, and W. E. Rudge, "An Atomic Switch Realized with the Scanning Tunneling Microscope," *Nature,* vol. 352, pp. 600-603, Aug 15 1991.

[6] T. W. Ebbesen and P. M. Ajayan, "Large-Scale Synthesis of Carbon Nanotubes," *Nature,* vol. 358, pp. 220-222, Jul 16 1992.

[7] A. Thess, R. Lee, P. Nikolaev, H. J. Dai, P. Petit, J. Robert, C. H. Xu, Y. H. Lee, S. G. Kim, A. G. Rinzler, D. T. Colbert, G. E. Scuseria, D. Tomanek, J. E. Fischer, and R. E. Smalley, "Crystalline ropes of metallic carbon nanotubes," *Science,* vol. 273, pp. 483-487, Jul 26 1996.

[8] Z. F. Ren, Z. P. Huang, J. W. Xu, J. H. Wang, P. Bush, M. P. Siegal, and P. N. Provencio, "Synthesis of large arrays of well-aligned carbon nanotubes on glass," *Science,* vol. 282, pp. 1105-1107, Nov 6 1998.

[9] X. Wang, "Large Scale Patterned Oxide Nanostructures: Fabrication, Characterization and Applications," in *Materials Science and Engineering*. vol. PhD Atlanta, GA: Georgia Institute of Technology, 2005.

[10] **www.nanoscienceworks.org**.

[11] **www.rdg.ac.uk**.

[12] Z. Yao, C. L. Kane, and C. Dekker, "High-field electrical transport in single-wall carbon nanotubes," *Physical Review Letters,* vol. 84, pp. 2941-2944, Mar 27 2000.

[13] M. F. Yu, O. Lourie, M. J. Dyer, K. Moloni, T. F. Kelly, and R. S. Ruoff, "Strength and breaking mechanism of multiwalled carbon nanotubes under tensile load," *Science,* vol. 287, pp. 637-640, Jan 28 2000.

[14] J. Cumings and A. Zettl, "Low-friction nanoscale linear bearing realized from multiwall carbon nanotubes," *Science,* vol. 289, pp. 602-604, Jul 28 2000.

[15] S. Iijima, "Helical Microtubules of Graphitic Carbon," *Nature,* vol. 354, pp. 56-58, Nov 7 1991.

[16] S. Iijima and T. Ichihashi, "Single-Shell Carbon Nanotubes of 1-Nm Diameter (Vol 363, Pg 603, 1993)," *Nature,* vol. 364, pp. 737-737, Aug 19 1993.

[17] D. S. Bethune, C. H. Kiang, M. S. Devries, G. Gorman, R. Savoy, J. Vazquez, and R. Beyers, "Cobalt-Catalyzed Growth of Carbon Nanotubes with Single-Atomic-Layerwalls," *Nature,* vol. 363, pp. 605-607, Jun 17 1993.

[18] A. Oberlin, M. Endo, and T. Koyama, "Filamentous Growth of Carbon through Benzene Decomposition," *Journal of Crystal Growth,* vol. 32, pp. 335-349, 1976.

[19] L. V. Radushkevich and V. M. Lukyanovich, "O strukture ugleroda, obrazujucegosja pri termiceskom razlozenii okisi ugleroda na zeleznom kontakte," *Zurn Fisic Chim,* vol. 111, pp. 24-34, 1952.

[20] M. Monthioux and V. L. Kuznetsov, "Who Should be Given the Credit for Discovery of the Carbon Nanotube," *Carbon,* vol. 44, 2006.

[21] K. E. Drexler, *Engines of Creation*. New York: Anchor Books, 1986.

[22] N. N. Initiative.

[23] H. W. Kroto, J. R. Heath, S. C. Obrien, R. F. Curl, and R. E. Smalley, "C-60 - Buckminsterfullerene," *Nature,* vol. 318, pp. 162-163, 1985.

[24] B. O. Dabbousi, J. RodriguezViejo, F. V. Mikulec, J. R. Heine, H. Mattoussi, R. Ober, K. F. Jensen, and M. G. Bawendi, "(CdSe)ZnS core-shell quantum dots: Synthesis and characterization of a size series of highly luminescent nanocrystallites," *Journal of Physical Chemistry B,* vol. 101, pp. 9463-9475, Nov 13 1997.

[25] J. L. Vossen and W. Kern, *Thin Film Processes*. London, UK: Academic Press, Inc., 1978.

[26] S. D. Senturia, *Microsystem Design*. Norwell, MA: Kluwer Academic Publishers, 2001.

[27] C. R. Martin, "Membrane-based synthesis of nanomaterials," *Chemistry of Materials,* vol. 8, pp. 1739-1746, Aug 1996.

[28] Y. N. Xia, P. D. Yang, Y. G. Sun, Y. Y. Wu, B. Mayers, B. Gates, Y. D. Yin, F. Kim, and Y. Q. Yan, "One-dimensional nanostructures: Synthesis, characterization, and applications," *Advanced Materials,* vol. 15, pp. 353-389, Mar 4 2003.

[29] P. Avouris, R. Martel, V. Derycke, and J. Appenzeller, "Carbon nanotube transistors and logic circuits," *Physica B-Condensed Matter,* vol. 323, pp. 6-14, Oct 2002.

[30] S. J. Tans, A. R. M. Verschueren, and C. Dekker, "Room-temperature transistor based on a single carbon nanotube," *Nature,* vol. 393, pp. 49-52, May 7 1998.

[31] W. A. Deheer, W. S. Bacsa, A. Chatelain, T. Gerfin, R. Humphreybaker, L. Forro, and D. Ugarte, "Aligned Carbon Nanotube Films - Production and Optical and Electronic-Properties," *Science,* vol. 268, pp. 845-847, May 12 1995.

[32] W. A. Deheer, A. Chatelain, and D. Ugarte, "A Carbon Nanotube Field-Emission Electron Source," *Science,* vol. 270, pp. 1179-1180, Nov 17 1995.

[33] S. Frank, P. Poncharal, Z. L. Wang, and W. A. de Heer, "Carbon nanotube quantum resistors," *Science,* vol. 280, pp. 1744-1746, Jun 12 1998.

[34] J. Kong, N. R. Franklin, C. W. Zhou, M. G. Chapline, S. Peng, K. J. Cho, and H. J. Dai, "Nanotube molecular wires as chemical sensors," *Science,* vol. 287, pp. 622-625, Jan 28 2000.

[35] X. F. Duan, Y. Huang, Y. Cui, J. F. Wang, and C. M. Lieber, "Indium phosphide nanowires as building blocks for nanoscale electronic and optoelectronic devices," *Nature,* vol. 409, pp. 66-69, Jan 4 2001.

[36] M. S. Arnold, P. Avouris, Z. W. Pan, and Z. L. Wang, "Field-effect transistors based on single semiconducting oxide nanobelts," *Journal of Physical Chemistry B,* vol. 107, pp. 659-663, Jan 23 2003.

[37] E. Comini, G. Faglia, G. Sberveglieri, Z. W. Pan, and Z. L. Wang, "Stable and highly sensitive gas sensors based on semiconducting oxide nanobelts," *Applied Physics Letters,* vol. 81, pp. 1869-1871, Sep 2 2002.

[38] X. D. Bai, P. X. Gao, Z. L. Wang, and E. G. Wang, "Dual-mode mechanical resonance of individual ZnO nanobelts," *Applied Physics Letters,* vol. 82, pp. 4806-4808, Jun 30 2003.

[39] V. Sazonova, Y. Yaish, H. Ustunel, D. Roundy, T. A. Arias, and P. L. McEuen, "A tunable carbon nanotube electromechanical oscillator," *Nature,* vol. 431, pp. 284-287, Sep 16 2004.

[40] R. S. Friedman, M. C. McAlpine, D. S. Ricketts, D. Ham, and C. M. Lieber, "High-speed integrated nanowire circuits," *Nature,* vol. 434, pp. 1085-1085, Apr 28 2005.

[41] M. S. Gudiksen, L. J. Lauhon, J. Wang, D. C. Smith, and C. M. Lieber, "Growth of nanowire superlattice structures for nanoscale photonics and electronics," *Nature,* vol. 415, pp. 617-620, Feb 7 2002.

[42] L. J. Lauhon, M. S. Gudiksen, C. L. Wang, and C. M. Lieber, "Epitaxial core-shell and core-multishell nanowire heterostructures," *Nature,* vol. 420, pp. 57-61, Nov 7 2002.

[43] J. Xiang, W. Lu, Y. J. Hu, Y. Wu, H. Yan, and C. M. Lieber, "Ge/Si nanowire heterostructures as high-performance field-effect transistors," *Nature,* vol. 441, pp. 489-493, May 25 2006.

[44] B. A. Buchine, W. L. Hughes, F. L. Degertekin, and Z. L. Wang, "Bulk acoustic resonator based on piezoelectric ZnO belts," *Nano Letters,* vol. 6, pp. 1155-1159, Jun 2006.

[45] E. W. Wong, P. E. Sheehan, and C. M. Lieber, "Nanobeam mechanics: Elasticity, strength, and toughness of nanorods and nanotubes," *Science,* vol. 277, pp. 1971-1975, Sep 26 1997.

[46] J. D. Holmes, K. P. Johnston, R. C. Doty, and B. A. Korgel, "Control of thickness and orientation of solution-grown silicon nanowires," *Science,* vol. 287, pp. 1471-1473, Feb 25 2000.

[47] L. D. Hicks, T. C. Harman, X. Sun, and M. S. Dresselhaus, "Experimental study of the effect of quantum-well structures on the thermoelectric figure of merit," *Physical Review B,* vol. 53, pp. 10493-10496, Apr 15 1996.

[48] M. H. Huang, S. Mao, H. Feick, H. Q. Yan, Y. Y. Wu, H. Kind, E. Weber, R. Russo, and P. D. Yang, "Room-temperature ultraviolet nanowire nanolasers," *Science,* vol. 292, pp. 1897-1899, Jun 8 2001.

[49] Y. Y. Wu, R. Fan, and P. D. Yang, "Block-by-block growth of single-crystalline Si/SiGe superlattice nanowires," *Nano Letters,* vol. 2, pp. 83-86, Feb 2002.

[50] Y. Y. Wu and P. D. Yang, "Germanium nanowire growth via simple vapor transport," *Chemistry of Materials,* vol. 12, pp. 605-+, Mar 2000.

[51] X. L. Chen, J. Y. Li, Y. G. Cao, Y. C. Lan, H. Li, M. He, C. Y. Wang, Z. Zhang, and Z. Y. Qiao, "Straight and smooth GaN nanowires," *Advanced Materials,* vol. 12, pp. 1432-1434, Oct 2 2000.

[52] J. Noborisaka, J. Motohisa, and T. Fukui, "Catalyst-free growth of GaAs nanowires by selective-area metalorganic vapor-phase epitaxy," *Applied Physics Letters,* vol. 86, pp. -, May 23 2005.

[53] M. Yazawa, M. Koguchi, A. Muto, M. Ozawa, and K. Hiruma, "Effect of One Monolayer of Surface Gold Atoms on the Epitaxial-Growth of Inas Nanowhiskers," *Applied Physics Letters,* vol. 61, pp. 2051-2053, Oct 26 1992.

[54] Z. L. Wang, *Nanowires and Nanobelts: Materials, Properties, and Devices* vol. 2. Boston, MA: Kluwer Academic Publishers, 2003.

[55] H. J. Dai, E. W. Wong, Y. Z. Lu, S. S. Fan, and C. M. Lieber, "Synthesis and Characterization of Carbide Nanorods," *Nature,* vol. 375, pp. 769-772, Jun 29 1995.

[56] A. M. Morales and C. M. Lieber, "A laser ablation method for the synthesis of crystalline semiconductor nanowires," *Science,* vol. 279, pp. 208-211, Jan 9 1998.

[57] Z. W. Pan, Z. R. Dai, and Z. L. Wang, "Nanobelts of semiconducting oxides," *Science,* vol. 291, pp. 1947-1949, Mar 9 2001.

[58] P. Gao, "Piezoelectric Nanostructures of ZnO: Synthesis, Characterization and Devices," in *Materials Science and Engineering*. vol. PhD Atlanta, GA: Georgia Institute of Technology, 2005.

[59] X. Y. Kong, Y. Ding, R. Yang, and Z. L. Wang, "Single-crystal nanorings formed by epitaxial self-coiling of polar nanobelts," *Science,* vol. 303, pp. 1348-1351, Feb 27 2004.

[60] R. S. Yang, Y. Ding, and Z. L. Wang, "Deformation-free single-crystal nanohelixes of polar nanowires," *Nano Letters,* vol. 4, pp. 1309-1312, Jul 2004.

[61] C. Ma, "Systematic Investigation on the Growth of One-Dimensional Wurtzite Nanostructures," in *Materials Science and Engineering*. vol. PhD Atlanta, Ga: Georgia Institute of Technology, 2005.

[62] W. L. Hughes, "Synthesis and Characterization of ZnO Nanostructures for Piezoelectric Applications," in *Materials Science and Engineering*. vol. PhD Atlanta, GA: Georgia Institute of Technology, 2006.

[63] C. J. Lee and J. Park, "Growth model of bamboo-shaped carbon nanotubes by thermal chemical vapor deposition," *Applied Physics Letters,* vol. 77, pp. 3397-3399, Nov 20 2000.

[64] J. C. Wang, S. Q. Feng, and D. P. Yu, "High-quality GaN nanowires synthesized using a CVD approach," *Applied Physics a-Materials Science & Processing,* vol. 75, pp. 691-693, Dec 2002.

[65] J. R. Morber, Y. Ding, M. S. Haluska, Y. Li, P. Liu, Z. L. Wang, and R. L. Snyder, "PLD-assisted VLS growth of aligned ferrite nanorods, nanowires, and nanobelts-synthesis, and properties," *Journal of Physical Chemistry B,* vol. 110, pp. 21672-21679, Nov 2 2006.

[66] H. Hasegawa and S. Kasai, "Hexagonal binary decision diagram quantum logic circuits using Schottky in-plane and wrap-gate control of GaAs and InGaAs nanowires," *Physica E,* vol. 11, pp. 149-154, Oct 2001.

[67] M. Piccin, G. Bais, V. Grillo, F. Jabeen, S. De Franceschi, E. Carlino, M. Lazzarino, F. Romanato, L. Businaro, S. Rubini, F. Martelli, and A. Franciosi, "Growth by molecular beam epitaxy and electrical characterization of GaAs nanowires," *Physica E-Low-Dimensional Systems & Nanostructures,* vol. 37, pp. 134-137, Mar 2007.

[68] T. Sato, I. Tamai, C. Jiang, and H. Hasegawa, "Selective MBE growth of GaAs/AlGaAs nanowires on patterned GaAs (001) substrates and its application to hexagonal nanowire network formation," *Compound Semiconductors 2001,* pp. 325-330, 2002.

[69] B. D. Min, J. S. Lee, K. G. Cho, J. W. Hwang, H. Kim, M. Y. Sung, S. Kim, J. Park, H. W. Seo, S. Y. Bae, M. S. Lee, S. O. Park, and J. T. Moon,

"Semiconductor nanowires surrounded by cylindrical Al2O3 shells," *Journal of Electronic Materials,* vol. 32, pp. 1344-1348, Nov 2003.

[70] L. K. Tan, A. S. M. Chong, X. S. E. Tang, and H. Gao, "Combining atomic layer deposition with a template-assisted approach to fabricate size-reduced nanowire arrays on substrates and their electrochemical characterization," *Journal of Physical Chemistry C,* vol. 111, pp. 4964-4968, Apr 5 2007.

[71] H. W. Kim, J. W. Lee, and C. Lee, "Ternperature-controlled fabrication of crystalline beta-Bi2O3 nanowires through an MOCVD process," *Journal of the Korean Physical Society,* vol. 50, pp. 1308-1311, May 2007.

[72] H. W. Kim, N. H. Kim, J. H. Shim, N. H. Cho, and C. Lee, "Catalyst-free MOCVD growth of ZnO nanorods and their structural characterization," *Journal of Materials Science-Materials in Electronics,* vol. 16, pp. 13-15, Jan 2005.

[73] S. K. Lee, H. J. Choi, P. Pauzauskie, P. D. Yang, N. K. Cho, H. D. Park, E. K. Suh, K. Y. Lim, and H. J. Lee, "Gallium nitride nanowires with a metal initiated metal-organic chemical vapor deposition (MOCVD) approach," *Physica Status Solidi B-Basic Research,* vol. 241, pp. 2775-2778, Oct 2004.

[74] M. A. Verges, A. Mifsud, and C. J. Serna, "Formation of Rod-Like Zinc-Oxide Microcrystals in Homogeneous Solutions," *Journal of the Chemical Society-Faraday Transactions,* vol. 86, pp. 959-963, Mar 21 1990.

[75] Z. R. R. Tian, J. A. Voigt, J. Liu, B. McKenzie, M. J. McDermott, M. A. Rodriguez, H. Konishi, and H. F. Xu, "Complex and oriented ZnO nanostructures," *Nature Materials,* vol. 2, pp. 821-826, Dec 2003.

[76] L. Vayssieres, "Growth of arrayed nanorods and nanowires of ZnO from aqueous solutions," *Advanced Materials,* vol. 15, pp. 464-466, Mar 4 2003.

[77] L. Schmidt-Mende and J. L. MacManus-Driscoll, "ZnO – nanostructures, defects, and devices," *Materials Today,* vol. 10, May 2007.

[78] J. Curie and P. Curie, "Development, par pression, de l'electicite polarise dans les crystaux hemiedbes et fares inclines," *Comp. Rend.,* vol. 91, p. 4, 1880.

[79] W. G. Cady, *Piezoelectricity*. New York, NY: Dover Publications, Inc., 1964.

[80] G. J. Lipmann, "Principe de la conservation de l'electicite ou second principe de la th'eorie des phenomnes electriques," *Annales De Chomoe et de Physique,* vol. 24, 1881.

[81] S. O. R. Moheinani and A. J. Fleming, *Piezoelectric Transducers for Vibration Control and Damping*. London, UK: Springer-Verlag, 2006.

[82] J. F. Rosenbaum, *Bulk Acoustic Wave Theory and Devices*. Boston, MA: Artech House, 1988.

[83] D. Halliday, R. Resnick, and J. Walker, *Fundamentals of Physics*, fifth edition ed. New York, NY: John Wiley and Sons, Inc., 1997.

[84] V. E. Bottom, *Introduction to Quartz Crystal Unit Design*. New York, NY: Ban Nostrand Reinhold Company, 1982.

[85] W. L. Hughes and Z. L. Wang, "Nanobelts as nanocantilevers," *Applied Physics Letters,* vol. 82, pp. 2886-2888, Apr 28 2003.

[86] IEEE, "Publication and Proposed Revision of ANSI/IEEE Standard 176-1987," *IEEE Transaction on Ultrasonics, Ferroelectrics, and Frequency Control,* vol. 43, 1996.

[87] T. Ikeda, *Fundamentals of Piezoelectricity*. Tokyo, Japan: Oxford University Press, 1990.

[88] T. M. Parker, N. G. Condon, R. Lindsay, F. M. Leibsle, and G. Thornton, "Imaging the polar (000(1)over-bar) and non-polar (10(1)over-bar0) surfaces of ZnO with STM," *Surface Science,* vol. 415, pp. L1046-L1050, Oct 9 1998.

[89] S. C. Minne, S. R. Manalis, and C. F. Quate, "Parallel atomic force microscopy using cantilevers with integrated piezoresistive sensors and integrated

piezoelectric actuators," *Applied Physics Letters,* vol. 67, pp. 3918-3920, Dec 25 1995.

[90] C. R. Gorla, N. W. Emanetoglu, S. Liang, W. E. Mayo, Y. Lu, M. Wraback, and H. Shen, "Structural, optical, and surface acoustic wave properties of epitaxial ZnO films grown on (01(1)over-bar2) sapphire by metalorganic chemical vapor deposition," *Journal of Applied Physics,* vol. 85, pp. 2595-2602, Mar 1 1999.

[91] X. D. Wang, C. J. Summers, and Z. L. Wang, "Large-scale hexagonal-patterned growth of aligned ZnO nanorods for nano-optoelectronics and nanosensor arrays," *Nano Letters,* vol. 4, pp. 423-426, Mar 2004.

[92] D. S. Ballantine, R. M. White, S. J. Martin, A. J. Ricco, E. T. Zellers, G. C. Frye, and H. Wohltjen, *Acoustic Wave Sensors: Theory, Design, and Physico-Chemical Applications*. San Diego, CA: Academic Press, 1997.

[93] D. Russel, "Acoustics and Vibration Animations (**http://www.kettering.edu/~drussell/demos.html),**" Flint, MI, 2002.

[94] J. Du, G. L. Harding, J. A. Ogilvy, P. R. Dencher, and M. Lake, "A study of Love-wave acoustic sensors," *Sensors and Actuators A: Physical,* vol. 56, pp. 211-219, 1996.

[95] D. N. Alleyne and P. Cawley, "The interaction of Lamb waves with defects," *Ultrasonics, Ferroelectrics and Frequency Control, IEEE Transactions on,* vol. 39, pp. 381-397, 1992.

[96] R. Briers, O. Leroy, G. N. Shkerdin, and Y. V. Gulyaev, "Mode theory as a framework for the investigation of the generation of a Stoneley wave at a liquid--solid interface," *The Journal of the Acoustical Society of America,* vol. 95, pp. 1953-1966, 1994.

[97] S. W. Wenzel and R. M. White, "Analytic comparison of the sensitivities of bulk-wave, surface-wave, and flexural plate-wave ultrasonic gravimetric sensors," *Applied Physics Letters,* vol. 54, pp. 1976-1978, 1989.

[98] H. H. Cheng, C. N. Andrew, and M. M. Alkaisi, "The fabrication and characterisation of metallic nanotransistors," *Microelectronic Engineering,* vol. 83, pp. 1749-1752, Apr-Sep 2006.

[99] H. W. Huang, J. T. Chu, C. C. Kao, T. H. Hseuh, T. C. Lu, H. C. Kuo, S. C. Wang, and C. C. Yu, "Enhanced light output of an InGaN/GaN light emitting diode with a nano-roughened p-GaN surface," *Nanotechnology,* vol. 16, pp. 1844-1848, Sep 2005.

[100] T. Toriyama, Y. Tanimoto, and S. Sugiyama, "Single crystal silicon nano-wire piezoresistors for mechanical sensors," *Journal of Microelectromechanical Systems,* vol. 11, pp. 605-611, Oct 2002.

[101] X. D. Wang, J. H. Song, J. Liu, and Z. L. Wang, "Direct-current nanogenerator driven by ultrasonic waves," *Science,* vol. 316, pp. 102-105, Apr 6 2007.

[102] C. A. Mirkin, R. L. Letsinger, R. C. Mucic, and J. J. Storhoff, "A DNA-based method for rationally assembling nanoparticles into macroscopic materials," *Nature,* vol. 382, pp. 607-609, 1996.

[103] M. R. Falvo, J. Steele, R. M. Taylor, and R. Superfine, "Gearlike rolling motion mediated by commensurate contact: Carbon nanotubes on HOPG," *Physical Review B,* vol. 62, pp. R10665-R10667, Oct 15 2000.

[104] R. Krupke, F. Hennrich, H. von Lohneysen, and M. M. Kappes, "Separation of metallic from semiconducting single-walled carbon nanotubes," *Science,* vol. 301, pp. 344-347, Jul 18 2003.

[105] P. J. Pauzauskie, A. Radenovic, E. Trepagnier, H. Shroff, P. D. Yang, and J. Liphardt, "Optical trapping and integration of semiconductor nanowire assemblies in water," *Nature Materials,* vol. 5, pp. 97-101, Feb 2006.

[106] M. Chen, L. Sun, J. E. Bonevich, D. H. Reich, C. L. Chien, and P. C. Searson, "Tuning the response of magnetic suspensions," *Applied Physics Letters,* vol. 82, pp. 3310-3312, May 12 2003.

[107] P. D. Yang, "Wires on water," *Nature,* vol. 425, pp. 243-244, Sep 18 2003.

[108] B. Messer, J. H. Song, and P. D. Yang, "Microchannel networks for nanowire patterning," *Journal of the American Chemical Society,* vol. 122, pp. 10232-10233, Oct 18 2000.

[109] L. A. Giannuzzi and F. A. Stevie, *Introduction to Focused Ion Beams*: Springer, 2005.

[110] J. A. Rogers, A. A. Maznev, M. J. Banet, and K. A. Nelson, "Optical generation and characterization of acoustic waves in thin films: Fundamentals and applications," *Annual Review of Materials Science,* vol. 30, pp. 117-157, 2000.

[111] J. A. Rogers, "Complex acoustic waveforms excited with multiple picosecond transient gratings formed using specially designed phase-only beam-shaping optics," *J. Acoust. Soc. Am.,* vol. 104, 1998.

[112] A. I. Persson, B. J. Ohlsson, S. Jeppesen, and L. Samuelson, "Growth mechanisms for GaAs nanowires grown in CBE," *Journal of Crystal Growth,* vol. 272, pp. 167-174, Dec 10 2004.

[113] K. B. Howell, *Principles of Fourier Analysis*: Chapman and Hall/CRC, 2001.

[114] A. Hirose and K. E. Lonngren, "Introduction to Wave Phenomena," John Wiley & Sons, 1985.

[115] C. Claudio, K. Shant, B. B. Djordjevic, E. G. Robert, and P. Antonino, "Generation of narrowband antisymmetric lamb waves using a formed laser source in the ablative regime," *Ultrasonics, Ferroelectrics and Frequency Control, IEEE Transactions on,* vol. 54, pp. 147-156, 2007.

[116] B. A. Buchine, R. Westafer, and D. H. William, "Acoustic "Tweezers" For Non-Contact Manipulation of One-Dimensional Microstructures and Nanomaterials," *Pending Submission,* 2007.

[117] D. M. Pozar, *Microwave Engineering*, Third Edition ed. Hoboken, NJ: John Whiley and Sons, Inc., 2005.

[118] A. L. Kipling and M. Thompson, "Network Analysis Method Applied to Liquid-Phase Acoustic-Wave Sensors," *Analytical Chemistry,* vol. 62, pp. 1514-1519, Jul 15 1990.

[119] A. Arnau, *Piezoelectric Transducers and Applications*. New York, NY: Springer, 2004.

[120] D. Damjanovic, "Ferroelectric, dielectric and piezoelectric properties of ferroelectric thin films and ceramics," *Reports on Progress in Physics,* vol. 61, pp. 1267-1324, Sep 1998.

[121] G. Sauerbrey, *Zeitschrift Fur Physik,* vol. 155, pp. 206-222, 1959.

[122] B. D. Vogt, E. K. Lin, W. L. Wu, and C. C. White, "Effect of film thickness on the validity of the Sauerbrey equation for hydrated polyelectrolyte films," *Journal of Physical Chemistry B,* vol. 108, pp. 12685-12690, Aug 26 2004.

[123] C. G. Fox and J. F. Alder, "Surface Acoustic-Wave Sensors for Atmospheric Gas Monitoring - a Review," *Analyst,* vol. 114, pp. 997-1004, Sep 1989.

[124] B. Navinsek, P. Panjan, and A. Zabkar, "A Comparison of Sputtered Ni/Cr Interface Depth Resolution as Obtained by the Quartz Crystal Microbalance Mass-Loss Method and Auger-Spectroscopy," *Journal of Vacuum Science & Technology a-Vacuum Surfaces and Films,* vol. 3, pp. 671-673, 1985.

[125] Y. Okahata and H. Ebato, "Application of a Quartz-Crystal Microbalance for Detection of Phase-Transitions in Liquid-Crystals and Lipid Multibilayers," *Analytical Chemistry,* vol. 61, pp. 2185-2188, Oct 1 1989.

[126] M. I. S. Verissimo, J. A. B. P. Oliveira, and M. T. S. R. Gomes, "The evaluation of copper contamination of food cooked in copper pans using a piezoelectric quartz crystal resonator," *Sensors and Actuators B-Chemical,* vol. 111, pp. 587-591, Nov 11 2005.

[127] J. Rickert, T. Weiss, W. Kraas, G. Jung, and W. Gopel, "A new affinity biosensor: Self-assembled thiols as selective monolayer coatings of quartz crystal microbalances," *Biosensors & Bioelectronics,* vol. 11, pp. 591-598, 1996.

[128] C. T. C. Nguyen, "Micromechanical resonators for oscillators and filters," 1995, pp. 489-499 vol.1.

[129] K. M. Lakin, "Thin film resonators and filters," 1999, pp. 895-906 vol.2.

[130] M.-A. Dubois, "Thin Film Bulk Acoustic Wave Resonator: A Technology Overview," *MEMSWAVE 03,* 2003.

[131] Q. X. Su, P. Kirby, E. Komuro, M. Imura, Q. Zhang, and R. Whatmore, "Thin-film bulk acoustic resonators and filters using ZnO and lead-zirconium-titanate thin films," *Microwave Theory and Techniques, IEEE Transactions on,* vol. 49, pp. 769-778, 2001.

[132] R. C. Ruby, P. Bradley, Y. Oshmyansky, A. Chien, and J. D. Larson, III, "Thin film bulk wave acoustic resonators (FBAR) for wireless applications," 2001, pp. 813-821 vol.1.

[133] D. L. DeVoe, "Piezoelectric thin film micromechanical beam resonators," *Sensors and Actuators a-Physical,* vol. 88, pp. 263-272, Mar 5 2001.

[134] G. Piazza, R. Abdolvand, G. K. Ho, and F. Ayazi, "Voltage-tunable piezoelectrically-transduced single-crystal silicon micromechanical resonators," *Sensors and Actuators a-Physical,* vol. 111, pp. 71-78, Mar 1 2004.

[135] Y. Ahn, H. Guckel, and J. D. Zook, "Capacitive microbeam resonator design," *Journal of Micromechanics and Microengineering,* vol. 11, pp. 70-80, Jan 2001.

[136] J. D. Zook, D. W. Burns, H. Guckel, J. J. Sniegowski, R. L. Engelstad, and Z. Feng, "Characteristics of Polysilicon Resonant Microbeams," *Sensors and Actuators a-Physical,* vol. 35, pp. 51-59, Oct 1992.

[137] S. H. Park, B. C. Seo, G. Yoon, and H. D. Park, "Two-step deposition process of piezoelectric ZnO film and its application for film bulk acoustic resonators,"

Journal of Vacuum Science & Technology a-Vacuum Surfaces and Films, vol. 18, pp. 2432-2436, Sep-Oct 2000.

[138] T. Xu, G. Y. Wu, G. B. ZHang, and Y. L. Hao, "The compatibility of ZnO piezoelectric film with micromachining process," *Sensors and Actuators a-Physical,* vol. 104, pp. 61-67, Mar 15 2003.

[139] Agilent, "Exploring the Architecture of Network Analyzers," *Application Note,* vol. 1287-2, p. 12, 2000.

[140] Agilent, "Network Analysis - Fundamentals of Vector Network Analysis," *Application Note,* vol. 1287-1, 2000.

[141] R. Krimholt, D. A. Leedom, and G. L. Matthaei, "New Equivalent Circuit for Elementary Piezoelectric Transducers," *Electronics Letters,* vol. 6, p. 2, 1970.

[142] Harrie A.C. Tilmans, Dominicus A. Untema, and J. H. J. Fluitman, "Single Element Excitation and Detection of (Micro-) Mechanical Resonators," *Proc. Transducers'91,* 1991.

[143] L. A. Giannuzzi and F. A. Stevie, *Introduction to Focused Ion Beams*: Springer, 2005.

[144] Agilent, "Network Analysis Basics - Applying Error Correction To Network Analyzer Measurements," *Application Note,* vol. 1287-3, 2002.

[145] J. F. Rosenbaum, *Bulk Acoustic Wave Theory and Devices*. Norwood, MA: Artech House, Inc., 1945.

[146] R. C. Ruby, P. Bradley, Y. Oshmyansky, A. Chien, and J. L. III, "Thin Film Bulk Wave Acoustic Resonators (FBAR) For Wireless Applications," *Agilent Technologies*.

[147] C. D. Corso, A. Dickherber, and W. D. Hunt, "Lateral field excitation of thickness shear mode waves in a thin film ZnO solidly mounted resonator," *Journal of Applied Physics,* vol. 101, p. 054514, 2007.

[148] W. Pang, H. Yu, J. W. Kwon, H. Zhang, and E. S. Kim, "Self-aligned lateral field excitation film acoustic resonator with very large electromechanical coupling [FBAR]," in *Frequency Control Symposium and Exposition, 2004*, 2004, pp. 558-561.

[149] M. J. Madou, *Fundamentals of Microfabrication: The Science of Miniaturization*, 2nd ed.: CRC Press LLC, 2002.

[150] J. H. Song, X. D. Wang, E. Riedo, and Z. L. Wang, "Elastic property of vertically aligned nanowires," *Nano Letters,* vol. 5, pp. 1954-1958, Oct 2005.

[151] X. G. Liu, L. Fu, S. H. Hong, V. P. Dravid, and C. A. Mirkin, "Arrays of magnetic nanoparticles patterned via "dip-pen" nanolithography," *Advanced Materials,* vol. 14, pp. 231-+, Feb 5 2002.

[152] J. Tien, A. Terfort, and G. M. Whitesides, "Microfabrication through electrostatic self-assembly," *Langmuir,* vol. 13, pp. 5349-5355, Oct 1 1997.

[153] R. R. He, D. Gao, R. Fan, A. I. Hochbaum, C. Carraro, R. Maboudian, and P. D. Yang, "Si nanowire bridges in microtrenches: Integration of growth into device fabrication," *Advanced Materials,* vol. 17, pp. 2098-+, Sep 5 2005.

[154] R. R. He and P. D. Yang, "Giant piezoresistance effect in silicon nanowires," *Nature Nanotechnology,* vol. 1, pp. 42-46, Oct 2006.

[155] J. F. Conley, L. Stecker, and Y. Ono, "Directed integration of ZnO nanobridge devices on a Si substrate," *Applied Physics Letters,* vol. 87, pp. -, Nov 28 2005.

[156] P. X. Gao, J. H. Song, J. Liu, and Z. L. Wang, "Nanowire piezoelectric nanogenerators on plastic substrates as flexible power sources for nanodevices," *Advanced Materials,* vol. 19, pp. 67-+, Jan 8 2007.

[157] P. Gao, J. Liu, B. A. Buchine, B. Weintraub, Z. L. Wang, and J. L. Lee, "Bridged ZnO Nanowires Across Trenched Electodes," *Submitted to Applied Physics Letters,* 2007.

[158] B. A. Buchine, B. Weintraub, and Z. L. Wang, "Site-Specific Growth of 1-Dimensional Nanostructures for MEMS Integration and Bulk Fabrication," *Pending Submission,* 2007.

[159] C. Multiphysics, "COMSOL user's Guide," 2006.

[160] D. Halliday, R. Resnick, and J. Walker, *Fundamentals of Physics Extended*, 5th ed.: John Wiley & Sons, Inc., 1997.